INVESTIGATION ON SOLAR-INTERPLANETARY AND MAGNETOSPHERE COUPLING AND GEOEFFECTIVENESS

by

R. SELVAKUMARAN

A Thesis submitted to the Andhra University
for the degree of

DOCTOR OF PHILOSOPHY
in
PHYSICS
September, 2016

Under the Supervision of

Prof. B.VEENADHARI
Research Supervisor (Internal)
Indian Institute of Geomagnetism
Kalamboli Highway
New Panvel
Navi Mumbai – 410218

Prof. D.S.V.V.D. PRASAD
Research Supervisor (External)
Department of Physics
Andhra University
Visakhapatnam
Andhra Pradesh – 530003

Research work carried out at

Indian Institute of Geomagnetism

Navi Mumbai, India

Dedicated to my parents and brothers...

Declaration

I hereby declare that the thesis entitled **Investigation on Solar-interplanetary and magnetosphere coupling and geoeffectiveness** is my original research work carried out at the Indian Institute of Geomagnetism (IIG), and that no part thereof has been submitted for any other degree or diploma in any University or Institution.

The literature related to the problem investigated has been clearly indicated as such and included in the references. Due acknowledgements have been made wherever necessary.

R.Selvakumaran
Indian Institute of Geomagnetism
New Panvel, Navi Mumbai
Maharashtra
India- 410218

Certificate

This is to certify that the thesis entitled "Investigation on Solar-interplanetary and magnetosphere coupling and geoeffectiveness" submitted by Mr. R. Selvakumaran to Andhra University for the degree of Doctor of Philosophy is based on his original studies carried out by him under our supervision. We hereby certify that neither this thesis nor any part of it has been submitted for any degree/diploma or any other academic award anywhere before. It is further certified that the material obtained from other sources have been duly acknowledged in the thesis.

Prof. B. Veenadhari
Research Supervisor (Internal)
Indian Institute of Geomagnetism
New Panvel
Navi Mumbai
Maharashtra
India- 410218

Prof. D.S.V.V.D. Prasad
Research Supervisor (External)
Department of Physics
College of Science and Technology
Andhra University
Visakhapatnam
India- 530017

Acknowledgements

One of my dream comes true by completing the Ph.D. thesis. I have taken much efforts in completing this thesis, however it wouldn't have been possible without kind support and help of many individuals. Foremost, I would like to express my sincere gratitude to my research advisor Prof. B.Veenadhari for the continuous support of my Ph.D study and research, for her patience, motivation, enthusiasm, and immense knowledge. Her guidance helped me in all the time of research and writing of this thesis. I could not have imagined having a better advisor and mentor for my Ph.D study. Besides my advisor, I would like to thank Dr. Rajesh Singh for his insightful comments and encouragement, but also for the hard question which made me to widen my research from various perspectives. He has taught me, both consciously and unconsciously, how good experimental physics is done. I appreciate all his contributions of time, ideas to make my Ph.D. experience productive and stimulating.

My sincere thanks also goes to Prof. D.S.V.V.D. Prasad for being my external guide from the Department of Physics, Andhra University. Without his kind and generous help during my registration and further official formalities, it would never have been possible to attain this completion. I also would like to thank the academic staffs at the Physics department, Andhra University for extending their help in whatever possible means. One more person from Andhra University I wish to thank is Ph.D. student Srinivas, Andhra university, he was very helpful since from the process of registration till my submission of theis. My word fall short to thank Ramana sir. He was the person behind all the stages of my official process at Andhra University. I am grateful to have a well wisher like him in my life.

I would like to express my sincere thanks to Prof. D.S Ramesh, Director, Indian Institute of Geomagnetism (IIG), Navi Mumbai and Ex-Directors of IIG, for their kind cooperation and encouragement which helped me in completion of my Ph.D. and concern. I wish to thank the academic committee of IIG for cooperation and encouragement during the course of my thesis. I thank all admin, documentation, computer section and Library staff for their invaluable help during my Ph.D work.

I take this opportunity to sincerely thank Prof Nat Gopalswamy, GSFC, NASA and his team, who has fulfilled one of my precious dream of carrying out research work at NASA for three months. The scientific discussions and knowledge gained at NASA is very much valuable for my research career.

I will be very thankful to my senior Dr. Ajeet Kumar Maurya. He was not only senior, but was like companion thorough out my research career. Starting from programming, data analysis and many more aspects of my current research was taught by him. And the field experience shared with him is really a memorable one. Next my thanks goes to Sandeep kumar, we have shared lots of memorable moments in research as well enjoyous moment outside. Next comes another junior whom I wish to thank is Sneha. She was very helpful in the later part of my research career. And she is the one who stood with me during my tough times at IIG. I would like to thank and appreciate her for being with me. I would also like to thank Venky, who is always cheerful and we shared many happy moments in research as well as personal life.

Well, One of the most important person in my life and because of him am here and completing my thesis thats Dr Deva anna. He is my first point of contact at IIG and still he is the one with me, hope this tells every ting about this relation. What more I can say he is my brother and he will be. Next comes a turn to thank my dear senior friends Dr. Chins and Dr. Remya. They were like a family to me at IIG. They took care of me as their brother. Never heard a no from them either it is academic, personal or financial. I was blessed to be with them. Next comes my friend Mahesh babu whom I can share every thing. He deserves a big thanks from me and he is the person whom I trust and can talk freely with out any hesitation. I wish to express my thanks to Dr. Jeni. Though he is at EGRL we share each and every moment in our life. This has shown me distance doesn't matter. My special thanks goes to Dr Nisha, who is such a friendly senior and friend of mine through out my Ph.D. and still goes on. I would like to thank Mrs Ritu who has joined Ph.D. with me and she was my first Hindi teacher at IIG. We cherished many beautiful moments together at the start of my Ph.D.

Apart from this I express my sincere thanks to my seniors Anand ji, Reshmi ji, Prasant ji, Arif ji,

Mahesh ji, Lakshmi anna, Manu anna and Jayashree ka, my first sister at IIG. I record my sincere thanks to my other friends at IIG Viru, Jayant, Ankush, and Sreeba with whom I spent most of my personal time. A Person who deserves special thanks is Mr Sreeraj T. Never seen such a perfect man ever before, and he was there to help me when ever needed. I extend my sincere gratitude to Rahul ji. Never felt he was very much senior to me. He is very friendly and he has helped me when ever I had problem in programming.

The best relationship in a life one can get is the friendship. I am lucky enough to have them as count as stars. At first i would like to thank my childhood friends Deepak, Kums and Abu. Our friendship have grown big as like our age. I never felt lonely or down through out my research career is because of big bunch of my school friends. Few to mention Baba, Nattu, Vidya, Ayya, Kali, Machi, Donk, Sundi, Gopi, Deepan, Subbu, Arun, Ravi, Siva, Vinoth, kanna, Monk and many more. When I start chatting with them in group literally I go to school age, free from all worries in the World. I am lucky to have them still in contact more than one and half decade. I cannot end with out thanking my OIC friends Criccs, Jack, cool, Nisha, Jim, Mokkai, Srini, Auto and Covai Uncle. I have shared most of my funniest moment with them in last 5 years.

Finally the words close to my heart mom, dad and my brothers. The person what am now was their dream and I am very much grateful to them. I could with stand my tough time at IIG is only because of the will power which my mom and dad gave and the support which my karthi anna and Vinoth anna gave. And I also would like to thank both my sister in laws being part of this support. I am nothing with out them in my life. And at last I would like to thank super natural power who drives us all in the universe.

R.Selvakumaran
Navi Mumbai

Contents

List of publications

1) **R. Selvakumaran**, Ajeet K.Maurya, Sneha A.Gokani, B.Veenadhari, Sushil Kumar, K. Venkatesham, D. V. Phanikumar, Abhay K.Singh, Devendraa Siingh, Rajesh Singh, Solar flares induced D-region ionospheric and geomagnetic perturbations, J. Atmos. Space Terr. Phys., 123(2015) 102112.

2) B. Veenadhari, **R. Selvakumaran**, R. Singh, A. K. Maurya, N. Gopalswamy, S. Kumar, T. Kikuchi (2012), CME-driven shocks and the associated sudden commencements/sudden impulses, J. Geophysical. Res., 117, A04210, doi:10.1029/2011JA017216.

3) **R. Selvakumaran** , B.Veenadhari , S.Akiyama, Megha Pandya , N.Gopalswamy, S. Yashiro, Sandeep kumar, P. Makela , H. Xie, On the reduced geoeffectiveness of solar cycle 24: a moderate storm perspective, J. Geophysical. Res., 121, 10.1002/2016JA022885.

4) **R. Selvakumaran** , B.Veenadhari ,Y. Ebihara, Sandeep kumar, D.S.V.V.D Prasad The role of interplanetary shock orientation on SC/SI rise time and geoeffectiveness, ASR, 10.1016/j.asr 2016.12.010.

5) Sandeep Kumar, B Veenadhari, S Tulasi Ram, **R. Selvakumaran**, Shyamoli Mukherjee, Rajesh Singh, BD Kadam (2015), Estimation of interplanetary electric field conditions for historical geomagnetic storms, J. Geophysical. Res., 120, 10.1002/2015JA021661.

6) Sneha A. Gokani, Rajesh Singh, Morris B. Cohen, Sushil Kumar, K. Venkatesham, Ajeet K. Maurya, **R. Selvakumaran** and J. Litchtenberger (2015), Very low latitude (L=1.08) whistlers and correlation with lightning activity, J. Geophysical. Res., 10.1002/2015JA021058.

7) R. Singh, A. K. Maurya, **R. Selvakumaran**, S. A. Gokani, R. Selvakumaran, M. B. Cohen, O. Chanrion, T. Neubert (2014), First Observations of Transient Luminous Events (TLEs) in Indian sub-continent, Current Science, 107, 7, October 2014

8) Srivastava, P. R., S. A. Gokani, A. K. Maurya, R. Singh, S. Kumar, B. Veenadhari, **R. Selvakumaran**, A. K. Singh, J. Lichtenberger (2013), One-to-one relationship between low latitude

whistlers and conjugate source lightning discharges and their propagation characteristics, ASR, 52, 1966-1973.

9) Maurya, A. K., B. Veenadhari, R. Singh, S. Kumar, M. B. Cohen, **R. Selvakumaran**, S. Gokani, P. Pant, A. K. Singh, and U. S. Inan (2012), Nighttime D-region electron density measurements from ELF-VLF tweek radio atmospherics recorded at low latitudes, J. Geophysical. Res., 117, A11308, 10.1029/2012JA017876.

10) Maurya, A. K., R. Singh, B. Veenadhari, S. Kumar, M. B. Cohen, **R. Selvakumaran**, P. Pant, A. K. Singh, D. Siingh and U. S. Inan (2012), Morphological features of tweeks and nighttime D-region ionosphere at tweek reflection height from the observations in the low latitude Indian Sector, J. Geophysical. Res., 117, A05301, 10.1029/2011JA016976.

11) Singh, R., B. Veenadhari, A. K. Maurya, M. B. Cohen, S. Kumar, **R. Selvakumaran**, P. Pant, A. K. Singh, and U. S. Inan (2011), D region ionosphere response to the total solar eclipse of 22 July 2009 deduced from ELFVLF tweek observations in the Indian sector, JGR, 116, A10301, 10.1029/2011JA016641.

12) A. K. Maurya, **R. Selvakumaran**, R. Singh, B. Veenadhari (2011), Characteristics of tweeks radio atmospherics observed in Indian low latitude region using AWESOME VLF receiver, XXXth URSI General Assembly, IEEE Xplore Conference Proceedings, 13-20, 1109/URSIGASS.2011.6051176.

Presentation in Conference / Symposium / Workshop:

1) R. Selvakumaran, Ajeet K Maurya, B.Veenadhari and Rajesh Singh, Studies of Solar flares induced perturbation in D region ionosphere, Asia Oceania Geosciences Society (AOGS), 5-9 July, 2010, Hyderabad, India. (Oral)

2) Ajeet K. Maurya, Rajesh Singh, R. Selva kumaran and B. Veenadhari, Seismic effects on the sub-ionospheric VLF signals: Results from the studies of some recent Earthquakes, International Workshop on Seismo-Electricomagnetics and Atmospheric Science (IWES-AS-2010), 16-18 November, 2010. (Oral)

3) R. Selvakumaran ,Ajeet K. Maurya, Rajesh Singh, and B. Veenadhari, Application of tweek radio atmospherics in D region ionosphere studies, International Workshop on Seismo-Electricomagnetics and Atmospheric Science (IWES-AS-2010), 16-18 November, 2010. (Oral)

4) Ajeet K Maurya, R. Selvakumaran, R. Singh, B. Veenadhari, , Characteristics of tweek radio atmospheric observed in Indian low latitude region using AWESOME VLF receiver, XXX URSI general assembly, Istanbul, Turkey, August 13-20, 2011 (Poster).

5) R. Singh, Ajeet K Maurya, B.Veenadhari, R. Selvakumaran, D-region electron density measurements from tweek radio atmospherics observations in India, XXX URSI general assembly, Istanbul, Turkey, August 13-20, 2011 (Poster).

6) Maurya, A. K., R. Singh, B. Veenadhari, S. Kumar, M. B. Cohen, R. Selvakumaran, P. Pant, A. K. Singh, and U. S. Inan, Night time D-region electron density measurements from tweek radio atmospherics recorded at low latitudes, AWESEOM, VLF workshop, GOA, India, (Oral)

7) R. Selvakumaran, Ajeet K. Maurya, B. Veenadhari, Rajesh Singh, P.Pant, Solar flare effects on D region ionosphere using VLF waves and modeling, AWESEOM, VLF workshop, GOA, India, (Oral).

8) P. Pant, Ajeet K. Maurya, R. Selvakumaran, Rajesh Singh, B. Veenadhari and Abhay K. Singh, Amplitude and phase variations of VLF wave during major space weather events in February 2011, AWESEOM, VLF workshop, GOA, India, (Poster).

9) R. Selvakumaran, B. Veenadhari Rajesh Singh, A. K. Maurya, N. Gopalswamy, Sushil Kumar, T. Kikuchi, CME-driven shocks and the associated sudden commencements/sudden impulses, Poster presented in NSSS, held at Mysore, Feb14-17, 2012.

10) R. Selvakumaran, Ajeet K Maurya, B.Veenadhari, Rajesh Singh, P.Pant(2012), Study of Solar flare effects on D-region ionosphere and signatures on equatorial geomagnetic observations and Modeling, Paper presented in 39th Cospar assembly held at Mysore, India ,July 14-22 ,2012.

11) Ajeet K Maurya, B.Veenadhari, Rajesh Singh, R. Selvakumaran, H.Ohyo, P.Pant, A.K.Singh, Space Studies of the Upper Atmospheres of the Earth and Planets including Reference Atmospheres, Paper presented in 39th Cospar assembly held at Mysore, India ,July 14-22 ,2012.

12) GokaniSneha,Ajeet Maurya, RajeshSingh, R. Selvakumaran,B.Veenadhari, Low Latitude (L=1.17) Whistlers: Correlation with its causative Lightning activity and Geomagnetic activity dependence, Paper presented in 39th Cospar assembly held at Mysore, India ,July 14-22 ,2012

13) B.Veenadhari, Rajesh Singh, Ajeet K Maurya ,Tulasiram Sudarsanam, R.Selvakumaran, Response of topside ionosphere to a geomagnetic storm and total solar eclipse, Paper presented in 39th Cospar assembly held at Mysore, India ,July 14-22 ,2012.

14) R.Selvakumaran, B.Veenadhari, Sandeep kumar , P.K. Manoharan, Long term geomagnetic variation in comparison with Interplanetary scintillation measurements, ISSTP conference November 2012,Pune.(Poster).

15) R.Selvakumaran, B.Veenadhari, Sandeepkumar, P.K.Manoharan, Long term geomagnetic variation in comparison with Interplanetary scintillation measurements, Poster presented in ISSTP, held at Pune , Nov 6-9, 2013.

16) R.Selvakumaran, B.Veenadhari, Sandeepkumar, N. Gopalswamy, Coronal Mass Ejection-driven IP shocks and associated magnetic storms of solar cycle 23, Poster presented in AOGS 2013, held at Brisbane, Australia, June 24-28, 2013.

List of Figures

List of Tables

Chapter 1

Introduction

1.1 General background: Space Weather

The Sun is a fiery ball of gas that reaches such extreme temperatures such that the gas flies out from it at very high speeds. In fact, many of the electrons in the Sun's atoms have enough energy to leave the atoms. The abandoned charged atoms are called ions. These ions and electrons flow outward from the Sun, and together they are known as the Solar wind. When the solar wind travels with the interplanetary magnetic field for short, the charged particles and magnetic fields interact with Earth's magnetic field. Earth's magnetic field as its stretches out in space is known as magnetosphere.The solarwind pushes on the side of the magnetosphere facing the Sun, pulls it out on the side facing away from the Sun.

The fiery Sun goes through some markedly different cycles and this cause changes in the geospace environment. The dynamic and variable conditions in the geospace including those in the Sun, in the interplanetary medium and in the ionosphere-magnetosphere system to the ground referred as Space weather. Space weather is greatly influenced by the speed and density of the solar wind and the interplanetary magnetic field (IMF) carried by the solar wind plasma. A variety of physical systems are associated with space weather. These include storms, substorms, energization

of Van Allen radiation belts, geomagnetic activity, ionospheric disturbances scintillations, aurorae and geomagnetically induced currents at Earth′s surface. Solar flares, Coronal mass ejections, Solar energetic particles are important drivers of space weather as they can compress magnetosphere, trigger geomagnetic storms and damage many electronics installation onboard spacecraft and affect human life. As our dependance on technological systems operating in and through the outer reaches of our terrestrial environment is continuously increasing we are now concerned more than even before on conditions in the upper atmosphere, the ionosphere, the magnetosphere, the interplanetary space and the Sun itself which is primary source not only to our terrestrial system but also to the entire interplanetary domain.

As the sophistication of our space based technological systems increases rapidly, their vulnerability of disturbance in space weather also increases. Our competence in not only understanding but also in predicting space weather should be built up to protect our space systems and also to design robust systems that will be less suspectable to hazards from space weather conditions. Performance of modern satellites used in global communications, weather predictions, remote sensing, defense system and a variety of ground-based scientific and operational systems depends on information we have on space weather. It is for this very purpose in this thesis, the efforts have been taken to study the cause and effect of space weather phenomena.

1.2 The Sun: As Star

The Sun is the closest star to the Earth and it is the center of our solar system. Like all other stars, the Sun is a giant, spinning ball of very hot gas, and it is fuelled by nuclear fusion reactions and held together by its own gravity. The Sun is a normal main-sequence G2 star, one of more than 100 billion stars in our galaxy. It is often said that the Sun is an “ordinary” star. That’s true in the sense that there are many others similar to it. The median size of stars in our galaxy is probably less than half the mass of the Sun. The sun lies at the heart of the solar system, where it is by far the largest object. The age of the Sun is 4.6 billion years and is at the average distance of 1.4×10^{8}

km from the Earth [Noyes, 1982]. The Sun is the largest object in the Solar System, accounting for 99.86% of the mass. The Sun has the diameter that is measured to be 1.39×10^{9}m and the mass estimated to be 1.98×10^{30} kg. The Sun has an enormous amount of mass, and so it has a lot of gravity. The Sun's gravity pulls all of its mass (mostly hydrogen and helium) in to an almost perfect sphere. The Sun is mostly made up of hydrogen (about 92.1% of the number of atoms, 75% of the mass). Helium can also be found in the Sun (7.8% of the number of atoms and 25% of the mass). The other 0.1% is made up of heavier elements, mainly carbon, nitrogen, oxygen, neon, magnesium, silicon and iron. The Sun is neither a solid nor a gas but is actually plasma. This plasma is tenuous and gaseous near the surface, but gets denser down towards the Sun's fusion core. Down at the core of the Sun, the temperatures and pressures are so high that fusion reactions are possible. Since Sun is not a solid mass body it posses a differential rotation. Observations of the Sun reveal that different parts of the Sun rotate at different speeds. At its visible surface, the sun's equator rotates in 27-days and in 35-days near to the poles. The total energy emission of the sun, or luminosity, is 4×10^{26} watts. The Sun radiates energy in wide band that extends from Gamma rays, X-rays, UV light, visible light, heat waves and radio waves. These different wavelengths of light originate in the different part of the solar atmosphere. [Zirker, 2001].

1.3 Structure of the Sun

Much like the Earth, the Sun has many different layers that define its structure. Unlike the earth, the Sun is completely gaseous, there is no solid surface on the Sun. Although the Sun is completely made up of gas, the density and temperature of the gas changes drastically as one travel from the center to the outermost regions.

The Sun and its atmosphere are divided into several zones and layers. The solar interior, from the inside out, is made up of the core, radiative zone and the convective zone. The solar atmosphere above that consists of the photosphere, chromosphere, a transition region and the corona. Beyond that is the solar wind, an outflow of gas from the corona shown in Figure 1.1.

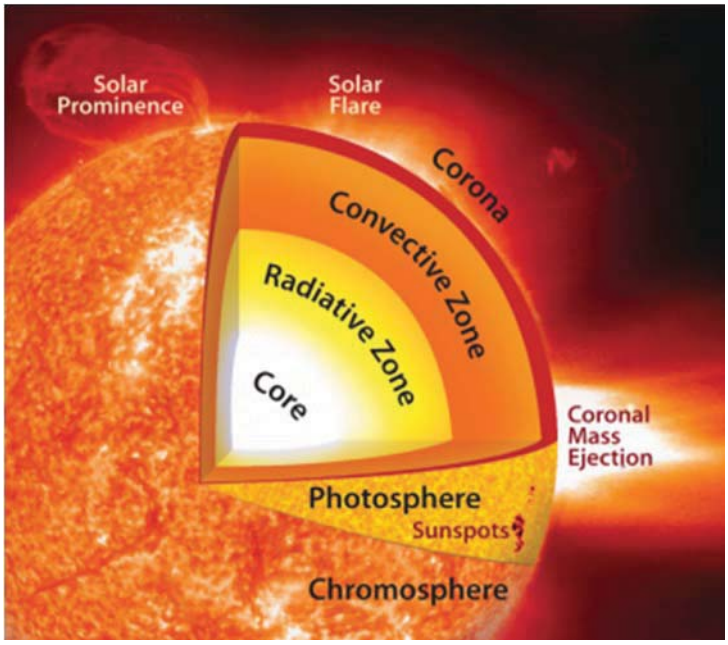

Figure 1.1: The Structure of Sun [www.nasa.gov].

1.3.1 Core

The extremely dense solar core holds about 50% of the Sun's total mass, but takes up only about 1.5 % of its total volume. The Sun's core has a very high temperature, more than 15 million K, and the material in the core is very tightly packed or dense. The high temperature provides the protons and electrons with a large amount of thermal energy and as a result they move around quite quickly. This motion, combined with the high density of the plasma, causes the particles to continuously slam into one another creating nuclear reactions. It is the fusion, or slamming together, of particular combinations of particles that provides the energy source of the Sun [Jenkins, 2009].

1.3.2 Radiation zone

The physical transport of energy from its production site to the surrounding regions can be done in a number of ways. However, for a star like the Sun, the most efficient means of transferring energy near the core is by radiation. Consequently, the region surrounding the core of the Sun is known as the radiation zone Throughout this region of the solar interior, energy, in the form of radiation is transferred by its interaction with the surrounding atoms. In the radiation zone of the Sun the temperature is little cooler than the core and as a result some atoms are able to remain intact. These intact atoms are able to absorb energy, store it for a while, and then later emit that energy as new radiation. In this manner the energy that is generated in the core is passed from atom to atom through the radiation zone [Seeds, 1994].

1.3.3 Convection zone

The convection zone reaches up to the Sun's surface, and makes up 66% of the Sun's volume but only a little more than 2 % of its mass. Roiling "convection cells" of gas dominate this zone. Two main kinds of solar convection cells exist, granulation cells about 600 miles (1,000 kilometers) wide and supergranulation cells about 20,000 miles (30,000 kilometers) in diameter. The most efficient means of energy transfer is now convection and we find ourselves in the region of the Sun's interior know as the convection zone. As the hot material reaches the top of the convection zone it begins to cool and sink, and as it sinks it heats up again and will rise. The hot material follows a direct path through the convective zone and the energy is transferred much faster than it is by radiation. It takes only a little more than a week for the hot material to carry its energy to the top of the convection zone [Seeds, 1994].

1.3.4 Photosphere

The photosphere is the beginning of the solar atmosphere and the lowest level one can see visually on the Sun. Below this layer, gas is so opaque that it is impossible to see through. It is about 300 miles (500 km) thick, although most of the light comes from its lowest third. Temperatures in the photosphere range from 11,000 K at bottom to 7,460 K at top. Energy is transported through the photosphere once again by radiation. Although the temperature of the photosphere is cool, about 5800 degrees K, the gas is thin enough that the atoms absorb and release energy. In fact, most of the light that we receive from the Sun on earth is energy that was released by atoms in the photosphere. It takes light from the Sun just over eight minutes to reach the earth. When the Sun is viewed through a solar telescope dark spots can be observed on the surface. These continuously changing dark regions are called Sunspots. The spots appear dark to the eye because they are cooler than the surrounding gas although they are still quite hot. The photosphere has a temperature of about 5800 degrees K and a typical Sunspot has a temperature about 3500 degrees K.

1.3.5 Chromosphere

Above the photosphere is a layer of gas, approximately 2000 km thick, known as the chromosphere or sphere of color. In the chromosphere energy continues to be transported by radiation. Hydrogen atoms absorb energy from the photosphere and most of the energy is then emitted as red light. The chromosphere is most easily viewed by filtering out all other wavelengths of light from the Sun and only letting the red light from the chromosphere through. Chromosphere show larger convective cell patterns. This large scale convection is known as super-granulation. Above the chromosphere is a very thin layer of the Sun's atmosphere about 100 km thick over which the temperature rises drastically from 20,000 degrees Kelvin in the upper chromosphere to over 2 million degrees Kelvin in the corona. This region is called the transition region.

1.3.6 Corona

The outermost layer of the Sun is called the corona. It gets its name from the crown like appearance evident during a total solar eclipse. The corona stretches far out into space and, in fact, particles from the corona reach the Earth's orbit. The corona is very thin and faint and therefore can only be seen from Earth during a total solar eclipse or by using a coronagraph telescope which simulates an eclipse by covering the bright solar disk. The temperature in the corona increases as we move outward. In lower corona, the temperature is about 500,000 K and in outer corona the temperature is about 35,00,000 K. The density of the outer corona is only about 1-10 atoms/cm^3. The shape of the corona is mostly determined by the magnetic field of the Sun. Particles from the corona also stream out along the magnetic field lines of the Sun that extend into interstellar space. The hot gases of the corona blow away from the Sun as solar wind. Here, solar wind is the moving outer extension of the corona [Seeds,1994].

1.4 The active Sun

The Sun shows a variety of signs of being active and dynamic. The Sun has long-term variations such as the solar cycle with a peak of activity every eleven years. On shorter time scales we see that the Sun also rotates about its axis. Sunspots and active regions appear around the Sun's eastern edge and disappear behind its western edge as the Sun rotates. In the coming section we will discuss the long and short term variation in the Sun.

1.4.1 Sunspots

Sunspots are dark, planet-sized regions that appear on the surface of the Sun. Sunspots are dark because they are colder than the areas around them. Sunspots correspond to concentrations of magnetic field flux that inhibit convection and result in reduced surface temperature compared

to the surrounding photosphere.The powerful magnetic field causes a sunspot by inhibiting a circulation. The center of the sunspot is at the temperature around 4240 K while the temperature of the photosphere is 5800 K. Figure 1.2 shows the appearance of the sunspot on the surface of the photosphere.

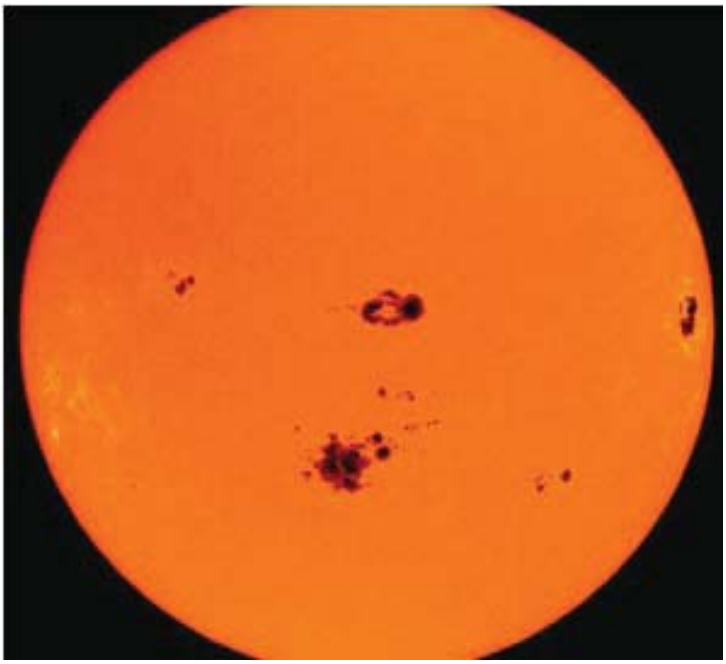

Figure 1.2: Appearance of Sunspot on the photosphere[www.nasa.gov]

.

Sunspots are only dark in contrast to the bright face of the Sun. Sunspots have a lighter outer section called the penumbra, and a darker middle region named the umbra. Figure 1.3 shows the schematic representation of Sunspot and the magnetic loops emerge out of the Sun from the cold region of the Sunspot in the photosphere.

Sunspots are caused by the Sun's magnetic field welling up to the photosphere, the Sun's visible surface. The powerful magnetic fields around sunspots produce active regions on the Sun. Sunspots form over periods lasting from days to weeks, and can last for weeks or even months. The average number of spots that can be seen on the face of the Sun is not always the same. The number of sunspots varies in a period of about 11 years. This is known as sunspot or Solar cycle. This solar

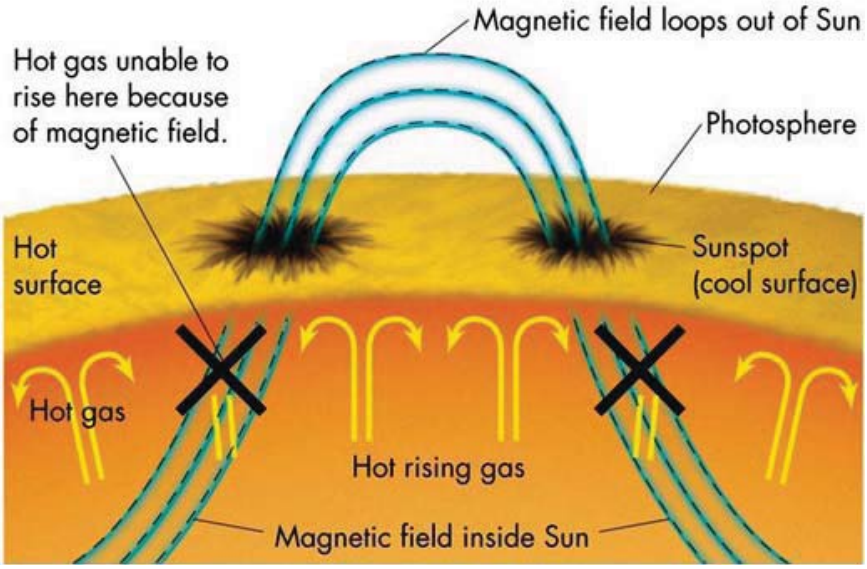

Figure 1.3: Schematic representation of Sunspot mechanism.[www.nasa.gov]

.

cycle was discovered in 1843 by Samuel Heinrich Schwabe, who after 17 years of observations noticed a periodic variation in the average number of sunspots seen from year to year on the solar disk [Schwabe, 1851].

At sunspot maximum there are often as many as 100 spots visible at any time, but at sunspot minimum there are only few sunspots. At the beginning of the sunspot cycle the spot begins to appear in the sun's middle latitudes about 35° above and below the sun's equator. As the cycle proceeds, the spots appear at lower latitudes, until, near the end of the cycle, they appear within the 5° of the sun's equator. If we plot the latitude of the appearance of sunspot versus time, the diagram takes the appearance of the butterfly wings. Such diagram is known as Maunder Butterfly diagram [Maunder, 1904] along with sunspot number presented in figure 1.4.

During a sunspot cycle, the faculae actually overwhelms the activity of the sunspots and make the Sun appear slightly (about 0.1%) brighter at sunspot maximum than at sunspot minimum. The sunspot number is calculated by first counting the number of sunspot groups and the number of

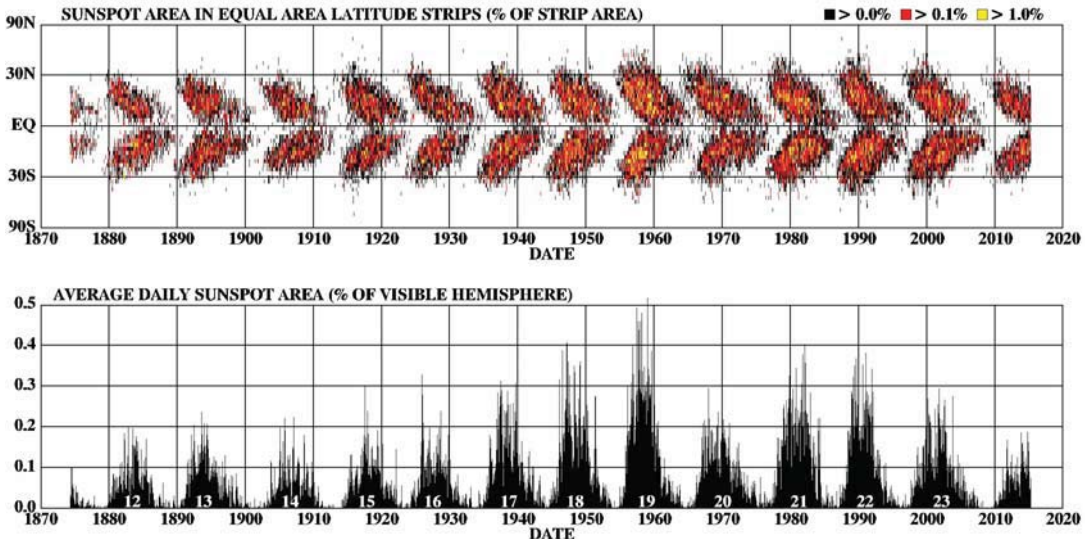

Figure 1.4: Butterfly diagram and sunspot number for solar cycles 11-23 [www.nasa.gov]

.

individual sunspots. Solar activity rises and falls with an 11-year cycle that affects the Earth's upper atmosphere by increase in extreme ultraviolet and X-ray emissions from the sun. Although the change in the total solar irradiance seems too small to produce significant terrestrial climatic effects, the earth's climate heats and cools up to certain extent as solar activity rises and falls [Hathaway, 2010]. This sunspots are said to be active regions resulting in short-term variation like solar flares, Coronal Mass Ejections (CMEs) and it affects Earth's magnetosphere ionosphere.

1.4.2 Solar eruptions

Solar eruptions are the natural phenomena occurring within the magnetically heated outer atmospheres in the Sun. These phenomena take many forms, including solar wind, radio wave flux, energy bursts such as solar flares, CMEs or solar eruptions, coronal heating and sunspots. These phenomena are generated by a helical dynamo near the center of the Sun's mass that generates strong magnetic fields and a chaotic dynamo near the surface that generates smaller magnetic field fluctuations. As discussed above the Sun can erupt energy in different ways which can reach Earth

and affect its environment.

1.4.3 Solar wind

The Sun emits the ionised gas, containing proton and electrons, in nearly equal number and is accompanied by trace amount of heavier elements such as helium, carbon, oxygen and iron. It is highly conducting plasma that blows away from the Sun in all directions, at the speed of several hundred to several thousand km per second, into the interplanetary space due to expansion of solar corona. This plasma, called the solar wind, varies in density, speed, temperature, strength and orientation of the magnetic field embedded within the flow. The solar wind plasma carries some of the solar magnetic field lines through interplanetary space [Akasofu and Kamide, 1987]. The solar magnetic field is frozen in the solar wind plasma because of its very high conductivity.

When the interplanetary magnetic field (IMF) changes from one polarity to other a current sheet is produced, called neutral sheet. This is termed as neutral sheet because the IMF shortly becomes zero as we move from one side to the other. The solar wind pulls the dominantly inward polarity below the current sheet and outward into the heliospehere. In this region the fast wind catches up and interacts with the slow wind. This interaction gives rise to solar wind compression region, where pressure, density, temperature, and magnetic field are enhanced. The interaction of IMF with the magnetosphere of a planet energizes the magnetospheric plasma and releases the magnetic energy, which causes geomagnetic storms and substorms [Baumjohann et al., 1996]. During the declining phase of the solar cycle, the Earth is affected by the coronal holes. Coronal holes emit fast solar wind, which when interacts with slow solar wind gives interaction region called corotating interaction region (CIR) [Tsurutani et. al., 2006].

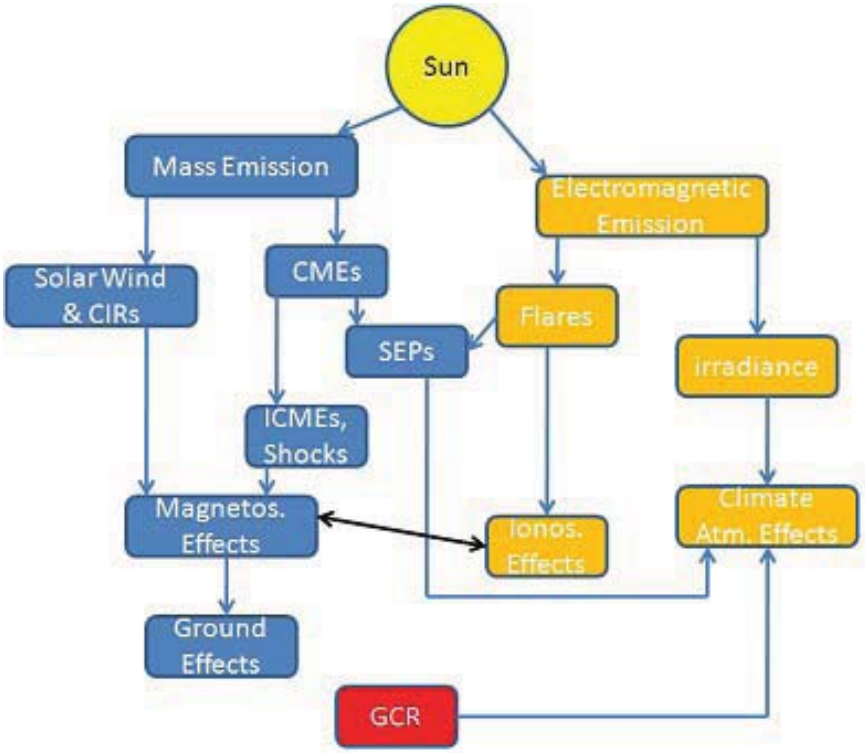

Figure 1.5: The two primary outputs (mass and electromagnetic emissions) from the Sun [Gopalswamy, 2007]

.

1.4.4 Primary outputs of active Sun

Figure 1.5 illustrates the two primary outputs (mass and electromagnetic emissions) from the Sun, whose variability affects the heliosphere in general and the geospace in particular [Gopalswamy, 2007]. The mass emission can be of Solar wind or CME. CMEs propagate in to the solar wind and drive shocks; the shocks accelerate Solar Energetic Particles (SEPs). When CMEs arrive at earth, they interact with earth's magnetosphere causing geomagnetic storms, which have multitude effects from the magnetosphere to the ground. This emission has nothing to do with mass like solar flares. Solar flares also accelerate particles, but generally over shorter duration and to lower intensity levels [Emslie et al ., 2004]. Both these emission have adverse effects in ionosphere as

well as magnetosphere.

1.4.5 Solar flares

Solar flares are sudden and intense brightening in localized area on the Sun's atmosphere. These are catastrophic release of energy extending over the entire electromagnetic spectrum from radio waves at the long wavelength end, through optical emission to X-rays and gamma rays at the short wavelength end. The energy released during a flare is typically of the order of 10^{27} ergs per second. Large flares can emit up to 10^{32} ergs of energy. Solar flares seems to be clearly linked to the magnetic field and they almost occur near the sunspot groups. Flare was first discovered in white light independently by two English amateur astronomers, R.Hodgson and R.C.Carrington while making sunspot sketches on September 1 , 1859 [Carrington, 1859 ; Hodgson, 1859]. They saw two bright patches breakout, intensify ($<$60 sec), move and then fade away all in 5 minutes.

The main driving force behind solar flares is the energy contained in the Sun's magnetic field. Like an elastic band, magnetic field stores energy when it is twisted on the Sun. The motions of the solar surface from which the field emanates does the twisting. This stores energy in the field in the form of additional tension and pressure. Solar flare occurs because the magnetic field can only store a limited amount of energy. When the energy in the field gets too large it is suddenly released into the solar atmosphere. It is not known exactly how the energy is released or how the complex magnetic configuration becomes unstable and the flare is triggered. Even it is unclear what happens after the energy is released and what fraction of energy goes into heating, particle acceleration, electromagnetic radiation, and mass motion, etc. It is also important to know the magnetic configuration in the pre-flare phase [Svestka 1976; Gosling 1993]. There are typically three stages to a solar flare. First is the precursor stage, where the release of magnetic energy is triggered. Soft X-ray emission is detected in this stage. In the second or impulsive stage, protons and electrons are accelerated to energies exceeding 1 MeV [http://hesperia.gsfc.nasa.gov/sftheory]. During the impulsive stage, radio waves, hard X-rays, and gamma rays are emitted. The gradual build up and decay of soft X-rays can be detected in the third, decay stage. The duration of these

stages can be as short as a few seconds or as long as an hour. Solar flares extend out to the layer of the Sun called the corona from the photosphere. Inside a flare, the temperature typically reaches up to 10 or 20 K, and can be as high as 100 million K. The frequency of flares coincides with the Sun's eleven year cycle.

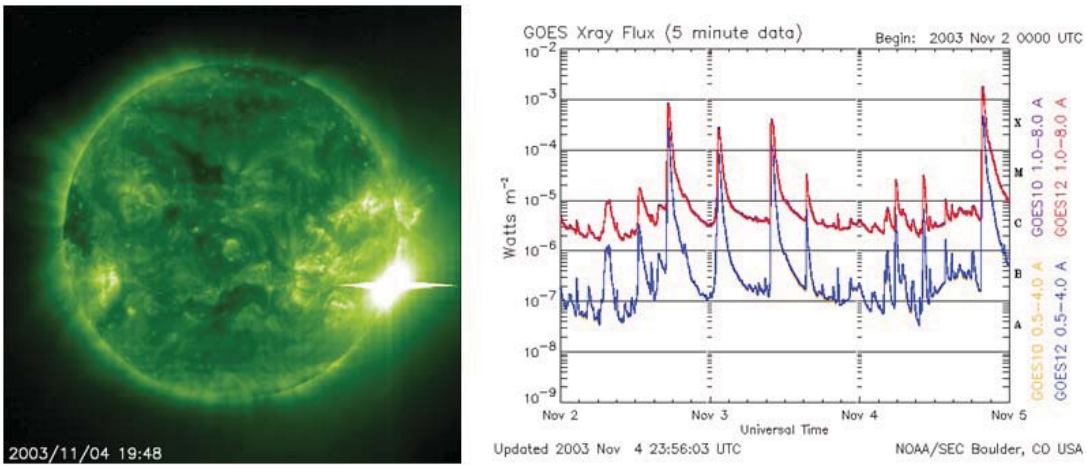

Figure 1.6: Solar flare brightening and flux intensity GOES satellite.[www.spaceweather.com]

.

An earlier flare classification is based on Hα spectral observations. The scheme uses both the intensity and emitting surface. Based on topology, solar flares are classified as a compact or simple-loop flares and two- ribbon flares [Messerotti et al. 2009]. Compact flares occur in single loops whose shape and volume do not change significantly during the flare and which do not emit charged particles. Flares that occur in magnetic arcades and show two regions of particle emission on both sides of a magnetic inversion line in the lower atmosphere are called two parallel flare/ribbon flares. The solar flare observed during the Halloween event of October and November 2003 was a parallel ribbon flare [Crosby et al. 2006]. Different kinds of radiation emanate from different parts of the flare and are released at different times of the flare process [Schwenn, 2006]. The first visible signature of a flare appears in soft X-rays (0.1-10 nm) at energies up to a few tens of keV originating from the sudden heating of coronal plasma. A few minutes after the soft X-ray bursts, non-thermal hard X-rays with energies of tens of keV to a few MeV are observed

in many, but not all, flares [Garcia, 2004]. The classification in intensity is qualitative, referring to the flares as: (f)aint, (n)ormal or (b)rilliant. But the recent and well accepted classification is based on the X ray flux emitted during solar flare. Solar flares are classified as A, B, C, M or X according to the peak flux (W/m^2) of 1 to 8 Angstrom X-rays near Earth, as measured on the Geostationary Operational Environmental Satellite (GOES) spacecraft. Each class has a peak flux ten times greater than the preceding [Bhatnagar and Livingston,2005]. Each category for X-ray flares has nine subdivisions ranging from, e.g., C1 to C9, M1 to M9, and X1 to X9. The more powerful M and X class flares are often associated with a variety of effects on the near-Earth space environment. Although the GOES classification is commonly used to indicate the size of a flare, it is only one measure. Figure 1.6 shows the EUV image of solar flare observed from the SOHO satellite. The brightening due to solar flare is clearly seen from the image. The GOES x ray flux in the image shows the intensity and the flare class classification based on the flux. These flare are causes changes in the lower ionosphere and magnetosphere.

1.4.6 CMEs

CMEs are large eruptions of plasma, magnetic field and energy from the Sun with magnetic field lines that are blown away from closed field regions on the Sun (active regions and quiescent filament regions) and propagate into the heliosphere. The first proof of these dynamic events came from observations made with a coronagraph on the OSO 7 spacecraft between 1971 and 1973 [Tousey, 1973; MacQueen et al., 1974]. A coronagraph produces an artificial eclipse of the Sun by placing an ”occulting disk” over the image of the Sun. During a natural eclipse of the Sun the corona is only visible for a few minutes at most, too short period of time to notice any changes in coronal features. With ground based coronagraphs only the innermost corona is visible above the brightness of the sky. From space the corona is visible out to large distances from the Sun and can be viewed continuously. CMEs are very faint and can not be observed otherwise. The Solar and Heliospheric Observatory (SOHO) and Solar Terrestrial Relations Observatory (STEREO) missions [Brueckner et al ., 1995] have white-light coronagraphs onboard to detect CMEs.

CMEs are often associated with other forms of solar activity, most notably solar flares or filament eruptions, but a broadly accepted theoretical understanding of these relationships has not been established. CMEs most often originate from active regions on the Sun's surface, such as groupings of sunspots associated with frequent flares [Webb and Howard, 1994]. These regions have closed magnetic field lines, in which the magnetic field strength is large enough to contain the plasma. These field lines must be broken or weakened for the ejection to escape from the Sun. Near solar maxima, the Sun produces about three CMEs every day, whereas near solar minima, there is about one CME every five days [Webb and Howard, 1994].

The current CME initiation models are based on magnetic flux rope structures being either present before the eruption takes place or created during the eruption as a consequence of magnetic reconnection [Roussev and Sokolov, 2006; Forbes et al., 2006]. They are based on the fact that (a) helical structures in images of erupting prominences and CMEs are observed, (b) correlations between interplanetary CMEs and Magnetic clouds (MCs) are observed, and (c) CMEs and erupting prominences possess some amount of twisted magnetic field. The initial flux rope is assumed to be suspended in the corona by a balance between magnetic pressure and tension forces. A highly twisted field is required to produce the eruption. Numerical simulation shows the evolution of a twisted magnetic flux-rope from below the photosphere into the corona [Amari et al., 2004; Fan and Gibson 2007]. If a flux-rope does not exist prior to the eruption, then it is formed in the course of eruption by magnetic reconnection [Mikic and Linker, 1994; Jacobs et al., 2006]. Shearing motions continuing for a long time energize the magnetic field and might lead to the formation of a flux-rope [Jacobs et al., 2006] by reconnecting the opposite polarity feet of a sheared magnetic arcade. In the case of a multipolar (complex) magnetic topology, the breakout model for CME eruption is used [DeVore and Antiochos, 2008; Lynch et al., 2008], in which the eruption is triggered by magnetic reconnection taking place in the current sheet located above the sheared arcade. Observational studies of the CME source region show the presence of both bipolar and quadrapolar topology [Li and Luhmann 2006; Ugarte-Urra et al., 2007], although bipolar topology is more common.

The basic features of a CME are its speed, width, acceleration, and Central Position Angle (CPA), referred to the sky plane. These properties can be identified from the time-sequence of coronagraphic images, in which the CME can be recognized as a moving feature from the surface of the Sun. The angular extent of the moving feature defines the width. The central angle of this extent with reference to solar north is called CPA. The CME speeds can be calculated from the height-time (h-t) slopes obtained from the plots. Most of the h-t plots fall into three types: accelerating; constant speed and decelerating, indicating different degrees of propelling and retarding forces acting on CMEs. A typical CME has a mass of 10^{11}-10^{12} kg and has a speed between 400-3000 km/s. The CME angular width ranges from $< 5^{\circ}$ to 360° (Halo CME) [Howard et al., 1982]. The CME contains coronal material at a temperature of a few million kelvin in the outer structure with cool prominence material (8000 K) in the core. About one third of CMEs observed at 1 AU have a flux rope structure (magnetic clouds). Non-cloud CMEs generally originate at larger distances from the Sun centre.

An image of CME is shown in figure 1.3 which is observed by Large Angle and Spectrometric Coronagraph Experiment (LASCO) coronagraph on board SOHO [Brueckner et al ., 1995], shows a classic three part structure: A leading edge (probably a flux rope) followed by a dark cavity region, followed by a bright filament [Gopalswamy, 2007]. The prominence is denser by three orders of magnitude, which is the reason it appears as the brightest in white light images. The void region is inferred to have a lower density compared to the frontal structure. The electrons must be trapped in the void region of the CMEs, which is thought to be a flux rope. The frontal structure is of higher density and lower magnetic field strength compared to the void region [www.nasa.gov].

CMEs disrupt the flow of the solar wind and produce disturbances that strike the Earth with sometimes catastrophic results. The geo impact of CMEs generally falls into two categories: geo-effetiveness and SEP effectiveness [Ryan et al ., 2000]. Geoeffective CMEs cause transient geomagnetic storms, while SEP effective CMEs cause the gradual and long-lasting SEP events with an intensity of minimum 10 particle flux unit (pfu) in the >10 MeV channels of particle detectors such as on GOES [Gopalswamy, 2007].

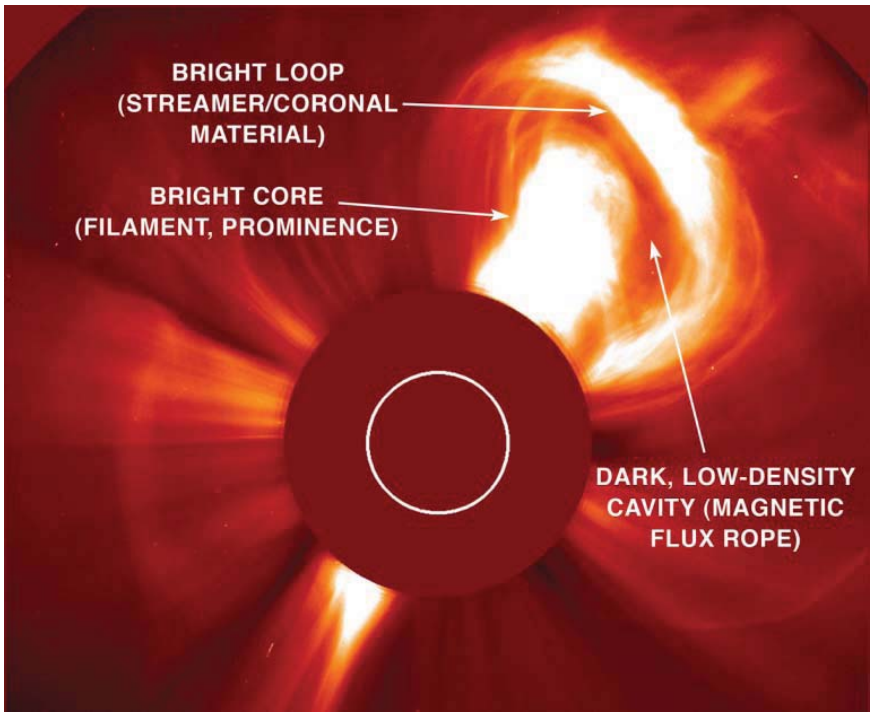

Figure 1.7: Three Part Structure of CME.[www.nasa.gov]

.

1.4.7 CIRs

When the high speed solar wind emanating from a coronal hole runs into the slower solar wind, there is a compression of the plasma and the magnetic field; this forms a Corotating Interaction Region (CIR) [Crooker et al., 1999]. A schematic diagram showing the structure of a typical high speed stream with the embedded CIR is shown in Figure 1.8

CIRs are long lasting large-scale plasma structures generated in low and middle latitude regions of the heliosphere by the interaction of a stable fast solar wind stream with the surrounding slow solar wind. Associated with these plasma structures are recurrent MeV-ion events and recurrent decreases of the galactic and anomalous cosmic ray intensities. Prior to the Ulysses-mission

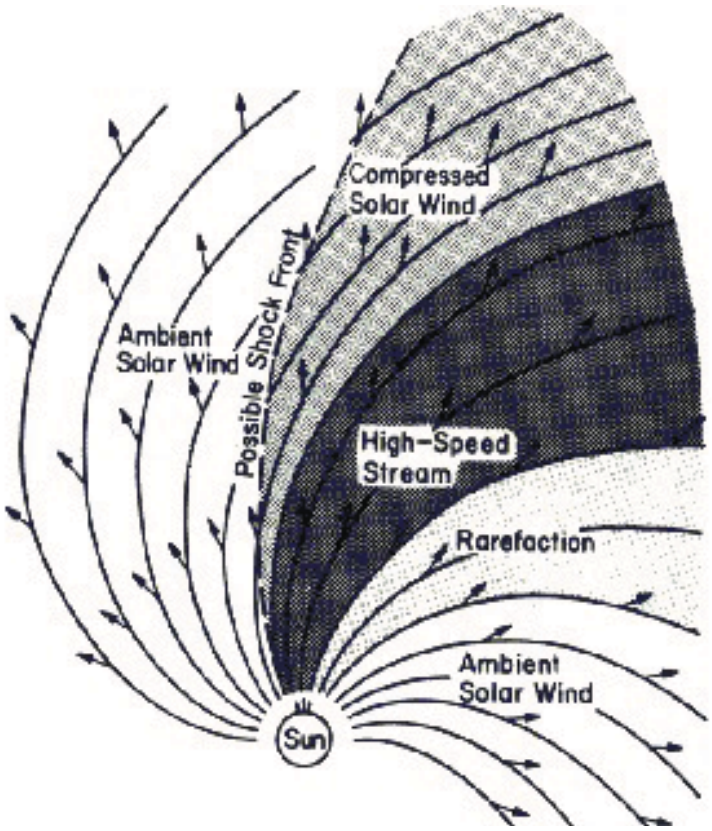

Figure 1.8: Schmetaic diagram of CIR.

the effect of CIRs could only be observed at low or moderate heliographic latitudes. The three-dimensional extent and their role in structuring the quiet heliosphere became clear after Ulysses high latitude observations had became available. CIRs possibly play a role in determining solar modulation of galactic and anomalous cosmic rays during periods of low to moderate solar activity.

The CIRs seldom have fast shocks or continuous, strongly southward interplanetary magnetic field (IMF) and thus drive only moderate geomagnetic activity [Scholer, 1999; Alves et al., 2006; Borovsky and Denton, 2006]. It is generally believed that geomagnetic disturbances recurring at 27 day intervals could be associated with CIRs. Studies show that both CMEs and CIRs produce magnetic fields significantly larger than the normal IMF [Lindsay et al., 1995]. CIRs associated

with compressed plasma and fields often produce larger dynamic pressure than the CMEs [Watari, 1997]. The increase of IMF fluctuations in CIRs is due to the presence of large amplitude Alfven waves within the body of the corotating streams [Tsurutani et al., 1995a], which has been confirmed by Ulysses observations [Tsurutani et al., 1995b]. Ulysses observations showed the tilted latitudinal structure of the CIRs; the tilt of the CIRs decreases with increasing distance from the Sun [Gosling et al., 1993]. Thus, high speed solar wind emanating from out of the ecliptic plane, particularly in the vicinity of magnetic sector boundaries (where a CIR is easily formed) can also become effective in producing geomagnetic disturbances [Gosling et al., 1976; Scholer, 1999].

1.5 Interplanetary Coronal Mass Ejections

A CME, which is at a much larger distances from the sun ($>$ 50 Sun Radii) is called as Interplanetary Coronal Mass Ejection (ICME) which is also regarded as the heliospheric counterpart of CME. ICMEs have large masses and contain a magnetic field, but generally are not too fast. This is almost certainly due to the large deceleration imposed on fast CME by the surrounding solar wind [Howard, 2011]. The magnetic structures inside an ICME are varied, but are typically greater in magnitude than the surrounding interplanetary magnetic fields. Often, a highly structured helical magnetic field is observed within ICMEs and these are called MCs [Burlaga, 1981]. Although STEREO mission is capable of observing CMEs over the entire Sun-Earth distance [Harrison et al., 2008], the current knowledge on ICMEs comes mainly from in situ observations [Gopalswamy, 2007]. ICMEs are identified in a variety of ways: solar wind plasma signatures (temperature, plasma beta, flow speed), magnetic signatures (field strength, field rotation), compositional and charge state signatures, and particle (thermal and nonthermal) flux signatures [Howard et al ., 2006].

Magnetic-field signatures are most useful to identify flux ropes of ICMEs. The Magnetic clouds (MCs) associated with an ICME may include one or more signatures, such as (i) strong magnetic field, (ii) smooth latitudinal rotation of the field, and (iii) low proton temperature or plasma β

[Klein and Burlaga, 1982]. An important unsolved question about MCs is whether they have a root in the Sun or disconnected from the solar surface [Akasofu, 2007]. Observations of Bidirections electrons (BDEs) fluxes favour the root hypothesis [Burlaga, 1991] while the huge dimensions of MCs deduced from Ulysses measurements favour the disconnection hypothesis (Watermann et al. 2009a, b). On the other hand, an ejecta (EJ) can be identified based on (i) weaker magnetic field, (ii) higher proton temperature or higher plasma β, (iii) no clear rotation in magnetic field and (iv) enhanced Nα /Np ratio [Gopalswamy et al., 2010; Riley and Richardson, 2012]. At 1 AU, for each shock-ICME pair, the MC or EJ classification has been made from near-Earth spacecraft such as Advanced Composition Explorer (ACE) and Wind. The flux rope types and their connection to the solar source regions have been extensively discussed in the literature [Bothmer and Schwenn, 1994; Mulligan et al., 1998; Li and Luhmann, 2004; Yurchyshyn, 2008]. In general, MCs have their axis parallel to the neutral line in the source active region on the Sun. The internal structure of MCs is helpful in understanding their solar origin. They also have important implications for their geoeffectiveness.

Based on the interference of CME at 1 AU in the Sun Earth line the possibility of the region interacts with Earth magnetosphere given in the figure 1.9. Six possible tracks of an observing spacecraft through an MC with a leading shock (left) and another without (right). Tracks 1 and 2 never encounter the MC proper. Track 3 passes through the nose of the MC. Trajectory 4 passes through the shock, sheath, and through the edge of the MC. Tracks 5 and 6 are similar to 4 and 3, respectively, except that the MC is slow and hence it does not drive a shock [Kim et al ., 2013]. Only trajectories 3 and 6 are expected to observe an MC structure [Gopalswamy, 2006].

1.5.1 Types of magnetic clouds

A magnetic cloud is a transient ejection in the solar wind defined by relatively strong magnetic fields, a large and smooth rotation of the magnetic field direction over approximately 0.25AU at 1AU, and a low proton temperature [Burlaga et al., 1981]. Magnetic clouds are ideal objects for solar-terrestrial studies because of their simplicity and their extended intervals of southward and

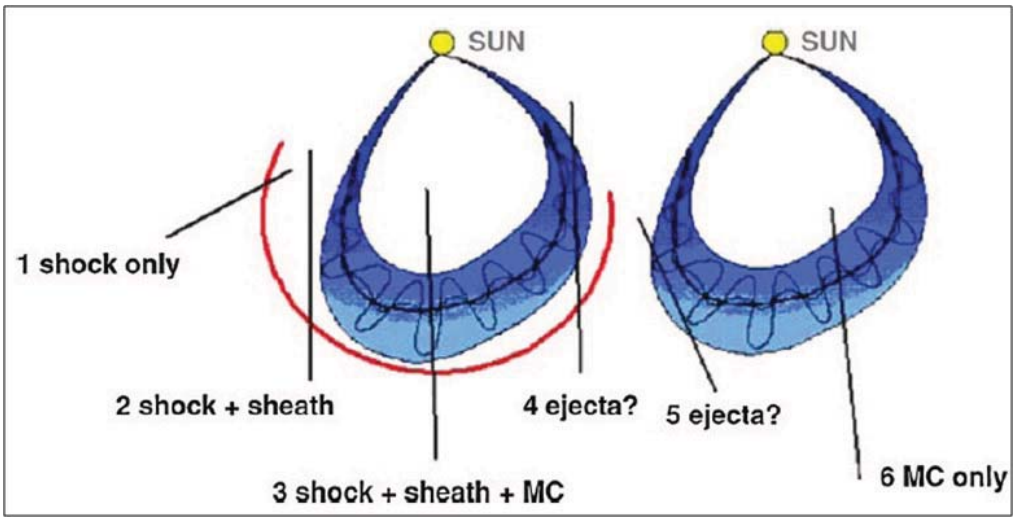

Figure 1.9: Possible tracks of MC observed at 1 AU [from Kim et al ., 2013].

northward magnetic fields [Burlaga et al., 1990]. Based on the turning of Bz of the interplanetary magnetic field at 1 AU the magnetic clouds are differentiated as four. In the case of MCs, the ejecta portion has a well defined structure with Bz showing a smooth rotation from north to south (NS) or south to north (SN) as illustrated in figure 1.10. This happens when the MC axis is close to the ecliptic (Z = 0 in GSE coordinates).

Bz is the azimuthal component of the flux rope that defines the MCs. When the MC axis makes an angle >45 to ecliptic, Bz is due to the axial field. For such high-inclination MCs, the azimuthal field (By) shows smooth rotation in the east-west direction. High-inclination MCs are known as unipolar MCs (Mulligan et al., 1998) because the axis points fully to the north (FN) or south (FS) throughout the MC interval (see Figure 1.9). Thus the SN, NS, FN, and FS MCs constitute the four basic types of flux ropes. Note that the each MC type can have two subtypes: the bipolar MCs can have their axes pointing to the east (SEN, NES) or west (SWN, NWS); the unipolar MCs can have their rotation from east to west (ESW, ENW) or west to east (WSE, WNE)(Gopalswamy et al ., 2007).

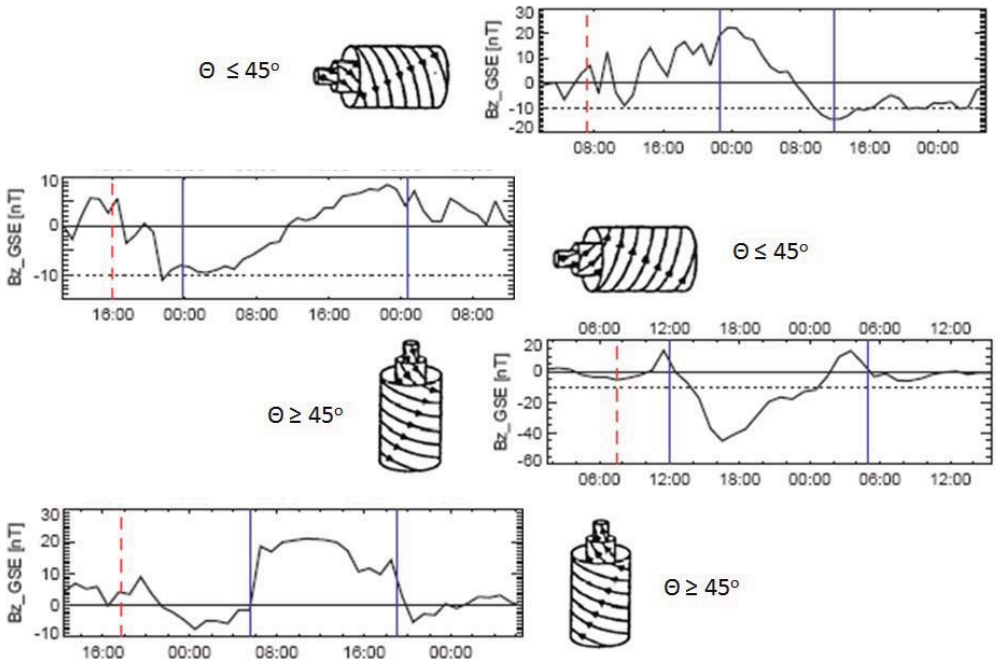

Figure 1.10: Four basic types of MC based on the Bz orientation.[from Gopalswamy et al ., 2007].

1.5.2 Interplanetary shocks

Many CMEs move through the heliosphere at speeds much greater than the sound speed of the surrounding interplanetary medium [Burlaga, 1971]. They are often supersonic and so give rise to collisionless shocks that form ahead of the CME structure. These shocks are said to be Interplanetary (IP) shocks. Mostly these IP shocks are associated with CME. The magnetic field and plasma at the shock front gives rise to a forward shock which can easily be identified by a sudden increase in magnetic field strength, solar wind plasma density, solar wind strength and temperature. Similarly, a reverse shock can be identified by a sudden decrease in magnetic field and density but increase in solar wind speed and temperature. As it moves away from the Sun a fast CME, pushes an interplanetary shock wave before it, amplifying the solar wind speed (V) and magnetic field strength (B). The shock characteristics of general interest in these studies include the following: Mach number strength; character (fast, slow, or intermediate), obliquity (parallel,

perpendicular, oblique, depending on the angle between the up-stream magnetic field direction and the shock surface normal), sense of travel (forward or reverse, i.e., the shock is moving generally 'away from' or towards the Sun in the solar wind frame of reference), and separated according to cause, such as due to a Coronal Mass Ejection and/or a Magnetic Cloud acting as a shock driver, or a transient blast of plasma at the Sun, or from a solar wind stream impinging on another stream, often causing a corotating shock geometry, to name the prominent ones. Figure 1.11 shows the interplanetary shock with parallel, perpendicular and oblique orientation.

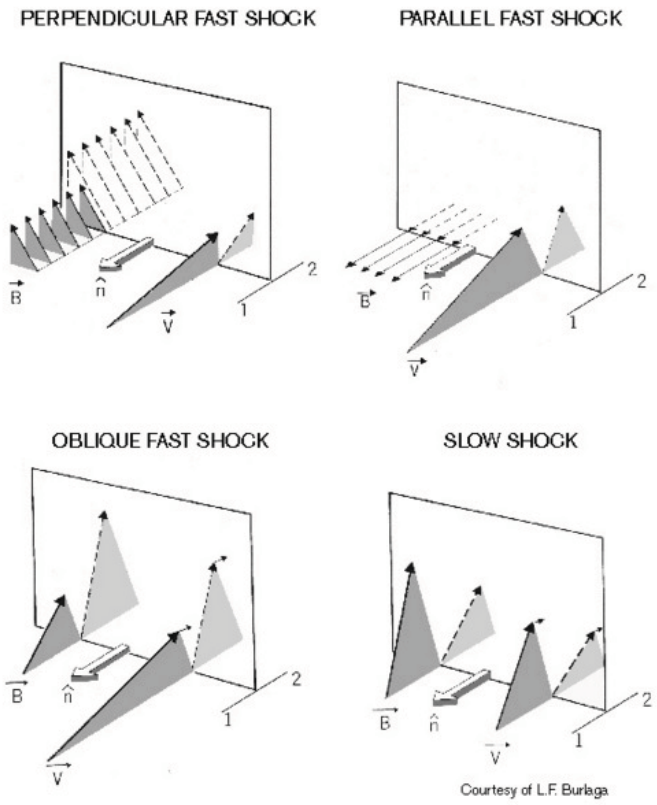

Figure 1.11: Interplanetary shocks with different orientaion.[from L.F Burlaga].

The CME produces a speed increase all the way to the shock front, where the wind motion then slows down precipitously to its steady, unperturbed speed. Compression, resulting from the

relative motion between the fast CME and its surroundings, produces strong magnetic fields in a broad region extending sunward from the shock. The strong magnetic fields and high flow speeds commonly associated with interplanetary disturbances driven by fast CMEs are what make such events effective in stimulating geomagnetic activity. This IP shocks approaches earth resulting in the compression of the earth magnetosphere and are associated with the sudden change in the dynamic pressure. Until recently it was thought that some shocks observed in the solar wind were associated with blast waves initiated by flares and others were driven ahead of plasma clouds ejected from the Sun CME. Now, however, the current belief is that all interplanetary shocks are associated with CMEs.

Interplanetary shocks interact with the Earth's magnetosphere, resulting in different phenomena. Using results of global MHD simulations, this interaction is investigated. In particular, the simulations predict that interplanetary shocks reflect from the inner numerical boundary of the global models. The reflection results in some phenomena, like an anti-earthward bow shock motion, which are really observed. However, it is unclear where the reflecting boundary is placed in reality. Initially, the boundary was assumed to be the plasmapause, but Samsonov et al. [2007] showed that most of the energy of an incoming interplanetary shock can penetrate into the plasmasphere. Thus, a forward fast MHD shock (or fast wave) may reach the ionosphere. In principle, the same phenomenon is the cavity mode, i.e. a compressional wave oscillating between some inner and outer boundaries. Again, the definite boundaries are difficult to locate. Observed global mode frequencies do not confirm an assumption that the oscillating region is bounded by the plasmapause and magnetopause, but observations do not contradict the idea that the oscillations occur between the ionosphere and magnetopause.

1.5.3 Sun-Earth Interaction

Space weather is concerned with the time varying conditions between Sun and the Earth, including the solar wind, and especially the space surrounding the Earth, including conditions in the magnetosphere, ionosphere, and thermosphere. The ejections from the sun makes a great

impact in the space weather resulting in the altering of Earth ionosphere and magnetopshere. When the ejection from the Sun is directed towards Earth and reaches the shock wave of the travelling mass of SEPs disrupt Earth's magnetosphere, compressing it on the day side and extending in the night-side magneto tail. Solar flares produce high energy particles and radiation that are dangerous to living organisms. However, at the surface of the Earth are well protected from the effects of solar flares and other solar activity by the Earth's magnetic field and atmosphere. The most dangerous effects due to flares are because of energetic charged particles (primarily high-energy protons) and electromagnetic radiation (X-rays). These effects will be discussed detail in later sections.

1.6 The Earth's Magnetosphere

The Earth has a magnetic field with north and south poles which reaches 36,000 miles into space. The magnetic field of the Earth is surrounded in a region called the magnetosphere. The Earth core is a good conductor of electricity. The observation argue for a mechanism within the Earth's interior that continually generates the geomagnetic field from the outer core region of the earth. There exists driving force which can give rise to motion in the liquid outer core. Currents which flow in the outer core as a result of this give rise to a magnetic field and the cycle can be sustained when this magnetic field reinforces the original field. This mechanism is termed as the dynamo effect [Merrill and McElhinny, 1983]. This geodynamo results in the dipolar magnetic field surrounding the Earth.

The interaction with the solar wind deforms the Earth's basic dipolar magnetic field, compressing the field lines on the day side and stretching them out to form a long comet-like tail (the magnetotail) on the night side. On the day side, the magnetosphere extends out to a distance of approximately 10 Earth radii (under quiet conditions), while the magnetotail extends several hundred Earth radii in the antisunward direction. The magnetosphere contains various large-scale regions, which vary in terms of the composition, energies, and densities of the plasmas that occupy them. The sources of the plasmas that populate these regions are the solar wind and the

Earth's ionosphere; the relative contributions of these two sources to the magnetospheric plasma vary according to the level of geomagnetic activity.

1.6.1 Regions of Magnetosphere

The major regions of the magnetosphere are bow shock, magnetosheath, magnetopause, Tail lobes and cusps as shown in Figure 1.12.

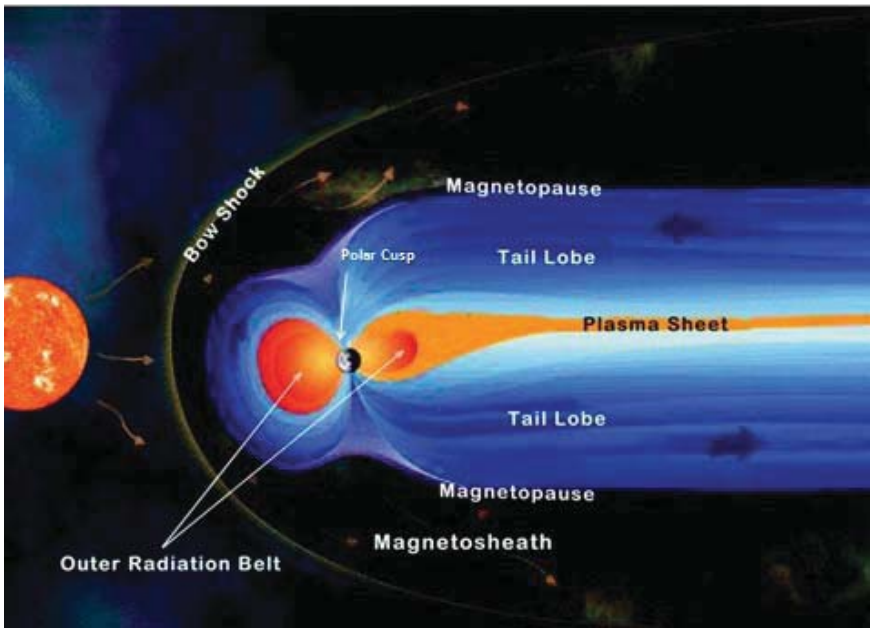

Figure 1.12: Structure of the earth's magnetosphere [www.nasa.com].

A collision-free *bow shock* forms in the solar wind ahead of Earth, typically at 13.5 R_E on the sunward side. It forms because the particles of the solar wind run into the Earth magnetosphere and interact with it because they are charged. At the bow shock the supersonic solar wind is slowed down and becomes subsonic. The *magnetosheath* is the next region of the magnetosphere formed between the bow shock and the magnetopause. It is formed mainly from solar wind, though it contains a small amount of plasma from the magnetosphere. It is an area exhibiting high

particle energy flux, where the direction and magnitude of the magnetic field varies erratically. This is caused by the collection of solar wind gas that has effectively undergone thermalization [Wolf, 1995]. The *magnetopause* is the area of the magnetosphere wherein the pressure from the planetary magnetic field is balanced with the pressure from the solar wind. Magnetopause is not a rigid boundary and fast, nonthermal charged particles can cross [Carpenter, 1963]. The location of the magnetopause is determined by the balance between the pressure of the dynamic planetary magnetic field and the dynamic pressure of the solar wind. As the solar wind pressure increases and decreases, the magnetopause moves inward and outward in response. Next is the *tail lobes* comprise the major part of the magnetotail, being found between the plasma sheet and the magnetopause. These are regions where the magnetic field pressure is large and the plasma pressure is small, in pressure balance with the rest of the magnetosphere. *Cusps* are narrow regions of recently "opened" or merged magnetic field lines mapping to the high-latitude ionosphere just poleward of the last closed field line on the Earth's day side. These regions are centered on local noon and extend approximately 2-3 hours in longitude and 1° in latitude. The open field lines of the cusps are connected with those of the interplanetary magnetic field, which allows the shocked solar wind plasma of the magnetosheath to enter the magnetosphere and to penetrate to the ionosphere. These regions are not rigid and they change with the solar activity, ejections from the Sun.

1.6.2 Magnetic reconnection

Magnetic reconnection refers to the breaking and reconnecting of oppositely directed magnetic field lines in a plasma. In the process, magnetic field energy is converted to plasma kinetic and thermal energy. Reconnection is at the heart of many spectacular events in our solar system. For example, solar flares which occur near sunspots are believed to be powered by magnetic reconnection. Solar magnetic activity, including flares, can eject high energy charged particles into space. When the particles reach Earth, they can disrupt power grids and communications systems and threaten spacecraft and satellites. A related phenomenon is the aurora seen near the polar regions

of Earth as well as on other magnetized planets. The Earth's own magnetic field is constantly perturbed by the impinging field from the Sun (called the solar wind). During strong bursts (such as those caused by extraordinary solar flares, CMEs) reconnection can be induced in the near-Earth magnetotail (a narrow magnetic field structure located on the night side many Earth-radii away). The tenuous plasma in that region is then accelerated down along magnetic field lines into the polar regions, striking Earth's atmosphere and exciting nitrogen and oxygen atoms as well as other atoms present in our atmosphere. The immediate de-excitation of these atoms then emit the wonderful and often intricate display of light we know as the aurora or northern (and southern) lights. Figure 1.13 shows the schematic representation and the mechanism of magnetic reconnection [Russel et al., 1990].

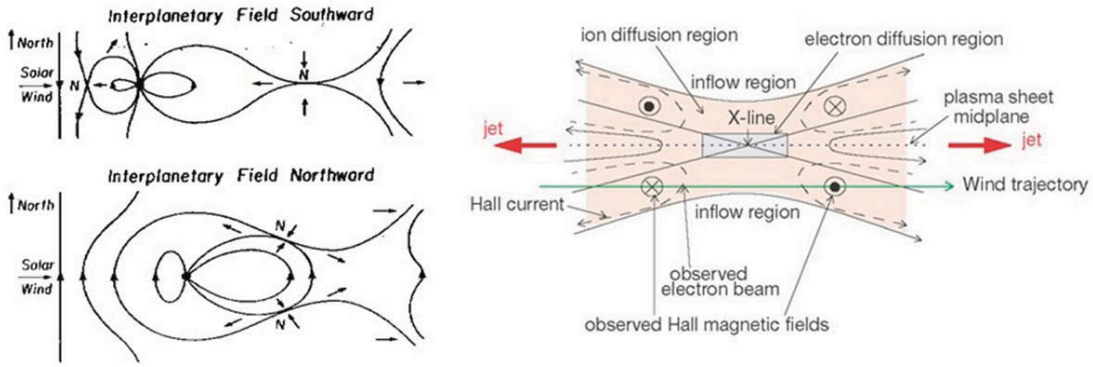

Figure 1.13: Schematic representation and mechanism of magnetic reconnection [from Rusell., 1990].

In plasma physics, it is well known that magnetic field lines are "frozen-in" to an infinitely conductive plasma. Since charged plasma particles are confined to circular orbits around magnetic field lines, this means that infinitely conductive plasmas will not diffuse across field lines and mix. Conversely, two distinct field lines will remain separate since they cannot penetrate the intervening plasma. In most cases, solar and magnetospheric plasmas can be described very accurately with such a theory since they are both very conductive. However, straightforward application of the theory would remove the possibility of ejected solar plasma penetrating the magnetosphere since the

plasmas would not be allowed to mix. Nevertheless, based on observations and known technological disruptions, we know that they must mix. It is because of the fact that when plasmas carrying oppositely directed magnetic field lines are brought together, a strong current sheet is established, in the presence of which even a vanishingly small amount of resistivity in a small volume can become important, allowing plasma diffusion and, thus, magnetic reconnection to occur.

1.6.3 Geomagnetic storm

Geomagnetic storms can be defined as disturbances of Earth's magnetosphere caused by the impact of IP magnetic field structures. Geomagnetic storm is a major disturbance of Earth's magnetosphere that occurs when there is a very efficient exchange of energy from the solar wind into the space environment surrounding Earth. These storms result from variations in the solar wind that produces major changes in the currents, plasmas, and fields in Earth's magnetosphere. The solar wind conditions that are effective for creating geomagnetic storms are sustained (for several hours) periods of high-speed solar wind, and most importantly, a southward solar wind magnetic field (opposite to the direction of Earth's field) at the day-side of the magnetosphere [Gonzalez et al ., 1994]. This condition is effective for transferring energy from the solar wind into Earth's magnetosphere. They are usually defined by ground based, low latitude geomagnetic field horizontal component(H) variations. The magnetic variations are the indirect measurements for the disturbance in plasma populations and current systems present in the magnetosphere.

The first observation of the effects of a geomagnetic storm occurred early in the 19^{th} century from May 1806 until June 1807 the German Alexander von Humboldt recorded the bearing of a magnetic compass in Berlin. On 21^{st} December 1806 he noticed that his compass had become erratic during a bright auroral event. On 1,2 September , 1859, the largest recorded geomagnetic storm occurred. From 28 August until 2 September,1859, numerous sunspots and solar flares were observed on the Sun, the largest flare occurring on September 1. This is referred as the Solar storm of 1859 or the Carrington Event [Carrington, 1859]. It can be assumed that a massive CME, associated with the flare, was launched from the Sun and reached the Earth within eighteen hours

a trip that normally takes three to four days. The horizontal intensity of geomagnetic field was reduced by 1600 nT as recorded by the Colaba Observatory(Geog.Lat. 18.5° N, Geog. Long. 72.9°E) [Tsurutani et al., 2003].

Geomagnetic storms result in intense currents in the magnetosphere, changes in the radiation belts and changes in the ionosphere, including heating of the ionosphere and upper atmosphere region called the thermosphere. The geomagnetic disturbances are measured through variety of geomagnetic indices, one of which is Disturbance storm time (Dst) index. When the transient plasma stream of the CME arrives the boundary of the magnetosphere with the speed substantially greater than the solar wind, the outer region of the magnetosphere experiences a strong impact. As a result a sudden compression of the magnetic field and plasma occurs in that region. This compression is transmitted as a hydromagnetic perturbation , which arriving at earth, is observed as a sudden increase in the magnetic filed. This is called as Sudden commencement/Sudden impulse (SC/SI) of the geomagnetic storm [Araki, 1977]. The principal means by which energy is transferred from the solar wind to the magnetosphere is a process known as “reconnection”, which occurs when the IMF is oriented antiparallel to the orientation of the Earth’s field lines. This orientation allows interplanetary and geomagnetic field lines to merge, resulting in the transfer of energy, mass, and momentum from the solar wind to the magnetosphere [Gonzalez et al ., 1994]. As a result of this reconnection there is a enhanced west ward ring current at about 3-4 earth radii.

This enhancement in westward ring current gives rise to depression in the horizontal magnetic field on the earth’s surface. This depression is said to be the main phase of the geomagnetic storm. The main phase is followed by a gradual return towards normal H- field and is called recovery phase. When the interplanetary field turns northward again, the rate of plasma energization and inward transport slows and the various loss processes that remove plasma from the ring current can begin to restore it to its pre-storm state [Singer, 1957; Dessler and Parker, 1959]. This ring current energy decays slowly over hours to maximum of 7 days. During the storm recovery phase, particle transport into the ring current slows, allowing various loss processes to reduce ring current particle fluxes to their quiet-time level. The primary loss process during both the main and recovery phases

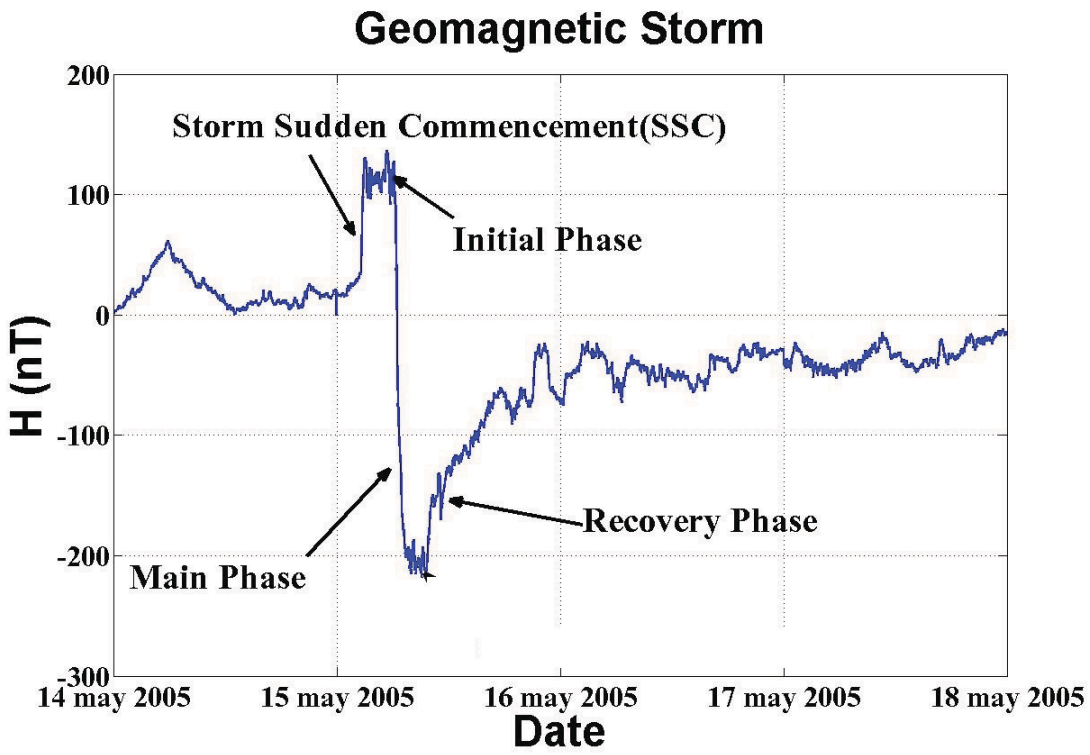

Figure 1.14: Geomagnetic storm on 15 May 2005 observed at Alibaug magnetic observatory, India.

is charge exchange with neutral hydrogen atoms in the geocorona. A second loss process, affecting principally low-energy ring current ions, involves Coulomb collisions with the thermal plasma of the plasmasphere. The third process thought to contribute to ring current decay is the precipitative loss of ring current particles into the atmosphere as a result of wave-particle interactions [Kozyra, 1989]. An example of a geomagnetic storm from Alibag (Geog.Lat. 18.5° N, Geog. Long. 72.9 °E) is given in figure 1.14

1.6.4 Ring current

The ring current is one of the major current systems in the Earth's magnetosphere. It circles the Earth in the equatorial plane and is generated by the longitudinal drift of energetic (10 to 200

keV) charged particles trapped on field lines between L 2 and 7. During geomagnetic storms, ring current particle fluxes are dramatically increased, with the peak enhancements occurring in the inner ring current (at L <4). The quiet-time ring current consists predominantly of H^+, while the storm-time ring current also contains a significant component of ionospheric O^+, whose contribution to ring current energy density may even exceed that of H^+ for brief periods near the maximum of particularly intense storms.

The formation of the storm-time ring current has been attributed to two different processes: (i) the injection of plasma into the inner magnetosphere during the expansion phase of magnetospheric substorms and (ii) increased convective transport of charged particles from the nightside plasma sheet deep (L $<$ 4) into the inner magnetosphere as a result of an intensification of the Earth's dawn-dusk convection electric field during extended periods of strong southward IMF. The present understanding of ring current formation tends to favor the enhanced convection model over the substorm plasma injection model; however, it is recognized that substorms, while not the primary driver, nonetheless play a significant role in the growth of the storm-time ring current.

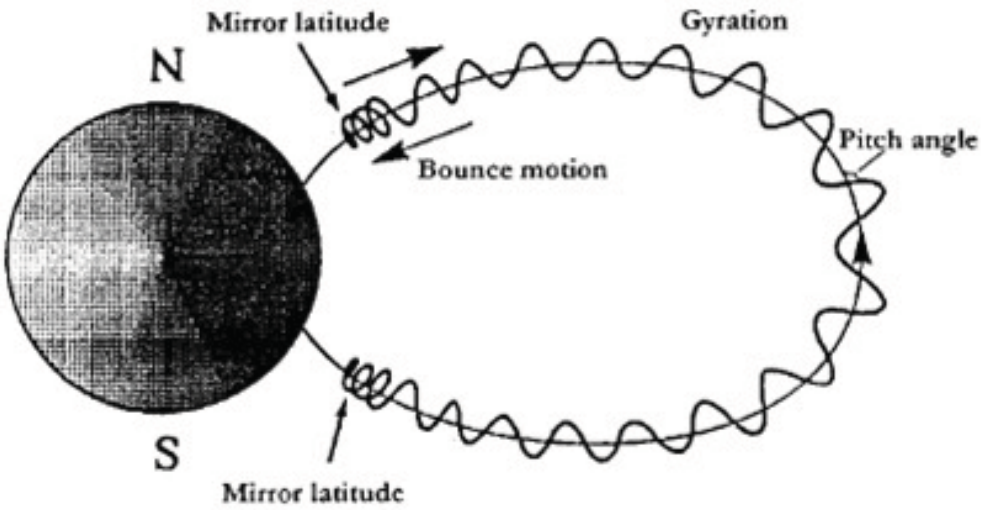

Figure 1.15: Schematic representation of Ring current.[from Daglis et al ., 1999].

Figure 1.15 gives the schematic representation of ring current. During quiet times, the ring current is distributed over the L parameter range 2 to 9 R_e, having average current density values of 1-4 nA m$^{-}2$ [e.g., Lui et al., 1992; De Michelis et al., 1997]. The storm time ring current density increases over its whole radial extent, and may exceed current density values of 7 nA m$^{-}2$ [Lui et al., 1987]. All the trapped particles in the inner magnetosphere contributes to the ring current, only ions in the medium-energy range of 10 keV to a few hundreds of keV contribute substantially to the total current density [Williams, 1987]. Electrons contribute little to the ring current on account of their negligible energy density [Baumjohann, 1993]. The immediate particle sources of the ring current are the magnetospheric plasma sheet and the terrestrial ionosphere. The plasma sheet population is supplied by the ionosphere and the solar wind. Hence the ultimate main sources of ring current particles are the solar wind and the terrestrial ionosphere.

1.7 The Earth's Ionosphere

The ionosphere is the region of the upper atmosphere of the Earth where charged particles (electrons and ions) of thermal energy are present, which are the result of ionization of the neutral atmospheric constituents by electromagnetic and corpuscular radiation. It is formed mainly due to the photo ionization of neutral particles by solar X-ray and UV radiation although precipitation of energetic charged particles can also contributes at higher latitudes. The ionosphere may extend from an altitude of approximately 60 km to 1000 km. The discovery of the Earth's ionosphere came from the observation of reflected radiowaves, whose properties could only be explained by the presence of a reflecting layer in the Earth's atmosphere composed of electrons and positive ions [Bauer, 1973].

The Earth's ionosphere is divided into several regions designated by the letters D,E, and F , the latter F being subdivided into F1 and F2. Historically, the division arose from the successive plateaus of electron density (Ne) observed on records of the time delay (i.e., virtual height) of radio reflections as the transmitted signal was swept through frequency. The "E layer" was the

first to be detected and was so labelled as being the atmospheric layer reflecting the E vector of the radio signal. Later the lower D and higher F layers were discovered. Distinct ionospheric regions develop because (a) the solar spectrum deposits its energy at various heights depending on the absorption characteristics of the atmosphere, (b) the physics of recombination depends on the density, and (c) the composition of the atmosphere changes with height. Thus the four main ionospheric regions can be associated with different governing physical processes, and this physics is the basis for labelling an ionospheric region on another planet as a D, E, F1, or F2 region shown in the Figure 1.16.

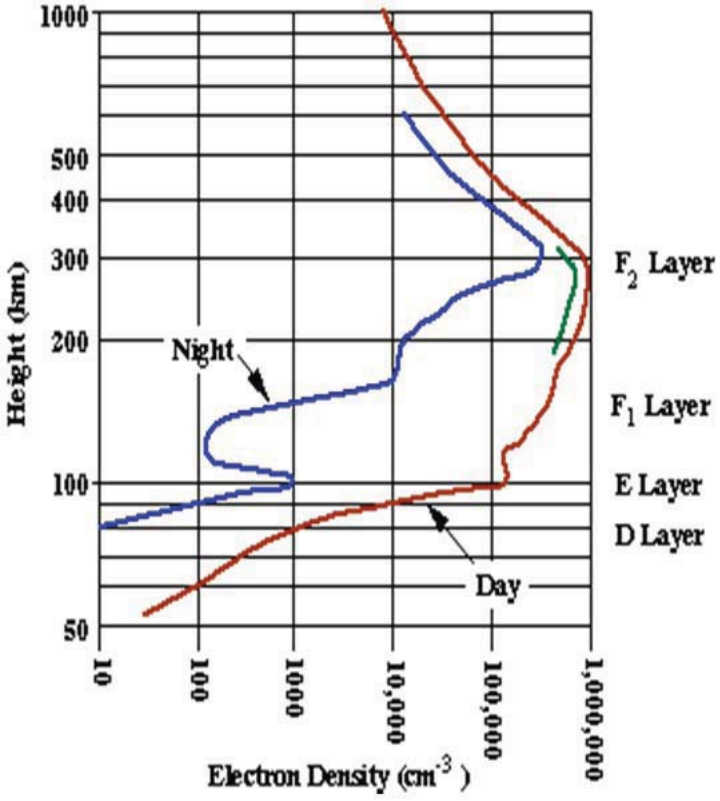

Figure 1.16: Ionospheric electron density profile for day and night amplitude with the solar flare intensity (dB).

All these ionospheric regions are highly variable, location of these layers vary by day and night and is shown in the Figure 1.16. The lower most region of the ionosphere is the D-region from 60

km to 90 km. Above the D layer is the E-region extending from 90 km to 150 km. The peak in the E region during day time is seen near 110 km. Above the E region is the F region consisting of two parts: the lower F1 region between 150 km and 180 km and the F2 region from 180 km and above. Note, the daytime densities are much larger than the nighttime densities. Let us see in detail the different layers with their chemical composition and their variations.

1.7.1 F-region Ionosphere

The F region extends upward from an altitude of about 150 to 500 km. This region has the greatest concentration of free electrons. This region reflects radio waves with frequencies up to about 35 MHz; the exact value depends on the peak amount of the electron concentration, typically 10^7 electrons per cubic mm, though with large variations caused by the sunspot cycle. During the day, F region can be distinguished by two layers, a small layer known as F1 and above it a more highly ionized dominant layer called F2. At night these two layers merge at about the level of the F2 layer, which is also called the Appleton layer.

The F1 region is attributed to that part of the solar spectrum between 2000 and 9000 nm, which is strongly absorbed in atomic oxygen. It is composed of a mixture of molecular ions O_2^+ and NO^+, and atomic ions O^+. The F1 layer has approximately 5×10^5 electrons/cm^3 at noontime and minimum sunspot activity, and increases to roughly 2×10^6 electrons/cm^3 during maximum sunspot activity. The density falls off to below 10^4 electrons/cm^3 at night. Above the F1 region, atomic oxygen becomes the dominant constituent because lighter particles tend to occupy higher altitudes above the turbopause (Hargreaves., 2003). This atomic oxygen provides the atomic ions that make up the F2 layer. The F2 layer exists from about 220 to 800 km above the surface of the Earth. The F2 layer is the principal reflecting layer for HF communications during both day and night. The F2 layer has about 10^6 electrons/cm^3. However, variations are usually large, irregular, and particularly pronounced during magnetic storms. The F layer behaviour is dominated by the complex thermospheric winds.

1.7.2 E-region Ionosphere

The E region is also called Kennelly-Heaviside layer, named for American electrical engineer Arthur E. Kennelly and English physicist Oliver Heaviside in 1902. It extends from an altitude of 90 km to about 150 km. The E region was responsible for the reflections involved in Guglielmo Marconi original transatlantic radio communication in 1902. The ionization density is typically 10^5 electrons/cm^3 during the day, though intermittent patches of stronger ionization are sometimes observed. Ionization is due to soft X-ray and far ultraviolet (UV) solar radiation ionization of O_2. The vertical structure of the E layer is primarily determined by the competing effects of ionization and recombination. At night the E layer weakens because the primary source of ionization is no longer present. After sunset an increase in the height of the E layer maximum increases the range to which radio waves can travel by reflection from the layer. In equatorial regions the normal quiet day (Sq) variation of the geomagnetic field shows a strong enhancement which is attributed to a narrow electrical current sheet flowing eastward along the magnetic dip equator and termed the Equatorial Electrojet (EEJ) [Chapman, 1951]. The EEJ is mainly driven by the eastward electric field generated due to the E-region dynamo. The zonal electric field over the equator originated from the dynamo driven Sq current system moves the electron in the E region vertically upward direction during the day time while the ions moves horizontally with neutral wind makes the charges to separate from one another. As the conductivity is gradually decreasing with altitude of E region, the upward moving electron encounters inhibiting boundary region which enables to build polarization charges that gives rise to polarization electric field. This process increases the conductivity in the eastward direction which is commonly known as cowling conductivity. This polarization electric field subsequently makes the electron move westward during daytime and a jet of current flows around 106 km region. This is the phenomena of the formation of EEJ.

1.7.3 D-region Ionosphere

The D region is the lowest of the regions within the ionosphere that affects radio communications signals. It is present at altitudes between about 60 and 90 km. It is sustained by the radiation from the Sun and levels of ionisation fall rapidly at dusk when the source of radiation is removed. The D region mainly has the affect of absorbing or attenuating radio communications signals particularly in the LF and MF portions of the radio spectrum, its effect reduces with frequency.

The D-region ionosphere is ionised by solar electromagnetic radiation, energetic particle precipitation and galactic cosmic rays [Hargreaves, 2003]. At daytime, the solar Lyman-α radiation ionises nitric oxide (NO) and EUV affects O_2. At altitudes below 60 km, the main quiet time ionisation source is galactic cosmic ray precipitation. These radiation sources produce quiet-time ionisation rates from 10^4 to 10^7 $m^{-3}s^{-1}$ at D-region altitudes [Brasseur and Solomon, 2005]. However, sporadic ionisation events, such as X-ray bursts from solar flares, relativistic electron precipitation from the radiation belts (affecting mid-latitudes), energetic auroral precipitation (at high latitudes) or solar proton events can increase the ionisation level, and the electron density, by several orders of magnitude. The D region seems to be stable during normal days. But during geomagnetically disturbed days the composition and the electron density of this region shows a drastic changes.

1.8 D-region ionospheric probing using VLF waves

The ionospheric D region (<95 km) is relatively inaccessible when compared to other layers and it is one of the least studied region. It is because the altitude (60-90 km) of this region which is too high for balloons and too low for satellites to reach, making continuous monitoring very difficult. And also it is generally difficult to measure the ionospheric D region electron density since ionosondes and incoherent scatter radars in the HF-VHF range do not receive echo's from this region, where electron density is typically $< 10^3$ cm^{-3}. In general, there are two possible

approaches available to observe any atmospheric or ionospheric parameters in the D region. The first option is obviously in-situ measurements, which are limited to rocket-borne instruments in this case. Therefore the current knowledge on D-region composition is found to a large extent on past rocket missions [Friedrich et al., 2004]. Besides the cost, sparse spatial and temporal coverage of the data is obviously the drawback of this approach.

Another option is to exploit electromagnetic (or even infrasonic) waves for atmospheric remote sensing. Here comes the Very low frequency (VLF) handy for remote sensing of the D region ionosphere. VLF (3-30 Khz) waves are useful scientifically because they largely reflect at the D region of the Earth's ionosphere. VLF energy radiated near the ground is reflected by the lower ionosphere and by the ground and thus propagates in a guided fashion between these two boundaries, which form what is known as the Earth Ionosphere Waveguide (EIWG). Figure 1.17 shows the cartoon of Earth Ionosphere Waveguide with VLF waves propagation.

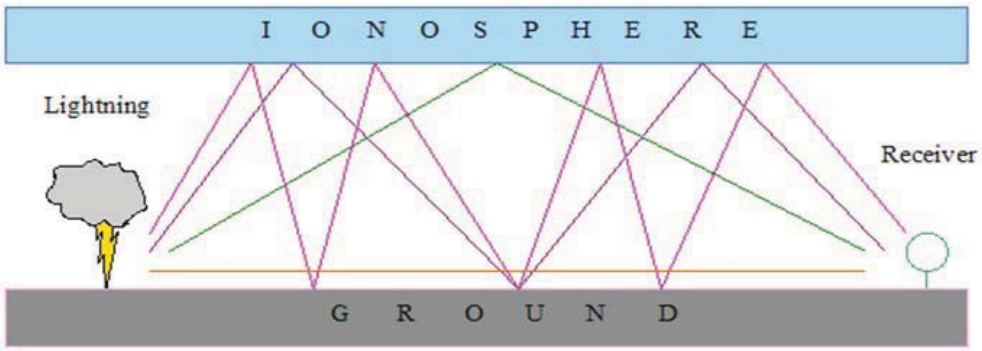

Figure 1.17: Cartoon of Earth ionosphere waveguide

Lightning discharges from thunderstorm are nature most significant source of electromagnetic waves, the energy in these radiated pulses vary over a wide frequency range from few Hz to several MHz. However, the maximum energy of this lightning is concentrated in Extreme Low Frequency(ELF)/VLF waves range. Radio atmospherics (or sferics) are the electromagnetic signals launched by individual lightning discharges. The broadband VLF sferic signals radiated by lightning strokes and reflected several times in the EIWG can be used to remote sense the ionospheric

D region electron density profile variations. By using the waveform of a sferic in time domain, researchers derived the D region reflection height of radio waves from the arrival time difference between the ground wave and sky waves. D region virtual height has been calculated as a function of local time (LT) from VLF/ELF electric fields radiated by intracloud lightning and recorded by the Los Alamos Sferic Array (LASA) [Smith et al., 2004]. Broadband VLF sferic spectra were also used to infer the D region electron density profiles by fitting the measured spectra to modelled spectra. Another form of remote sensing of D region using VLF waves is by measurements using single frequency or narrowband signals transmitted by large man-made transmitters and reflected by the lower ionosphere. Modern applications of this technique have measured amplitudes and phases for narrowband VLF signals sent by different transmitters and propagating long distances in the EIWG, and compared the measurements to Long Wave Propagation Capability (LWPC) [Pappert and Ferguson, 1986] simulations, so as to infer the average D region electron density profiles along the wave propagation paths [Thomson, 1993; Thomson and Clilverd, 2001; Thomson et al., 2004, 2005, 2007; Thomson and McRae, 2009; Thomson, 2010; McRae and Thomson, 2000, 2004; Selvakumaran et al., 2014].

1.9 Experimental set up and data

1.9.1 AWESOME VLF Setup

The ELF/VLF electromagnetic data used in this thesis work recorded using Atmospheric Weather Electromagnetic System for Observation Modeling and Education (AWESOME) receiver designed by Stanford University. The AWESOME-VLF receiver setup consists of four main components: (1) Antenna (2) Pre-amplifier (3) Long cable (4) Line receiver box as shown in Figure 1.18. The antennas gather necessary data for recording. The preamplifier box and line receiver box process the signals and pass them to the computer. Let us discuss this different parts in detail.

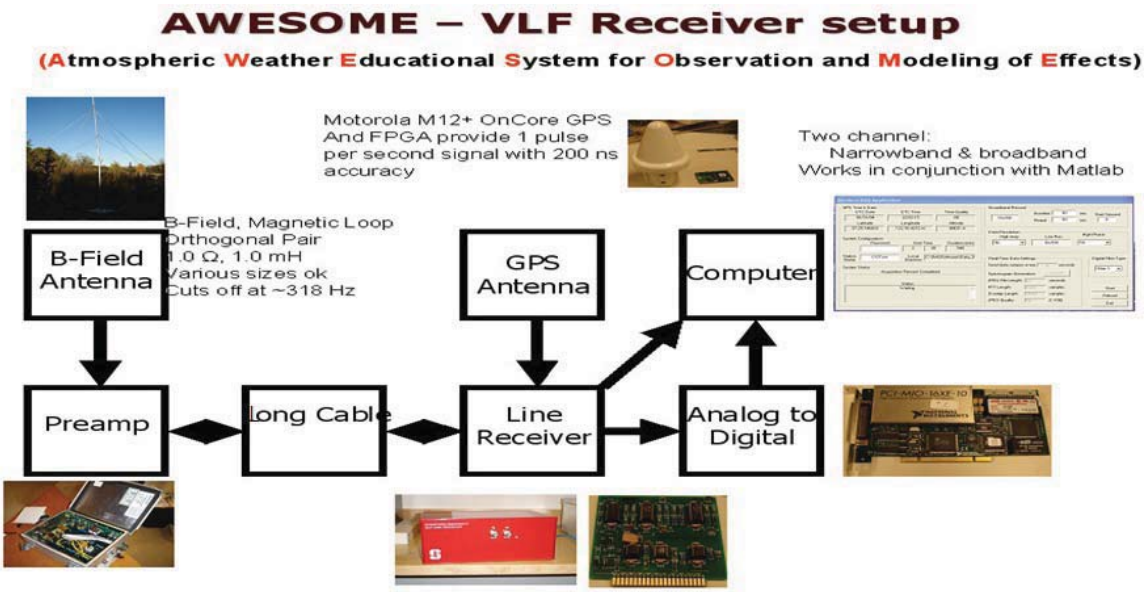

Figure 1.18: Pictorial representation of AWESOME VLF receiver set up.

Antenna

The system consists of crossed magnetic loop antennas which are orthogonal to each other and directed in North South (NS) and East West (EW) magnetic plane, so that the receiver picks up

magnetic fields (horizontal) parallel to the ground from any direction. The antenna corresponds to right isosceles triangles covering a geometrical area of roughly 25 m^2 and base 10 m. The antenna basically works on Faraday's law of electromagnetic induction which states that induced voltage is equal to the time rate of change of the magnetic field through the loops. The current induced increases with the frequency. However, the impedance of the line receiver is correctly matched to the impedance of the antenna then the output voltage can be made independent of frequency over limited range [Paschal, 1988].

Pre-amplifier

The loop antenna is connected to an aluminum weather-proof known as pre-amplifier, whose job is to collect and amplify the small signals from the antenna without introducing any significant noise. This preamplifier is placed near the antenna with impedance matched to enable maximum power transfer from antenna to the receiver. Apart from amplifying and filtering, the pre-amplifier consists of a matching input transformer, a differential amplifier and a line driver.

Long cable

The pre-amplifier is connected to the line receiver by long cable 300 m. This long cable has a 4 shielded AWG twisted pairs of wire. Out of the 4 pairs of wire three are used for collecting data from channels, the impedance of cable at both ends is matched with the customed designed line transformer. Apart from data transfer, the power 15 V to the pre-amplifier is fed by same cable from line receiver.

Line receiver

The line receiver performs anti−aliasing filtering, GPS time synchronization and post processing of the data. The line receiver then sends the acquired analogue data to the computer for

digitization which is done by A/D card fitted in the PCI slot of the computer. The line receiver serves many functions, including signal processing, digitization control, GPS management, power management, and system calibration. The data acquired is sampled at 16-bit and 100 Khz. The sampling of 100 kHz enables the signal detection up to 50 kHz.

Data acquisition

The VLF data received from the source through antenna is recorded in computer using a data acquisition software VLF-DAQ designed by Stanford university. The primary purpose of this software is to enable collection of two different type of data. The first is broadband, saves the waveform received from antenna exactly as it was digitized, at the full 100 kHz sampling rate. It thus includes information at a frequencies between the systems cutoffs (300 Hz $-$ 47 kHz). Broadband data is very large and takes about 1.5 GB per hour. As a result, broadband data is usually saved in a limited format. For instance, the "synoptic" format can capture selections of broadband on a periodic basis,one minute out of every 15. However, for larger scale broadband recordings during special campaigns or experiments,the continuous option can be used to record. The second type of data is called narrowband. This simply involves taking the amplitude and phase, separately of single narrow frequency range,specified in the software,and usually corresponds to the frequency of a VLF transmitter. Such data is generally saved in two different resolutions, hi$-$resolution (50Hz), and low$-$resolution (1Hz). Narrowband data takes up much smaller amount of space, 1 MB per hour, per transmitter, and for this reason most of the day can be recorded in a continuous fashion, even when as many as 15 transmitters are being monitored.

The three AWESOME ELF-VLF receivers were set up at three low latitude station shown in Figure 1.18, by Indian Institute of Geomagnetism in collaboration with Stanford University under International heliophysical year 2007. The details of AWESOME network in India can be found in Singh et al. [2010].

1.9.2 GOES satellite- X-ray Flux data

The X-ray flux used in this thesis is taken from the GOES satellite. GOES satellite continuously monitors X-ray flux emitted from the Sun along with many other onboard instruments. The GOES X-ray Sensor (XRS) is used to monitor the solar X-ray flux. GOES XRS measurements have been made since 1970s. On each GOES satellite there are two XRS which provide solar X-ray fluxes for the wavelength bands of 0.5 to 4 Å(short channel)and 1 to 8 Å(long channel). This XRS continuously monitors solar flares and helps predict solar proton events that can penetrate Earth's magnetic field. The XRS is important in monitoring X-ray input into the Earth's upper atmosphere and alerts scientists to X-ray flares that are strong enough to cause radio blackouts and aid in space weather predictions.

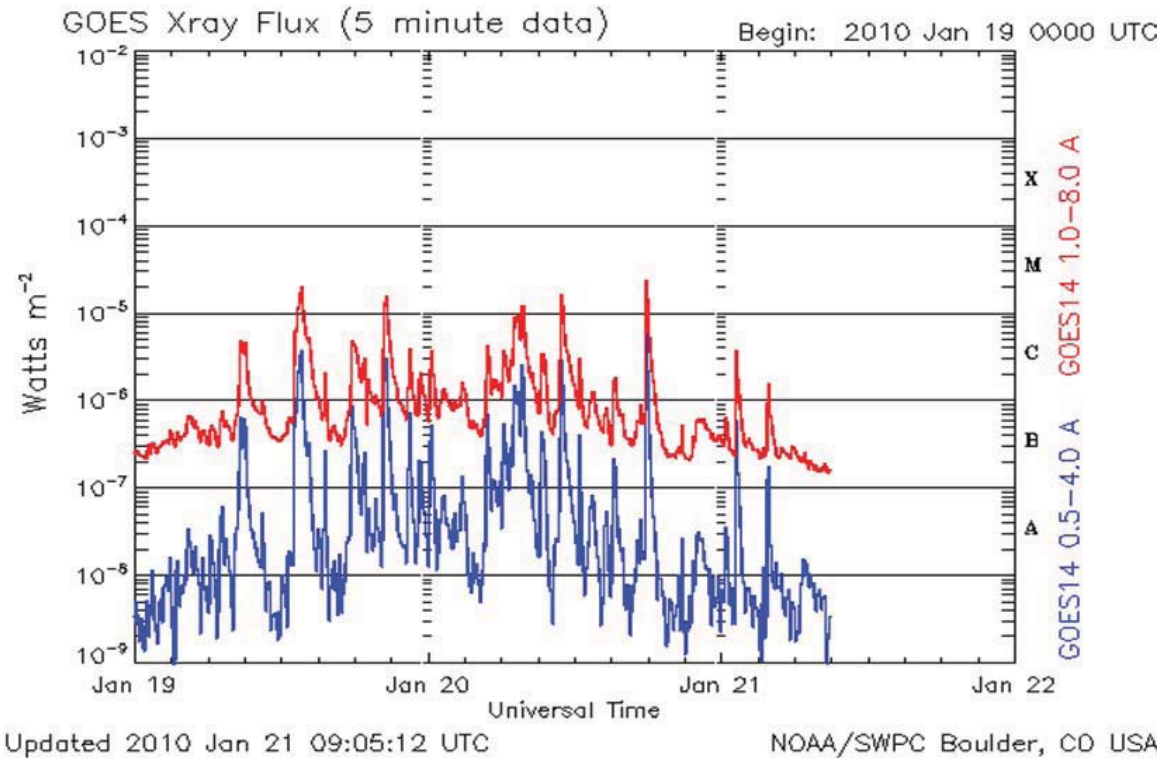

Figure 1.19: Example of GOES X-ray plot from Jan. 19-22, 2010.The peaks represent solar flares.

GOES X-ray plots show data in two wavelength bands 0.5-4.0 (Å) and 1.0-8.0 (Å) as shown in figure 1.19. The left axis gives the X-ray flux in W/m^{-2}, while the right hand axis gives the letter designation for each order of magnitude. Each flare is given a GOES classification consisting of this letter and a number, assigned according to the peak of the 1.0-8.0 Åemission.

1.9.3 Solar and Interplanetary data

SOHO

The Solar and Heliospheric Observatory (SOHO) project is a cooperative effort between the European Space Agency (ESA) and National Aeuronuatical space administration (NASA). SOHO was designed to study the internal structure of the Sun, its extensive outer atmosphere and the origin of the solar wind. SOHO was launched on December 2, 1995. Large Angle and Spectrometric Coronagraph (LASCO) is a set of three coronagraph telescopes on-board SOHO satellite, which records white light images of the solar corona from 1.1 through 30 solar radii. A coronagraph is a special type of telescope that uses a solid disk ("occulter" or "occulting disk") to cover the Sun itself, completely blocking direct sunlight, and allowing to see the atmosphere around the Sun (known as "corona"). LASCO is implemented to study the transport of mass, momentum, and energy through the corona and into the solar wind by measuring global distributions of plasma parameters and their evolution with time. One of the main ejection from corona part of the Sun is CME, their initial source location identification, evolution energy transfer can be inferred using this LASCO experiment.

STEREO

STEREO (Solar TErrestrial RElations Observatory) is the third mission in NASA's Solar Terrestrial Probes program (STP). The mission, launched in October 2006, has provided a unique and revolutionary view of the Sun-Earth System. The two nearly identical observatories - one ahead

of Earth in its orbit, the other trailing behind - have traced the flow of energy and matter from the Sun to Earth. STEREO has revealed the 3D structure of coronal mass ejections; violent eruptions of matter from the Sun that can disrupt satellites and power grids, and help us understand why they happen. STEREO is a key addition to the fleet of space weather detection satellites by providing more accurate alerts for the arrival time of Earth-directed solar ejections with its unique side-viewing perspective.

The two STEREO spacecraft were launched at 00:52 UTC on October 26, 2006, from Launch Pad 17B at the Cape Canaveral Air Force Station in Florida on a Delta II 7925-10L launcher into highly elliptical geocentric orbits. The apogee reached the Moon's orbit. On December 15, 2006, on the fifth orbit, the pair swung by the Moon for a gravitational slingshot. Because the two spacecraft were in slightly different orbits, the "ahead" (A) spacecraft was ejected to a heliocentric orbit inside Earth's orbit while the "behind" (B) spacecraft remained temporarily in a high Earth orbit. Each of the spacecraft carries cameras, particle experiments and radio detectors in four instrument packages: one among them is SECCHI - Sun Earth Connection Coronal and Heliospheric Investigation has four instruments: an extreme ultraviolet imager, two white-light coronagraphs and a heliospheric imager. These instruments study the 3-D evolution of coronal mass ejections from birth at the Sun's surface, through the corona and interplanetary medium, and to their eventual impacts at Earth.

SDO

The Solar Dynamics Observatory (SDO) has been launched on February 11, 2010 into an inclined geosynchronous orbit to understand the causes of solar variability and its impacts on the Earth. The inclined orbit allows continuous observations of the Sun. The scientific experiments aboard are the Atmospheric Imaging Assembly (AIA), the EUV Variability Experiment (EVE) and the Helioseismic and Magnetic Imager (HMI). These three instruments observe the Sun simultaneously, make the required measurements to understand the mechanisms involved in the quasi-periodic solar cycle (11-year) activity and its relation with the Sun's EUV spectral irradiance, the

state of active region magnetic flux topology before and after the occurrence of solar flares, CMEs and filament eruptions. These studies are aimed at making accurate and reliable forecasts of space weather to understand the mechanisms of the processes involved (http://sdo.gsfc.nasa.gov). The SDO will spot eruptions as they occur, giving forecasters an approximately 4-days warning time. SDO images the Sun every 0.75 s and transmits about 1.5 terabytes of data per day at a resolution 10 times better than today high resolution television [Klotz., 2010].

ACE and WIND

Advanced Composition Explorer (ACE) is a NASA's Explorers program Solar and space exploration mission to study matter comprising energetic particles from the solar wind, the interplanetary medium, and other sources. The Earth is constantly bombarded with a stream of accelerated particles arriving not only from the Sun, but also from interstellar and galactic sources. Study of these energetic particles contributes to our understanding of the formation and evolution of the solar system as well as the astrophysical processes involved. The ACE spacecraft carrying six high-resolution sensors and three monitoring instruments samples low-energy particles of solar origin and high-energy galactic particles with a collecting power that is 10 to 1000 times greater than past experiments. ACE orbits the L1 point which is a point of Earth-Sun gravitational equilibrium about 1.5 million km from Earth and 148.5 million km from the Sun. From its location at L1 ACE has a prime view of the solar wind, interplanetary magnetic field and higher energy particles accelerated by the Sun, as well as particles accelerated in the heliosphere.

This thesis comprises the data from two experiments of ACE on board, one is Solar Wind Electron Proton and Alpha Monitor (SWEPAM) and the other is Magnetometer (MAG). SWEPAM observations provide the context for elemental and isotopic composition with direct examination of numerous solar wind parameters such as speed, density, interplanetary shocks, and solar wind fine structure. MAG provides continuous measurements of the local magnetic field in the interplanetary medium.

Another mission which provides interplanetary parameters is Wind satellite, a spin stabilized spacecraft launched on 1 November, 1994 and placed in a halo orbit around the L1 Lagrange point, more than 200 Re upstream of Earth to observe the unperturbed solar wind that is about to impact the magnetosphere of Earth. Similar to ACE , Wind provides data of complete plasma, energetic particles and magnetic field for magnetospheric and ionospheric studies.

1.9.4 Ground Geomagnetic data

The transient variation of geomagnetic field at the Earth's surface are the signatures of the currents taking place in the entire magnetosphere, under the influence of the solar wind. They are composed of the effects of currents flowing in the ionosphere and in the magnetosphere, including field aligned currents, magnetopause currents. Complexity of the solarwind- magnetosphere-ionosphere coupling processes results in a large variety of magnetic signatures, depend on the state of magnetosphere which also differs with the geographic and geomagnetic location of the observatory. In order to identify the variations as a representative of isolated effect ground magnetic observation and indices serves the purpose to estimate the global energy input in ionosphere and magnetosphere.

Dst index

One of the most systematic effects seen in ground-based magnetometer data is a general depression of the horizontal magnetic field as recorded at near-equatorial observatories [Moos, 1910]. This is often interpreted as an enhancement of a westward magnetospheric equatorial ring current, whose magnetic field at the Earth's surface partially cancels the predominantly northernly component of the main field. The storm-time disturbance index Dst [Sugiura, 1964] is designed to measure this phenomenon. Dst measures primarily the ring-current magnetic field. It is based on hourly averages of the H component recorded at four low-latitude observatories, subtracting the average Sq and the permanent field from the disturbed magnetic field.They show the effect of

the globally symmetrical westward flowing high altitude equatorial ring current, which causes the "main phase" depression worldwide in the H-component field during large magnetic storms.

Magnetic observatories in India

In the historical evolution of magnetic measurements, Alexander von Humboldt and Carl Friedrich Gauss with Wilhelm Weber has left a key place in establishing network of magnetic observatories, in the development of instrumentation for measurements in absolute units and in the theory of geomagnetism. Humboldt was in the pioneering era of setting up magnetic observatories. India's participation in pursuing the study of the science of geomagnetism through observations at magnetic observatories initiated in 1836, when the country became a member of the Gittingen Magnetic Union, which was formed in 1836 by Gauss and colleagues.

The establishment of the magnetic observatory at Colaba (Bombay) took place in 1841, however, regular observations commenced in 1846. Indian institute of geomagnetism (IIG) operates a chain of magnetic observatories covering entire India to see the geomagnetic variation throughout Indian latitude. Continuous recording of magnetic field is carried out using digital fluxgate magnetometer at all observatories. Both absolute and variation measurement of geomagnetic field is made in the observatory. Alibag and tirunelveli data from IIG is used for the present research work, location is given in the Figure 1.20 along with all observatories operated by IIG. To obtain the EEJ strength values, by subtracting simultaneous measurements of horizontal component of earth's magnetic field (H) from dip equatorial station Tirunelveli and off equatorial station Alibag, which is outside the influence of electrojet, have been used.

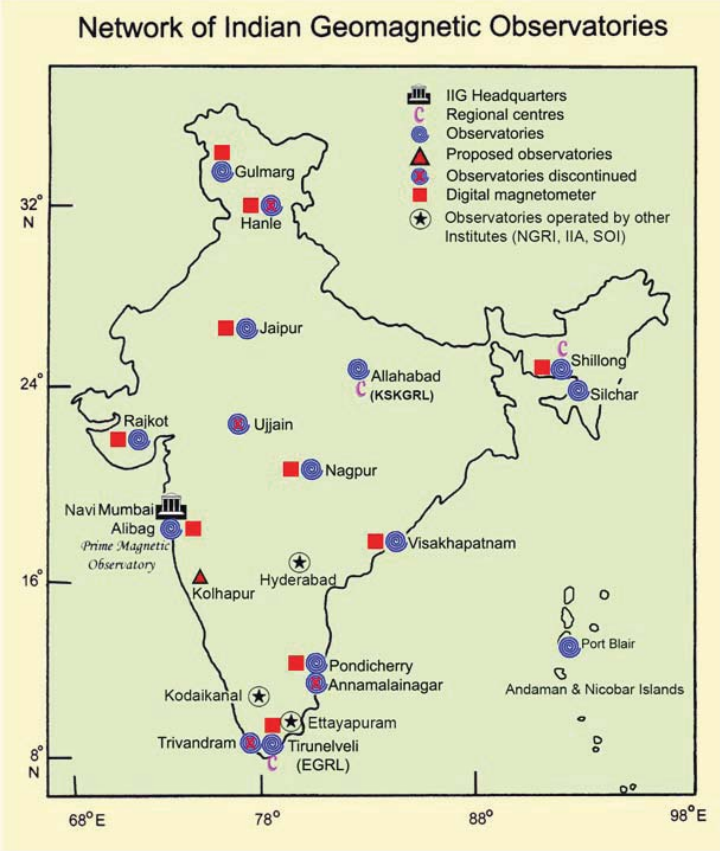

Figure 1.20: Magnetic observatories operated by IIG.

1.10 Thesis contributions

Thesis chapters deals with the study two major solar eruptions (Sola flares and CMEs) from the Sun and their disturbance caused in Earths magnetopshere and ionosphere.

The chapter of thesis are arranged in the order of

1) The D-region ionospheric perturbations caused by solar flares which occurred during January 2010 - February 2011, a low solar activity period of current solar cycle 24, have been examined on NWC transmitter signal (19.8 kHz) recorded at an Indian low latitude station, Allahabad. A total of 41 solar flares, including 21 C-class, 19 M-class and 01 X-class, occurred during the

daylight part of the NWC-Allahabad transmitter receiver great circle path. The local time dependence of solar flare effects on the change in the VLF amplitude, time delay between VLF peak amplitude and X-ray flux peak have been studied during morning, noon and evening periods of local daytime. Solar flare effects on the horizontal component (H) of the Earth's magnetic field over an equatorial station, Tirunelveli have also been studied for the same period.

2) Interplanetary (IP) shocks are mainly responsible for the sudden compression of the magnetosphere, causing storm sudden commencement (SC) and sudden impulses (SIs) which are detected by ground-based magnetometers. Based on the IP shocks list compiled by Gopalswamy et al. (2010), the dependence of SC/SIs amplitudes on the speed of the coronal mass ejections (CMEs) that drive the shocks near the Sun as well as in the interplanetary medium is investigated. The shocks were grouped according to their ability to produce type II radio burst in the interplanetary medium, to see their importance in determining SC/SI amplitude and geoeffectiveness. IP shocks also divided according to the type of IP counterpart of interplanetary CMEs (ICMEs): magnetic clouds (MCs) and nonmagnetic clouds (EJ) to see their influence in SC/SI amplitude as well as in the geoeffectiveness.

3) The moderate and intense geomagnetic storms are identified for the first 77 months of solar cycle 23 and 24. The solar sources responsible for the moderate geomagnetic storms are identified during the same epoch for both the cycles. Solar cycle 24 has shown nearly 80 $\%$ reduction in the occurrence of intense storms where as it is only 40 $\%$ in case of moderate storms when compared to previous cycle. The solar and interplanetary characteristics of the moderate storms driven by CME are compared for solar cycle 23 and 24 in order to see reduction in geoeffectiveness has anything to do with the occurrence of moderate storm. The solar source parameters like CME speed, mass and width is investigated to see any difference in two cycles. The correlation between VBz and Dst is determined for both the cycles. The magnetospheric energy flux parameter epsilon (ε) is estimated during the main phase of all moderate storms for solar cycles 23 and 24.

4) Interplanetary (IP) shocks interact with the Earth′s magnetosphere, resulting in compression of the magnetosphere which in turn increases the Earth′s magnetic field termed as sudden

commencement/Sudden impulse (SC/SI). Apart from IP shock speed, solar wind dynamic pressure, the IP orientation angle plays a major role in deciding the SC/SI rise time. In the present study, the IP shock orientation angle and SC/SI rise time for 179 IP shocks are estimated which occurred during solar cycle 23. The SC/SI rise time decreases with the increase of the orientation angle and also with the IP shock speed. The main motivation behind the present work is to establish the importance of radio characteristic of CME and ICME structure along with IP shock orientation angle in determining SC/SI rise time as well as geoeffectiveness. MHD simulations is used to confirm the importance of orientation angle in determining the geoeffectiveness.

Chapter 2

Solar flares induced D-region ionospheric and geomagnetic perturbations

2.1 Solar flare

In 1859, R. Carrington, a solar astronomer, observed an intense, short-lived brightening on the surface of the Sun in the vicinity of a sunspot [Carrington 1960]. Such brightening on the surface of the Sun are now known as solar flares and have been the objects of extensive research during the present century. A large solar flare can release 10^{25} J. The energy of the flare spread throughout the electromagnetic spectrum. Solar flares are clearly linked to magnetic field. They almost occur near the sunspots. Solar flare can have important effect on the earth. X-ray and ultravoilet radiation reaches earth in 8 minutes and increase the ionization in the upper atmosphere. This alters the reflection of radio signals and can absorb them completely, thereby interfering with communication. In case of solar flare the most of the energy released stored in the X ray. During the normal time the X-ray cannot penetrate much in to D region causing major ionisation. During flare it brings out major changed in the ionization. Figure 2.1 shows the X-ray flux reaches the lower ionospheric region during solar flare.

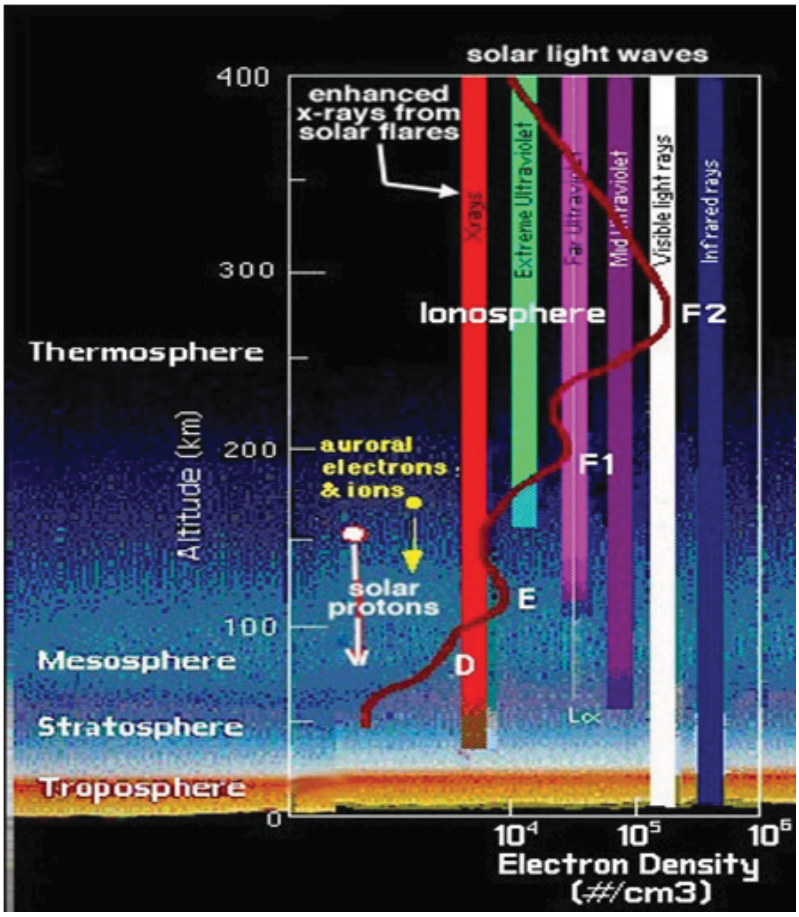

Figure 2.1: Different wavelengths reaching different regions of ionosphere.

2.2 Effects of Solar flare in D region ionosphere and Earths magnetic field

The D-region(60-90 km) lowest region of the ionosphere the level of ionization depends on the solar zenith angle and the solar radiation by Chapman theory. In the daytime, the ionization in the D-region ionosphere is maintained mainly by direct Lyman-α radiation (121.6 nm) from the Sun which partially ionizes the nitric oxide (N_2O, at 70 km altitude), a minor neutral constituent in the D-region. Under the normal conditions the solar X-ray flux is too small to be a significant source

of ionization but during solar flares the increased X-ray flux from the Sun in the wavelength range of 0.2 to 0.8 nm ionizes neutral constituents along with the major species O_2 and N_2 [Hargreaves, 2003; Mitra, 1974]. Solar flares are known to cause ionospheric perturbations in the daytime [Mitra, 1974; Davies, 1990; Tsurutani et al., 2009] but it is the D-region of the ionosphere which is perturbed most [Mitra, 1974; Zigman et al., 2007]. The perturbation modifies the electron density in the D-region ionosphere and hence changes the propagation conditions of Very Low Frequency (VLF, 3-30 kHz) waves in the Earth-ionosphere waveguide (EIWG) formed between the D-region ionosphere and the Earth's surface [Thomson et al., 2005].

The measurement of VLF signals, generated by navigational transmitters has emerged as one of the reliable tools for remote sensing of the D-region electron density perturbations associated with solar flares [Mitra, 1974; Ananthakrishnan et al., 1973; Thomson et al., 2004; Grubor et al., 2005; Kumar and Kumar, 2014; Maurya et al., 2014]. The D-region monitoring is rather difficult due to its altitude range, which is too high for balloons and too low for satellite measurements. Rockets and Radars have been used, but they have poor spatial and temporal resolutions and hence cannot be used for continuous monitoring of the D-region ionosphere. The VLF remote sensing is also a cost-effective technique for understanding the dynamical processes in the D-region ionosphere [Bainbridge and Inan, 2003; Maurya et al., 2010; Phanikumar et al., 2014; Singh et al., 2011; Singh et al., 2012; Thomson et al., 2007; Thomson and MacRae, 2009].

There have been several studies [e.g.,Ananthakrishnan et al., 1973; Pant, 1993; Thomson and Cliverd, 2001; McRae and Thomson, 2000; McRae and Thomson, 2004; Thomson et al., 2005; Grubor et al., 2005; Zigman et al., 2007; Singh et al., 2013] on the D-region solar flare effects using VLF waves, transmitted by the navigational transmitters. Some studies mainly focused on the comparative investigations between the changes in the VLF signal amplitude/phase and time delay with respect to solar X-ray flux [Ananthakrishnan et al., 1973; Pant, 1993] however local time dependence of these perturbations is not considered. Several studies [e.g.,Thomson and Cliverd, 2001; McRae and Thomson, 2004; Thomson et al., 2005; Grubar et al., 2005, 2008; Zigman et al., 2007] on the D-region solar flare effects using Long Wave Propagation Capability (LWPC) code

(developed by Naval Ocean Systems Center (NOSC), San Diego, USA) (Morfitt and Shellman, 1976), have estimated Wait ionospheric parameters; D-region reflection height ($H^{/}$) in km and D-region electron density gradient or sharpness factor (β) in km^{-1} (Wait and Spices, 1964). The quantification of the D-region reflection height and electron density changes during flare events had been reported by several researchers [Thomson and Cliverd, 2001; McRae and Thomson 2004; Thomson et al., 2005; Zigman et al., 2007; Singh et al., 2013]. The increased ionization due to a flare lowers the $H^{/}$ roughly in proportion to the logarithm of the X-ray flares $H^{/}$ intensity [McRae and Thomson, 2004].

In this chapter we have focused on the study of D-region ionospheric perturbations caused by solar flares during January 2010 to February 2011 on NWC transmitter signal (19.8 kHz) recorded at an Indian low latitude station, Allahabad. Solar flare effects on the horizontal component (H) of the Earth's magnetic field over an equatorial station Tirunelveli have also been studied for the same period which falls under the low solar activity period of beginning of new solar cycle 24 after an extended solar minimum. The sub-ionospheric amplitude perturbations due to 41 solar flares which include 21 C-class, 19 M-Class and 1 X-class flare have been analyzed. Further local time variation of solar flare effects on the change in the VLF amplitude (ΔA), time delay (Δt) between VLF peak amplitude and X-ray flux peak, D-region reflection height $H^{/}$ and sharpness factor (β) are examined.

2.3 Data

A wide range of data sets have been to used to study the perturbation in D region ionosphere and geomagnetic during solar flare. AWESOME VLF receiver located at Allahabad (Geographic lat. 25.40 °N, long. 81.93 °E; Geomagnetic lat., 16.25 °N) is used to record the VLF signal transmitted by Australian narrow band NWC transmitter (Geographic lat. 21.80 °S, long. 114.20 °E) at 19.8 kHz. The Transmitter Receiver Great Circle Path (TRGCP) from NWC Australian Transmitter to receiving station at Allahabad is shown in Figure 2.2. TRGCP path length is about 6400

km for NWC-Allahabad path,which comes under medium path length as described by Clilverd et al. (2001). The solar flares of C, M and X classes which occurred during January 2010 to February 2011 are selected depending on the availability of VLF data at Allahabad. The Earth's geomagnetic field horizontal component (H) data (one second resolution) is obtained from equatorial station, Tirunelveli (Geographic lat. 8.7 °N, long. 77.8 °E, dip latitude: 0.4 °N), to study the changes in the H due to solar flares. ΔH is obtained by subtracting the midnight value of H to avoid the Earth's main field effect on the H component. The X-ray flux data recorded by the GOES satellites is obtained from the USA National Oceanic and Atmospheric Administration (www.sec.noaa.gov). The Local time (LT) = Universal Time (UT) + 5.5 hrs. In the present study we have estimated change in VLF amplitude due to flare ΔA as: ΔA = $A_{perturb}$ - A_{normal} , where $A_{perturb}$ is the maximum VLF amplitude observed during given solar flare event and A_{normal} is the mean for five normal days close to flare event and time delay Δt as: $\Delta t = t_{\Delta Amax} - t_{ff}$ where $t_{\Delta Amax}$ is the amplitude peak time of VLF signal and t_{FF} is flare flux peak time.

2.4 Observations

2.4.1 Solar flare effect on NWC signal at low latitude station: Allahabad

After the long solar minima, the Sun unleashed the first C-class flare of solar cycle 24 on 19th January 2010 at 14:17 LT, the strongest solar flare detected in almost two years. During January 2010 to February 2011, nearly 41 solar flare events (21 C-class, 19-M class and 01 X-class flare) have been analyzed to examine the changes in VLF amplitude, Wait parameters, electron density and their local time dependence. Figure 2.3 (a and b) shows an example plot of the amplitude perturbations in the NWC VLF signal received at Allahabad corresponding to the X-ray flux (GOES data) for 20th January 2010 and 15th February 2011 solar flares, respectively. The amplitude enhancements in NWC VLF signal are observed for 3C and 3 M class flares that occurred on 20th January 2010 and one C, one M and one X class flares on 15th February 2011 due to additional ionization. The extra ionization sharpens the D-region or upper boundary of the EIWG and causes it to

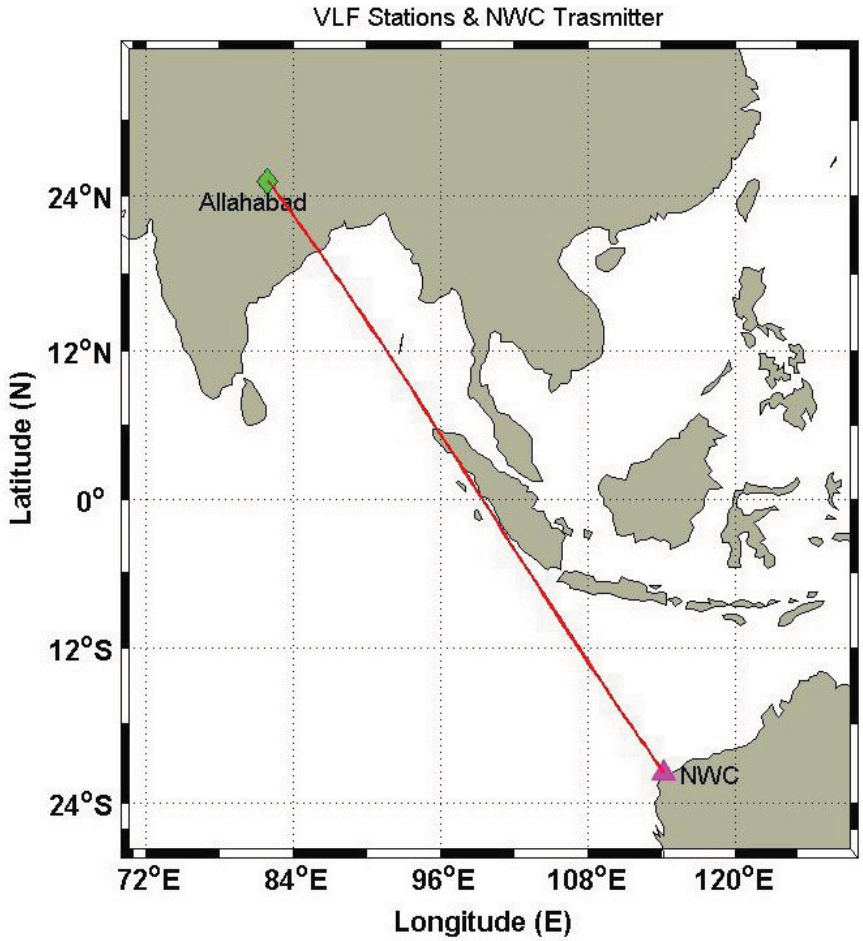

Figure 2.2: Great Circle path between VLF transmitter NWC (pink triangle) and low latitude receiving stations in India Allahabad (green diamond).

descend up to several km depending upon the intensity of solar flare flux [Thomson and Clilverd, 2001; Grubar et al., 2005].When VLF signal propagates through the region of enhanced electron concentration, it finds a sharper boundary which gives a mirror type of reflection [Grubar et al., 2005] as a result the amplitude of the VLF signals is increased.

The table 2.1 below gives the details of all the solar flare events considered in the present study. The change in the VLF signal amplitude (ΔA) depends on the flare strength (solar X-ray flux) which can be effectively utilized to estimate the electron density changes due to solar flares

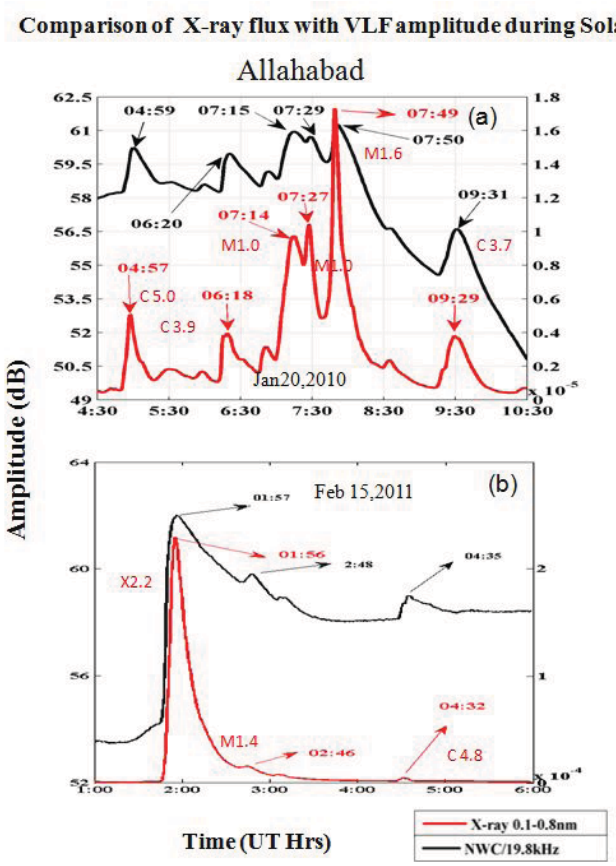

Figure 2.3: An example of variation of X-ray flux (red line) detected by GOES and NWC VLF signal amplitude (black line) at Allahabad station on 20th January and 15th February 2011.

[Grubar et al., 2005; Zigman et al., 2007]. Figure 2.4 shows variation in the ΔA of NWC signal with solar flare intensity measured in dB relative to 1 W/m2 for all 41 solar flares. It can be seen that ΔA varies between 1.21 to 2.73 dB for C class solar flares and between 2.88 to 5.45 dB for M class solar flares.

The lowest flare which produced the perturbation in the signal amplitude is a C 2.0 class flare (1.21dB).The maximum ΔA of 6.8 dB was observed for an X2.2 solar flare. The solar flare X-ray flux intensities are expressed in decibel (dB) unit. A third-degree polynomial is used to fit. McRae and Thomson (2004) estimated the best-fit curve for the amplitude perturbation versus flare power,

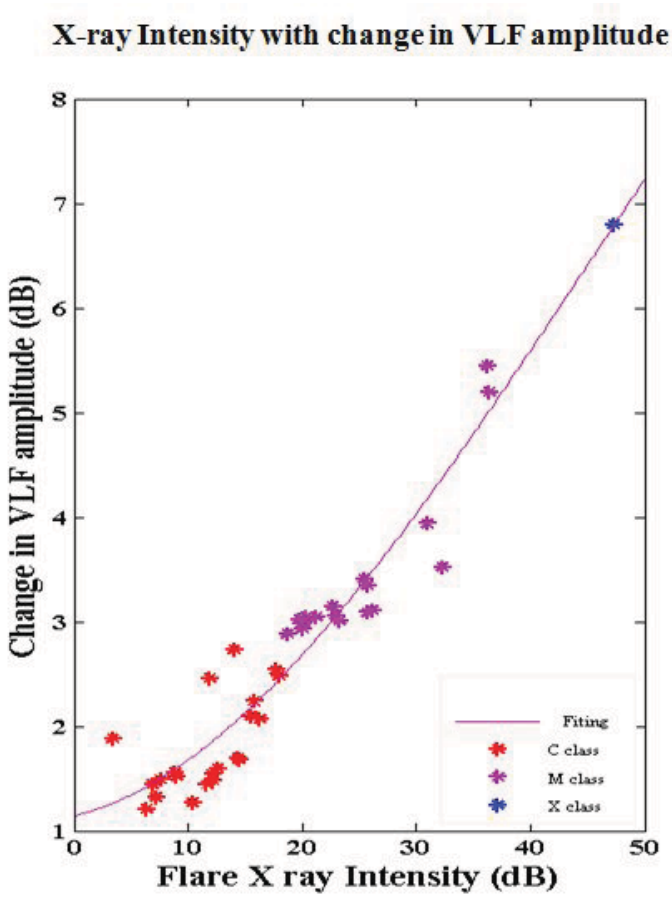

Figure 2.4: Variation of change in the VLF amplitude with the solar flare intensity (dB).

which can be used to determine the flare of higher classes (>X17) when GOES detector saturates.

In general, as the intensity of the flare increases, the ΔA also increases but not linearly. For example, the ΔA for three C-class flares, C5.0, C3.9 and C3.7 occurred on 20 January 2010, were estimated 2.73 dB, 2.46 dB and 1.44 dB, respectively. However some inconsistency in the ΔA values were seen when solar flares of same class/strength occurred on different days. For example, C5.2 flare on 19 January 2010 (at 14:37 LT) produced ΔA 1.68 dB which is less as compared to C3.9 class flare on 20 January 2010 (11:50 LT) with ΔA 2.46 dB. The nonlinearity comes from the fact that ΔA also depends upon pre-flare flux condition and local time. In order to check it we have made a detailed analysis of the pre-flare X-ray flux for all the 41 flare events. A window of 15

minutes for solar X-ray flux is taken for all the solar flares before the onset and the average flux in this window is calculated (pre-flare level). This average flux is then subtracted from the peak flux value to obtain absolute enhancement in the flux level. The pre-flare flux conditions give better results when multiple solar flares occur in a short time. Based upon calculations, in general, it is observed that the pre-flare flux values follow the linear trend with the class of flares. But the pre flux values show discrepancy when a flare is followed by another flare depending upon its class, i.e., if the given flare is preceded by a higher class flare, the pre flux value is more but the absolute enhancement in the flux is less. For example, on 15 February 2011, three successive flares occurred in the morning period (X 2.2, M1.4 and C4.8). The absolute flux enhancement is highest (2.29 x 10^{-4} W/m^2) for X2.2 flare among all the flares considered in the study. For M 1.4 flare which was followed by X 2.2, the flux level was stable as seen from Figure 2.2 , so the pre flux level for M1.4 flare is more (9.63 x 10^{-5} W/m^2) as compared to that of X 2.2 (9.07 x 10^{-7} W/m^2). For C 4.8 class flare the pre flux level came nearly to the normal value (2.14 x 10^{-6} W/m^2). Similarly, C5.2 flare on 19 January 2010 had pre flux of 3.95 x 10^{-7} W/m^2 which is less as compared to C 3.9 flare with pre-flux of 2.15 x 10^{-6} W/m^2 due to the fact that the later flare was followed by C 5.0 flare.

2.4.2 Local time dependance

The one main reason for the nonlinearity is the local time dependence of solar flare effect. The local daytime taken into consideration is the daytime at the receiving station, Allahabad, between 06-18 LT (00:30-12:30 UT). In order to clearly understand local time dependence of ΔA and other D-region parameters, whole local daytime is divided in three periods: morning (06-10 LT), noon (10-15 LT) and evening (15-18 LT). Table 2.1 presents the average values of ΔA, Δt, H$'$ and β for C and M-class flares. From Table 2.1, it can be seen that the average ΔA for C-class flares increases as the day progresses and attains its maximum value at noon and then decreases in the evening period. For M-class flares, the average value of ΔA during noon is less than that in the morning and evening periods. This is because of the occurrence of high intensity M-class flares in

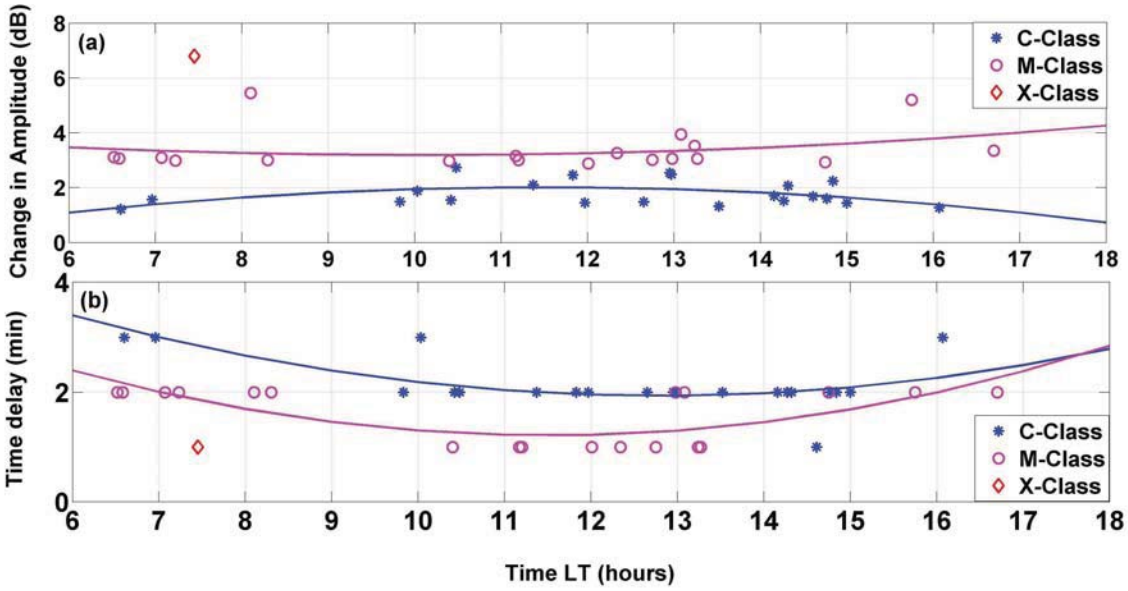

Figure 2.5: (a) Local time variation of change in the VLF NWC signal amplitude estimated with respect to normal day for C, M and X-classes of flare. (b) Local time variation of time delay for C, M and X-classes of flares. The trends of variation are shown by the quadratic fit lines.

the morning (M6.4 at 08:06 LT) and evening period (M6.0 at 15:45 LT) as compared to noon, which results in higher ΔA (5.45 dB and 5.2 dB, respectively). Fig. 2.5a shows the dependence of ΔA on the local time. As we have only one X-class flare event during the period of the present study, it is not possible to study local time dependence for X-class solar flare effects. Thomson and Cliverd, [2001] studied solar flare effects both on long (12000 km) and short (617 km) VLF propagation paths and showed that ΔA variation is less pronounced for long path as compared to the short path. Our present work shows that ΔA variation due to flares depends on the class of flares, pre flare condition and local time. Solar flare effect also shows time delay (Δt) in the occurrence of the VLF peak amplitude when compared to the time of X-ray flux peak. For example, on 20 January 2010, six peaks in the VLF amplitude were matched with the peaks in GOES X-ray flux data. The peaks of the C-class flare flux data occurred at 4:57 UT, 6:18 UT and 9:29 UT and the corresponding peaks in the VLF amplitude occurred at 4:59 UT, 6:20 UT and 9:31 UT, respectively. For M-class flares the X-ray flux peaks occurred at 7:14 UT, 7:27 UT and 7:49 UT and the corresponding peaks

in the VLF amplitude occurred at 7:15 UT, 7:29 UT and 7:50 UT. From the above example; it can be seen that Δt is different for different classes of flares and it may also depend on the local time at the receiving station at the time of occurrence of solar flare. In order to examine this, we have plotted Δt versus local time for C, M and X-class flares in Figure 2.5(b). Figure 2.5b shows that, Δt for all flares, varies from 1-3 min, which is different for different class of flares and also varies according to their occurrence time. In general, Δt is minimum for higher class (X) and maximum for lower class (C) flares. For C-class flares, Δt varies between 1-3 minutes which is higher in the morning and evening periods and lower in the noon period as seen from Table 2.1. For M-class flares, Δt is 2 min in the morning and evening periods and 1 min in the noon period. For X class flare, Δt is approximately 1 min. The Δt observed in the present work has been discussed by many workers with different terminology such as sluggishness [Appleton, 1953; Valnicek and Ranzinger, 1972] and relaxation time [Mitra, 1974]. But the detailed study on the dependence of Δt on the class of flares was not examined. The Δt is caused by the D-region recombination-ionization processes to recover balance under the increased X-ray irradiance of the flare [Zigman et al., 2007]. The Δt for all solar flares are given in table 2.1. The Δt varies between 1-3 min and is consistent with previous observations [Mitra, 1974; Zigman et al., 2007; Gurbor et al., 2005, Kumar and Kumar, 2014].

Mitra, [1974] established a relationship between Δt and maximum electron density and showed that Δt is inversely related to the electron density, which is lower for higher electron density, i.e., ionospheric response is faster when electron density is high. Hence, for the X-class flare the D-region response is fastest, resulting in minimum Δt value. Valnicek and Ranzinger, [1972] using the X-ray data obtained by Inter-Cosmos 1 satellite, showed that sluggishness (Δt) decreases when solar induced ionization increases and vice versa. Grubor et al. [2005] studied the VLF response to solar flares for short (2000 km) path and showed that the Δt also depends on the solar zenith angle. The results presented here for medium (6000 km) path length [Clilverd et al., 2001] at the Indian low latitude station show significant variation in Δ t due to solar flares depending upon their classes and time of occurrence.

Table 2.1: Values of $H^{/}$ and β for different classes of flares calculated for VLF signal observed at Allahabad from the NWC transmitter signal using LWPC V 2.1.

Solar flare day	UT (hrs)	LT (hrs)	Flare class	ΔA (dB)	$H^{/}$ (km)	β ($km^{-}1$)	Delay time Δt (mins)	ΔH_s (nT)
20100119	08:47	14:17	C 5.2	1.7	72	0.35	2	
	09:07	14:37	C 5.2	1.68	72.2	0.35	2	
20100120	4:59	10:29	C 5.0	2.73	69.9	0.38	2	
	06:20	11:50	C 3.9	2.46	70.5	0.37	2	
	07:15	12:45	M1.0	3.02	68	0.39	1	
	07:29	12:59	M1.0	3.05	68.5	0.39	2	
	07:50	13:20	M 1.6	3.26	67.5	0.35	2	
	09:31	15:01	C 3.7	1.44	76	0.28	2	
20100206	05:40	11:10	M1.3	3.15	68	0.4	1	
	07:09	12:39	C 4.0	1.48	73	0.34	2	3.57
20100207	02:36	08:06	M6.4	5.45	66	0.4	2	
	04:54	10:24	M1.0	2.98	68.8	0.38	1	5.36
20100208	07:44	13:14	M 4.0	3.52	66	0.42	1	10.3
	8:46	14:16	C 2.8	1.52	73.2	0.33	2	
20100209	01:28	6:58	C3.0	1.56	76.1	0.3	3	
	04:20	9:50	C3.0	1.49	73.4	0.32	2	
20100212	07:28	12:58	C8.0	2.48	70.5	0.37	2	6.17
20100612	01:01	6:31	M2.0	3.11	71	0.35	2	
	09:20	15:50	C6.0	2.24	72.4	0.33	2	1.2
	11:12	16:42	M2.0	3.35	67	0.37	2	

Solar flare day	UT (hrs)	LT (hrs)	Flare class	ΔA (dB)	$H^{/}$ (km)	β $(km^{-}1)$	Delay time Δt (mins)	ΔH_s (nT)
20100613	05:42	11:12	M1.0	3.01	68.1	0.39	1	8.52
20110128	01:05	6:35	M1.4	3.06	70.8	0.36	2	
20110209	01:34	7:04	M1.9	3.09	70.4	0.37	2	
20110214	08:01	13:31	C3.0	1.32	73.4	0.32	2	2.5
	08:49	14:19	C6.0	2.07	71	0.37	2	
20110215	01:57	7:27	X2.2	6.8	64	0.42	1	4.2
	02:48	8:18	M1.4	3.01	71.1	0.39	2	
	04:32	10:02	C4.8	1.88	72.1	0.36	3	
20110216	01:06	6:36	C2.0	1.21	76.6	0.27	3	
	01:44	7:14	M1.0	2.99	71	0.39	2	
	05:52	11:22	C6.0	2.1	71	0.37	2	4.5
	06:28	11:58	C3.0	1.45	73.5	0.33	2	
	07:46	13:16	M1.0	3.05	71	0.39	1	
	09:15	14:45	M1.1	2.93	71.8	0.33	2	
	10:34	16:04	C3.0	1.27	76.7	0.27	3	
20110218	04:55	10:25	C4.0	1.54	73.1	0.33	2	5.4
	06:36	12:06	M1.0	2.88	69.5	0.39	1	
	07:27	12:57	C8.0	2.54	70.4	0.37	2	5.83
	09:16	14:46	C4.2	1.6	76	0.3	2	
	10:15	15:45	M6.0	5.2	66	0.39	2	
20110224	07:35	13:05	M3.5	3.94	67	0.38	2	

2.5 Solar flare effect on Earth's magnetic field H component at the Indian equatorial station

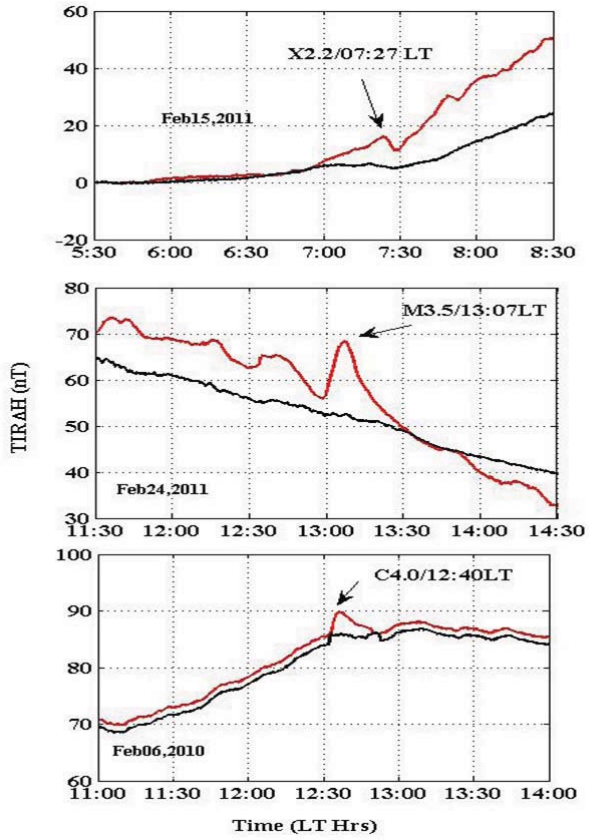

Figure 2.6: Variation in the Earth's magnetic field horizontal component (H) obtained using one second magnetic data from the Indian equatorial station Tirunelveli for solar flare events of C, M and X-classes.

The variation in the horizontal component (H) of the Earth$'s$ magnetic field observed at Tirunelveli, an equatorial station (Geographic lat. 0.03° N, long. 150.40° E, dip latitude: 0.4° N), Indian sector, for solar flares (January 2010 to February 2011), is examined and the change in ΔH ΔH_s due to flares is quantitatively studied. The geomagnetic activity is also examined during flare events to identify any effect of geomagnetic storms on the (ΔH). Chakrabarty et al. [2013], extensively

investigated the moderate and low intensity solar flares effects on equatorial electrojet current. The transient electric field disturbances can occur during storm sudden commencement (SC) and prompt penetration electric field associated with sub storms [Chakrabarty et al ., 2010), which can mask the signatures caused by low and moderate solar flares in Δ H [Chakrabarty et al., 2013]. The observations considered in this work are carefully investigated for the effects of transient field due to SSC and sub storms by looking in to the IEFy along with AL and Sym-H [Chakrabarty et al., 2013]. After careful investigation, the possibility of any influence of transient electric field disturbances, during solar flares, associated with the current study cannot be completely ruled out. It was found that 12 out of 41 flare events (07 C-class, 04 M-class and 01 X-class) have shown changes in the ΔH. For example, the variations in ΔH for the flares of 6 February 2010, 15 and 24 February 2011, are shown in Figure 2.6. The ΔH values on flare day (red line) and averaged on 3 international quiet days (black line) are plotted for three hour durations with respect to flare occurrence time in order to find the change in the ΔH due to solar flares.

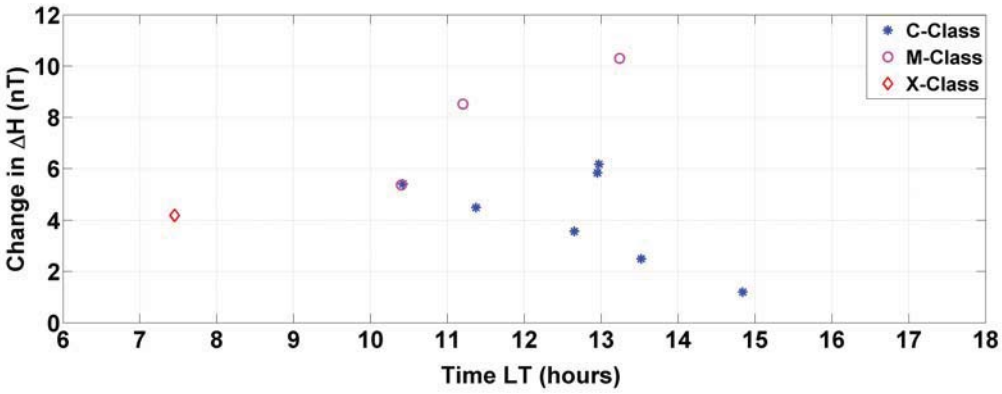

Figure 2.7: Local time variation in the changes in the horizontal component (ΔH) of geomagnetic field for C, M and X-class of flares.

The C 4.0 solar flare on 06 February 2010 had start, peak and end times at 12:30 LT, 12:39 LT and 12:44 LT, respectively. The corresponding response times in ΔH were identified at 12:31 LT, 12:40 LT and 12:45 LT, respectively. The M 3.5 solar flare on 24 February 2011 started at 12:53 LT, with maximum flux at 13:05 LT and ended at 13:12 LT. The corresponding response in the ΔH is observed at 12:57 LT, 13:07 LT and 13:17 LT, respectively. Similarly, for the X2.2

solar flare on 15 February 2011 starting at 7:14 LT with its peak at 7:26 LT and ending at 7:36 LT, the corresponding response times in the ΔH was observed at 7:20 LT, 7:28 LT and 7:39 LT, respectively. Moderate increase of 3.57 nT and 4.2 nT in ΔH given by ΔH_s is seen during the solar flares on 06 February 2010 and 15 February 2011 for C4.0 and X2.2, respectively. **At 7.28 LT, the maximum increase in H observed to be 4.2 nT and it decreases / recovers to the normal day H value at 7:39 LT.** On 24 February 2011, a significant increase in ΔH of 13 nT is observed for M3.5 class flare which occurred at 13:07 LT. Similarly, from Table 1, significant increase in ΔH is observed for the flare events in the noon time when equatorial electrojet (EEJ) strength is maximum at the equatorial stations.**The change in ΔH indicates the equal contribution from electric field and conductivity. In our analysis we have seen C and M class flares could affect significantly in H during noon, which is resultant of increase in conductivity as well as electric field. The same C and M class flare could not produce the same impact when it occurred in non noon hours. This shows the effect is dependant of local time as well as strength. Though a single X2.2 flare occurred during 7.28 LT it could affect the ionization because of higher strength.** Rastogi et al. [1999] observed positive impulse (increase) in the ΔH at equatorial and near equatorial stations. Figure 2.7 shows the local time dependence of ΔH for 12 selected flare events that have shown change in ΔH. It is clear from Figure 2.6 that only those flare events which occurred during noon period have shown the significant change in ΔH except for X class flares which occurred in the morning period (07:27 LT) and produced the significant increase in ΔH giving ΔH_s of 4.2 nT.

The solar flare of M 3.5 class on 24 February 2011 produced a significant increase of about 13 nT. Some of the earlier works show that the solar flares can decrease the H component of Earth's magnetic field at the electrojet stations and outside the electrojet region [Sastri, 1975]. Based on the study of several solar flare events over Indo-Russian region, Rastogi et al. [1990] found that during normal equatorial electrojet (EEJ) events, solar flares show a positive increase in H component at all stations. Rastogi et al. [1999] studied the changes in the H component (ΔH) in response with solar flares at different latitudes. The ΔH during solar flare follows the latitude which is similar to solar quiet Sq [Rastogi et al., 1999] variation. The change in EEJ system corresponding to the

solar flare has been studied by Manju et al. [2009]. Solar flares increase the ΔH during electrojet events and decrease the ΔH_sH during the counter electrojet times [Manju and Viswanathan, 2005] similar to our observations. The local time dependence of solar flare effect shows that effect is more pronounced in the noon period for C and M class flares. This non linearity in ΔH_sH can be attributed to the local time variation of E region zonal electric field in the equatorial region [Chakrabarty 2013]. The absence of background changes in E-region ionization with the local time may result in the linear change in ΔH_s with respect to the flare intensity. Recently, Sripathi et al. [2013] for X7/2B flare on 09 August 2011 with peak flux at 08:05 UT (13:35 LT hrs) observed a decrease in H at Tirunelveli and suggested that it is due to change in E-region electron density and the strong ionospheric currents due to presence of counter electrojet during the flare occurrence time. However, we have not observed any decrease in ΔH_s for the solar flare events considered in the present study.

2.6 Estimation of Wait D-region Parameters: LWPC modeling

In order to quantify the solar flare induced perturbations in the D-region ionosphere, we have utilized the Long Wavelength Propagation Capability (LWPC) code v 2.1 developed by US Navy [Ferguson, 1998] to calculate the changes in Wait ionospheric parameters [Wait and Spices, 1964]: ionospheric reflection height ($H^{/}$) and exponential sharpness factor (β), due to solar flares.

Figure 2.8 shows the normal day (unperturbed) diurnal variation of the NWC signal (amplitude and phase averaged for 5 days) received at Allahabad (blue line) matched with the LWPC modeled VLF amplitude (red line). The VLF amplitude and phase have been modeled for three separate periods of local day time: 00:30 - 4:30 UT (06.00 - 10: 00 LT hrs) near the morning terminator (morning period), 09:30 - 12:30 UT (15:00 - 18:00 LT hrs) near evening terminator (evening period) and the period between morning and evening terminators 04:30 - 9:30 UT or 10:00 - 15:00 LT hrs (noon period) during which the VLF amplitude is almost constant. In order to match the observed VLF amplitude and phase of NWC signal on the normal day with that given by LWPC,

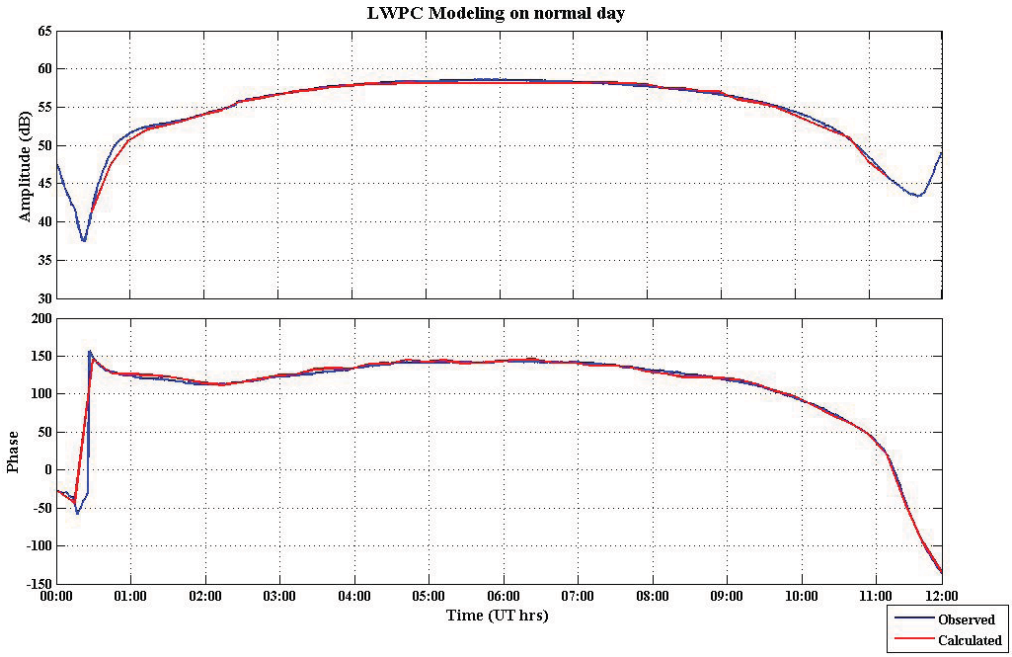

Figure 2.8: An example of normal day time amplitude (upper panel) and Phase (lower panel) variation of NWC signal (19.8 kHz) at Allahabad, India (blue line). The modeled variation using LWPC is shown by red line.

the values of amplitude and phase of NWC signals recorded with AWESOME receiver were added 35 dB and 15 degrees, respectively, to calibrate it and then the model was run for every 15 minutes from 0 UT to 12 UT to account for the temporal changes in the signal amplitude and phase. The $H^{/}$ and β were chosen for best matching between the LWPC amplitude and phase and the recorded amplitude and phase. The values of $H^{/}$ and β parameters are found almost same for both morning and evening periods. The average values of $H^{/}$ and β for unperturbed (normal) daytime ionosphere are estimated as (a) β = 0.26 km^{-1} and $H^{/}$ = 77 km for the interval near terminators (morning and evening periods) and (b) β = 0.30 km-1 and $H^{/}$ = 74 km for the noon period. The noon time values of $H^{/}$ and β for normal day match well with previous studies [McRae and Thomson, 2004; Thomson et al., 2005; Grubar et al., 2005, 2008; Zigman et al., 2007] for low and mid latitude regions.

During solar flares the amplitude enhances and the phase advances of the sub-ionospheric VLF

wave. The observed perturbed day amplitude is also modeled in the same way as for normal day. In order to match the model values with the observed values, the LWPC code was run for every 5 minutes and the output values were noted. Figure 2.9 shows the modeling plot of the amplitude and phase of NWC signals for the solar flare on 20th January 2010. The $H^{/}$ and β values estimated by using LWPC modeling for solar flares considered in the present study are given in Table 2.1.

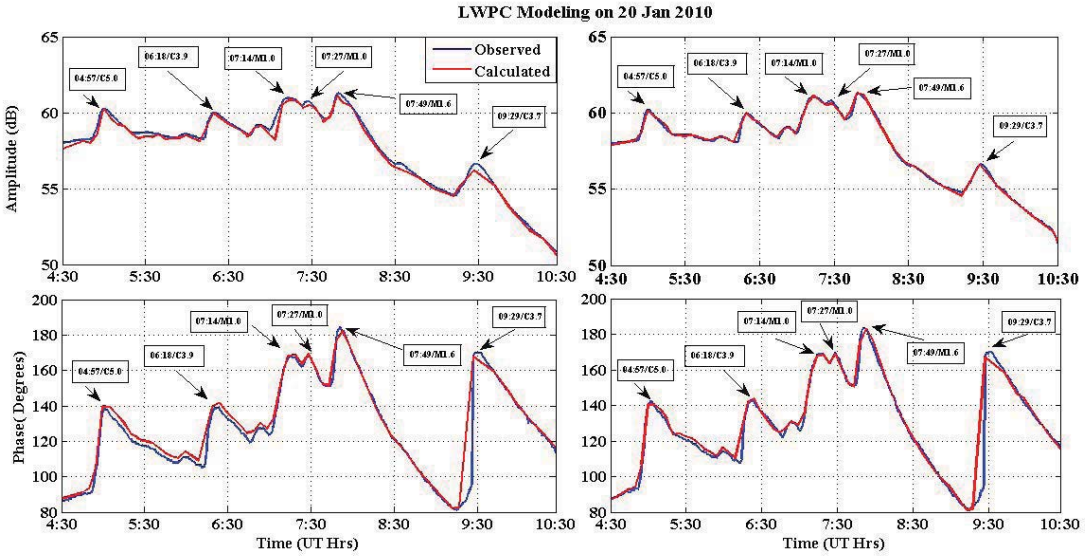

Figure 2.9: Modeled VLF amplitude and phase for 20 January 2010 solar flare using LWPC code v 2.1.

2.7 Results and Discussion

2.7.1 Variation in Wait D-region ionospheric parameters due to solar flares

During solar flares, the increased ionization results in descent of upper edge of EIWG which reflects as decrease in $H^{/}$ and increase in β values [Grubor et al ., 2008]. Table 2.1 shows the $H^{/}$ and β values estimated using LWPC model for different classes of solar flares considered in the present study. For C class solar flares of 20 January 2010 the $H^{/}$ andβ values are estimated as 3

km and 0.06 km-1, respectively, whereas for M class flares these values are 6 km and 0.1 km^{-1} , respectively, with respect to the normal daytime values. The strongest solar flare of class-X on 15 February 2011 (occurred in the morning period) showed highest decrease in $H^{/}$ by 13 km and increase in β by 0.16 km^{-1} with respect to unperturbed day values.

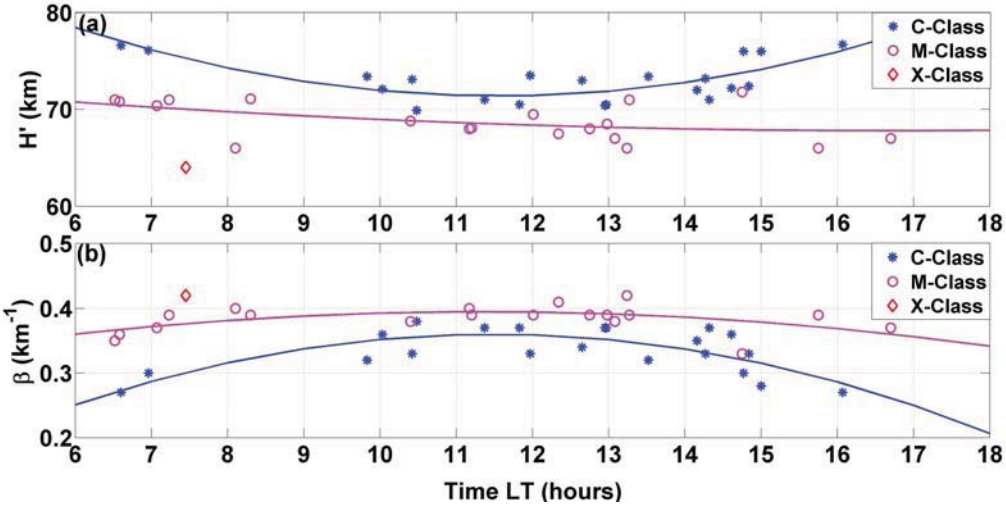

Figure 2.10: (a) Local time variation of reflection height ($H^{/}$) with respect to normal day for C, M and X classes of flare. (b) Local time variation of sharpness factor (β) for C, M and X classes of flares. The trends of variation are shown by the quadratic fit lines.

Above discussion again indicates that $H^{/}$ and β values are different for different classes of flares and vary with local time. In order to understand this, we have plotted $H^{/}$ and β versus local time for C, M and X class of flares as shown in Figure 2.10a and b. From Figure 2.10a it is seen that $H^{/}$ depends on the flare flux (class of flares) and is minimum for X class flare and maximum for C class flares. From Table-2.2 it is seen that average $H^{/}$ value is maximum in the morning and evening periods and minimum in the noon period. The $H^{/}$ varies from 69.9 -76.6 km for C-class flares. The $H^{/}$ for the M-class flares shows a similar trend. Table 2.2 shows that β follows an opposite trend as compared to $H^{/}$. The β is maximum for X-class flare and minimum for C-class flares. The average value of β for C-class flare shows that it is minimum in the morning and evening periods and maximum in the noon period. The β varies from 0.27 - 0.42 km^{-1} for C-class

Table 2.2: Average values of ΔA, Δt, H$^{/}$ and β during three different time periods (morning, noon, evening) for C and M class flares

Time period	Delay time(Δt)(min)	ΔA (dB)	β (km^{-1})	H$^{/}$ (km)
C class				
Morning(6-10 LT)	2.67	1.42	0.30	75.37
Noon(10-15 LT)	2.00	1.92	0.35	72.14
Evening(15-18 LT)	2.50	1.36	0.28	76.35
M class				
Morning(6-10 LT)	2.00	3.45	0.38	70.05
Noon(10-15 LT)	1.27	3.16	0.39	68.56
Evening(15-18 LT)	2.00	4.28	0.38	66.50

flares. The β for the M-class flares shows similar trend. The maximum and minimum changes in H$^{/}$ and β are estimated to be 13 km, 0.16 km-1 for X2.2 flare and 0.4 km, 0. 01 km^{-1} for C2.0 flares, respectively.

McRae and Thomson, [2004] showed that solar flares reduce the H$^{/}$ which is proportional to the logarithm of X-ray flux intensity.They found that the H$^{/}$ reduced down to 58 km from a normal unperturbed day value of 71 km and β significantly increased and reached a saturation value of about 0.52 km^{-1} for flares of magnitude greater than about X17. Thomson and Cliverd [2001] estimated the H$^{/}$ andβ to be 64.6 km and 0.485 km^{-1} respectively, for M2.4 class as compared to standard values of H$^{/}$ = 71 km and β = 0.43 km^{-1}. Zigman et al. [2007] observed a decrease in H$^{/}$ to 69 km and an increase in β to about 0.54 km^{-1} from unperturbed values of H$^{/}$ = 74 km and β = 0.30 km^{-1} for NAA (24.0 kHz) transmitter amplitude signal received at Belgrade. Our estimations of wait parameters H$^{/}$ and β are in agreement with previous studies as discussed above.

2.7.2 Enhancement in D-region electron density due to Solar flares

The normal day time D-region ionosphere is maintained by the Solar Lyman alpha (121.5nm) radiation which ionizes minor constituent nitric oxide and forms the main source of ionization. It has been known that cosmic rays also cause a significant proportion of ionization in the D-region ionosphere [Rishbeth and Garriot, 1969]. During solar flares the X-ray flux from the solar flare becomes the dominant source of ionization and overcomes ionization caused by galactic cosmic rays and the Lyman α radiation, thereby significantly increasing the ionization which results in lowering of the reflection height $H^{/}$ and increase in the value of β [Grubor et al., 2008]. The electron density profile can be estimated by using equation given below which uses $H^{/}$ and β obtained by running LWPC model [Wait and Species, 1964].

$$N_e(z) = 1.43 \times 10^7 e^{(-0.15H^{/})} e^{(\beta-0.15)(z-H^{/})} \tag{2.1}$$

where $N_e(z)$ is the electron density in cm^{-3} . The electron density profile obtained by this method is valid up to 100 km altitude. We have estimated an increase in electron density in the height range of 60 to 80 km using Wait parameters obtained from the LWPC model.

Figure 2.11 represents the electron density profile obtained from modeled $H^{/}$ and β values for the flares occurred on 20 January 2010 , 9 and 15 February 2011 in the (a) noon time and (b) morning and evening time and their comparison with normal day profile (green line). The strongest flare recorded in this present study (X2.2) showed a maximum variation of electron density when compared with all other solar flares. The VLF amplitude response to the flare induced increase in the electron density is almost instantaneous, behaving as a monotonic function of the electron density [Zigman et al., 2007].

The extra ionization during any flare does not only increase the electron concentration at the reflection height but also changes the electron concentration along height of the D-region [Thomson and Cliverd, 2001]. The change in electron density has been computed for all flares at a reference

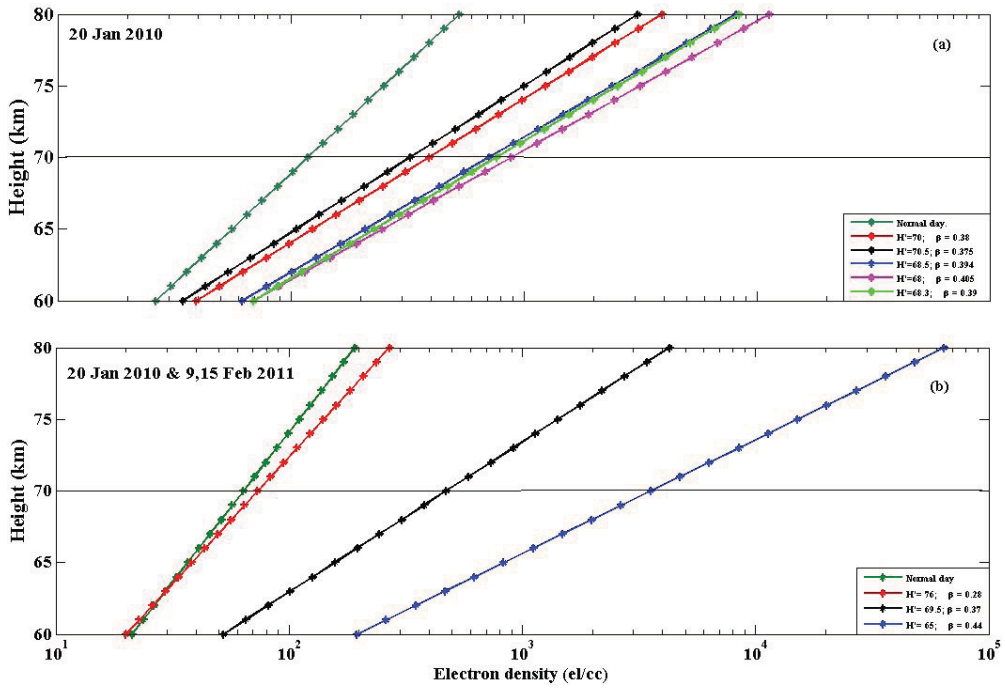

Figure 2.11: (a) Comparison of electron density profiles for flares on 20 January 2010 in the noon period (10-15 LT hrs) and on normal day at Allahabad. (b) Comparison of the electron density profile for solar flares on 20 January 2010 and 9 and 15 February 2011 in the morning and evening periods (06-10 LT hrs and 15-18 LT hrs) with the normal day for Allahabad. (Horizontal line at 70 km is added as reference height for comparison of electron density).

height of 70 km and presented in Table 2.1. The C- class flares of 20 January 2010 and one on 15 February 2011 perturbed the daytime D-region ionosphere increasing the electron density by 20 times with respect to the normal day time values. The two M-class flares observed on 20th January 2010 and one each on 9 and 24 February 2011 increased electron density by 41 times as compared to normal day values. The X- class flare observed on 15th February 2011 showed the highest change in the electron density which is 80 times over the normal day value. The electron density profile is completely altered by the change in β resulting change in the VLF amplitude [Thomson and Clilverd, 2001; McRae and Thomson, 2004].For a C-class flare the change in the electron density ranges from minimum of 5 el/cc to a maximum of 220 el/cc at an estimated reference height of 70 km.

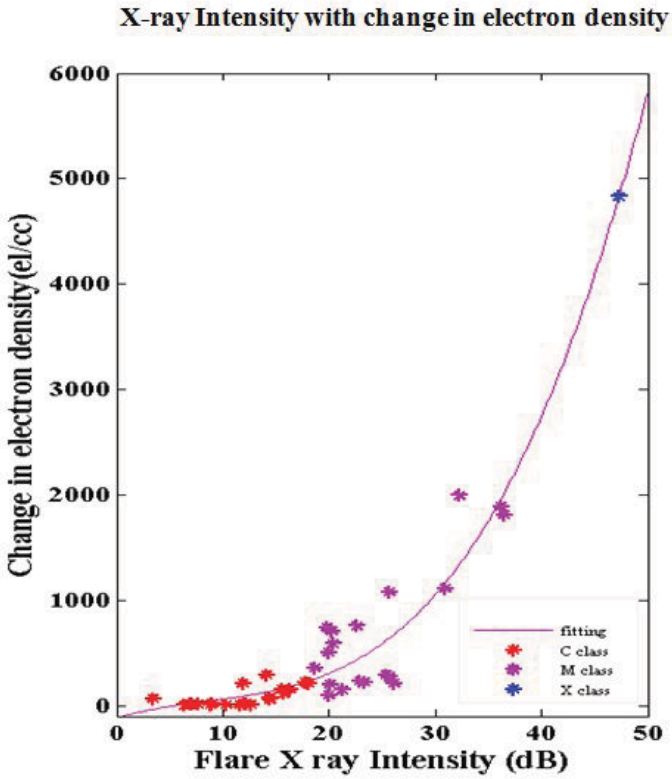

Figure 2.12: Comparison of electron density at 70 km with the solar flare intensity (dB).

Kolarski and Grubor [2009] for M class flare estimated increase in the electron density of the order of two for the GQD and NAA transmitter received at Belgrade, Serbia. Our results from an Indian low latitude station are almost consistent with previous observations in other parts of the world [Zigman et al., 2007, Grubor et al., 2005]. Figure 2.12 shows the change in the electron density with flare X-ray flux in dB. The change in the electron density is computed by taking difference of electron density during flare event and during normal day at reference height of 70 km. The change in electron density is minimum for the C-class flares and maximum for X2.2 flare. The best fit lines show that electron density increases with increase in solar flux intensity and follows almost logarithmic trend. There are few events where C-class flares have produced more electron density changes compared to M-class flares. This can be attributed to local time as well as to day-to-day variability of D-region ionosphere [Han and Cummer 2010; Ohya et al., 2011;

Maurya et al., 2012a,b].

2.8 Summary

Solar flare effects on the sub-ionospheric VLF signals are identified by the sudden increase in their amplitudes and advancement in the phases. These sudden changes are manifestations of rapid enhancements in the D-region ionospheric plasma density associated with flares. We have analyzed the effect of C, M and X-class solar flares on NWC signal (19.8 kHz) recorded at Allahabad, a low latitude station in the Indian region, during the period of one year from January 2010 to February 2011. Also the solar flare effect on the horizontal component of the Earth's magnetic field (H) at the Indian equatorial station, has been examined. The period of study falls under low solar activity of the current solar cycle 24. It is found that change in the VLF amplitude (ΔA), time delay (Δt) between VLF peak amplitude and X-ray flux peak and D-region ionospheric parameters ($H^{/}$ and β) strongly depend on the intensity (class) of flares, pre-flare condition and local time of flare occurrence. This dependence has been tested for C, M and X-class of flares during morning, noon and evening periods of local day time (06-18 LT). The results show that ΔA varies between 1.21 - 6.8 dB for C to X-class of flares. The Δt varies from 1-3 min for different classes of flares and is minimum for X class of flare. The local time dependence for ΔA and Δt indicates an opposite trend withΔA increasing as the day progresses and attaining its maximum value at noon and then decreasing until evening. The maximum increase of 7 dB in the NWC signal amplitude was observed for X 2.2 solar flare event on 15 February 2011. The LWPC modeling code has been utilized to estimate the changes in the reflection height $H^{/}$ and sharpness factor β for all the solar flare events. Reduction in the $H^{/}$ and increase in the β are estimated during the flares as compared to the normal day time values. The maximum change in the $H^{/}$ and β is estimated for X-class flare followed by M-class and C-class flares which is consistent with earlier studies [Zigman et al., 2007; Grubor et al., 2008]. The local time dependence of changes in $H^{/}$ and β indicates an opposite trend and change is maximum during the noon period. The electron density profiles estimated during the solar flare events show a maximum increase in electron density of the order

of 80 times as compared to the normal day values for X-class flare at the reference altitude of 70 km. The increase of about 13 nT in ΔH_s for solar flare of M-class was observed at Tirunelveli which could be accounted for the enhanced electrojet during the solar flares. The investigation is in progress for high solar activity of the current solar cycle which will provide us further opportunity to study the D-region and geomagnetic field response to solar flares with larger data set.

Chapter 3

CME-driven shocks and the associated sudden commencements/sudden impulses, geoeffectiveness

3.1 Coronal Mass ejections

The another major eruption from the Sun is CMEs. The following thesis will deal with the study of CMEs , interplanetary drives and their geoeffectivness. CMEs are defined as huge bubbles of gas threaded with magnetic field lines that are ejected from the Sun over the course of several hours CMEs typically reach Earth one to five days after leaving the Sun. During their propagation, CMEs interact with the solar wind and the interplanetary magnetic field (IMF). As a consequence, slow CMEs are accelerated toward the speed of the solar wind and fast CMEs are decelerated toward the speed of the solar wind. CMEs faster than about 500 km/s eventually drive a shock wave. Most CMEs are associated with eruptive prominences. As these occurs through out the solar activity cycle, CMEs have been evident in both lower and high-activity periods [Phillips, 1995].

3.2 CME driven-Interplanetary shocks and geoeffectiveness

Interplanetary shocks (IP) driven by coronal mass ejections (CMEs) originating close to the solar disk center often arrive at the Earth and responsible for the sudden compression of magnetosphere causing storm sudden commencement (SC) and sudden impulses (SI) which are detected by ground based magnetometers. In addition to IP shocks, sudden increases in the solar wind dynamic pressure can also affect the magnetosphere causing sudden impulses (SI) which are identified with sudden increase in magnetic field at geo-synchronous orbit and also at the ground by magnetometers [Araki et al., 1977; Takeuchi et al., 2002a; Wilken et al., 1982; Chi et al., 2006]. SC/SIs can be clearly seen as an increase in the ground based magnetic field intensity which typically lasts for tens of minutes and then followed by a geomagnetic storm. The term SC is used when it occurs at the beginning of the initial phase of a magnetic storm whereas SI is a general term including occurrences outside the storm interval.

There have been a number of studies that have shown that most (80 - 90$\%$) of the SC/SIs are associated with IP shocks and only a small number is caused by tangential discontinuities [Chao and Lepping, 1974; Smith et al., 1986]. Wang et al. [2006] surveyed IP shocks and SCs observed from 1995 to 2004 and found that about 75$\%$ of SCs are associated with IP shocks. They also reported that the SC rise time is dependent on IP shock speed. IP shock orientation also plays an important role in determining the SC rise time as a highly oblique shock requires more time to compress the forward part of magnetosphere [Wang et al., 2006].

Wang et al. [2009] performed a statistical survey of the relation between geosynchronous magnetic field changes and sudden impulses due to IP shocks observed from 1998 to 2005. They found that 216 of the 250 IP shocks (88$\%$) produced changes in the geosynchronous magnetic field observed by GOES satellites and SIs as detected by the change in the SYM-H index and 75$\%$ negative responses (negative sudden impulses) in the midnight sector were associated with southward interplanetary magnetic field. Recently, Wang et al. [2010] suggested that SIs can be used to estimate some of the interplanetary parameters at the L1 point and at geosynchronous

orbit, including the changes in solar wind dynamic pressure across the shock and the associated geosynchronous magnetic field changes near the sub solar region.

The geomagnetic disturbances and storms characterized by various sets of well-defined indices result from the energy transfer from the interplanetary magnetized plasma structures to the Earth's magnetosphere via magnetic reconnection [Dungey, 1961; Gonzalez et al., 1994]. Many facets of the solar and interplanetary origin of the geomagnetic activity have been studied previously by several researchers [e.g., Gonzalez et al., 1999, 2011; Wu and Lepping, 2002, 2006 and 2011; Zhang et al., 2007 and 2008a, b]. These studies include mostly individual events as well as set of events. It is established that major storms are related to the impact (and reconnection) of intense interplanetary magnetic field (IMF) at the Earth and specifically to the long-duration period of its southward directed component (Bz) [Gonzalez and Tsurutani, 1987; Gonzalez et al., 1994].

The above mentioned studies are confined to IP shocks observed in the solar wind near the Earth. But IP shocks undergo considerable changes as they propagate from near the Sun to the L1 point. The best way to characterize them is to examine the CMEs that drive them. CMEs can be observed by coronagraphs very close to the Sun (one to 2 solar radii above the surface). Such early observations can provide advance warning of shocks arriving at the Earth by more than half a day to a few days. Shocks near the Sun are inferred from type II radio bursts in the solar corona and IP medium. Every large solar energetic particle (SEP) event is associated with a type II radio burst which is used as a strong evidence for particle acceleration by shocks. When shocks arrive at the Earth, they can be identified from the energetic storm particle (ESP) events. The energetic electrons are unstable to Langmuir waves, which get converted into radio emission at the local plasma frequency and its harmonics. This radio emission is said to be type II radio burst. The shocks which produce the type II radio burst are said to be Radio Loud (RL) and those which do not produce a type II burst are said to be Radio Quiet (RQ) [Gopalswamy et al., 2010]. The CMEs associated with RL shocks are said to be RL CMEs and those followed by the IP shocks are said to be RL IP shocks, or simply RL shocks. Similarly, there are RQ CMEs and RQ IP shocks (or simply RQ shocks). Electrons accelerated in CME-driven shocks generate type II radio bursts observed in

dynamic radio spectra as intermittent or continuous sweeps that slowly decrease in the frequency.

Recently, Cho et al. [2010] considered 26 RL CMEs and the resulting IP shocks. They found that the CME speed is highly correlated with SC amplitude and concluded that only fast CMEs (speed greater than 1600km/s) could cause the magnetopause crossing of geosynchronous orbit. Cho et al. [2010] investigation considered only 10% of all IP shocks and confined only to a small number of RL CMEs. Of course, not all IP shocks are associated with type II radio bursts, but one can still identify the driving CMEs from coronagraphic observations. Such radio-quiet (RQ)shocks constitute a large fraction (34%) of all IP shocks [Gopalswamy et al., 2010]. Therefore, it is very important to consider both the RL and RQ CMEs that result in IP shocks and the resulting dynamic pressure increases at L1 as well as the SCs. The RL CMEs considered by Cho et al. [2010] were based on metric type II bursts alone, but it is well known that type II bursts occur at all wavelengths from metric to kilometric domain corresponding to the corona and IP medium [Gopalswamy et al., 2005]. Thus, we consider all CME-driven shocks from those that do not produce type II radio emission to those that produce radio emission at all wavelengths.

3.3 Interplanetary CME

When shock-driving CMEs arrive at the Earth, they can be observed as a magnetic cloud (MC) or non-cloud ejecta (EJ). It is also important to consider the ICME type (MC or EJ) because they seem to represent head-on and glancing blows to the magnetosphere [Gopalswamy, 2009] and hence may have implications to the resulting SCs. The CME and radio emission characteristics are useful in understanding the shock-driving ability of CMEs near the Sun because type II bursts are the earliest indicators of shocks and contain information on both the shock and the ambient medium in which shock propagates [Gopalswamy et al., 2008b, 2008c]. The new findings reveal that some of the shocks are not associated with type II bursts near the Sun or in the IP medium. It is of interest to know how the CMEs with and without the associated radio bursts affect the magnetosphere, as indicated by SC/SI.

Gopalsamy et al ., 2010 used a lager data set of 222 IP shocks detected by spacecraft at the Sun-Earth L1 during solar cycle 23 (1996 to 2006, inclusive) to carry out an extensive study of RL and RQ IP shocks. This work is divided in to two parts. The first part of the work deals with the importance of radio characteristics in determining the amplitude of SC/SIs. We make use of the extensive data base on IP shocks, ICMEs, CMEs, and type II radio bursts [Gopalsamy et al., 2010] in our attempt to understand the characteristics of SC/SIs and geoeffectiveness. The second part of this work deals with the geoeffectiveness of ICMEs associated with IP shocks.

3.4 Data

The 222 IP shocks listed in Gopalsamy et al., 2010 were observed at 1 AU by one or more of the three spacecraft: the Advanced Composition Explore (ACE), the Solar and Heliosphere Observatory (SOHO), and the Wind spacecraft during solar cycle 23 (1996 - 2006, inclusive). Table 1 in Gopalsamy et al.[2010] gives the properties of all the relevant phenomena associated with the IP shocks: ICME type (MC or EJ), CME properties, solar sources, and the radio emission characteristics. The geomagnetic storms are classified based on the Dst index which is obtained from http://wdc.kugi.kyoto-u.ac.jp/index.html.

Based on the IP shocks and their arrival times listed in Paper I, we have identified the SC/SIs events and measured their amplitudes from the SYM-H index [Iyemori, 1990; Iyemori and Rao, 1996] with a time resolution of 1 minute obtained from World Data Center, Kyoto, Japan. An SC/SI event is defined as an abrupt increase of the SYM-H value with time variation of more than 1.5 nT/min and an amplitude increase of more than 5 nT, as in Shinbori et al. [2002, 2003b]. For each SC event, the onset time is determined from the H-component geomagnetic variation in the rapid sampling records (with the time resolution of 1m) obtained at Alibag observatory(ABG) magnetic observatory of IIG, India. Only those SC/SIs events that temporally correspond with the IP shock timings have been selected. The SC events have been taken from the available geomagnetic data

yearly bulletins which are published by IIG. The IP shocks and related SC/SI amplitudes in H-component and timings have been noted from the ABG. The ABG observatory, away from the influence of Equatorial Electrojet (EEJ) currents, is one of the prime contributors of geomagnetic field data to World Data Center (WDC), Kyoto, Japan for calculating the Dst.

It is found that there is not much difference between the SC/SI amplitudes obtained from SYM H and from ABG H-component. The IIG data bulletins consist of complete list of SCs which are followed by geomagnetic storms observed at all Indian magnetic observatories and published every year. Some of the SCs without magnetic storms are not listed in the bulletins. Due to this, we have used both data sets of Sym-H and ABG-H components constituting 30% and 70%, respectively. In this paper, we use the term SC/SI, because we are considering the both events. Both these data sets provide almost complete list of clear SC/SI events that match well with the IP shocks timings. For 19 IP shocks, the corresponding SC/SI events could not be identified, probably due to the very weak or unclear signatures. However, the above criterion of SC/SI events (Sym-H $\geq$ 5 nT) possibly includes other geomagnetic disturbances such as an abrupt increase of the H-component geomagnetic field during the early recovery phase of geomagnetic storms or positive bay phenomena associated with the onset of substorms [Shinbori et al., 2009]. These geomagnetic disturbance events in the SYM-H index were excluded after checking the H component geomagnetic field data obtained from several stations in the low-latitude region or a sudden enhancement of solar wind dynamic pressure in the ACE data. Elimination of these unclear events resulted in a set of 203 IP shocks. Out of the 203 shocks, 130 were RL and the remaining 73 were RQ. The fraction of RQ shocks (36%) is similar to the one reported in Gopalsamy et al. [2010] (34%).

Figure 3.1 shows an example of a SC event observed at 1610 UT on 17 July 2002. The SC/SI amplitude of 44 nT is noted in the SYM H data, while an amplitude of 54 nT in the H-component can be found in the ABG data. This SC/SI was observed following the IP shock arrival at 1550 UT at L1 with a speed of 493 km/s (as listed in Gopalsamy et al ., 2010). The IP shock was found to be driven by EJ with a speed of 450 km/s. The source of the IP shock disturbances is a CME at the Sun originating from close to the Sun center (heliographic coordinates N18W01). The CME

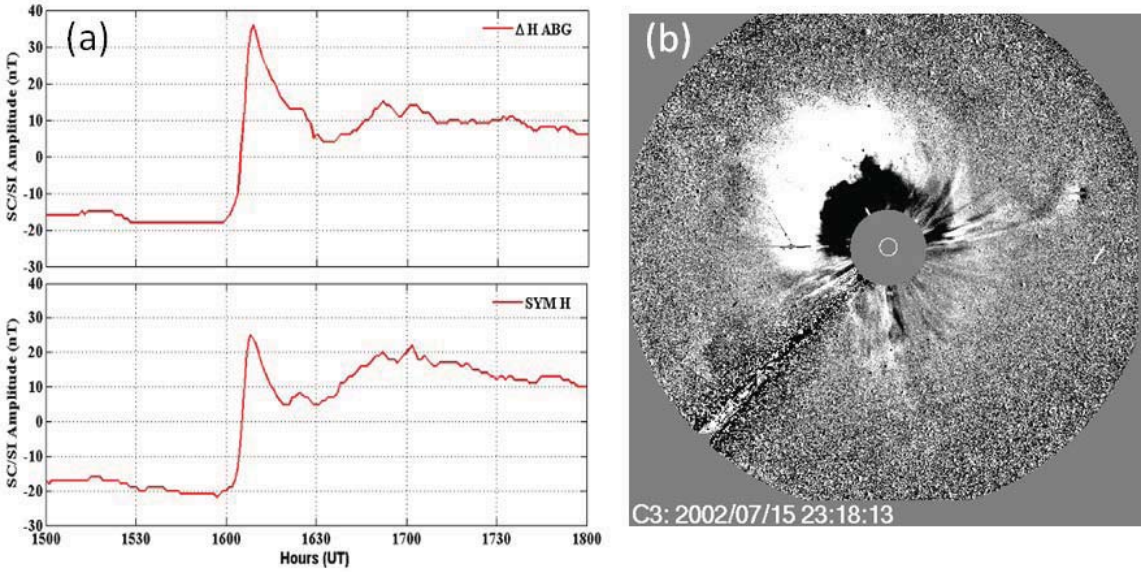

Figure 3.1: An example of the SC/SI amplitude (from the ABG data - top and the sym-H index - bottom)observed on 17 July 2002 at 1610 UT, which is followed by the IP shock at 1550 UT. (b) a snapshot of the CME at 23:18 UT observed by the Large Angle and Spectrometric Coronagraph (LASCO) on board SOHO. The bright material in the NE direction is the CME. The fuzzy feature surrounding the CME is the CME-driven shock.

first appeared in the SOHO coronagraph field of view at 2130 UT and traveled towards the Earth with a speed of 1300 km/s. A snapshot of the CME can be seen in Fig. 3.1(b). The small ICME and shock speed at 1 AU suggest that this CME underwent severe deceleration between the Sun and Earth. The CME was associated with a type II radio burst observed by the WAVES experiment onboard the Wind spacecraft, and hence is a RL CME. Details on the CME and the radio burst can be found in Gopalsamy et al., 2010 and in the CME catalog:http://cdaw.gsfc.nasa.gov/CME list[Gopalswamy et al., 2009d]. The CME was also associated with a large solar energetic particle event [Gopalswamy et al., 2004], which is another indication of the CME-driven shock near the Sun. Figure 3.2, shows the scatter plot between the CME speed and SC/SI amplitudes for all the events (203) considered in this paper. The SC amplitude ranges from 5 nT to 128 nT, while the CME speed ranges from 100 km/s to more than 3000 km/s. There is a clear indication that faster CMEs produce stronger SC/SI events, although the scatter is relatively large.

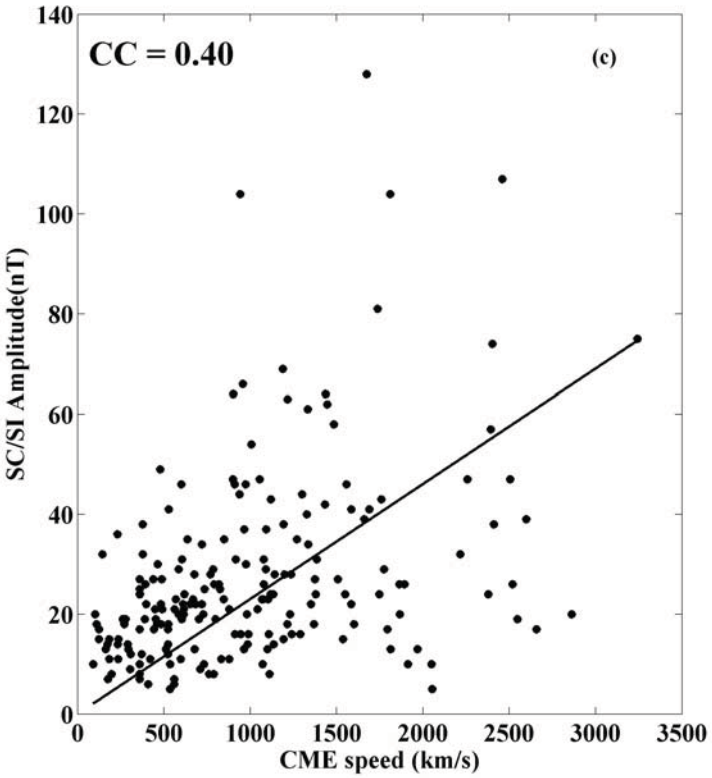

Figure 3.2: Scatter plot between SC/SI amplitude and CME speed. The CC is 0.40 and SC amplitude ranges from 5 nT to 128nT.

The CME speeds are measured near to the Sun. Basically CME associated IP shocks results in the SC/SI. We have observed the minimum CME speed of 136 km/s which resulted in the SC/SI. We observed these lower speed CME associated IP shocks resulted in SC/SI, because, these CMEs with lower speed propagate through the interplanetary medium and gets accelerated by the back ground solar wind or CME with higher speed ejected behind the lower speed CMEs, which in turn accelerates the IP shock associated with it. These are two possible reasons for acceleration of lower speed CMEs to around 450 km/s which then results in SC/SI

Table 3.1: The average values of Solar Latitude and Longitude for All, RL and RQ Shocks

	Latitude (°N)	Latitude (°S)	Longitude (°E)	Longitude (°W)
All shocks	15	18	23	23.5
RL shocks	14.5	17	28	25
RQ shocks	16	19.5	17	22

3.5 CMEs driving shocks and ICMEs associated SC/SIs

In this section, we compare the properties of CMEs/ICMEs/IP shocks with those of SC/SI events. Figure 3.3 shows the distributions of CME, ICME, and IP shock speeds associated with the SC/SI events. The average and median speeds and the standard deviation in speeds are given in figure 3.3. The general details on the CME, ICME, and IP shock speeds can be found in figure 2 and 4 in Gopalsamy et al .[2010], irrespective of their association with SC. The average speed of CMEs is 1015 km/s, which is about a factor 2 higher than the average speed of the general population of CMEs (457 km/s). The average speed of SC-causing CMEs is slightly higher than all shock-driving CMEs (999 km/s) (Figure 4 in Paper I). The high CME average speed indicates that SC/SI associated CMEs are more energetic than the general CMEs. The average ICME speed is 530 km/s (Figure 3.3), which is slightly higher than the general RQ ICME speed (446 km/s) and less than the RL ICME speed (572 km/s). (The numbers in parentheses are taken from Table 4 in Gopalsamy et al ., 2010). The average speed of IP shock is 557 km/s which is also higher than the general average RQ IP shock speed (455 km/s) and less than the average RL IP shock speed (608 km/s). This analysis suggests that the RL ICMEs and IP shocks speeds are strong enough to produce higher SC/SI than RQ ICMEs/ IP shocks speeds which are consistent with the studies of Gopalsamy et al .[2010] and with the results of Gopalswamy et al. [2008c].

Figure 3.4 (a, b, c, d, e, f) shows the plot of SC/SI amplitude as a function of solar latitude and longitude for all, RL, and RQ shocks with sub groups of MC and EJ. The solar source locations

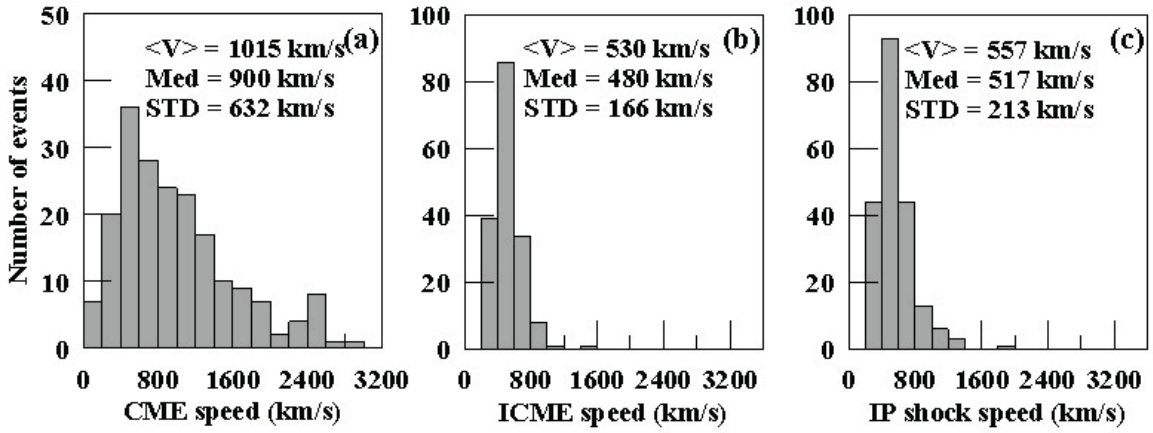

Figure 3.3: The distribution of CME/ICME/IP shock speeds for SC/SI producing events. The bin size is 200 km/s, for all panels. The average mean (<V>), median and standard deviation (STD) of speeds in each case are given in plots.

Table 3.2: The average values of Solar Latitude and Longitude for MC and EJ

	Latitude (°N)		Latitude (°S)		Longitude (°E)		Longitude (°W)	
	MC	EJ	MC	EJ	MC	EJ	MC	EJ
All shocks	15	15.5	19.5	17	19.5	27	20	27
RL shocks	13	16	18.5	16	22.5	34	19.5	30
RQ shocks	17	15	20.5	18.5	16.5	17.5	21	23.5

for CMEs given in Paper I have been used for their associated IP shocks with sub groups of RL and RQ. The average latitudes and longitudes are provided in Tables 3.1 and 3.2.

The latitudinal distribution of the SC/SI producing RL and RQ shock sources shows a decline towards limbs with the sharp cutoff around $\pm 30^{\circ}$ latitude for all events. Most of shocks are observed between the northern and southern active regions which are much more pronounced for RL shocks than RQ shocks. The average latitude for RL shocks is less than for RQ, which suggests that the shock-driving CMEs originate in the active region belt as these regions have higher magnetic field, thus resulting more energetic CMEs. The average latitude for MC-associated RL shocks is

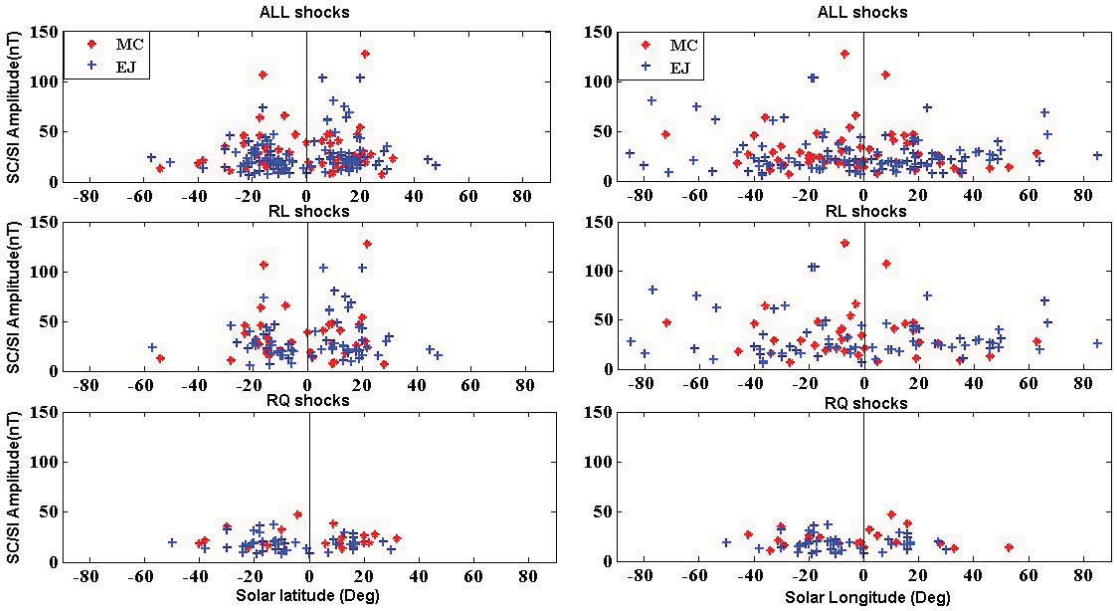

Figure 3.4: SC/SI amplitude variation with solar latitude and longitude for All, RL and RQ shocks. The ICMES are divided in MCs (red plus marks) and EJs (blue Plus marks) are shown. The average values of All shocks, RL and RQ shocks with separation of MCs and EJs are given in table 3.1 and 3.2.

higher than that of the EJ associated RL shocks. In the case of solar longitude, it is found that the longitude distribution spreads over entire longitude belt for RL shocks than RQ shocks. The average value of CME longitude for MC associated RL shocks is less than that for EJ-associated RL shocks. The latitudinal distribution combined longitudinal distribution shows that the source locations are different for RL and RQ shocks with RL shocks distributed more widely along longitudes. The average longitude of the distribution is higher for RL shocks than for RQ shocks.

3.6 ICMEs structure

Most of the shocks are followed by the ICMEs, which are either MCs or non cloud EJ. There were 109 EJ and 56 MC events in the list of Gopalsamy et al. [2010]. Figure 3.5 shows the

scatter plots of SC/SI amplitude against the speeds of ICMEs (MC and EJ shown separately) and IP shocks. Table 3.3 shows the comparison of the average ICME and shock speeds and the corresponding SC amplitudes. The shock speeds are generally higher for the MCs and the corresponding SC amplitudes are also higher. The difference in speeds is attributed to the fact that the MC associated shocks are measured at their noses, hence they have higher the speed, whereas EJ associated shocks are measured between their nose and flanks, so they have lesser speed and hence give the difference in the SC/SI amplitudes.

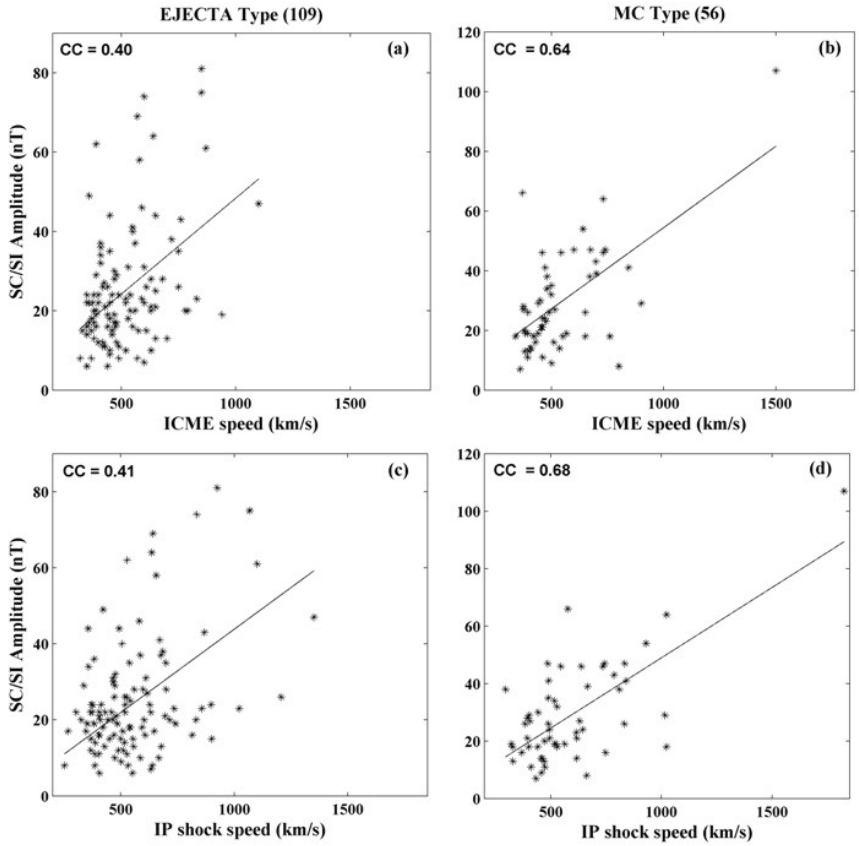

Figure 3.5: The scatter plot between the ICME/IP shock speed with SC/SI amplitude for MCs (56) and EJs (109). The Correlation Coefficients (CC) are given in each plot.

The CME speeds associated with MC and EJ events are also shown in Table 3.3. The CME speed near the Sun is generally opposite to that seen in ICMEs. The CME speeds are much

Table 3.3: Comparison of IP Shock speeds and SC/SI amplitudes for EJ and MC

	EJ	MC
	Average SC/SI amplitude (nT)	
IP shock	22.34	29.01
	Average Speed(km/s)	
ICME	488.07	520.92
IP shock	519.77	589.87
CME	1119	1058
	Correlation Coefficients	
ICME	0.40	0.64
IP shock	0.41	0.68

higher near the Sun than those of the IP counterparts because CMEs undergo deceleration in the IP medium due to the interaction with the solar wind [see e.g., Gopalswamy et al., 2000]. The higher speeds of EJ CMEs compared to the MC CMEs can be attributed to the fact that the latter are subject to more projection effects due to their origin close to the disk center. This explanation is based on the commonly accepted view that all ICMEs are flux ropes and the appearance as EJ or MC is an observational effect. This has been shown to be true in the zeroth order approximation [Gopalswamy et al., 2006]. There can be a significant deviation from the approximation. One can see EJ sources and even driverless shock sources from the disk center. The driverless shocks from the disk center have been explained by nearby coronal holes [Gopalswamy et al., 2009c] such that disk center CMEs behave like limb CMEs. There may be many reasons as to why disk center CMEs become EJs rather than MCs non-radial eruption, CME deflection and other propagation effects. Table 3.3 summarizes the resulting correlation coefficients (CC). All correlations are positive with CC $\geq$40.

The MC speeds and their shocks show better correlations with the SC amplitude (0.64 and 0.68, respectively). The best correlation is between speeds of MC-driven shocks and the SC amplitude.

These results are consistent with the fact that the associated CMEs originate close to the disk center of the Sun and hence represent a direct impact on the magnetosphere. Since the SC is caused by the shock rather than the ICME, the MC-driven shocks are the most effective in producing higher SC/SI amplitudes. The EJ-CMEs originate from intermediate central meridian region on the Sun and hence represent slightly reduced impact on the magnetosphere, thus contributing to the decorrelation between shock speed and SC amplitude. Also, a large number of SC/SIs is produced by the ICME and IP shocks with lower speeds on the average.

3.7 Radio-loud and Radio quiet shocks associated SC/SIs

We have divided the SC/SI events into two sub groups associated with RL and RQ shocks. Figure 3.6 shows the number of SC/SI produced events in each category of CME, ICME, and IP shock for RL and RQ shocks (Figure 3.6a). It is obvious from Figure 3.6b that RL shock associated events occur more frequently than the RQ shock associated events. The comparison of the average SC/SI amplitudes for RL and RQ shocks in all CME, ICME, IP Shock categories shown in Figure 6b reveals that RL shocks are most effective in causing SC/SI events. We divided the SC/SI events into two sub groups associated with RL and RQ shocks.

Figure 3.7 shows the SC/SI amplitude distributions for all (RL+RQ) shocks, RL shocks, and RQ shocks. It can be seen from Figure 3.6 that SC/SI amplitudes associated with RL shocks are higher (average 32 nT) than those associated with RQ shocks (average 19 nT). The average SC/SI amplitude for RL shocks is almost a factor of 1.6 higher than that for RQ shocks. The higher average SC/SI amplitude observed for RL shocks suggests that the RL shocks are more energetic than the RQ shocks and hence are more effective in producing SCs.

The correlation of SC/SI amplitude with CME and IP shock speeds for RL and RQ shocks is shown in Figure 3.7. We have not considered ICMEs because there is not much difference between the average speeds of ICMEs and IP shocks. The MCs and EJ are shown separately for all, RL and

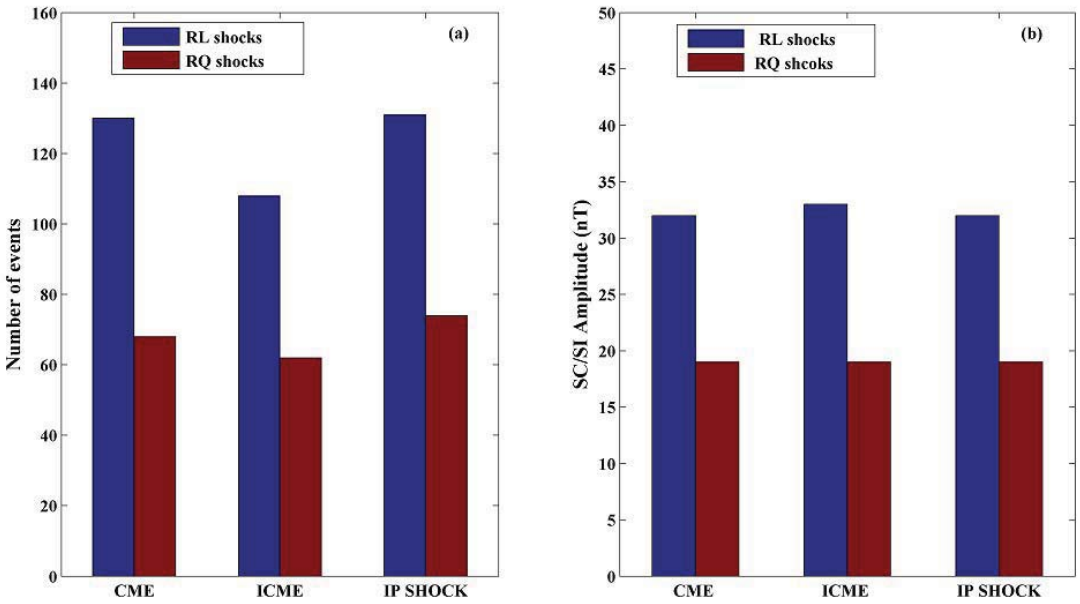

Figure 3.6: (a) The distribution of CME/ICME/IP shocks for RL and RQ events, (b) The average SC/SI amplitude for RL and RQ shocks with the distribution of CME/ICME/IP shock.

RQ shocks.Table 3.4 shows the average SC/SI amplitude and average CME speed and IP shock speed for RL and RQ sub-groups. Table 3.5 gives the comparison of the correlation coefficients (from Fig. 3.8) showing that the correlation is better for RL shocks in the category of MCs than EJs. The poor correlation coefficients obtained for the RQ shocks in three categories (Fig. 3.8 e, f) are due to the difference in locations where shock speed is measured and the shock evolution between the Sun and Earth.

MCs head directly toward Earth, so the shock measurement is made at the nose where the speed is the maximum. For EJ, the CME heads not directly at Earth, so the shock speed is measured slightly away from the nose hence the speed may be smaller. This explains the difference between MC and EJ correlations because of the speed difference. As for the difference between RL and RQ shocks, the associated CMEs have different kinematic evolution. The RL CMEs start with very high speed near the Sun and slowly decelerate. On the other hand, the RQ CMEs start out very slowly and reach higher speeds far into the IP medium, where they start driving a shock. The CME

Table 3.4: Average SC/SI amplitude and speed of CME and IP Shocks for RL and RQ

	RL	RQ
	Average SC/SI amplitude (nT)	
CME	31.81	18.74
IP shock	31.67	18.54
	Average Speed(km/s)	
CME	1259	476
IP shock	617	457

speed for the RL shocks is thus better correlated with the SC/SI amplitude. The RQ shocks are generally slower because the associated CMEs barely become super-Alfvenic (they do not produce a type II burst). It can be noted from Table 3.4 that average speed and amplitude for RL shocks are higher than for RQ shocks which explains that the RL shocks are more effective in generating SC/SIs than RQ shocks.

In order to further quantify the strength of the shocks associated with SC/SI amplitude, we have compared the Alfvenic Mach numbers (M_A) of the IP shocks from Paper I with the associated SC/SI amplitudes. In Figure 3.9 (a, b, c), we have plotted the SC/SI amplitude as a function of the Mach number for all, RL, and RQ shocks. The SC/SI amplitudes for RQ shocks are generally low compared to those of RL shocks and the M_A have a similar distribution. The correlation coefficient between SC/SI amplitude and MA is higher for RL shocks compared to RQ shocks.The average M_A(2.6) for RQ shocks is less than that for RL shocks (3.4) by 31%. This difference is also consistent with the SC/SI amplitudes for RL shocks. The difference in M_A reflects the difference in CME speed for RQ and RL shocks and also confirms that RQ shocks are weaker.

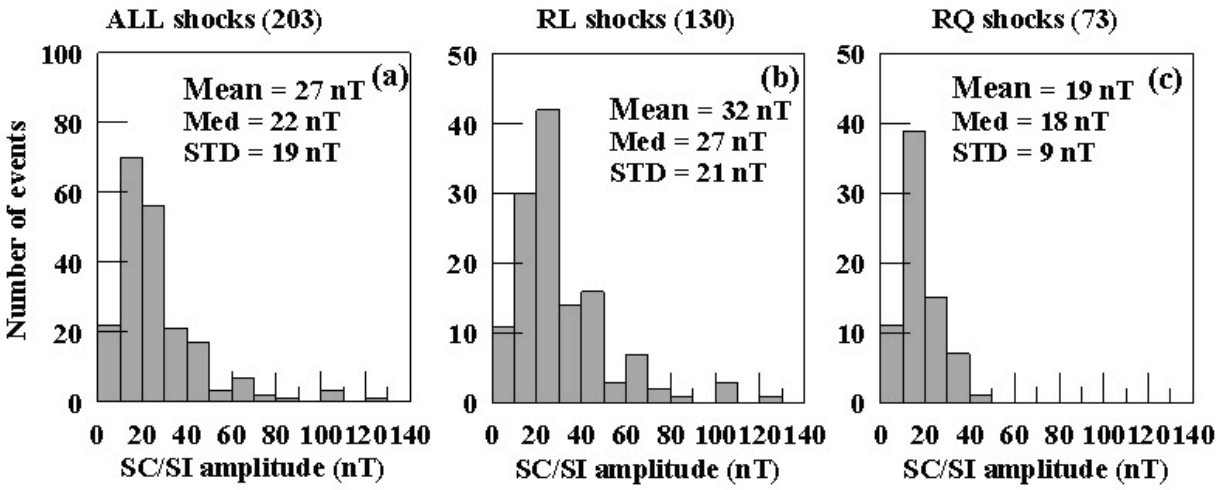

Figure 3.7: The distribution of SC/SI amplitude for ALL (a), RL (b) and RQ (c) shocks. The average mean (<V>), median, and standard devation (STD) for each case are given in the plots. The bin size is 20nT for all panels.

3.8 Geoeffectiveness of shock driving ICMEs

The intensity of the storms is highly dependent on the speed of the associated CME as well as on the IP shock parameters [e.g., Srivastava and Venkatakrishnan, 2002, 2004; Jurac et al., 2002; Gopalswamy et al., 2008; Gopalswamy, 2009; Kilick et al., 2011]. However, such studies have been made only for intense geomagnetic storms. For example, Srivastava and Venkatakrishnan [2004] studied the solar and interplanetary origin of the major storms observed during the period

Table 3.5: Correlation Coefficients for All Shocks, RL Shocks and RQ Shocks with separation of ICME types : MC and EJ

	CME		IP shock	
	MC	EJ	MC	EJ
All shocks	0.55	0.45	0.73	0.36
RL shocks	0.50	0.31	0.74	0.29
RQ shocks	0.50	0.18	0.07	-0.02

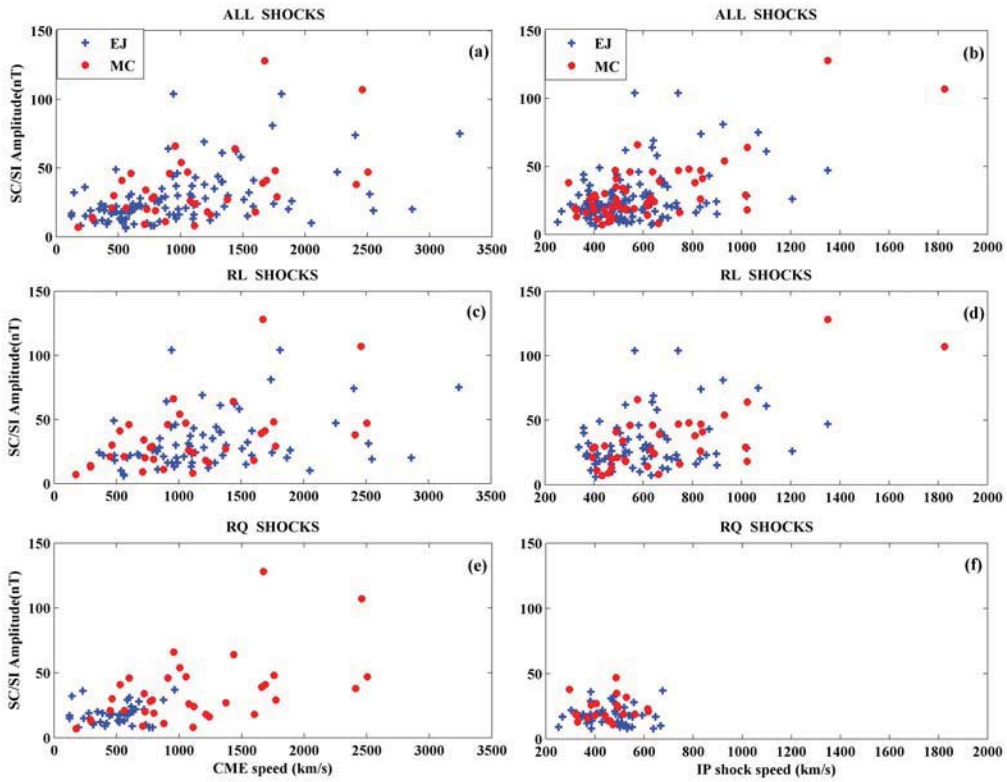

Figure 3.8: The scatter plot for CME/IP shock speed with SC/SI amplitude for All, RL and RQ shocks for MCs (red plus sign) and EJs (blue plus sign). The average values of SC amplitude and speed are given in Table 3.4. The Correlation Coefficients (CC) are given in the Table 3.5.

1996-2002. They found that the intensity of storm was highly dependent on the southward component of the IMF and next in importance to the speed of the CME and its ram pressure at the Earth.

It is known that CMEs from the Sun and Corotating Interaction Regions (CIRs) formed in the IP medium are the most important causes of geomagnetic disturbances [Watari and Watanabe, 1998; Alves et al., 2006; Tsurutani et al., 2006; Gopalswamy, 2008]. In particular, IP shock-driving ICMEs are important in causing geomagnetic activity. When ICME-driven shocks arrive at Earth, they can compresses Earth's magnetosphere producing storm sudden commencements and are often followed by magnetic storms if the shock-driving ICMEs and/or the preceding sheaths have south-ward magnetic field [Tsurutani et al., 1988; Gonzalez et al., 1994, 1999; Gopalswamy

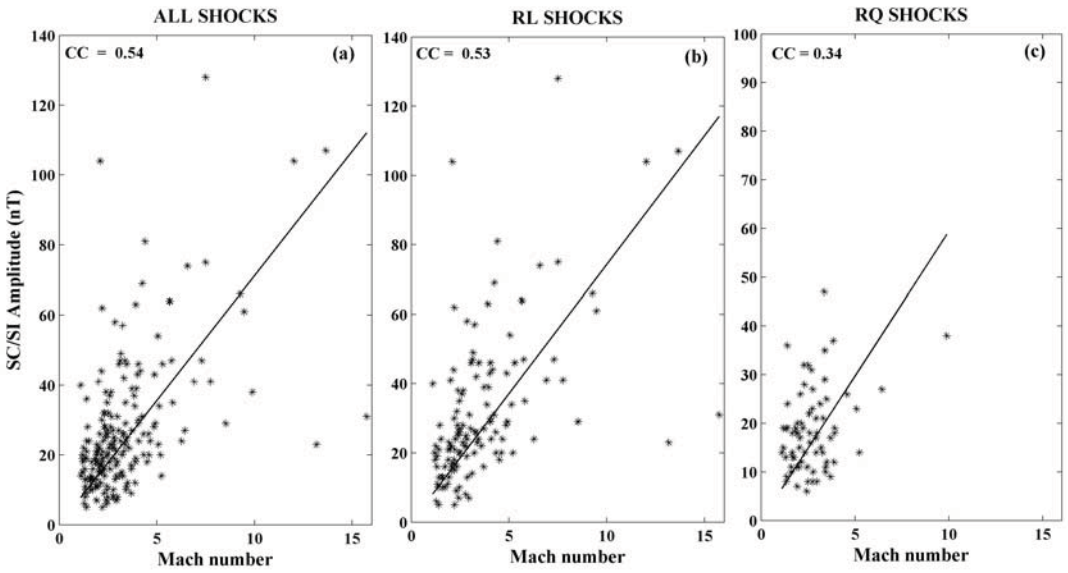

Figure 3.9: Scatter plot of the Mach number with SC/SI amplitude for ALL, RL and RQ shocks. The correlation coefficients (CC) are given in the plots.

et al., 2010; Veenadhari et al., 2012].

In this part of work, we investigate the geoeffectiveness of shock-driving ICMEs for the period 1996-2006 (solar cycle 23) as function of ICME, and IP shock parameters. We also study the geoeffectiveness in terms of solar origin of CME as well as the radio type II burst associated events. It is very clear that southward component of the IMF plays a major role is deciding the geoeffectiveness still an effort is made to see the importance of CME, ICME, and IP shock parameters in deciding the geoeffectivness.

3.8.1 Geoeffectiveness associated with radio characterstics and ICMEs structures

The IP shock list which is used for identification of SC/SI is taken for the identification of geomagnetic storms. We have identified 144 shock-driving ICMEs detected in situ at the Sun-Earth

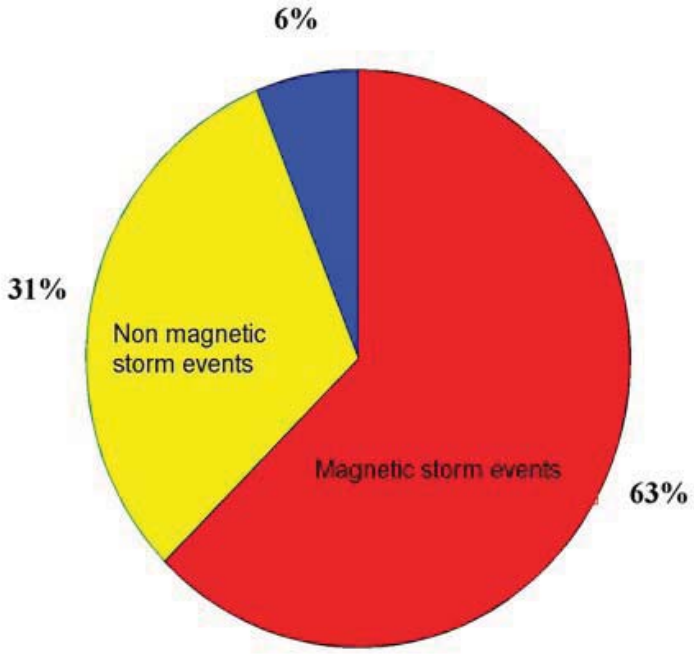

Figure 3.10: Percentage distribution of geomagnetic activity by shock associated ICME during 1996-2006.

L1 point which resulted in geomagnetic storms. Figure 3.10 shows the percentage distribution of geomagnetic activity level generated by the shock-associated ICMEs for Solar Cycle 23. Nearly 63% shock driving ICME resulted in geomagnetic storms, 31% did not result in geomagnetic storms and the remaining 6% is data gap and few due to double CME (Figure 3.10). This shows that not all Earth directed shock driving ICME results in geomagnetic storms.

In order to understand the importance of radio characteristic, the IP shocks are classified as RL and RQ. Figure 3.11 shows the distribution of Dst index for all, RL and RQ events. The total number of events are observed to be 145, in which RL is 95 whereas RQ is 50. It is clear that, nearly 65% of geoeffective CME are resulted to be RL shocks. The average Dst for the total events is estimated to be -110.5 nT. The average Dst for RL events is -117 nT and for RQ it is estimated to be -89 nT. Though Bz place a major role in deciding the geoeffectiveness, the RL associated CME shown more geoeffectiveness when compared to RQ shocks. It is concluded that the radio

characteristics also plays a role in determing the geoeffectiveness.

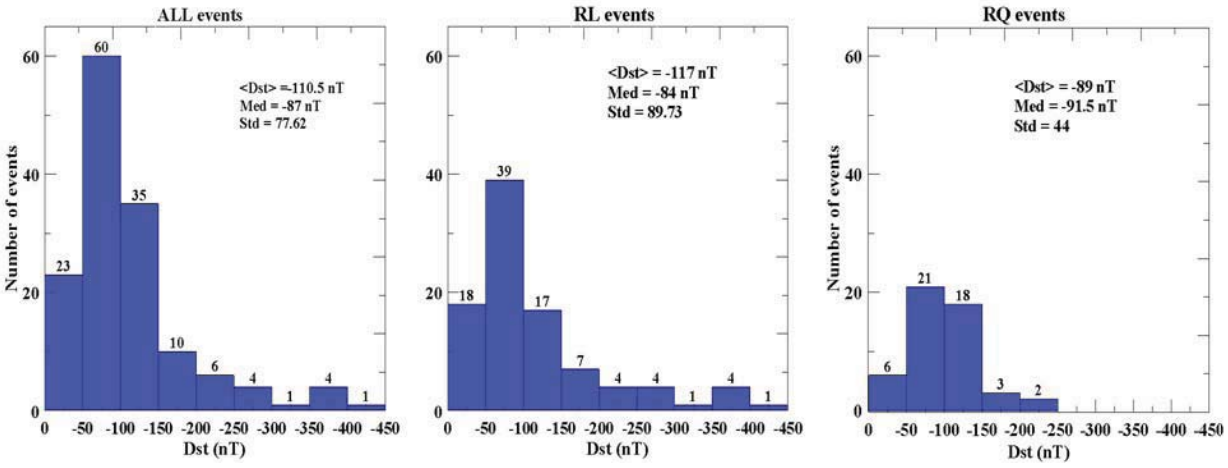

Figure 3.11: Distribution of Dst for all, RL and RQ events.

After looking in to the importance of radio characteristics of CME in determining geoeffectiveness, the next step is to check the role played by ICME counterpart. The distribution of all, MC, EJ is shown in the figure 3.12. The sheath associated geomagnetic storms are excluded in the statistics. The average Dst associated for MC is observed to be - 138 nT and for EJ is observed to be -99 nT. It is clear the MC associated ICME is more geoeffective when compared to EJ. CMEs have flux rope structure (MCs) but their different propagation directions with respect to the Sun-Earth line and angular widths determine whether they are viewed as MCs or EJs by the observing spacecraft [Gopalswamy, 2006; Xie et al., 2013]. Therefore, the geoeffectiveness of the IP structures depends on the direction of propagation (i.e., do they propagate along the Sun-Earth line or away from the Sun-Earth line), which decides the effect of their interaction with Earth's magnetosphere. This may be one of the reason for reduced geoeffectiveness.

3.8.2 Solar wind parameters

Several authors tried to find empirical relationship between Dst and VBz and reported that for a given ICME speed, Dst value depends on Bz [Wu and Lepping, 2002; Gopalswamy, 2010]. The

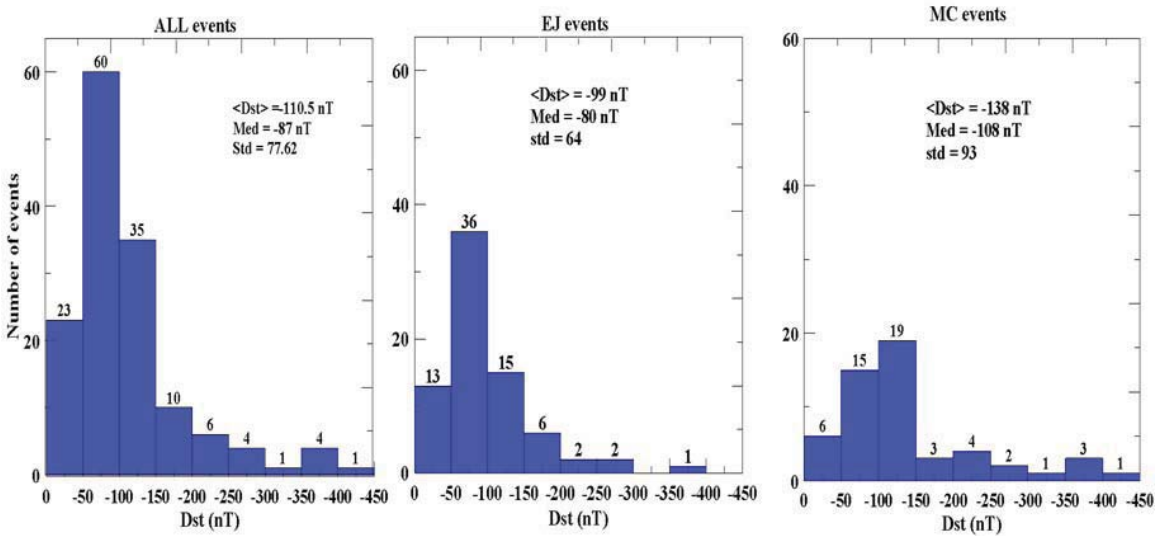

Figure 3.12: Distribution of Dst for all, EJ and MC occured during 1996-2006.

ring current intensity depends on the rate at which the particles enter through the open field lines by the process of reconnection [Chapman and Bartels, 1940, Gonzalez et al., 1994]. In turn the entry of particles is proportional to the duration and strength of Bz as well as the solar wind ICME speed at the front [Balan et al ., 2014]. In order to see whether the Dst-VBz relation holds, the Dst value is plotted against VBz for all, MC and EJ as shown in Figure 3.13. The plot shows a linear variation with negative slopes for all the cases. The correlation is found to be best with value of 0.83, 0.88 and 0.84 for all, MC and EJ respectively. The MC shown a better correlation for VBz-Dst when compared to all and EJ. Since the speed of MC is measured at nose it is expected to give a better correlation.

3.9 Discussion

Using the list of CME-driven shocks observed at 1 AU and their association with type II radio bursts compiled in Gopalsamy et al ., 2010, we have analyzed the corresponding SC/SI events and geoeffectiveness. We subdivided the IP shocks into RL and RQ shocks and found that RL

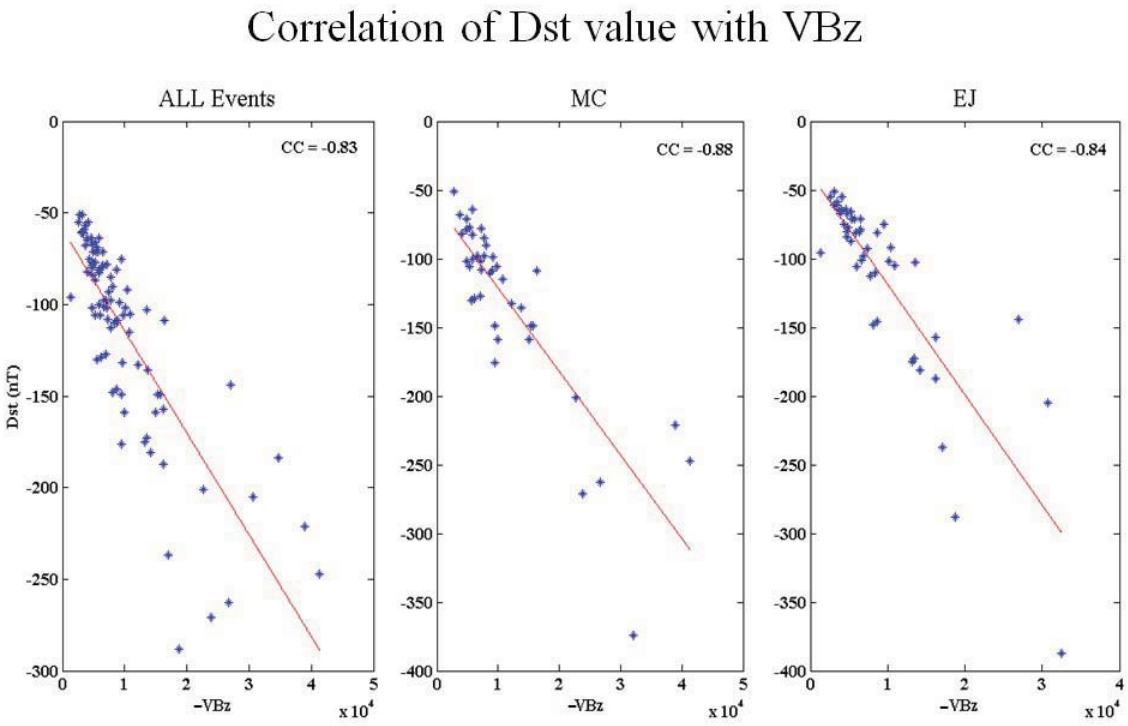

Figure 3.13: Correlation between VBz-Dst for all MC and EJ.

shocks are generally more effective in producing SC/SI as well as geoeffectiveness. We have further investigated the SC/SI amplitude and geoeffective variation with ICME (associated with MC and EJ) speeds and shock M_A. The shocks associated with MC type ICMEs are more effective in causing SC events. As shown in Gopalsamy et al. [2010], CMEs associated with RQ shocks have lower energy compared to the RL shocks. These two shock populations differ in many other aspects such as speed and acceleration. In general, all the parameters of RQ CMEs show lower CME energy, resulting in weaker shocks and hence weaker SCs. However, the average speed of CMEs associated with RQ shocks slightly higher than that of the general population of CMEs. The importance of identifying RL CMEs from near the disk center is thus clearly of forecast value because such CMEs result in strong SC events.

Cho et al. [2010] found a better correlation (CC = 0.67) between CME speed and the SC/SI amplitude caused by IP shocks for fast CMEs (VCME ¿ 1000 km/s) using only 26 type II burst

IP shocks. But we have considered 203 IP shocks (including RL and RQ shocks) and correlation coefficient is 0.55 between CME speed and SC/SI amplitude (Fig. 3.8). We further isolate RL and RQ shocks which are associated with MCs and EJs, the correlation (0.50) is better for RL and RQ shocks associated with MCs than EJs (Table 3.5). This correlation is lower than the correlation obtained by Cho et al. [2010] due to analysis of large number IP shocks. The average SC/SI amplitude and CME speed are higher for RL shocks than RQ shocks.

Gopalsamy et al ., 2010,showed that out of a total 180 shocks associated with ICMEs, 32% of shocks were driven by MCs, 68% were driven by non-cloud EJ. Also 42 out of 222 IP shocks (19%) were driverless.The present study shows better correlation for SC/SI amplitude with MCs-associated shocks than EJ associated shocks. Though the MC-associated shocks have lower CME speed than EJ-associated shocks but MCs have the strong effect in producing SC/SIs due to their difference in solar source distributions. Also, the better correlation between SC/SI amplitude and MC speed is due to the difference in the way the speeds were measured. The MC-associated shocks are measured at their noses where they have highest speed (625 km/s) and the EJ-associated shocks are measured between their nose and flanks where they have intermediate speed (549 km/s). Thus, MCs are more effective in producing higher SC/SI amplitudes.

Our analysis clearly shows that RQ shocks produce smaller SC/SI amplitude than the RL shocks do. According to Gopalsamy et al ., 2010, a positive acceleration is shown by most of the CMEs associated with RQ shocks and a negative acceleration of the CMEs associated with RL shocks. This means that the RQ shocks are formed generally at large distances from the Sun ($>$10 Rs) where the driving CMEs become super-Alfvenic. Thus, RQ shocks are the weakest, followed by shocks producing the type II radio bursts, and the shocks producing radio emission at higher frequencies. The primary characteristic that distinguishes between RQ and RL shocks seems to be the kinetic energy of the CME drivers. The low M_A for RQ shocks is consistent with the low-energy drivers associated with them whereas RL shocks have large average (3.4) M_A. One of the practical implications of these results is that when a CME near the Sun does not produce a type II radio burst, it is unlikely that this CME will result in a large SC event. Such a conclusion was

also derived from the occurrence of another 1-AU event, viz., energetic storm particle (ESP) events caused by IP shocks by Makela et al. [2011]. They found that RL shocks associated with the MC events produce the largest ESP events. It must be noted that the same shock produces SC and ESP event at 1 AU by different physical mechanisms.

Gopalsamy et al .[2010] reported that a significant number of (42 out of 222 or 19%) driverless shocks, which means that the shocks may not be followed by discernible driver. In this work, there are 38 driverless shocks which are associated with SC/SI events (38 out of 203 or 18.7%) with 25 RL and 13 RQ shocks. The average SC amplitude is 25 nT and 15 nT for RL and RQ shocks (driverless) respectively. The average SC/SI amplitude for driverless RL shocks is higher than the shocks which are associated with EJ and is lower than for the shocks with MCs.

The distribution of solar sources over the solar surface shows that the RL shocks are spread over the entire longitude belt (Figure 3.4) than RQ shocks of which the source region is mainly confined to $\pm 30^{\circ}$. So, the RQ and RL source distributions reflect the width of the shock front ahead of a propagating CME. Gopalswamy et al. [2010] reported that the RL CMEs and the associated shocks are faster, i.e. are more energetic, than the RQ CMEs and shocks. Faster CMEs are generally wider, therefore the wider RL shocks with a larger longitudinal separation between the solar source and the observer can still be detected at 1 AU. In a study of CME widths, Michalek et al. [2007] reported that RL CMEs are almost two times wider than RQ CMEs [Gopalswamy et al., 2008b]. The source distribution of RQ and RL shocks considerably different from that of RQ and RL fast and wide CMEs [Gopalswamy et al., 2008b]. They found that the sources of RQ CMEs are located near the limbs whereas for RL CMEs occur in center-west regions of the solar disk. There exists a similar variation in SC/SI amplitudes with respect to the solar latitude and longitude. The difference in the source distribution is due to the selection effect because we consider only CMEs that produce a shock signature at 1 AU.

The geoeffectiveness of 145 CMEs associated with Ip shocks are investigated. The average Dst of RL associated shocks are observed to be higher when compared to RQ shocks. Similarly MC shown a higher Dst average when compared to EJ. In the case of CME originating close to

the center of the Sun, the center portion of the MC or EJ may pass the Earth and it may have ordered flux rope geometry to cause long-duration of southward IMF. In the case of EJs, the lack of intense storms shows that the impact delivered by them on Earth's magnetosphere is diminished for some reason. One possible explanation is that these CME are possibly deflected by a nearby coronal hole away from the Sun-Earth line and therefore they are able to provide only a glancing blow to Earth, which results in the diminished levels of geomagnetic activity [Gopalswamy et al., 2005, 2009; Mohamed et al., 2012]. It has been shown that MC-associated CMEs are more likely deflected towards and the EJ associated CMEs deflected away from the Sun-Earth line [Makela et al., 2013]. The VBZ-Dst relation shown better correlation for MC events.

3.10 Conclusion

The main findings of the present study are summarized as follows.

About 91% of shocks produced clear SC/SI events and nearly 63% of shocks are found to be geoeffective. The average speed of SC/SI associated CME is 1015 km/s, which is almost a factor of 2 higher than that of the general CME population. MC- associated shock speeds are better correlated with SC/SI amplitudes as compared to the EJ shocks. Also SC/SI amplitudes are higher for MCs than EJs associated shocks. The average SC/SI amplitudes for RL and RQ shocks are 32 nT and 19 nT, respectively. RL shocks are more effective in producing SC/SI events than the RQ shocks. The average M_A is higher for RL shocks than for RQ shocks. The SC/SI amplitudes and M_A of the shocks are better correlated for RL than for RQ shocks. Thus if we observe a RL CME near the Sun originating close to the disk center, it is highly likely that the shock produces a large SC/SI event at the Earth. There is a significant difference in the latitudinal and longitudinal distribution for RL and RQ shocks associated with SC/SI amplitudes. RL shocks are more spread over the longitude belt than RQ shocks. RQ shock source region is confined to $\pm 30^{\circ}$. The average Dst is higher for RL shocks and MC when compared to RQ shocks and EJ, respectively.

Chapter 4

On the reduced geoeffectiveness of solar cycle 24: a moderate storm perspective

4.1 Introduction

Geomagnetic storms are major disturbances in the Earth's magnetosphere caused by energetic solar wind magnetic structures impacting and injecting material into the magnetosphere by the process of reconnection [Dungey, 1961; Gonzalez et al., 1994]. Geomagnetic storms are marked by a decrease in the horizontal intensity of the Earth's magnetic field, which results from ring current enhancement due to the increase in the population of magnetopsheric trapped particles [Chapman and Bartels, 1940, Gonzalez et al., 1994]. It is now well understood that geomagnetic storms are caused by coronal mass ejections (CMEs) and corotating interaction regions (CIRs) originating from the Sun that evolve through the interplanetary medium before impacting the magnetosphere [Brueckner et al., 1998; Webb et al., 2001; Berdichevsky et al., 2002; Zhang et al., 2003; dal Lago et al., 2004; Zhang et al., 2007; Gopalswamy et al., 2007; Gopalswamy, 2010]. CMEs generates severe storms while CIRs cause moderate storms [Gosling et al., 1991; Tsurutani and Gonzalez, 1997; Richardson et al., 2002; Tsurutani et al., 2006; Gopalswamy, 2008, Zhang et al., 2007].

The counterpart of CMEs in the interplanetary medium are termed as interplanetary coronal mass ejections (ICMEs), which are usually categorized as Magnetic clouds (MCs) and Non-magnetic clouds or Ejecta (EJ) based on their in-situ plasma and magnetic signatures [Klein and Burlaga, 1982; Gopalswamy et al., 2010; Riley and Richardson, 2012 and references therein]. CIRs develop when high speed solar wind streams (HSS) emanating from coronal holes interact with streams of lower speed. CIRs consist of enhanced density and magnetic field, which when associated with southward IMF, result in geomagnetic storms [Smith and Wolfe, 1976; Gosling, 1996; Gosling and Pizzo, 1999].

The type of IP structure causing geomagnetic storms varies with the solar cycle: CME-associated storms dominate during solar maxima whereas CIR storms mostly occur during the declining phase of solar cycles [Webb, 1991; Yashiro et al., 2004; Mursula and Zieger, 1996]. Geomagnetic storms result in intense currents in the magnetosphere, changes in the radiation belts, and heating of the ionosphere and upper atmospheric region. Geomagnetic disturbances are measured using a variety of indices, one of which is the Disturbance storm time (Dst) index [Sugiura, 1964]. The Dst index represents changes in the magnetic field caused by magnetopsheric currents such as the ring current, tail current, asymmetric ring current, and magnetopause current [Alexeev et al., 1996; Daglis and Thorne, 1999; Turner et al., 2000; Liemohn et al., 2001; Lopez et al., 2015]. Using Dst, geomagnetic storms are classified as weak (-30 $<$ Dst $<$ -50 nT), moderate (-50 $<$ Dst $<$ -100 nT) and intense (Dst $<$-100 nT) [Gonzalez et al., 1994, Sugiura and Chapman, 1960].

Identification of CMEs comes from two spatial domains: the near-Sun (up to 30 solar radii) region remote-sensed by coronagraphs and in situ observations made by spacecraft in the solar wind. The origin and evolution of CMEs through the interplanetary medium can be understood by comparing observations from these two domains [Gopalswamy, 2002]. Most of the geomagnetic storms do not associate with a unique CME originating from front-side solar disk. Complex solar wind flows have been reported before, and they are speculated to be caused by multiple CME interaction in interplanetary space resulting in geoeffectiveness [Burlaga et al., 1987; Bothmer and Schwenn, 1995]. Though locating the exact solar source for observed geoeffectiveness is not so

easy due to the complexity involved with identifying the CME and its evolution, many researchers tried to look for the source location of the geoeffective CMEs [Zhang et al., 2003, 2007, 2013, Gopalswamy et al., 2007,2014, Zhen et al., 2014] Based on the observations by Large Angle Spectrometric Coronagraph Experiment (LASCO) from Solar and Heliospheric Observatory (SOHO), and Solar Terrestrial Relations Observatory (STEREO) it is now possible to track the CME from the emission observed at C2 to the L1 point. The combination of remote sensing solar observations and in situ solar wind observations provides an integrated approach to the identification of the heliospheric process and the evolution involved in the generation of geomagnetic storms.

There are several studies on intense geomagnetic storms and the associated solar sources and the interplanetary conditions [Tsurutani et al., 1988, 1992, 1995, 2006 Gonzalez et al., 1999, 2007, 2011; Gonzalez and Echer, 2005; Zhang et al., 2006, 2007; Echer et al., 2008]. Geomagnetic storms are intensified when southward interplanetary magnetic field (IMF) that allows efficient energy transfer from the solar wind into the Earth's magnetosphere [Dungey 1961; Gonzalez and Tsurutani, 1987; Gonzalez et al., 1994; Echer et al., 2005; Echer et al., 2013]. The magnetosphere-solar wind coupling has also been considered using the energy flux parameter epsilon (ε) for severe geomagnetic storms [Perrault and Akasofu, 1978; Nishida, 1983; Mac-Mahon and Gonzalez., 1997; Holzer and Slavin, 1979; Sibeck et al., 1991; Alex et al ., 2006]. The ε parameter gives the maximum energy transferred to the magnetosphere from the solar wind during the geomagnetic storms and it is highly dependent on the magnetic field component and the solar wind velocity. The solar wind- magnetosphere dynamo is generated during the interaction of IMF with the magnetosphere and the energy transfer is in the range of 10^{12} - 10^{13} W during geomagnetic storms [Weiss et al., 1992; Mahon and Gonzalez., 1997; Alex et al., 2006].

As the Sun emerged from the deep solar minimum to the rising phase of the solar cycle 24, the Sunspot number (SSN) was relatively small [Gopalswamy et al., 2012; Solomon et al., 2013; Lean et al., 2014; Potgieter et al,. 2014, Kilpua et al., 2014]. Although SSN decreased by 40$\%$ in solar cycle 24, the CME rate was similar to that in cycle 23 [Gopalswamy et al., 2014]. There is not much diminution observed in the number of halo CMEs, which are generally more geoeffective.

However, there was a severe reduction in the geoeffectiveness of CMEs as indicated by the drastic decrease in the number of intense geomagnetic storms during solar cycle 24. An average reduction in Dst from -66 to -55 nT was found for MC-associated storms during the first 73 months of solar cycle 24 compared to the same epoch in cycle 23. This has been attributed to the anomalous expansion of CME in the current solar cycle [Gopalswamy et al., 2015a]. In another study [Gopalswamy et al ., 2015b] a significant reduction in CME mass and increase in CME width for limb CMEs is found in solar cycle 24 when compared to cycle 23.

While the reduction in intense storms is clear, it is of interest to know what happens to moderate storms. Although there are other works on cycle-23 moderate storms [Tsurutani and Gonzalez, 1997; Wang et al., 2003; Zhang et al., 2006; Xu et al., 2009; Echer et al., 2011; 2013; Hutchinson et al., 2011; Tsurutani et al., 2011], there is no comparative study between solar cycles 23 and 24. This work attempts to see if there is any change in the occurrence of moderate storms between solar cycles 23 and 24. This work involves the identification of the source of the moderate geomagnetic storms in solar cycles 23 and 24 and comparison of the interplanetary parameters. The response of magnetopshere is investigated to explain the solarwind- magnetosphere coupling during moderate storms for solar cycle 23 and 24.

4.2 Data and Observations

This study concerns moderate geomagnetic storms that occurred during the first 77 months of cycles 23 (01 May 1996 to 30 September 2002) and 24 (01 September 2008 to 31 January 2015). Based on the availability, final, provisional and real time Dst values are obtained from (http://wdc.kugi.kyoto-u.ac.jp/index.html). The Dst values are carefully examined to identify moderate storms by eliminating Dst excursions due to prior geomagnetic storms in progress. Only occurrences when a prior storm recovered up to 80% have been considered. We use the source CME identification for solar cycle 23 reported in the Interplanetary (IP) shock catalogue by Gopalswamy et al. [2010a] and the list provided by Richardson and Cane [2010] online (http://www.srl.caltech.

edu/ACE/ASC/DATA/level3/icmetable2.htm). For cycle 24, the CMEs are identified by running movies of coronograph images available at (http://cdaw.gsfc.nasa.gov/CMElist/index.html). A few identifications are taken from the list given by Richardson and Cane as mentioned above. The solar source location is taken from the halo CME catalogue (http://cdaw.gsfc.nasa.gov/CMElist/halo /halo.html [Gopalswamy et al., 2010b]. For other CMEs we identify the solar source from the flare locations given in the on-line Solar Geophysical Data (SGD) report. For events not listed in SGD, the sources are identified using images from the Extreme ultraviolet Imaging Telescope (EIT) on board SOHO, the Atmospheric Imaging Assembly (AIA) on board the Solar Dynamics Observatory (SDO), and H-alpha observatories (as detailed in Gopalswamy et al., 2007). Mass and width of the CMEs are taken from the CME catalog (http://cdaw.gsfc.nasa.gov/CMElist/index.html) [Gopalswamy et al., 2009]. The solar wind plasma and magnetic parameters with one-min resolution are obtained from CDAWeb (http://cdaweb.gsfc.nasa.gov/cgi-bin/eval1.cgi).

Based on the Dst index criterion as mentioned in section 1, a total of 166 moderate and intense geomagnetic storms are identified in Solar cycle 23 and 67 in cycle-24 (hereafter all the comparisons of solar cycles 23 and 24 storms refer to the corresponding epoch of 77 months in each cycle). We see that the storm occurrence rate in cycle 24 is reduced by 57.5% compared to that in cycle 23. The monthly average SSN is 69 and 40 for solar cycles 23 and 24, respectively. So, nearly 40 % decrease is observed in SSN for solar cycle 24 when compared to solar cycle 23 [Gopalswamy et al., 2014]. The storm occurrence rate reduced more than SSN did. The decrease in SSN is not sufficient to explain the observed reduction in geoeffectiveness in solar cycle 24.

Not all storm sources follow the Sun spot activity, so in order to understand the relation between solar activity and the occurrence of storms it is necessary to differentiate the storms of different origin. The distribution of geomagnetic storms between CME and CIR sources is given in Figure 4.1(a-d) for cycles 23 and 24. The combined set of intense and moderate storms, are compared with the moderate storms.

There was a small data gap (DG) in solar cycle 23 because there was no CME observation for a brief period (3 months in 1998 and 1 month in 1999) when the SOHO spacecraft was temporarily

Table 4.1: Intense and moderate storms during the first 77 months of cycles 23 and 24

		All	Moderate	Intense
Solar cycle 23	CME	111(66.8%)	63(56.7%)	48(88.8%)
	CIR	43(25.9%)	40(36%)	3(5.5%)
	Data gap	12(7.2%)	8(7.2%)	3(5.5%)
	Total	116	111	54
Solar cycle 24	CME	52 (77.6%)	41 (74.5%)	11 (91.7%)
	CIR	14 (25.5%)	14 (25.5%)	1 (8.3%)
	Data gap	–	–	–
	Total	67	55	12

disabled. Apart from the data gap, 5 moderate storms are not included in the study. The first two occurred on 17 September 2000 and 09 October 2001. These cases are complex and no CME is detected by SOHO. No shocks are detected in situ in these events. The 17 September 2000 storm is associated with a narrow negative Bz interval. The other three occurred on 12 April 2014, 30 April 2014 and 07 January 2015 with a minimum Dst of -80 nT, -67 nT and -99 nT, respectively. The 07 January 2015 is probably associated with the 04 January 2015 CME, but the confidence in the association is not high since the CME could not be tracked to 1AU. The solar source location of the 30 April 2014 storm is identified from SDO images, but LASCO did not detect it may be the CME was too narrow. No STEREO observations exist during this period making it difficult to trace the CME at 1 AU.

The CME-driven storms are examined based on the ICME structure observed at 1 AU. Similarly, CIR-associated storms are identified by examining the variation in total magnetic field, proton temperature and density at 1 AU. Table 4.1 gives the statistics on the moderate and intense storms occurring in the two cycles. From Table 4.1 and Figure 4.1 it is clear that CME storms constitute the majority in both cycles. In cycle 23, out of a total 166 storms, 111 (66.8%) are of CME origin,

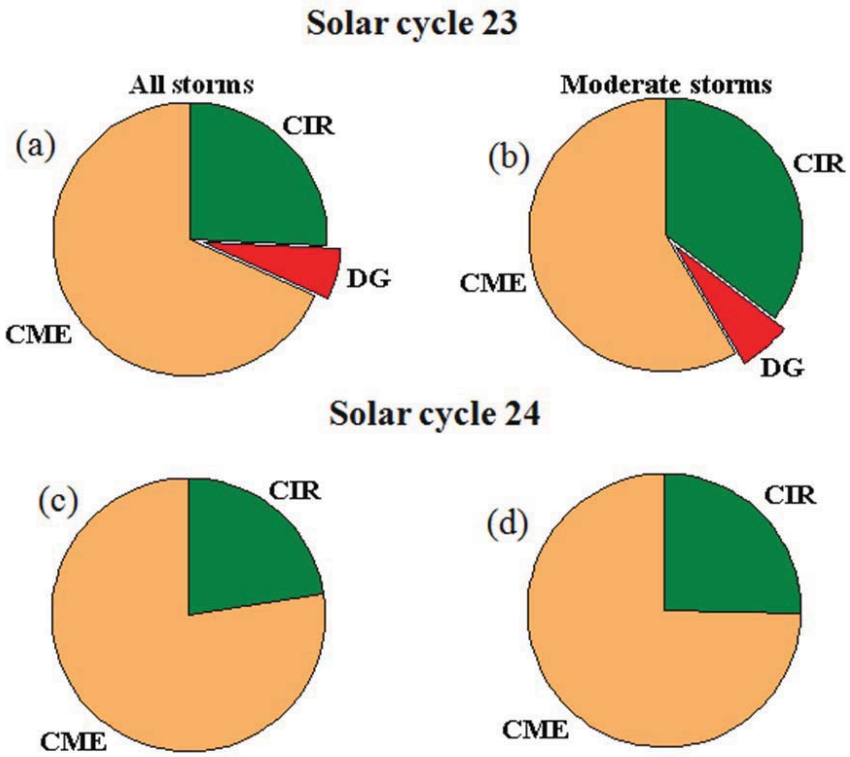

Figure 4.1: Distribution of CME and CIR driven for all storms and moderate storms during SC 23 (a,b) and SC 24 (c,d). DG denotes storms whose sources are unkown due to data gap.

43 (25.9%) of CIR origin and 12 (7.2%) have a data gap. Out of the 111 moderate storms in cycle 23, 63 (56.7%) are of CME origin, 40 (36%) of CIR origin and 8 (7.2%) have a data gap. Echer et al. [2013] investigated 213 moderate storms from cycle 23 (1996-2008) and found that the moderate storms were due to: CIRs and pure High speed streams (HSSs) (47.9%), MCs and non-cloud ICMEs (20.6%), pure sheath fields (10.8%), and sheath - ICME combination (9.9%). The difference between Echer et al. [2013] and our results can be attributed to the different periods considered for analysis. In solar cycle 24, 77.6% (52 out of 67) of all storms (the combined set of intense and moderate storms) are of CME origin and only 22.3 % (15 out of 67) are of CIR origin. Considering only the moderate storms of cycle 24, we find that 74.5 % (41 out of 55) are of CME origin whereas 25.5 % (14 out of 55) are of CIR origin. Table 4.1 also shows that there were 48

CME-driven intense storms in cycle 23 compared to only 11 in cycle 24, which corresponds to a reduction of 78%.

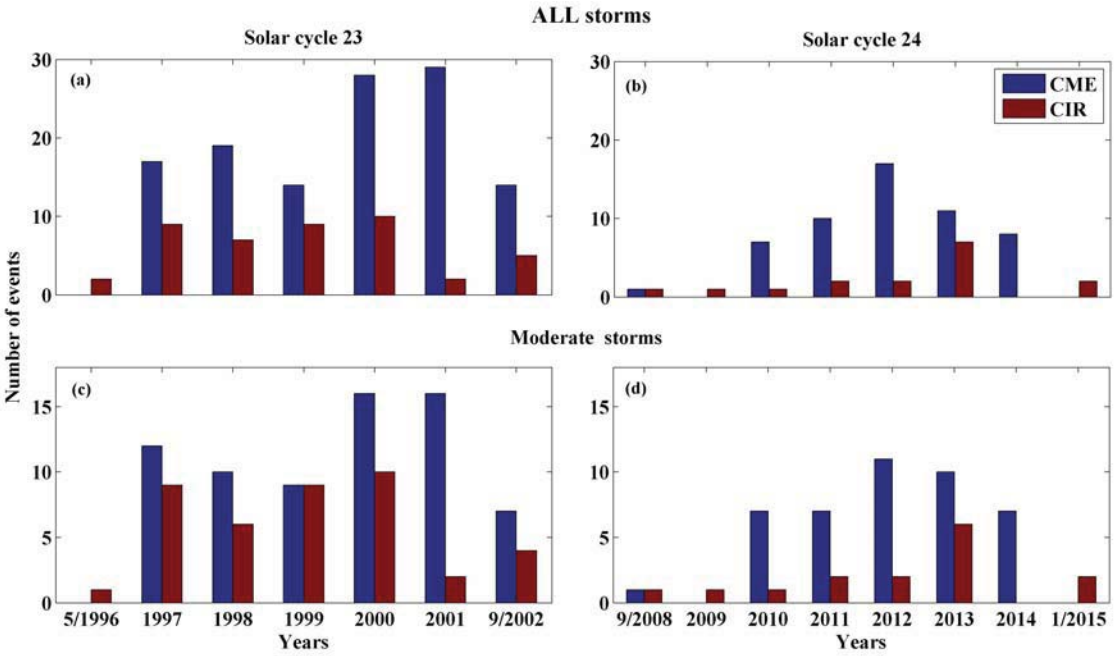

Figure 4.2: Yearly occurrence of CME and CIR driven storms: All storms and moderate storms for SC 23 (a,b) and SC 24 (c,d).

Figure 4.2 shows the yearly distribution of CME and CIR-driven storms grouped into all storms (a,b) and moderate storms (c,d) of cycles 23 and 24, respectively. The occurrence rate of all storms peaks around 2001 for solar cycle 23 and around 2012 for solar cycle 24 when CME-associated storms is considered. The occurrence rate of CME-associated moderate storms peaks around 2000 and sustains till 2001 in solar cycle 23 (Figure 4.2c). The behaviour of moderate storms in cycle 24 is similar to that in cycle 23 (Figure 4.2d). All CIR-associated storms peak around 2000 (cycle 23) and around 2011 (cycle 24). The peak of CME storms in solar cycle 23 matches with the SSN peak. Echer et al. [2013] observed two different peaks in the storm occurrence rate during solar cycle 23, one in 2001 and other during 2003 - 2005. The first peak during the solar maximum phase and the second one is in the declining phase of the cycle. Our peak matches with Echer et al. [2013] when source region of the moderate storms are not separated.

4.3 Comparison of solar source , interplanetary parameters, magnetopheric response of moderate storms

4.3.1 Dst value and source location distribution

Figure 4.3 shows that the distribution of Dst in moderate storms is narrower in solar cycle 24 than in cycle 23. Most (68 %) of the moderate storms in solar cycle 24 had Dst in the range of -50 nT to -75 nT. The average Dst values for the two cycles is comparable (-70 nT), though there is nearly 40 % reduction is observed in number of events, the average values are same. Since we considered only moderate storms, we do not expect much change in the average Dst values. To verify whether there is significant difference in Dst distribution for solar cycle 23 and 24, we have used Kolmogorov-Smirnov (KS) test (http://www.physics.csbsju.edu/stats/KS-test.html). The KS test gives 95% confidence interval for the actual means. Based on the number of data points the KS statistic critical D value varies, which is the maximum difference between the cumulative distributions of two data sets. The critical values are D_c= 0.168 (for 63 events in cycle 23) and D_c= 0.210 (for 41 events in cycle 24). The KS statistical test results are given in Table 4.2. The resulting D value, 0.1178, is less than Dc indicating that the distributions are similar. The 95% confidence intervals of the means overlap (-73.33 and -66.87 nT for cycle 23 and -73.15 and -65.65 nT for cycle 24), again suggesting no significant difference between the distributions.

The solar source location of a CME plays a considerable role in deciding its geoeffectiveness. CMEs occurring near to the disk centre are most likely to hit the Earth directly and cause storms [Gopalswamy et al., 2007]. Gopalswamy et al. [2007] reported that the majority of 378 front side halo CMEs were geoeffective and the geoeffectiveness decreased for CME source locations farther from the disk center.

Figure 4.4 shows the CME source locations in heliospheric coordinates for the storms considered here. The moderate storms are differentiated using small (-50 to -75 nT) and large (-75 to

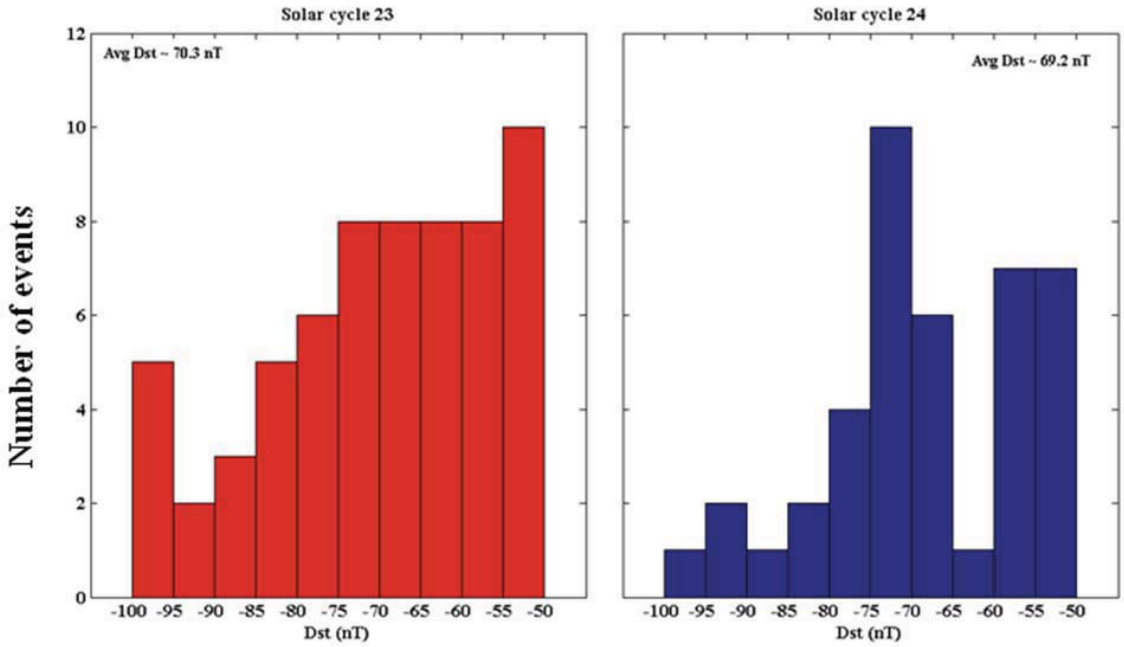

Figure 4.3: Distribution of Dst value for moderate storm occurred during SC 23 and 24.

-100 nT) circles. The two solar cycles are differentiated by the colour of the circles. We determined the average Dst value for the disk CME (central meridian (CMD) within 30 degrees) and non-disk CMEs (CMD $>$ 30 degrees). The averages are -72.4 nT for disk and 67.4 nT for non-disk CMEs in cycle 23; for cycle 24 they are -67.5 nT and -72.9 nT, respectively. These values do not show significant variation. Thus, moderate storms did not show any center-to-limb variation in the geoeffectivness of CMEs. The average speed of limb CMEs is observed to be 1100 km/s whereas the non limb CMEs average speed is 670 km/s in the sky plane. Although projection effects are expected, it appears that limb CMEs with higher CME speed are required to produce moderate storms.

Table 4.2: KS test result for moderate storm in SC 23 and 24

	Solar cycle 23 (n=63)			Solar cycle 24 (n=41)			
Parameters	Mean	Median	Confidence intervals	Mean	Median	Confidence intervals	D
Dst	-70.31	-68	-73.77 to -66.8	-70.32	-69	-73.15 to -65.6	0.1178
CME speed	716.3	562	602 to 830.4	668.8	561	538.1 to 799.5	0.11
Bz	-13.3	-12.52	-14.1 to -12.24	-12.44	-12.0	-13.6 to -11.6	0.288
VBz	-5822	-5201	-6406 to -5238	-5490	-5180	-6001 to -4979	0.08

4.3.2 CME speed, width, and mass distributions

Most of the geoeffective CMEs are halos; they mostly originate from close to the disk centre. Out of the 63 storms in cycle 23, 32 (50.7 %) are due to halo CMEs; in solar cycle 24 is 20 out of 41 (or 48.7 %) are due to halos. The fraction of halo CMEs in the two cycles are similar. The occurrence rate of all halo CMEs in cycles 23 and 24 are also similar [Gopalswamy et al., 2014; Gopalswamy et al., 2015 a,b]. The average CME speed for cycle-23 storms is 716 km/s compared to 671 km/s in cycle 24 (see Figure 4.5). Thus there is only a 5 % decrease in the average CME speeds; the difference is within the measurement errors. The CME speed distribution slightly broader in cycle 23: nearly 60% of the speeds are in the range of 300-900 km/s. The spread is narrower in cycle 24: 75% of the CME speed values are in the range of 300-700 km/s. The maximum CME speed is 2700 km/s (cycle 23) and 2300 km/s (cycle 24) and both are halo CMEs. The 95% confidence intervals of the means obtained from the KS test overlapped (602 to 830 km/s in cycle 23 and 538 to 800 km/s in cycle 24), indicating no statistically insignificant differences in CME speeds between the two cycles. Gopalswamy et al. [2014] reported a decrease

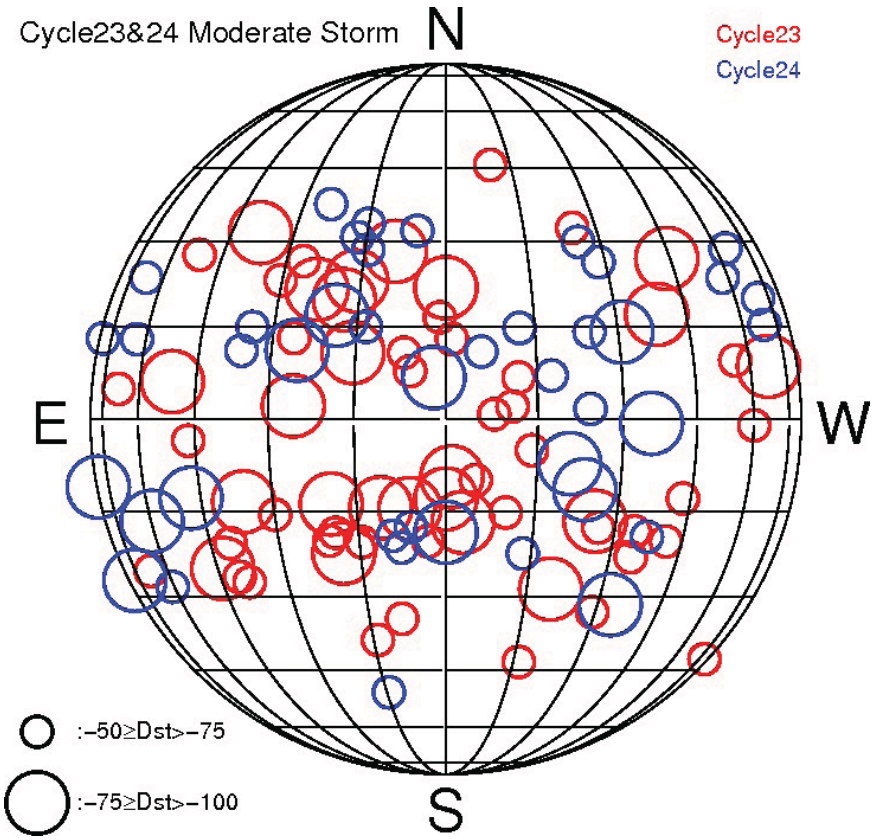

Figure 4.4: Solar source location of moderate storms occurred during SC 23 and 24. The size difference in the circle indicates the strength of the Dst produced and the range is mentioned in the figure. Red colour indicates the source location of SC 23 and blue denotes the cycle 24.

of 15% and 17% in MC and shock speeds respectively, but the white light observations do not show any such change in average CME speeds for both the cycles.

We now consider the mass and width of CMEs and the mass estimates are accurate to within a factor of 2. The disk-centre CME widths are likely to be affected by projection effects. Figure 4.6 shows the width distribution of CMEs associated with moderate storms in the two cycles. Halo CMEs represent the tallest bar in both the cycles. Excluding the halo CMEs, the average width is estimated to be 122° for solar cycle 23 and 141° for SC 24. The non-halo CME widths are consistent with the anomalous expansion of CME during cycle 24 when compared to the CME for cycle 23. But when the halo CMEs are included the average widths are similar (245°). Gopalswamy

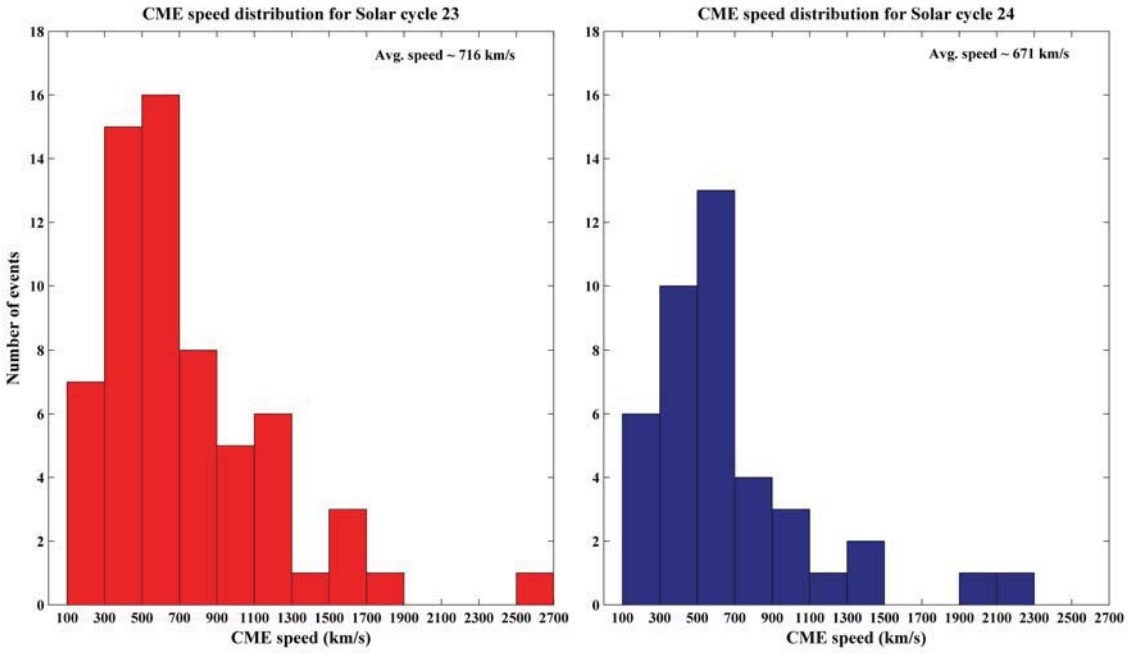

Figure 4.5: CME speed for moderate storm occurred during SC 23 and 24.

et al. [2014, 2015a,b] found an average width of 82.5° for cycle 23 compared to 98.1° for cycle 24 excluding halo CMEs, and observed 93.4° for cycle 23 and 133.5° for solar cycle 24 when included. They reported an anomalous expansion of CME for cycle 24 when compared to solar cycle 23 for same CME speed but the criteria is different in their work, only limb CMEs are considered along with that CMEs associated with solar flare c3 or larger. Limb CMEs are free from projection effect but the moderate storms are mainly from the disk centre and are subject to projection effects. Figure 4.7 gives the distribution of CME masses for the two cycles. There are a few events in both the cycles for which the mass could not be measured using LASCO or STEREO and hence are excluded from the CME mass distribution. The average mass of CMEs associated with moderate storms in solar cycle 23 is 8.24 x 10^{15} g and 7.4 x10^{15} g in cycle 24. Given the uncertainty in mass measurements, these values are not significantly different. The mass of limb CMEs during first 62 months of solar cycle 24 is decreased by a factor of 3 when compared to solar cycle 23 [Gopalswamy et al ., 2015b]. Also the average CME mass during the whole of cycle 23 was found to be greater than that in cycle 24 [Gopalswamy et al., 2010a; Vourlidas et al., 2011]. But CMEs

associated with moderate storms do not show much variation in mass.

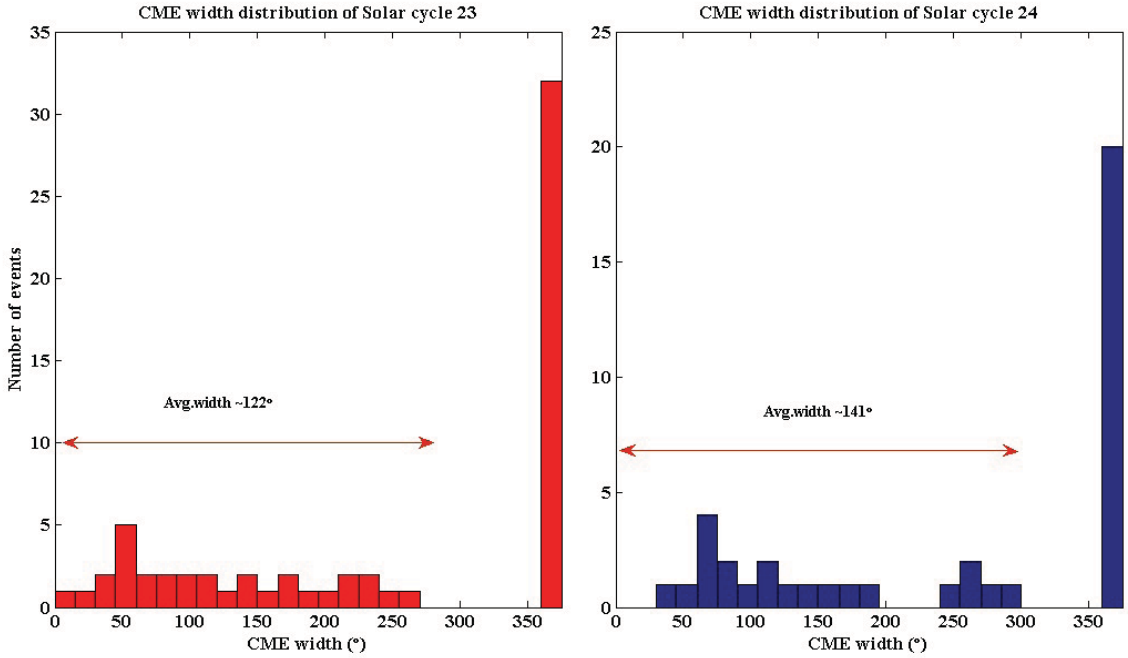

Figure 4.6: Distribution of CME width of moderate storm occurred during SC 23 and 24.

4.3.3 Interplanetary and magnetospheric response

The main relation between CMEs and geomagnetic storms owes to the presence of negative Bz component of interplanetary magnetic field [Gonzalez et al., 1994; Zhang et al., 2007; Gopalswamy, 2008; Echer et al., 2008a, 2008b, 2013; Cid et al., 2012]. The negative Bz is not only found in CME flux ropes (Wilson, 1987), but also in the compressed sheath region between the flux rope and the shock [Tsurutani et al., 1988; Veendhari et al., 2012]. The strength of a geomagnetic storm is proportional to the product VBz, where V is the speed of the solar wind structure causing the storm. In addition to this, the ring current injection rate depends on VBz along with the negative Bz duration and shock speed [Balan et al., 2014; Sandeep et al., 2015]. Since these two factors determine the geoeffectiveness, it is necessary to compare minimum Bz and VBz between the cycles. At 1 AU, ICMEs can be differentiated as MC, non-magnetic cloud or EJ and sheath

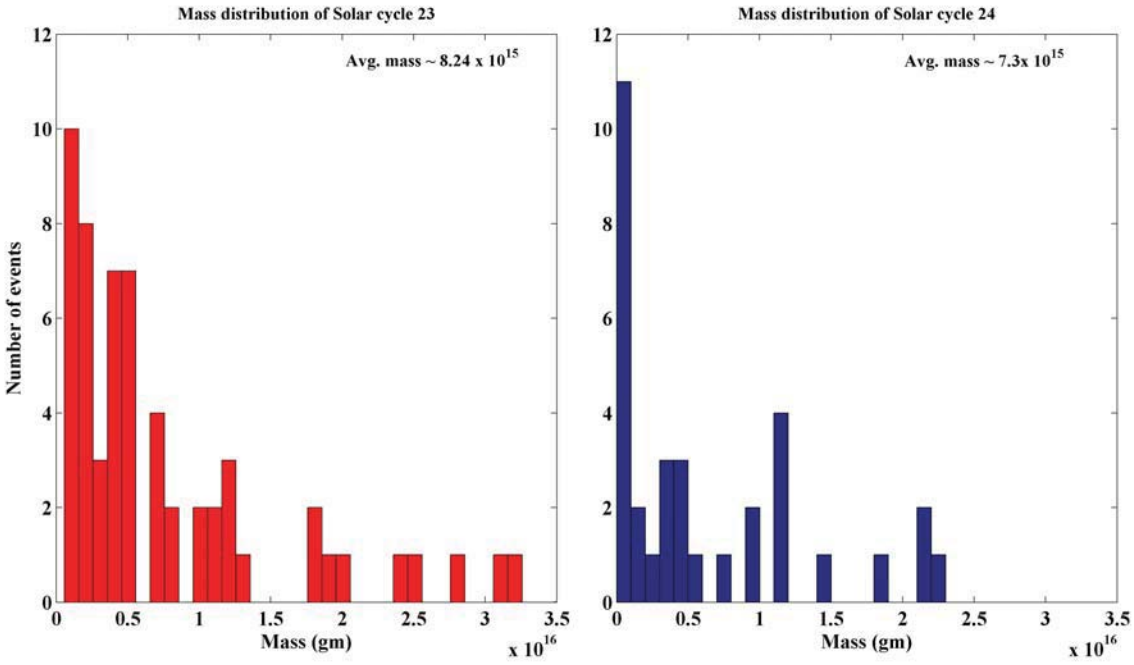

Figure 4.7: Distribution of CME mass of moderate storm occurred during SC 23 and 24.

based on the magnetic structure. In cycle 23, 26.9 % storms are caused by MC, 49.2 % by EJ and 16% by sheath. Majority of the moderate storms are from non-magnetic cloud in cycle 23. In cycle 24, the 41% of storms are caused by MCs, 38 % by EJs and 21% by sheaths. The average Dst values for MC-associated moderate storms is 73 nT in cycle 23 and 65 nT for cycle 24. Although we restricted to a narrow range of Dst values, the results are in agreement with Gopalswamy et al. [2015b].

Figure 4.9 shows the distribution of minimum Bz and VBz values for the storms in cycle 23 and 24. One moderate storm is not included in this statistics due to a OMNI data gap (10 November 2014). The Bz and VBz values are taken from the region responsible for the Dst minimum, irrespective of MC, EJ or sheath. The distribution of minimum Bz is longer in cycle 23 than that in cycle 24. The largest negative Bz observed is -30 nT and -20 nT for solar cycles 23 and 24, respectively. The smallest negative Bz is -7 nT for both the cycles. The average Bz values are -13.2 nT in cycle 23 and -12.5 nT in cycle 24. A difference of 0.7 nT is not significant. The right

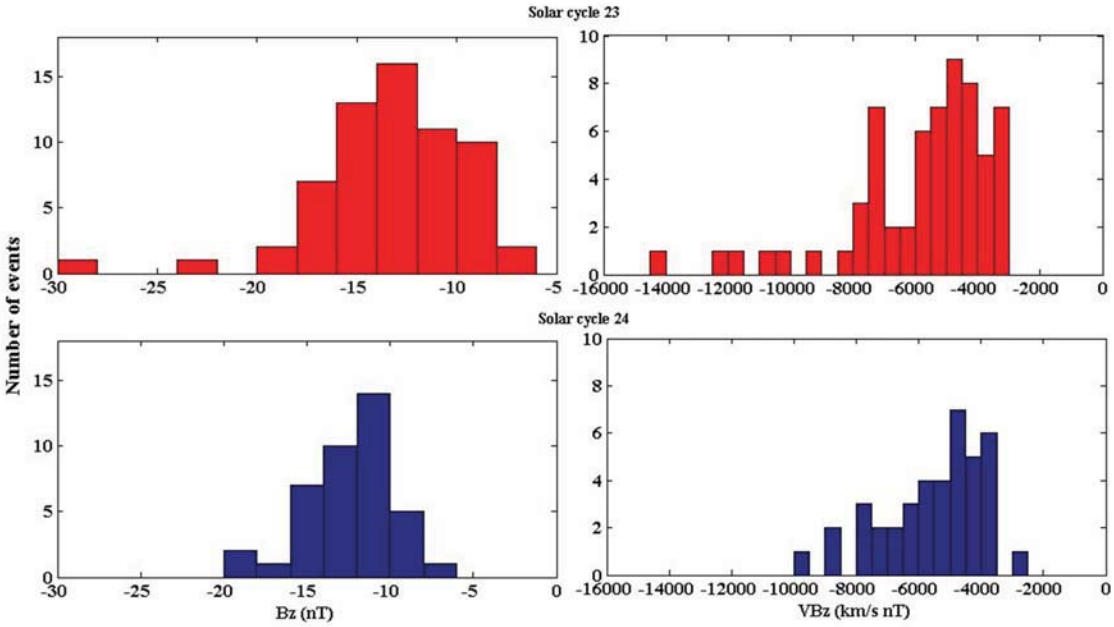

Figure 4.8: Distribution of Bz and VBz for SC 23 and 24 with respect to moderate storms.

side panel of Figure 4.8 shows the distribution of computed VBz for the storms. The largest negative value for cycle 23 is -14082 km/s nT and it is -9543 km/s nT for cycle 24. The average VBz values in solar cycle 23 and 24 are -5822 km/s nT and -5890 km/s nT respectively. These small variations are not significant. The KS test again shows overlap in the 95 % confidence intervals for both Bz and VBz. Gopalswamy et al. [2015a] observed a declination of 51% and 40% in average VBz with sheath and MC for solar cycle 24 when compared to 23 but in our work restriction of storm intensity (Dst) to a narrow range is expected to restrict the range of VBz (and Bz) to similar values. In Gopalswamy et al. [2014, 2015a] revealed the reduction in geoeffectiveness while considering total geoeffective CMEs. In the moderate storm case, the only indicator of reduced geoeffectiveness is the smaller number of moderate storms.

In order to see whether the Dst-VBz relation holds for moderate storms, Dst is plotted against VBz in Figure 4.9. The plot shows a linear variation with negative slopes for both the cycles. The correlation is found to be moderate with value of 0.68 for cycle 23 and 0.61 for cycle 24. Thus the Dst - VBz correlation did not change much. This means the storm process of converting solar

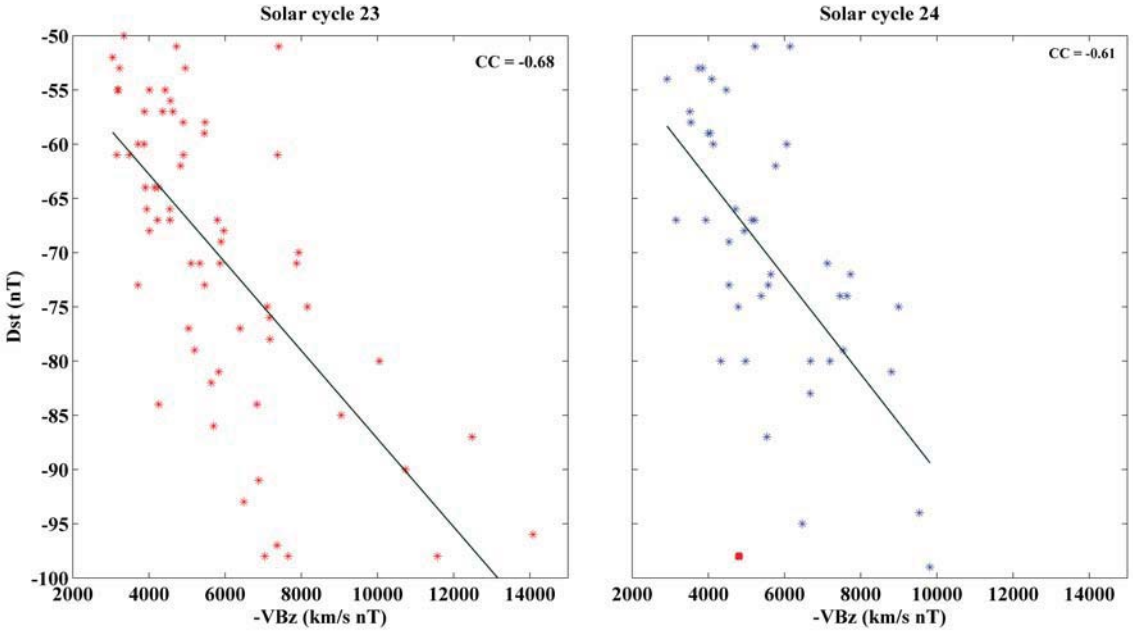

Figure 4.9: Correlation between Dst and VBz for SC 23 and 24.

wind energy to ring current energy did not change which is consistent with Gopalswamy et al. [2015a]. This correlation is statistically significant and it is double the critical value of Pearson's correlation coefficient (for P = 0.05). The plot shows a few outliers in cycle 23 and a little more for cycle 24; this might be because the storm source is not differentiated among sheath, magnetic cloud, and non-magnetic cloud that caused the Dst. In solar cycle 24 there was an extreme outlier due to the 29 June 2013 storm with a Dst of -98 nT with Bz -12.28 nT. In order to understand this discrepancy we examined the case separately. It was found that at 1 AU the CME was followed by an HSS with negative Bz, which made it last longer and resulted in a larger Dst magnitude.

In order to investigate the magnetopsheric response during moderate storms, we performed a superposed epoch analysis of Dst and the associated Interplanetary electric field (IEFy) for all the moderate storms that occurred during cycles 23 and 24. The results are shown in Figure 4.10(a,b). The time 0 hours (black line) in the figure indicates the main phase onset of all the moderate storms and the dark blue line refers to the average Dst and IEFy. Figure 4.10c shows the average plot of Dst and IEFy obtained from the superposed epoch analysis. We see that the average minimum Dst

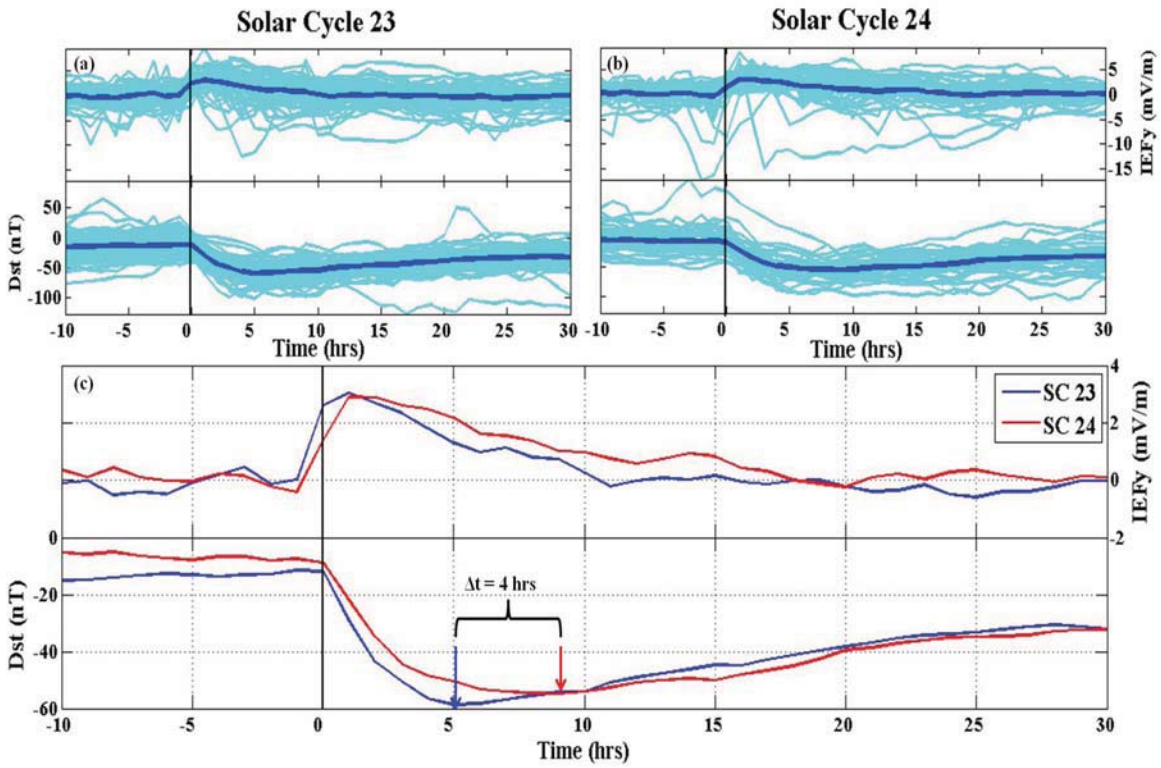

Figure 4.10: Superposed epoch plot of moderate storm Dst along with interplanetary electric field. (a) Solar cycle 23 (b) Solar cycle 24 and (c) Average values of cycle 23 and 24.

stands out to be -58.7 nT for cycle 23 and -54.9 nT for cycle 24 with a difference of 3.7 nT. The IEFy did not show much variation in their average values. The average time taken by the moderate storm to reach minimum Dst is less by 4 hours for cycle 23 when compared to cycle 24. This delay suggests that although the average IEFy is similar, the response of the magnetosphere and the rate of ring current injection is rapid for cycle 23. This observation can be confirmed by evaluating the total energy injected in to the magnetosphere for the two cycles. In order to check the response of magnetosphere, ε is estimated for the main phase of all moderate storms.

$$\varepsilon = vB^2 Sin^4(\frac{\theta}{2}) R_{CF}^2 \tag{4.1}$$

where v is the upstream solar wind speed, B the magnitude of the IMF, θ is the clock angle of

IMF which is determined based on B_z values

For $B_z < 0$

$$\theta = \tan^{-1}(\frac{|B_y|}{|B_z|}) \tag{4.2}$$

For $B_z > 0$

$$\theta = 180 - \tan^{-1}(\frac{|B_y|}{|B_z|}) \tag{4.3}$$

R_{CF} is determined by the below equation.

$$R_{CF} = (\frac{B_0^2}{4\pi\rho v^2})^{\frac{1}{6}} R_E \tag{4.4}$$

where B_0 is the magnetic field strength on the surface of the Earth equator.

ε gives the total energy transferred to the magnetosphere during the solar wind interaction [Perrault and Akasofu, 1978; Nishida, 1983]. R_{cf} is the distance at which the balance between solar wind kinetic plasma pressure and the magnetospheric magnetic pressure is obtained. We determined R_{cf} (equation 4.4) for all the moderate storms during the main phase and used it to estimate ε from equation 4.1 [Holzer and Slavin, 1979; Sibeck et al., 1991]. Figure 4.11 shows the energy transfer during moderate storms as a function of VBz for cycle 23 (blue) and 24 (red). Three events are excluded in solar cycle 23 due to unavailability of By required for calculating ϵ. The ϵ is estimated to be 1.83 x 10^{12} W for cycle 23 and 9.93 x 10^{11} W for cycle 24. So the average energy transfer is larger by 9.05 x 10^{11} W for cycle 23 than in cycle 24. Though VBz is the same for the moderate storms the energy transfer is different. The difference in the energy transfer has led to main cause for delay in the minimum Dst during solar cycle 24 and a rapid main phase is observed in ε cycle 23.

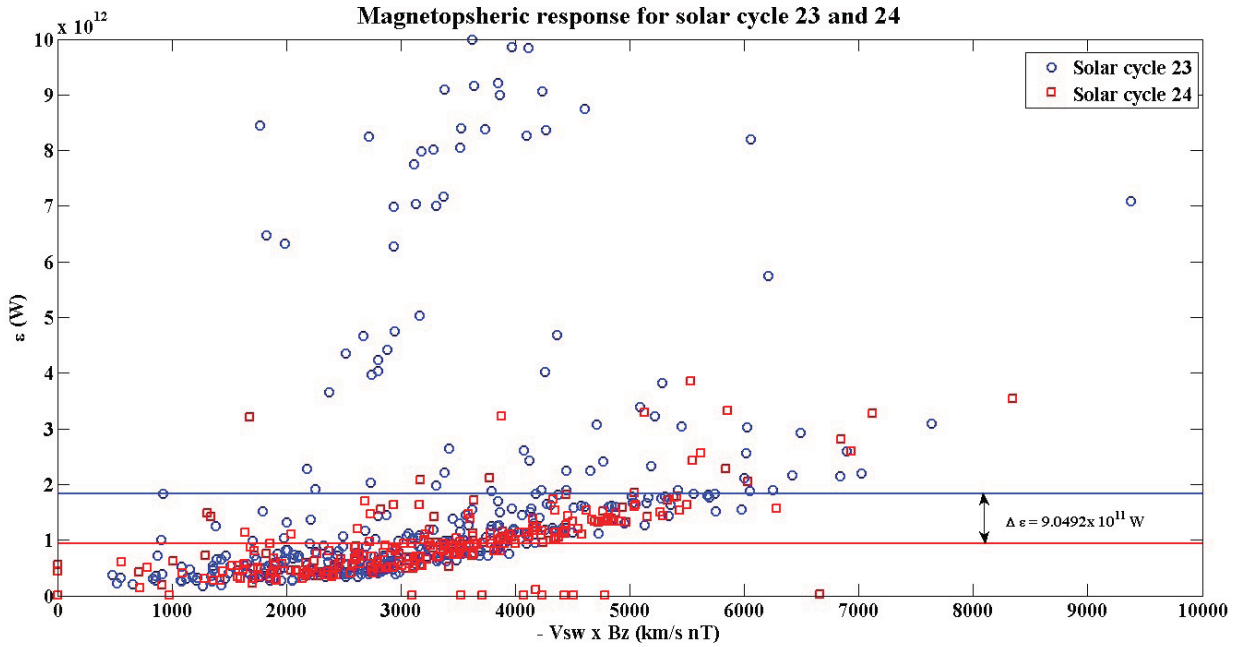

Figure 4.11: The variation of ε with VBz for solar cycle 23 and 24. Blue circle indicates cycle 23 and red square for cycle 24.

4.4 Discussion

We compared the characteristics and sources of moderate storms between cycles 23 and 24. The first study about the interplanetary association of moderate storms is carried out by Tsurutani and Gonzalez [1997]. They studied the moderate storms occurred in solar maximum (1978-1979) of solar cycle 21 and reported that 40% of the storms were associated with ICME and remaining are due to HSS, CIR and some phenomena related to Alfvenic fluctuations. Similarly Xu et al. [2009] made a statistical study on the identification of interplanetary structure of moderate storms occurred during the period of 1998-2008 and found that nearly 51 % of the moderate storms are due to by ICMEs. This result is similar to our result that 68.2 % of moderate storms are caused by ICMEs in cycle 23. The difference is clearly due to the consideration of different study periods, especially different phases of solar cycle.

Echer et al. [2013] found two peaks in the occurrence rate during the solar maximum and declining phases. Our results are consistent with this when the corresponding epochs are compared. They also reported that the CIR/ HSS were the dominant source of moderate storms in the whole of cycle 23 which is opposite to our result. This discrepancy is attributed to the fact that Echer et al. [2013] included the declining phase of the solar cycle in which more CIR/HSS storms are known to occur. Our study does not include the declining phase. Gopalswamy et al. [2014] showed that the anomalous expansion diminished the magnetic content of CMEs in cycle 24, which in turn led to the reduction of large geomagnetic storms. Our result of 75% reduction agrees well with this in case of intense storms although the moderate storms are reduced only by 40%. Since CME width is proportional to the speed, CMEs producing major storms probably have a larger dilution of the CME magnetic content because they are faster. The number of halo CMEs among those causing moderate storms is similar in the cycle in agreement with Gopalswamy et al. [2015a].

Gopalswamy et al. [2015b] observed a cycle-23 to cycle-24 reduction of the Dst index associated to MCs: from -66 nT to -33 nT in the sheath portion and from -55 nT to -23 nT in the cloud portion. They estimated the reduction in geoeffectiveness by considering Dst values associated with the sheath and cloud portions. In our study we have considered MCs, non-MC as well as their sheaths. Furthermore, we restricted the range of Dst, unlike Gopalswamy et al. [2015a]. These considerations reduced the difference between the two cycles. When MC-associated moderate storms are considered, there is a reduction in the average Dst values. . The average mass of CMEs associated with moderate storms also did not show much variation between the two cycles. Whereas Gopalswamy et al. [2015a] found a reduction of CME mass by factor 3 in limb CMEs in solar cycle 24 when compared to cycle 23, it was not found in CMEs causing moderate storms. This is likely to be due to the fact that the CMEs associated with moderate storms are mostly disk events, for which the mass estimate is difficult. Gopalswamy et al. [2015b] also reported that CMEs had the same average speed in two cycles but not the width: a 33° increase in CME width was found for non-halo limb CMEs in cycle 24. We found a change of 18° but the average width did not show much change when halo CMEs are included. Again, the main difference is that our CMEs are subject to projection effects because they are mostly disk events, whereas Gopalswamy

et al. [2015a] considered strictly limb events. We observed that limb CMEs with higher speeds are important to produce the moderate storms. But, as the limb CMEs have undergone anomalous expansion in cycle 24 (CMEs with flare C3 or greater) [Gopalswamy et al. 2014], they could not produce moderate storms even with higher CME speeds.

The empirical relationship between Dst and VBz for interplanetary magnetic structures causing storms [Wu and Lepping, 2002; Gopalswamy, 2010a]. Gopalswamy et al. [2015a] obtained high correlation between Dst and VBz for MCs in both cycles: correlation coefficients of 0.76 and 0.77 for the sheath and cloud portions in cycle 23 and 0.73 and 0.86 for cycle 24. We obtained moderate correlation between VBz and Dst of 0.68 and 0.61 for solar cycle 23 and 24. The moderate correlation is due to the fact we have included many storms driven by EJ and sheath portions of ICME. Echer et al .[2008] have obtained the best correlation for solar cycle-23 intense storms: 0.80 for Dst-Bs, 0.84 for Dst-Ey (where Ey is electric field) and 0.55 for Dst-Vsw (where Vsw is solar wind speed). For moderate storms, Echer et al. [2013] found a correlation coefficient of 0.55 between Ey and Dst, 0.48 between Bs and Dst and negligible correlation between Vsw and Dst. We obtained a better correlation because of the fact that we have considered only CME driven storms in which most of the cases have stable negative Bz and VBz. The transfer of energy in to the magnetosphere is less for cycle 23 than in cycle 24. As solar cycle 23 has undergone a long solar minimum, the background interplanetary condition in the cycle 24 has been low [Kalegaev et al., 2014] similar to the weak heliospheric conditions. As a result, the rate of magnetopsheric energy transfer and response of their current system is less for cycle 24 than the typical response in cycle 23 with the same interplanetary input. The CME with the optimum energy input which produced moderate storm in cycle 23 could not able produce the same in cycle 24. So apart from the anomalous expansion of CMEs the energy distribution in to the magnetosphere also played a major role in the reduction of moderate storms in solar cycle 24.

4.5 Conclusion

We investigated the solar source and the interplanetary characteristics of moderate geomagnetic storms that occurred during the first 77 months of solar cycles 23 and 24. We find that the distribution of CME speed and average mass is almost the same in both the cycles whereas slight variation was observed in average width of non-halo CMEs. The Dst values of moderate storms did not show considerable change with the source location of the CMEs in the two cycles. The minimum Bz values showed a wider distribution in cycle 23 when compared to cycle 24. From the statistical analysis, we find that moderate storms did not show much change when compared to cycle 23. This is because the restricted Dst range restricts the range of VBz. The reduced geoeffectiveness in cycle 24 is mainly due to the decrease in the intense storms and to a smaller extent in the number of moderate storms, which is the resultant of anomalous CME expansion and less magnetopsheric energy transfer in cycle 24. The main conclusions are

1) A total of 166 geomagnetic storms are identified during the first 77 months of solar cycles 23 and 67 in cycle 24 over the same epoch. The number of moderate storms are 111 and 55 in cycles 23 and 24, respectively. Solar cycle 24 has shown nearly 80$\%$ reduction in the occurrence of intense storms where as it is only 40 $\%$ in the case of moderate storms.

2) The occurrence of moderate storms approximately follows the SSN and peaks around the solar maximum for both the cycles.

3)Average CME speed and Dst values do not show much variation in the two cycles. Similarly, average CME mass did not show much variation whereas the CME width has shown a slight variation for non-halo CMEs when compared to cycle 23.

4) The correlation between VBz and Dst is found to be the highest with values of 0.68 for cycle 23 and 0.61 for cycle 24.

5) The magnetopsheric energy transfer decreased in solar cycle 24 with respect to that in cycle 23.

Chapter 5

The role of interplanetary shock orientation on SC/SI rise time and geoeffectiveness

5.1 Introduction

The plasma approaching from the Sun can cause disturbance in the Earth′s magnetic field which accounts for increase in the magnetic field [Chapman and Ferraro 1931, 1940], but the hydromagnetic (HM) aspects of magnetic disturbance were not dealt as the interplanetary space was considered to be vacuum. Later Hines, [1957] pointed out the importance of HM waves in the propagation of magnetic disturbance. This plasma in later 1970's termed as Coronal mass ejections (CMEs) [Tousey, 1973; MacQueenet al., 1974] which move through the heliosphere at speeds much greater than the sound speed in the surrounding interplanetary medium. As they are often supersonic, they give rise to collisionless shocks ahead of the CME structures, which are called as Interplanetary (IP) shocks. The magnetic field and plasma at the shock front gives rise to a forward shock which can easily be identified by a sudden increase in magnetic field strength, solar wind plasma density and temperature. The IP shocks approaches Earth resulting in the compression of the Earth′s magnetosphere and are associated with the sudden change in the

dynamic pressure resulting in the Earthward motion of the Chapman-Ferraro current. The change in this current is observed in ground based magnetic observatories as increase in Horizontal (H) component of geomagnetic field [Desseler et al ., 1968]. The sudden increase in the amplitude of the H component of geomagnetic field due to the shock is referred as sudden commencement (SC) or sudden impulse (SI) [Yokouchi, 1953, Desseler et al., 1960, Maeda et al., 1962, Araki., 1994, Tsunomura., 1998].

SC rise time is defined as the time between the onset of the SC and the maximum of the H-component magnetic field [Yokouchi, 1953, Maeda et al., 1962, Desseler et al., 1960, Araki et al., 2003]. It ranges from 2-10 minutes centered around 4 minutes. Yokouchi, [1953] first analyzed SC rise time observed at Kakioka for the period 1924-1951 and concluded that average SC rise time shows the diurnal variation. **It is well known that SC/SI amplitude depends on the solar wind dynamic pressure composed of the solar wind density as well as the solar wind speed. But the change in dynamic pressure basically decides the change in SC/SI amplitude not the rate at which SC/SI changes. Wang et al. [2010] derived the empirical relation between changes in SYM H with the square root of the solar wind dynamic pressure across an IP shock**. Nishida [1966] reasoned out different aspects that may determine the SC rise time; likely thickness of the shock and time taken by the interplanetary shock to sweep the geoeffective distance along the magnetosphere, difference in travel time of HM waves, and magnetospheric inertia. Along with all other factors mentioned by Nishida [1966] the IP shock orientation plays a major role in determining the rise time of the SC amplitude. **So basically, increase in the solar wind density depends on how fast the dynamic pressure changes and this in turn depends on the above factors mentioned by Nishida [1996] and IP shock orientation angle.** IP shock orientation angle is the angle between the shock normal and the Geomagnetic Solar Ecliptic (GSE) X-axis which points toward the Sun.

Several authors worked on the relationship between SC amplitude and rise time [Yokouchi, 1953; Dessler et al., 1960; Chapman and Bartels, 1962; Ondoh, 1963; Pisharoty and Srivastava, 1962; Nishida, 1964, 1966; Burlaga, 1970; Mayaud, 1975]. They concluded that the rise time

depends more on the time taken by the IP shock to sweep the geoeffective distance through the magnetosphere which in turn depends on the orientation angle of IP shocks. Takeuchi and Russell [2002] studied anomalous SC rise time of 30 minutes and concluded that orientation of shocks is one of most important factors determining it. The high inclination of IP shock impact resulted in the gradual compression and slow response in the magnetosphere resulted in longer rise time [Takeuchi and Russell, 2002]. Followed by them Cheng et al. [2005], reported that evolution processes of the IP shocks through the magnetosphere are remarkably different for two shocks of different orientations. In the same year, Wang et al. [2005] reported that, highly oblique shock requires more time to compress the forward part of the magnetosphere by analysing a case study of a SC. Later, Wang et al., [2006] made a statistical study of 225 IP shocks occurred between 1995 and 2004 and observed that the SC/SI rise time for the IP shocks with similar orientations and higher IP shock speeds is shorter. They also concluded that bigger the angle between the IP shock normal and the Sun-Earth line, the shorter is the rise time. Recently, Oliveira and Raeder., [2015] studied the IP shocks observed at 1 AU occurred from January 1995 to December 2013 and used open Global Geospace Circulation Model (GGCM) MHD code to simulate impact of three shocks with different inclinations in to the magnetosphere and concluded that the head on shocks are more geoefffective than the inclined shocks.

All the above mentioned works are based on IP shocks as observed in the solar wind near Earth, irrespective of their source without considering the IP medium and type of IP shock. In the present study, we tried to analyze SC/SI rise time by considering the details of IP shock types and associated counterpart of ICMEs. It is important to note that the IP shocks undergo considerable changes during their evolution in the interplanetary medium. By observing the CME, the early warning of IP shocks are predictable before arrival and the radio emission from CME is the earliest indicators of shocks and contains information on both the shock and the ambient medium in which shock propagates [Gopalswamy et al ., 2010, referred as Paper1]. Shocks near the Sun are inferred from type II radio bursts in the solar corona and IP medium, which produce type II radio burst are said to be radio loud (RL) and those which do not produce type II burst are said to be radio quiet (RQ) and associated CMEs are said to be RL CMEs and those followed by the IP shocks are said

to be RL IP shocks, or simply RL shocks. Similarly, there are RQ CMEs and RQ IP shocks (or simply RQ shocks). The other major classification in the CME arriving at the Earth can be referred as magnetic cloud (MC) or noncloud ejecta (EJ). Veenadhari et al [2012] studied the importance of radio characteristics and ICME structure classification in determining the SC/SI amplitude, and their dependence on RL shocks and RQ shocks, associated CMEs. It is observed that average SC/SI amplitudes for RL shocks are more when compared to RQ shocks and IP shock speed is better correlated with SC/SI amplitude for RL shocks. They focused only the importance of radio characteristics and ICME structure in the determination of SC/SIs amplitude. They have not considered the SC/SI rise time in dependence with IP shock orientation. The radio characteristics and ICME structure not only play major role in determining the amplitude of SC/SIs but also on the rise time along with the orientation angle.

The main motivation behind the present work is to establish the importance of radio characteristic of CME and ICME structure along with IP shock orientation angle in determining SC/SI rise time as well as geoeffectiveness. Using the larger data set (solar cycle 23) an attempt has been made to examine the importance of orientation angle along with all known factor about IP shocks like speed and its classifications based on radio emission and ICME magnetic structures in determining the SC/SI rise time and geoeffectiveness. This is the first attempt to include radio characteristics and magnetic structure in determining the rise time. The list of IP shocks associated with CME during 1996 to 2006 compiled in paper 1 forms the basis for the present study, details of which is briefly given in section 5.2. The paper is divided in to two parts, first part deals with the importance of radio characteristics of IP shock associated with CME along with impact angle resulting in SC/SI rise time and second part deals with the confirmation of the statistical results using MHD simulations by considering different orientation angles.

5.2 Data

The list of IP shocks used in this work are identified using data from three spacecrafts, the Solar and Heliospheric Observatory (SOHO), the Advanced Composition Explorer (ACE), and Wind. The radio characteristics of CME are determined from the Plasma Wave Experiment [WAVES; Bougeret et al., 1995] on board Wind. Based on the radio observations, the IP shocks which lack in detectable type II radio emission are referred as radio quiet (RQ), similar to the criterion used by Gopalswamy et al. [2008](More details given in Paper 1). The IP shock details and radio characteristics are taken from paper 1. All this IP shocks are associated with Earth directed CMEs. The IP shock arrival time is matched with the time of SC/SI events which are obtained from geomagnetic data bulletins, published by Indian Institute of Geomagnetism (IIG), India. The IP shocks and related SC/SI amplitudes in H component and their timings are noted from the Alibag magnetic observatory (ABG, Geo.Lat.18.62; Geo.Long.72.87; Geomag. Lat.10.17). For each IP shocks which produced SC/SI, the shock orientation angle is calculated from the IP shock normal listed in Wang et al. (2006, 2010). They determined the IP shock normal by using Magnetic Coplanarity (MC), Velocity Coplanarity (VC), three Mixed methods (MX1, MX2, MX3) (Schwartz, 1998), and the Rankine-Hugoniot method [Berdichevsky et al., 2000] . The IP shock orientation angle ranges from 90° to 180°. When the angle between the Sun Earth line and the shock normal vector is 180° it is called as quasi perpendicular shock ie., the shock orientation is parallel to the magnetosphere. The IP shock orientation angle nearer to 90° is said to be quasi parallel shocks. We use the same terminology as used by Wang et al. [2006] for the classification IP shock orientation.

Figure 5.1 shows the percentage distribution of CME associated IP shocks resulted in SC/SI during solar cycle 23. Based on the IP shocks list from paper 1, 179 (80 $\%$) IP shocks resulted in SC/SI out of total 222 events during 1996-2006. Few events in which the shock normal couldn′t be estimated are neglected. Out of 179, 118 are identified to be RL events and remaining 61 to be RQ events. The type II radio bursts are more dominated when compared to other radio type bursts during solar cycle 23. CME driven IP shocks are more during the solar maximum and get reduced during the solar minimum as CME occurrence follows the solar cycle [Gopalswamy et al ., 2008].

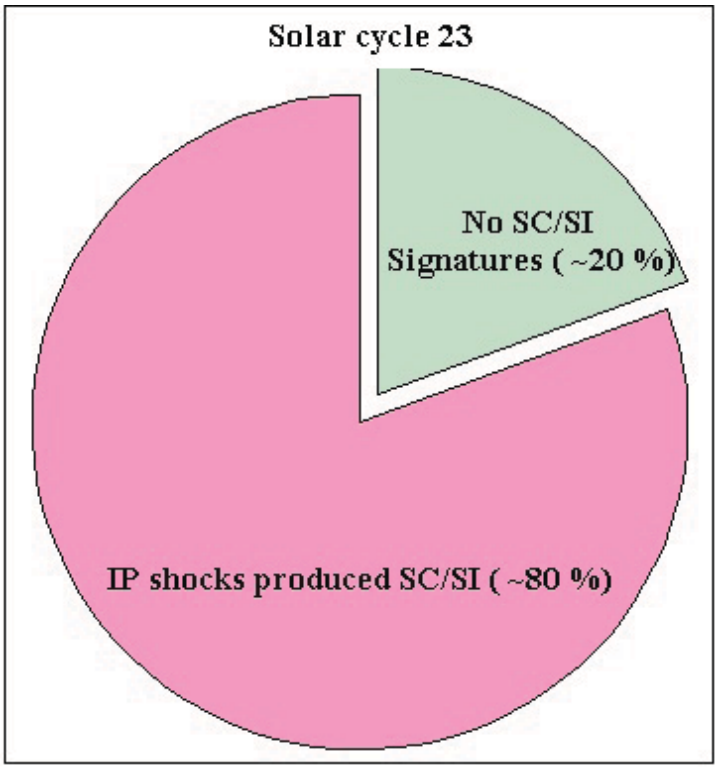

Figure 5.1: Distribution of CME driven IP shocks results in producing SC/SIs.

5.3 Analysis and Results

Figure 5.2(a,b) shows an example of a SC/SI event observed on 08 June 2000 and 04 April 2001 associated with the CMEs occurred on 06 June 2000 and 02 April 2001 respectively. The SC/SI event in figure 2a is driven by the IP shock speed of 868 km/s at L1 point. The speed of the CME associated with this IP shock observed at SOHO is 1119 km/s, which shows that CME is decelerated while travelling towards the L1 point from the Sun. Similarly, for the second event (Figure 5.2b) initial CME speed is estimated to be 2505 km/s but the speed at 1 AU of this IP shock shows that the CME underwent a large deceleration lead to 849 km/s during its journey towards the Earth. Because of this high deceleration the CME speed went down to one third of the original speed of the CME. As the CME undergoes a variable change during its propagation, it is necessary to consider the radio characteristics of CME which gives the initial information about CME. It can

be clearly seen that SC/SI rise time is different for both the events, the first event showed a rise time of 3 minutes (Figure 5.2a) whereas the next event showed a rise time of 7 minutes (Figure 5.2b). Though both the events are produced by IP shock of approximately same speed the rise time are different due to the fact that IP shock orientation angles are different for both the events. As the CME undergoes a variable change during its propagation, it is necessary to consider the radio characteristics of CME which gives the initial information about CME.

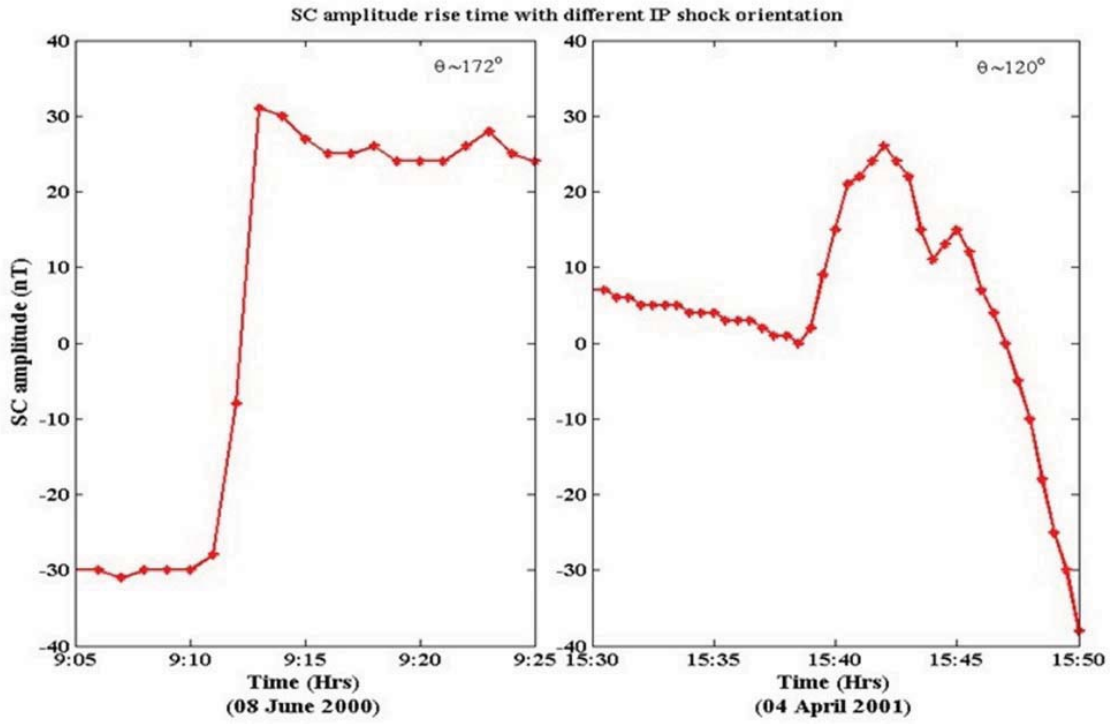

Figure 5.2: (a,b) Example showing the SC/SI rise time with the impingement of IP shock at the magnetopause for different IP shock orientation angle.

Figure 5.3 (a-c) shows the distribution of IP shock orientation angle for all, RL events and RQ events. Nearly 70 % of IP shock orientation is observed in the range of 130° to 160° in all the three categories. The average orientation angle is observed to be 145° for all the three cases. Nearly 18 % of the RL shocks are observed to be quasi perpendicular whereas the percentage occurrence for the RQ shocks is comparatively half (8%). IP shocks driven by CME from the disc centre

most probably should result in quasi perpendicular since they are almost aligned in the Sun-Earth line unless it is deviated by corotating interaction regions (CIRs) [Siscoe., 1976; Raeder., 2003; Gopalswamy et al ., 2007]. Though there are less number of quasi perpendicular shocks, they are more geoeffective in the evolution through the magnetosphere when compared to the quasi parallel shocks. This is due to the fact that sweeping of the magnetopause due to the quasi perpendicular shocks is symmetric and the impact is parallel [Wang et al., 2006, Oliveira et al ., 2015].

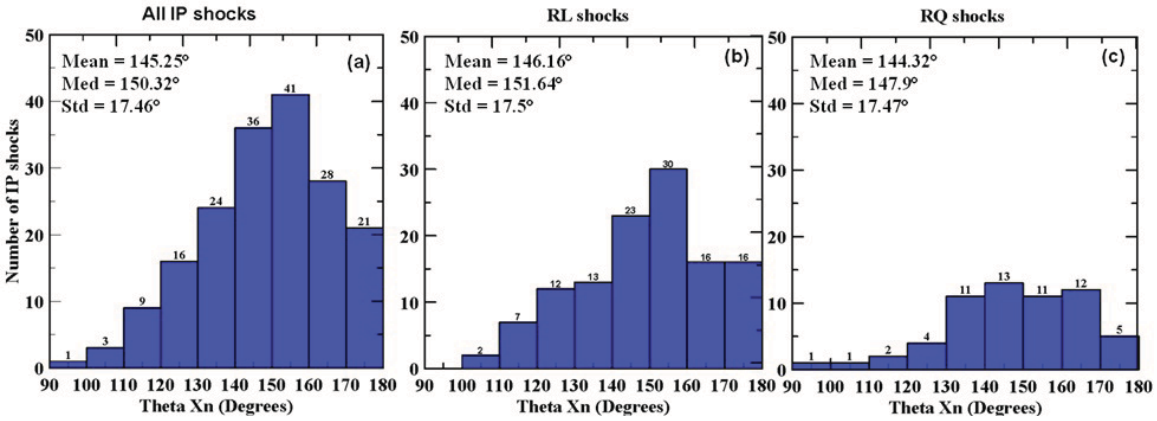

Figure 5.3: (a-c) Distribution of IP shock orientation angle for ALL, RL and RQ events.

The SC/SI rise time mainly depends on the evolution of the IP shock through the magnetopause. In order to check the overall trend of rise time with the IP shock orientation, the IP shock is divided in to three categories based on their orientation angles: (1) $<130^{\circ}$, nearly quasi parallel shocks (2) 130-150°, oblique angle shocks and (3) $>150^{\circ}$ nearly quasi perpendicular shocks. Figure 5.4 (a-c) shows the variation of SC/SI rise time with respect to IP shock speed for the three differently binned IP shock orientation angle. It is clear from the figure that the rise time decreases with the increase in the IP shock speed. The correlation coefficient (CC) is very less for the shocks $<130^{\circ}$ which is 0.35. And the CC for 130-150° and >150 are 0.5 and 0.65, respectively. Better correlation is obtained for nearly quasi perpendicular shocks (figure 5.4c). It is observed that less number of events are found for nearly quasi parallel, because higher latitude CME associated shocks results in nearly quasi parallel shocks [Gopalswamy et al ., 2008]. There is more possibility for higher latitude CME to miss reaching the Earth. It is clear from the trend that higher the IP

shock speed lesser the SC/SI rise time.

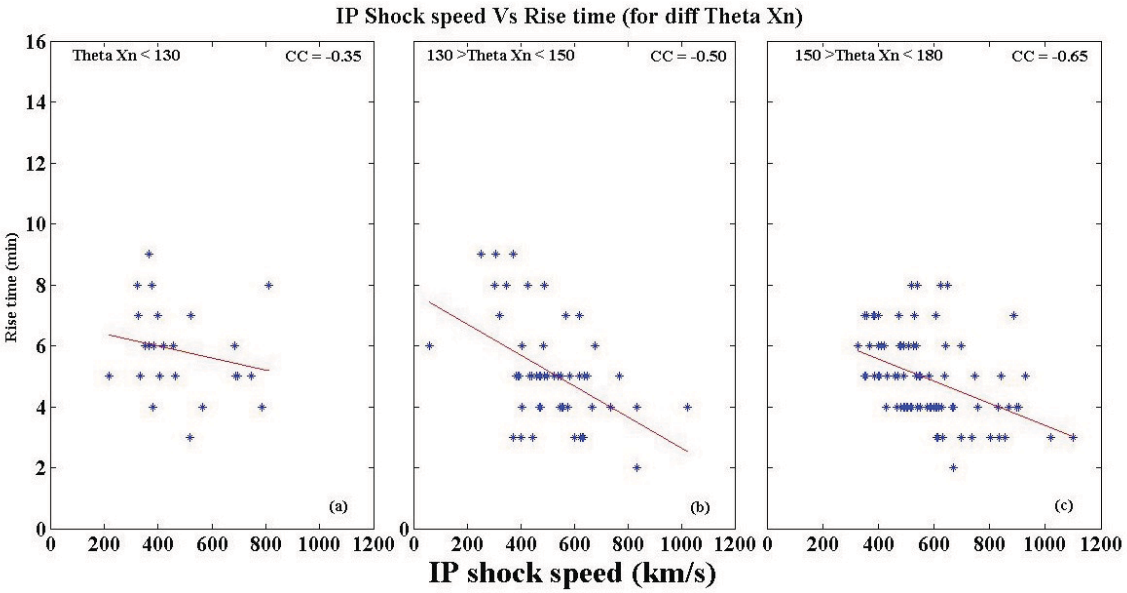

Figure 5.4: (a-c) IP shock speed with SC/SI rise time for different category of orientation angle.

The RL shocks are mostly associated with the high speed IP shocks since the type II radio burst are emitted by the higher acceleration of the electron in the shock front [Gopalswamy et al ., 2010]. Hence, it is important to consider the radio characteristics of CME along with the IP shock orientation angle in order to determine the SC/SI rise time. Figures 5.5(a-d) shows the distribution of SC/SI rise time with IP shocks speed for RL and RQ shocks with two binned IP shock orientation (1) $<150°$, (2) $>150°$. Due to very less number of events in nearly quasi perpendicular shocks the bin is categorized by merging nearly quasi parallel and oblique in one category and nearly quasi perpendicular in another category. Figure 5.5(a,b) shows the distribution for RL shocks and 5.5(c,d) shows the distribution for RQ shocks. It is observed that, as the IP shock speed increases the SC/SI rise time decreases for all the cases, but the steep variation is different for RL and RQ shocks. The correlation coefficient for RL shocks is observed to be -0.60 and -0.61 for two different binned orientations and it is -0.45 and -0.50 respectively in case of RQ shocks. It is clear from CC values that RL shocks have better correlation when compared to the RQ shocks irrespective of the orientation angle categorization. A significant difference is also observed in average rise time

values for RL and RQ shocks. The average rise time is observed to be 6 minutes for RQ shocks where as for RL shocks it is 4 minutes. The values of CC and average rise time evidently show the importance of RL shocks in determining the SC/SI rise time. It is claimed here that along with IP shocks orientation angle, the consideration of RL and RQ shocks is necessary in determining the rise time of SC/SI.

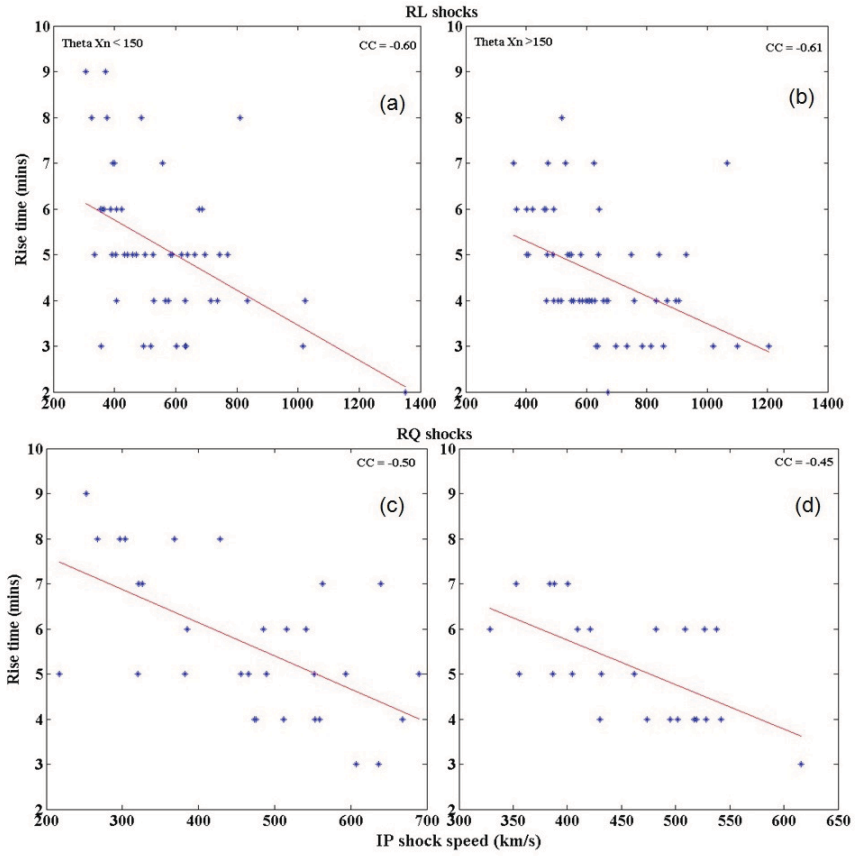

Figure 5.5: The IP shock speed with SC/SI rise time for RL and RQ shocks for two different IP orientation angles.

After looking in to the importance of radio characteristics of CME in determining SC/SI rise time the next step is to check the role played by ICME counterpart. Figures 5.6 (a-d) shows the variation of SC rise time with IP shock speed for two different bin of orientation angles (similar to bin used for RL and RQ) and for different interplanetary counter parts, MC and EJ. The negative

correlation of 0.62 and 0.65 is observed (Figure 5.6 a,b) for MC for nearly quasi parallel and nearly quasi perpendicular respectively. Similarly, for EJ the values are obtained to be -0.52 and -0.55 (Figure 5.6 c,d). The correlation between the SC/SI rise time and IP shock speed is observed to be better in case of MC than that of EJ. Though there are less number of events observed for MC the correlation and the steep decrease in the rise time is more when compared to EJ since MCs head directly towards the Earth [Gopalswamy et al .,2010; Veenadhari et al ., 2012].

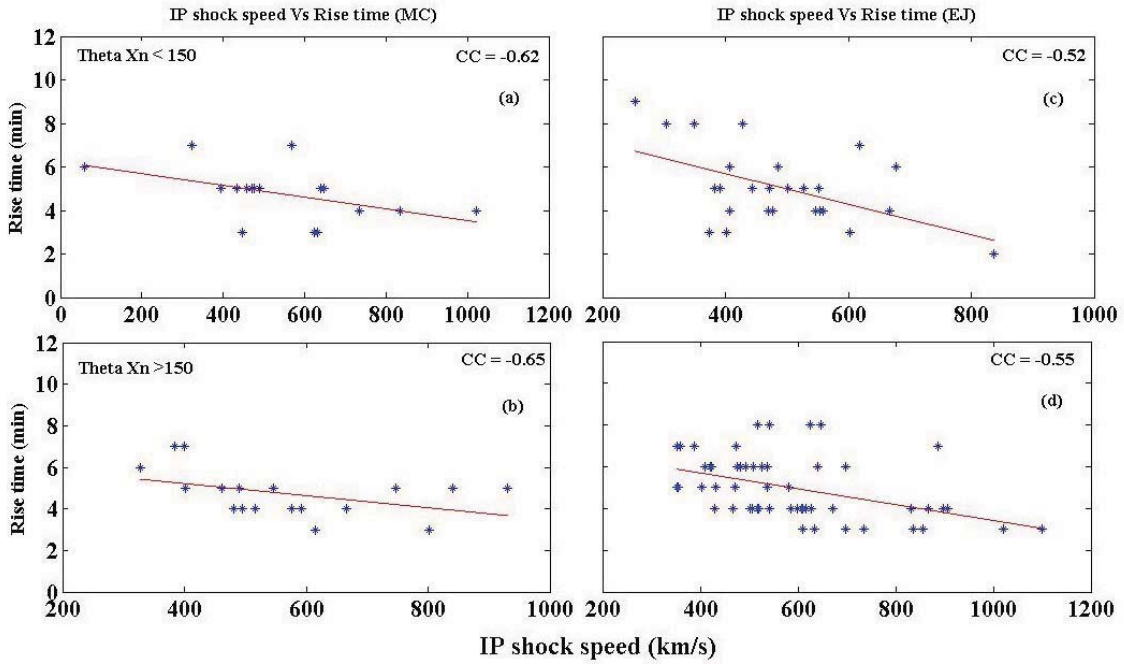

Figure 5.6: (a-d) The IP shock speed with SC/SI rise time for IP shocks with MC and EJ structures.

5.4 MHD Simulation results

The interaction between solar wind and magnetosphere has been studied extensively by means of Magnetohydrodynamics (MHD) [Ogino, 1986; Ogino et al., 1986; Watanabe and Sato, 1990; Ogino et al., 1992; Usadi et al., 1993; Walker et al., 1993, Fujita et al ., 2003a,b ; Tanaka. 1995,2010]. The magnetosphere compression due to IP shocks results in the enhancement of

dynamic pressure attributes in the formation of field-aligned currents (FACs). During the initial compression of magnetosphere by IP shocks, a pair of FAC is formed by the dusk-to-dawn electric field. Similarly, in later stage after the passage of compression HM wave from the tailward result in the enhancement of dawn to dusk electric field [Araki et al., 1977, 1994]. The transmission of magnetic field stress and energy involved in the solar wind-magnetosphere-ionosphere (SMI) coupling is carried through field aligned current (FAC) results in the main impulse of SC/SI. FAC and plasma convention plays a major role in the SMI coupling, so it is very important to study the changes in FAC during the interaction. Tanaka, [1995] proposed a three dimensional MHD simulation for SMI coupling with the use of finite volume method based on the conservation law [Vinokur, 1989]. In this study, the latest version of the global MHD simulation originally developed by Tanaka, [1994, 1995, 2000a, 2000b, 2007] and Tanaka et al. [2010] is used. This simulation uses grid system in which inner magnetosphere is divided in to a 12 pentagons. Each pentagon is again divided in to triangles resulting in 61440 triangles in total corresponding to 30,722 grid points on a sphere. This grid system does not have singular point. Readers may refer Tanaka [2015] and Ebihara and Tanaka [2015] for detailed description of the simulation. Fujita et al .[2003a,b] s tudied in detail about the transition of magnetosphere and ionosphere compound system during SC using MHD simulation. This MHD simulation is used for our study to examine the variation in the FAC , plasma pressure and magnetic field by considering IP shock with different orientation angles. The MHD simulations are conducted at 3Re from the Earth which is the region where magnetosphere and ionosphere coupling takes place.

The results discussed in section 2 show that the radio characteristics, ICME structure along with orientation angle plays a major role in determining the SC/SI rise time. Further the attempt has been made to see the variations in the geoeffectiveness with IP shock orientation angle by the means of MHD simulations. In order to check the importance of orientation angle and the evolution of IP shocks, the simulation is carried out for three different orientation angles of IP shock (θ_{xn}): (i) 180°, (ii) 135° and (iii) 90° representing the perpendicular, oblique and parallel shocks, respectively. The solar wind speed for the simulation is kept fixed nearly around the average speed of 500km/s. IMF By and Bz are held constant to be 1 and 3 nT, respectively.

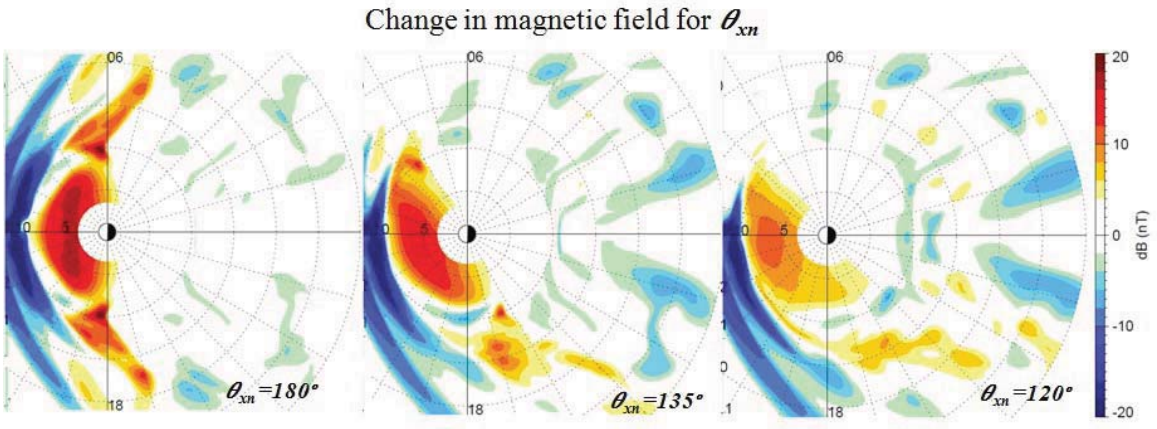

Figure 5.7: Frames of MHD simulation showing the change in magnetic field at a particular time for three different IP shock orientation angles.

Figure 5.7 shows the snap shots of evolution of IP shocks with three different orientation angle (mentioned above) with the change in magnetic field in equatorial meridian plane. The change in magnetic field is taken by subtracting the magnetic field just before IP shocks. The same time frame is chosen for the evolution of IP shocks with three different orientation angles. When the orientation angle is 180°, the evolution of the IP shock through the magnetosphere is almost symmetric about the midnight meridian and the intensity of the magnetic field is spread across the longitude. The change in magnetic intensity in case of perpendicular shocks is observed to be nearly 18 nT. Whereas in other two cases, the change is observed to be very less with the value of nearly 10 nT. The perpendicular shocks throughout the evolution from the magnetopause to the tail symmetry are preserved since the shock normal is aligned to Sun Earth line. The other two IP shocks with oblique and parallel angles did not show any symmetric evolution as perpendicular shocks. Also, the intensity and the distribution are towards the dusk side.

The geomagnetic activity for different IP shock orientation angle can be well determined by analysing the ionospheric current system. The SC is the state transition from magnetosphere to ionospheric system [Fujita et al.,2003a,b]. The magnetosphere is compressed initially due to IP shock and later results in enhanced magnetospheric convention due to the increase in density and

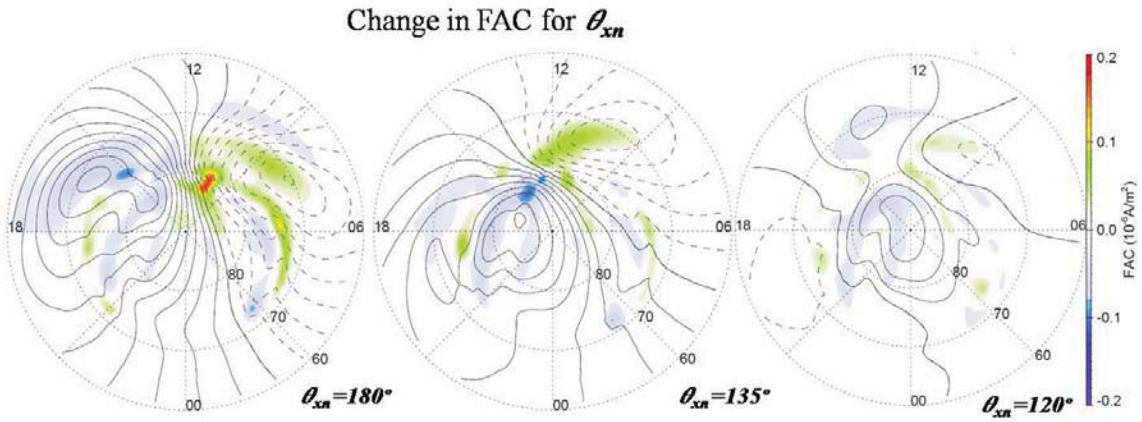

Figure 5.8: Frames of MHD simulation showing the FAC at a particular time for three different IP shock orientation angles.

velocity behind the shocks. This FAC and the FAC-induced twin vortex ionospheric currents produce the DPmi-field [Araki, 1977; Fujita et al ., 2003a]. Figure 5.8 shows the snap shots of FAC current density with the latitudinal coverage from 60° to 90° in the northern hemisphere. The red color shows the downward current while the blue color shows upward current. Wide difference is seen in the distribution and the intensity of FAC for different orientation angles. In case of perpendicular shocks the signature is seen to be broader and it covers symmetrically in the entire day side auroral region with clear two cell system (which is the same polarity as the DP2 current). Enhancement of FAC is immediate in case of perpendicular shocks.

To conceive our conclusion, the impact of IP shock orientation on change in pressure is examined. Figure 5.9 shows the pressure for the IP shock for different orientation angles. The change in pressure show smaller variation compared to changes seen in FAC and magnetic field evolution. The perpendicular shocks show symmetry about the noon-midnight meridian in the evolution of pressure and pressure is also stronger when compared to the oblique shocks. The oblique shocks show the gradient in the southern hemisphere. These all parametric study using MHD shows the impact angle play a major role in determining the geoeffectiveness along with the solar wind speed and IMF Bz.

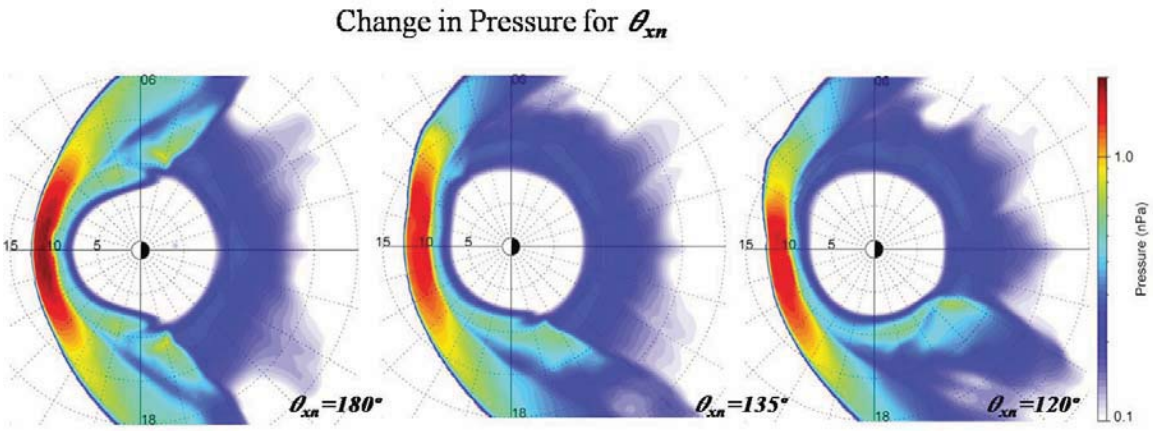

Figure 5.9: Frames of MHD simulation showing the change in pressure at a particular time for three different IP shock orientation angles.

5.5 Discussion

The orientation angle is determined for 179 IP shocks during solar cycle 23. The importance of radio characteristics and the ICME counterpart along with IP shock orientation in determining SC/SI rise time is examined. The CC values show better negative correlation of RL shocks associated SC/SI rise time with IP shock speed for differently binned orientation angle when compared to RQ shocks. Similarly, MC showed better correlation with SC/SI rise time when compared to EJ. The variation in magnetic field, FAC and pressure has shown a great difference in evolution with respect to impinge of IP shock with different orientation angle.

Wang et al. [2006] analyzed 225 IP shocks occurred between 1995 and 2004. They categorized the orientation angle in three windows: 135°-150°, 150°-165° and 165°-180° to study the importance of IP shock speed with similar orientation in determining the rise time. They obtained the correlation of 0.38, 0.68 and 0.56 respectively, for three different categories and they concluded that the SC/SI rise time decreases with increase in IP shock speed having similar orientation. Similarly, we also observed the decrease in SC/SI rise time with increase in IP shock speed for similar orientation. We found better correlation (CC = -0.65) for nearly quasiperpendicular shocks but

Wang et al., [2006] found it better for oblique shocks. It may be because they considered little different time period and orientation bins. Shock normal deviated much from the sun-earth line so that the interaction time between the shock and the magnetopause becomes longer [Takeuchi and Russell., 2002, Wang et al., 2006]. We obtained similar results of longer interaction time, since less dynamic pressure is exerted by the plasma with oblique orientations. The average value of orientation angle is obtained to be 145° which indicates that more IP shocks are driven by CME away from the disk center.

When radio characteristics are considered, the RL shocks showed a better correlation when compared to RQ shocks irrespective of orientation angle. There are two reasons for this better correlation, one is RQ CMEs is half in width than that of RL CMEs. The other is RL shocks are usually observed near disk centre with higher speeds while the RQ CMEs are observed at the limbs [Gopalswamy et al., 2008]. This source location along with IP shock speed and orientation angle resulted in the less correlation and more sweeping time of the magnetopause for RQ CMEs. The RL shocks usually have high speeds resulting in more geoeffectivness when compared to RQ shocks (low speeds). Through MHD model fowler, [2005] showed shocks with higher speed have faster rise time when compared to slower speed shocks. The compression $i.e.$, ratio of downstream to upstream is more in case of quasi perpendicular shocks when compared to quasi parallel shocks. The compression of the magnetopause is symmetric when the shocks are perpendicular resulting in the fast increase in the magnetopause current which in turn increases the ground magnetic field faster. Geoeffectiveness increases with shock strength along with the shock impact angle [Oliveira and Raeder, 2014]. We have observed better correlation of IP shock speed with SC/SI rise time for MC associated CME compared to EJ. MC plays a major role not only in determining the SC/SI amplitude but also the rise time with different categories of impact angle. Usually MCs head directly toward Earth and shock measurement at the nose in which the speed is maximum but in case of EJ it is totally opposite with head not directly towards Earth. The shock speed measured away from the nose for EJ is smaller when compared to MC. This could be a reason for better correlation for MC than EJ shocks.

The simulated change in magnetic field is nearly half for same time frame in case of perpendicular shocks when compared to parallel shocks. The magnetopsheric compression also rapid in case of perpendicular shocks resulting faster change in the pressure, which results in the faster SC/SI rise. The FAC response also differed with the IP shock orientation angle. **The enhancement of FAC is symmetric in the day side and through the evolution they spread more towards the night side**. The SC/SI is characterized by the switching of the magnetospheric electric field from the dusk-to-dawn to dawn-to-dusk direction [Araki et al ., 1977, Fujita et al., 2003a]. The distance between convention vortex centres decreases rapidly in case of perpendicular shocks which in turn enhances the dawn to dusk electric field which is then transmitted along the field lines when compared to parallel shocks accompanying FACs. In case of perpendicular shocks the switching of this electric field is faster which results in SC/SI, when compared to the parallel shocks. **The similar results is obtained in our simulation that is the positive change in the FAC is faster in case of perpendicular shocks. The preliminary implulse and main impulse of SC/SI electric fields are generated in the dayside part of the magnetosphere and moves toward the terminators [Fujita et al., 2003a,b]**. But it is slower in case of parallel shocks. In case of inclined IP shocks, the FAC enhancement occurs mainly behind the cusp [Oliveira and Raeder 2014].

5.6 Summary

The main findings of the present are summarized as follows The IP shock orientation angle and SC/SI rise time is estimated for 179 IP shocks during solar cycle 23. More than 50% of the Shock orientation is in the range of 140° to 160°. The RL associated IP shocks speeds shown a better correlation than RQ shocks with SC/SI rise time when categorized with different impact angle. The average rise time is less for RL shocks when compared to RQ shocks. MC associated shocks is dominating in producing less rise time when compared to EJ shocks. Simulation revealed that quasi perpendicular shocks are more geoeffective when compared to oblique shocks by means of change in magnetic field and FAC.

Chapter 6

Summary, Conclusion and Suggestions for future work

6.1 Solar flares induced D-region ionospheric and geomagnetic perturbations

In this chapter, solar flares of C, M and X classes which occurred during January 2010 to February 2011 are selected to see their effects on lower ionospheric and geomagnetic disturbance due to this flares. A wide range of data sets have been used to study the perturbation in D-region ionosphere and geomagnetic field during solar flare such as, VLF narrow band signal from AWESOME instrument, Earth′s geomagnetic field horizontal component (H) data is obtained from equatorial station, X-ray flux data recorded GOES satellites. The period under consideration encountered nearly 41 solar flare events (21 C-class, 19-M class and 01 X-class flare) have been analyzed to examine the changes in VLF amplitude, Wait parameters, electron density and their local time dependence. The change in the VLF signal amplitude (δA) depends on the flare strength (solar X-ray flux) which can be effectively utilized to estimate the electron density changes due to solar flares [Grubar et al., 2005; Zigman et al., 2007]. It is observed that δA varies between 1.21 to 2.73 dB

for C class solar flares and between 2.88 to 5.45 dB for M class solar flares. The lowest are which produced the perturbation in the signal amplitude is a C 2.0 class flare (1.21dB).The maximum δA of 6.8 dB was observed for an X2.2 solar flare.

As the intensity of the solar flare increases, the δA also increases but not linearly. Some inconsistency in δA values were seen when solar flares of same class/strength occurred on different days. The nonlinearity comes from the fact that δA also depends upon pre-flare flux condition and local time. Based upon calculations, in general, it is observed that the pre-flare flux values follow the linear trend with the class of flares. But the pre-flux values show discrepancy when a flare is followed by another flare depending upon its class, i.e., if the given flare is preceded by a higher class flare, the pre-flux value is more but the absolute enhancement in the flux is less. To investigate the dependance of this nonlinearity due to local time, the local day time is divided in three periods: morning (06-10 LT), noon (10-15 LT) and evening (15-18 LT). And it is observed that δA in the noon shows greater increase when compared to the occurence of same class flare occur in morning or evening time period. This work shows that δA variation due to flares depends on the class of flares, pre-flare condition and local time. Solar flare effect also shows time delay (δt) in the occurrence of the VLF peak amplitude when compared to the time of X-ray flux peak.

In order to quantify the solar flare induced perturbations in the D-region ionosphere, LWPC code is utilized, which is developed by US Navy [Ferguson, 1998] to calculate the changes in Wait ionospheric parameters. The change in the reflection height H$^{/}$ and sharpness factor β for all the solar flare events is estimated for all solar flare events. Reduction in the H$^{/}$ and increase in β are estimated during the flares as compared to the normal day time values. The maximum change in the H$^{/}$ and β is estimated for X-class flare followed by M-class and C-class flares. The electron density profiles estimated during the solar flare events show a maximum increase in electron density of the order of 80 times as compared to the normal day values for X- class flare at the reference altitude of 70 km. The increase of about 13 nT in ΔH_s for solar flare of M-class was observed at Tirunelveli which could be accounted for the enhanced electrojet during the solar flares. Solar flares causes greater perturbation in the D-region ionosphere as well as the Earth$'$ magnetic field.

6.2 CME-driven shocks and the associated sudden commencements/sudden impulses, geoeffectiveness

In this chapter, on the basis of the list of 222 IP shocks compiled by Gopalswamy et al. [2010] occurred during 1996-2006 of solar cycle 23, we have investigated the dependence of SC/SIs amplitudes on the speed of the coronal mass ejections (CMEs) that drive the shocks near the Sun as well as in the interplanetary medium. Apart from IP shock details for each SC event, the onset time is determined from the H component geomagnetic variation in the rapid sampling records (with the time resolution of 1 m) obtained at Alibag (ABG).

IP shocks undergo considerable changes as they propagate from near Sun to the L1 point. The best way to characterize them is to examine the CMEs that drive them. CMEs can be observed by coronagraphs very close to the Sun (1 to 2 solar radii above the surface). Such early observations can provide advance warning of shocks arriving at Earth by more than half day to a few days. The CMEs associated with RL shocks are said to be RL CMEs and those followed by the IP shocks are said to be RL IP shocks, or simply RL shocks. Similarly, there are RQ CMEs and RQ IP shocks (or simply RQ shocks). The CME and radio emission characteristics are useful in understanding the shock-driving ability of CMEs near the Sun because type II bursts are the earliest indicators of shocks and contain information on both the shock and the ambient medium in which shock propagates. Apart from radio classification, we also divided the IP shocks according to the type of IP counterpart of interplanetary CMEs (ICMEs): magnetic clouds (MCs) and nonmagnetic clouds. It is also important to consider the ICME type (MC or EJ) because they seem to represent head-on and glancing blows to the magnetosphere and hence have implications to the resulting SCs.

We find that about 91% of the IP shocks were associated with SC/SIs. The average speed of the SC/SI-associated CMEs is 1015 km/s, which is almost a factor of 2 higher than the general CME speed. When the shocks were grouped according to their ability to produce type II radio burst in the interplanetary medium, we find that the RL shocks produce a much larger SC/SI amplitude (average 32 nT) compared to the RQ shocks (average 19 nT). RL shocks are more effective in

producing SC/SI events than the RQ shocks. The average Mach number is higher for RL shocks than for RQ shocks. The SC/SI amplitudes and Mach number of the shocks are better correlated with RL shocks than with the RQ shocks. Thus, if we observe a RL CME near the Sun originating close to the disk center, it is highly likely that the shock produces a large SC/SI event at Earth. There is a significant difference in the latitudinal and longitudinal distribution for RL and RQ shocks associated with SC/SI amplitudes. RL shocks are spread over more of the longitude belt than RQ shocks. RQ shock source region is confined to 30.

During the same time period the shock-driving ICMEs and their associated geomagnetic storms are identified. Nearly 63% of the Earth directed CMEs results in the geomagnetic storms and 37 % of the Earth directed CME did not cause geomagnetic storms which are associated with IP shocks. The geomagnetic storm occurence follows the SSN for the solar cycle 23. The average Dst value for MC ICMEs is higher compared to EJ. This is true obviously because the MC associated in the ICME has more possibility to produce the magnetic storm when IMF Bz is southward. The Ds-VBz relations holds better for MC when compared to EJ. The radio characteristics and ICME magnetic structure plays a major role in deciding the amplitude of SC/SI as well as geoeffectiveness along with negative Bz.

6.3 On the reduced geoeffectiveness of solar cycle 24: a moderate storm perspective

Geomagnetic storm is a major disturbance of Earth's magnetosphere that occurs when there is an efficient exchange of energy from the solar wind into the space environment surrounding Earth. These storms result from variations in the solar wind that produces major changes in the currents, plasmas, and fields in Earth′s magnetosphere. In this chapter, the moderate and intense geomagnetic storms are identified for the first 77 months of solar cycle 23 and 24. The solar sources responsible for the moderate geomagnetic storms are identified during the same epoch for both the

cycles. Solar cycle 24 has shown nearly 80 % reduction in the occurrence of intense storms where as it is only 40 % in case of moderate storms when compared to previous cycle. While the reduction in intense storms is clear, it is of interest to know what happens to moderate storms. None of the works till now has attempted attempted to compare the occurrence of moderate storms during solar cycle 23 and 24 based on the source and interplanetary origin of it. This work is initiated to see if the reduction in geoeffectiveness has anything to do with the occurrence of moderate storm in cycle 23 and 24.

The period considered for the comparative study comprises of first 77 months of both the solar cycles, 23 (May 1996 to September 2002) and 24 (September 2008 to January 2015). A total of 166 geomagnetic storms are identified during the first 77 months of solar cycle 23 and 67 in cycle 24 over the same epoch. The number of moderate storms are 111 and 55 in cycles 23 and 24, respectively. The occurrence of moderate storms approximately follows the SSN and peaks around the solar maximum for both the cycles. The solar and interplanetary characteristics of the moderate storms driven by CME are compared for solar cycle 23 and 24 in order to see reduction in geoeffectiveness has anything to do with their occurrence. Though there is reduction in the occurrence of moderate storms, the Dst distribution does not show much difference. Similarly the solar source parameters like CME speed, mass and width did not show any significant variation in the average values as well as the distribution. Moderate storms did not show any center-to-limb variation in the geoeffectivness of CMEs. The average speed of limb CMEs is observed to be 1100 km/s whereas that of non limb CMEs average speed is 670 km/s in the sky plane. Although projection effects are expected, it appears that limb CMEs with higher CME speed are required to produce moderate storms. The correlation between VBz and Dst is determined and it is found to be moderate with value of 0.68 for cycle 23 and 0.61 for cycle 24. The magnetospheric energy flux parameter epsilon (ε) is estimated during the main phase of all moderate storms during solar cycles 23 and 24. The energy transfer decreased in solar cycle 24 when compared to cycle 23. These results are significantly different when all geomagnetic storms are taken in to consideration for both the solar cycles. The reduced geoeffectiveness in cycle 24 is mainly due to the decrease in the intense storms and to a smaller extent in the number of moderate storms, which is the resultant

of anomalous CME expansion and less magnetopsheric energy transfer in cycle 24.

6.4 The role of interplanetary shock orientation on SC/SI rise time and geoeffectiveness

In this chapter, the IP shock orientation angle and SC/SI rise time for 179 IP shocks are estimated which occurred during solar cycle 23. These events have been selected from Gopalswamy et al. [2010], who studied 230 IP shocks at 1 AU during 1996-2006.The previous work on SC/SI [Veenadhari et al ., 2012] focused importance of radio characteristics and ICME structure classification in determining the SC/SI amplitude, and their dependence on RL shocks and RQ shocks, associated CMEs [Veenadhari et al ., 2012]. We observed that average SC/SI amplitudes for RL shocks are more when compared to RQ shocks and IP shock speed is better correlated with SC/SI amplitude for RL shocks. They focused only the importance of radio characteristics and ICME structure in the determination of SC/SIs amplitude.The main motivation behind the present work is to establish the importance of radio characteristic of CME and ICME structure along with IP shock orientation angle in determining SC/SI rise time as well as geoeffectiveness. The chapter′ first part deals with the importance of radio characteristics of IP shock associated with CME along with impact angle resulting in SC/SI rise time and second part deals with the confirmation of the statistical results using MHD simulations by considering different orientation angles.

The IP shock orientation angle ranges from 90° to 180°. When the angle between the Sun Earth line and the shock normal vector is 180° it is called as quasi perpendicular shock ie., the shock orientation is parallel to the magnetosphere. The IP shock orientation angle nearer to 90° is said to be quasi parallel shocks. The SC/SI rise time decreases with the increase of the orientation angle and also with the IP shock speed. More than 50% of the shock orientation is in the range of 140° to 160°. The RL associated IP shocks speeds show a better correlation than RQ shocks with SC/SI rise time irrespective of the orientation angle. Magnetic Cloud (MC) associated shocks are

dominating in producing less rise time when compared to Ejecta (EJ) shocks. MHD simulations are used for three different IP shock orientation categories to see the importance of orientation angle in determining the geoeffectiveness. Simulations results revealed that shocks hitting parallel to the magnetosphere are more geoeffective when compared to oblique shocks by means of change in magnetic field, pressure and Field aligned current (FAC).

6.5 Future work

The geomagnetic disturbances are essentially caused by CMEs, which originate from the Sun and are directed towards the Earth, and CIRs which are formed at the interface of fast and slow solar wind streams and normally get intensified at about 1 AU or further heliocentric distances [e.g., Watari and Watanabe, 1998; Alves et al., 2006; Tsurutani et al., 2006; Gopalswamy, 2008; Manoharan, 2012]. An Interplanetary coronal mass ejections(ICMEs) is generally regarded as the heliospheric counterpart of the CME that is at much larger distance from Sun. Like CME, ICME have large masses and contain a magnetic field. The magnetic structures inside an ICME are varied, but are typically greater in magnitude than the surrounding interplanetary magnetic fields. The MCs are subset of ICMEs possessing well-defined magnetic properties. MC is a transient ejection in the solar wind defined by relatively strong magnetic fields, a large and smooth rotation of the magnetic field direction and a low proton temperature. The MC has different type based on the axial direction and the direction of smooth rotation, which are South- North (SN), North-South (NS), Fullysouth (FS) and Fully north (FN).

Owing to the weak polar magnetic field, the solar cycle 23 went into a prolonged minimum characterized by unusually large number of days without sunspots. This was marked by the reduced number of geomagnetic intense events during solar cycle 24 compared to solar cycle 23, even though the number of CMEs is same[Gopalswamy et al., 2015]. Magnetic clouds are ideal objects for solar-terrestrial studies because of their simplicity and their extended intervals of southward and northward magnetic fields. The MCs are considered to be highly geoeffective resulting in

moderate and intense storms occurred during solar cycle 23 and 24. The main motivation of the work to see the importance of the MC type in determining the geoeffectivness. Magnetic clouds will be selected through lists of ICMEs events.The geomagnetic storms will be identified associated with MC for the complete solar cycle 23 and 24. The interplanetary parameters will be estimated to see the difference in the geoeffectiveness associated with different MC type for both cycles. Along with that magnetopheric energy transfer will be estimated for the different type of MC associated geomagnetic storm, to see any difference in energy transfer for cycle 23 and 24.

Bibiliography

Akasofu, S. I and Kamide, Y (1987), Book-Review - the Solar Wind and the Earth, Journal of the British Astronomical Society, Vol. 98, NO. 1/DEC, P. 48.

Akasofu, S. I. (2007), Long-standing unsolved problems in solar terrestrial physics. IEEE Trans Plasma Sci, 35:751–758.

Alex, S., S. Mukherjeea, G. S. Lakhina (2006), Geomagnetic signatures during the intense geomagnetic storms of 29 October and 20 November 2003, J. Atmos. Sol. Terr. Phys., 68 769–780.

Alexeev, I. I., E. S. Belenkaya, V. V. Kalegaev, Y. I. Feldstein, and A. Grafe (1996), Magnetic storms and magnetotail currents, J. Geophys. Res., 101, 7737-7747.

Amari T, Luciani JF, Aly JJ (2004) Coronal magnetohydrodynamic evolution driven by Subphotospheric conditions. Astrophys J 615:L165–L168.

Ananthakrishnan, S., Abdu, M.A., Piazza, L.R., 1973. D-region recombination coefficients and the short wavelengths X-ray flux during a solar flare. Planet. Space Sci. 21, 367–375.

Araki, T, (1977), Global structure of geomagnetic sudden commencements, Planetary and Space Science, 25, 373–384.

Araki, T, (1994), A physical model of the geomagnetic sudden commencement, Geophysical Monograph, 81, 183–200.

Araki, T. Takeuchi, and Y. Araki (2003), Rise time of geomagnetic sudden commencements Statistical analysis of ground geomagnetic data. Earth Planets Space, 56, 289–293, 2004.

Bainbridge, G., Inan, U. S., 2003. Ionospheric D region electron density profiles derived from the measured interference pattern of VLF waveguide modes. Radio Sci, doi:10.1029/2002RS002686.

Balan, N., R. Skoug, S. Tulasi Ram, P. K. Rajesh, K. Shiokawa, Y. Otsuka, I. S. Batista, and T. Nakamura (2014), CME front and severe space weather, *J. Geophys. Res. Space Physics*, **119**, 10,041–10,058, doi:10.1002/2014JA020151.

Baumjohann, W., Y. Kamide, and R. Nakamura (1996), Substorms, storms, and the near-Earth tail, J. Geomagn.G eoelectr.4, 8, 177-185, 1996.

Baumjohann, W.,(1993), The near-Earth plasma sheet: An AMPTE/ IRM perspective, Space Sci. Rev., 64, 141-163, 1993.

Berdichevsky, D. B., C. J. Farrugia, B. J. Thompson, R. P. Lepping, D. V. Reames, M. L. Kaiser, J. T. Steinberg, S. P. Plunkett, and D. J. Michels (2002), Halo-coronal mass ejections near the 23rd solar minimum: Liftoff, inner heliosphere, and in situ (1 AU) signatures, Ann. Geophys., 20, 891– 916.

Bhatnagar, A., & Livingston, W. (2005), Fundamentals of Solar Astronomy (World Scientific: Singapore).

Borovsky JE, and Denton MH (2006), Differences between CME-driven storms and CIR-driven storms. J Geophys.Res 111:A07S08. doi:10.1029/2005JA011447.

Brueckner, G. E., J.-P. Delaboudiniere, R. A. Howard, S. E. Paswaters, O. C. St. Cyr, R. Schwenn, P. Lamy, G. M. Simnett, B. Thompson, and D. Wang (1998), Geomagnetic storms caused by coronal mass ejections (CMEs): March 1996 through June 1997, Geophys. Res. Lett., 25, 3019–3022.

Brueckner, G.E., Howard, R.A., Koomen, M.J., Korendyke, C.M., Michels, D.J., Moses, J.D., Socker, D.G, & Linker, J. (1995), The Large Angle Spectroscopic Coronagraph (LASCO) Sol. Phys., 162, 357.

Burlaga L. (1972), Discontinuities and shock waves in the interplanetary medium and their interaction with the magnetosphere (Solar wind discontinuities and shock waves in

interplanetary medium at magnetospheric boundary related to geomagnetic impulses). Solar-terrestrial physics/1970,1972:1972.

Carrington, R. C. (1859). "Description of a Singular Appearance seen in the Sun on September 1, 1859". Monthly Notices of the Royal Astronomical Society 20: 13–5. Bibcode:1859MNRAS..20...13C. doi:10.1093/mnras/20.1.13.

Chakrabarty, D., Mala Bagiya, S., Smitha thampi, V., Pathan, B. M., Sekar, R., (2013), Signatures of moderate (M-class) and low (C and B class) intensity solar flares on the equatorial electrojet current: Case studies. J. Atmos. Solar Terr. Phys., 105-106 (2013) 170–180.

Chakrabarty, D., Sekar, R., Sastri, J. H., Pathan, B. M., Reeves, G. D., Yumoto, K., Kikuchi, T., (2010), Evidence for OI 630.0 nm day glow variations over low latitudes during onset of a substorm.J.Geophys.Res.115,A10316,doi: 10.1029/ 2010JA015643.

Chao, J. K. and R. P. Lepping, (1974), A Correlative Study of ssc's Interplanetary Shocks, and Solar activity, J. Geophys. Res., 79, 1799-1807.

Chapman, S. and Ferraro, V.C.A. (1931), A new theory of magnetic storms, Terrestrial Magnetism and Atmospheric Electricity 36: doi: 10.1029/TE036i002p00077.

Chapman, S. and Ferraro, V.C.A. (1940), A new theory of magnetic storms, Teresstrial Magn. Atmos. Elect. 45:245.

Chapman, S. and J. Bartels (1962), Geomagnetism Vol. II, Clarendon Press, London,1962.

Chapman, S., and J. Bartels, Geomagnetism, vol. I chap.IX, Clarendon, Oxford, 1940.

Chi, P.J., D.-H. Lee, and C. T. Russell (2006), Tamao travel time of sudden impulses and its relationship to ionospheric convection vortices, J. Geophys. Res., 111, A08205, doi: 10.1029/2005JA011578.

Cho, K. S., S. C. Bong, Y. J. Moon, M. Dryer,3 S. E. Lee, and K. H. Kim (2010), An empirical relationship between coronal mass ejection initial speed and solar wind dynamic pressure, J. Geophys. Res., 115, A10111, doi: 10.1029/2009JA015139.

Cid, C., H. Cremades, A. Aran, C. Mandrini, B. Sanahuja, B. Schmieder, M. Menvielle, L. Rodriguez, E. Saiz, Y. Cerrato, S. Dasso, C. Jacobs, C. Lathuillere, and A. Zhukov., (2012)., Can a halo CME from the limb be geoeffective? , J. Geophys. Res., 117, A11102.

Cliverd, M. A., Rodger, C. J., Thomson, N. R., Lichtenberger, J., Steinbach, P., Cannon, P. and Angling, M. J., (2001), Total solar eclipse effects on VLF signals: Observation and modeling. Radio Sci., 36(4), 773-788.

Crosby NB, Rycroft MJ, Tulunay Y (2006), Overview of a graduate course delivered in Turkey, emphasizing solar-terrestrial physics and space weather. Surv Geophys 27:319–364.

Daglis, I. A., and R. M. Thorne (1999), The terrestrial ring current: Origin, formation, and decay, Rev. Geophys., 37, 407–438.

Dal Lago, A., L. E. A. VieiraI, E. Echer, W. D. Gonzalez, A. L. Clúa de Gonzalez, F. L. Guarnieri, L. Balmaceda, J. Santos, M. R. da Silva, A. de Lucas, N. J. Schuch (2004), Great geomagnetic storms in the rise and maximum of solar cycle 23, Braz. J. Phys., 34, 1542–1546.

Davies, K., 1990. Ionospheric Radio, Electromagnetic wave series 31 Peregrines. London.

Dessler, A. J and Parker, E. N (1959), Hydromagnetic theory of geomagnetic storms, Journal of Geophysical Research, Volume 64, Issue 12, pp. 2239-2252.

Dessler, A. J., W.E.Francis, and E. N. Parker (1960), Geomagnetic storm sudden commencement rise times, J. Geophys. Res., 65, 2715–2719, 1960.

DeVore CR, and Antiochos SK (2008) Homologous confined filament eruptions via magnetic breakout. Astrophys J 680:740–756.

Dungey, J. W. (1961), Interplanetary magnetic field and the auroral zones. Phys. Rev. Lett. 6, 47–48.

Ebihara, Y., and T. Tanaka (2015), Substorm simulation: Insights in to the mechanism of initial brightening, J. Geophys. Res., , 120, 7270–7288, 10.1002/2015JA021516. Los Angeles.

Echer E., B. T. Tsurutani , and W. D. Gonzalez (2013) Interplanetary origins of moderate (−100 nT < Dst ≤ −50 nT) geomagnetic storms during solar cycle 23 (1996-2008). JGR 118:385.

Echer, E., W. D. Gonzalez, and B. T. Tsurutani (2008b), Interplanetary conditions leading to superintense geomagnetic storms (Dst < -250) during solar cycle 23, Geophys. Res. Lett., 35, L06S03, doi:10.1029/ 2007GL031755.

Echer, E., W. D. Gonzalez, and B. T. Tsurutani (2011), Statistical studies of geomagnetic storms with peak Dst ≤ _50 nT from 1957 to 2008, J. Atmos. Sol. Terr. Phys., 73, 1454–1459.

Echer, E., W. D. Gonzalez, B. T. Tsurutani, and A. L. C. Gonzalez (2008a), Interplanetary conditions causing intense geomagnetic storms (Dst ≤ -100 nT) during solar cycle 23 (1996–2006), J. Geophys. Res., 113, A05221, doi:10.1029/2007JA012744.

Echer, E.,W. D. Gonzalez, F. L. Guarnieri, A. Dal Lago, and L. E. A. Vieira (2005), Introduction to space weather, Adv. Space Res., 35, 855–865.

Fan Y, and Gibson SE (2007), Onset of coronal mass ejections due to loss of confinement of coronal flux ropes, The Astrophysical Journal, 668:1232Y1245.

Ferguson, J. A., 1998. Computer Programs for Assessment of Long-Wavelength Radio Communications. Version 2.0, Space and Naval Warfare Systems Center, San Diego, CA.

Fujita, S., T. Tanaka, T. Kikuchi, K. Fujimoto, and M. Itonaga (2003b), A numerical simulation of the geomagnetic sudden commencement: 2. Plasma processes in the main impulse, J. Geophys. Res., 108(A12), 1417, doi:10.1029/2002JA009763.

Fujita, S., T. Tanaka, T. Kikuchi, K. Fujimoto, K. Hosokawa, and M. Itonaga (2003a), A numerical simulation of the geomagnetic sudden commencement: 1. Generation of the field‐aligned current associated with the preliminary impulse, J. Geophys. Res., 108(A12), 1416, doi:10.1029/ 2002JA009407.

Garcia, H. A. (2004) Forecasting methods for occurrence and magnitude of proton storms with solar hard X-rays. Space Weather, 2:S06003, 10. doi:10.1029/2003SW000035.

Gonzalez W. D., E. Echer, A. L. Clua-Gonzalez, and B. T. Tsurutani (2007), Interplanetary origin of intense geomagnetic storms (Dst <-100 nT) during solar cycle 23, Geophys. Res. Lett., 34, L06101, doi:10.1029/2006GL028879.

Gonzalez, W. D., and B. T. Tsurutani (1987), Criteria of interplanetary parameters causing intense magnetic storms (Dst < _100 nT), Planet. Space Sci., 35, 1101.

Gonzalez, W. D., and E. Echer (2005), A study on the peak Dst and peak negative Bz relationship during intense geomagnetic storms, Geophys. Res. Lett., 32, L18103, doi: 10.1029/2005GL023486.

Gonzalez, W. D., B. T. Tsurutani, and A. L. Clua de Gonzalez (1999), Interplanetary origin of geomagnetic storms, Space Sci. Rev., **88**, 529-562.

Gonzalez, W. D., E. Echer, B. T., Tsurutani, A. L. Gonzalez, and A., Dalago (2011),Interplanetary origin of intense, super intense and extreme geomagnetic storms, Space Sci. Rev., **158**, 69-89

Gonzalez, W. D., J. Joselyn, Y. Kamide, H. Kroehl, G. Rostoker, B. Tsurutani, and V. Vasyliunas, (1994), What is a magnetic storm?, J. Geophys. Res., 99, 5771-5784, doi:10.1029/93JA02867.

Gopalswamy N, Yashiro and S. Akiyama (2007), Geoeffectiveness of halo coronal mass ejections, J. Geophys. Res., 112, A06112.

Gopalswamy N, Yashiro S, Mäkelä P, Michalek G, Shibasaki K, Hathaway DH (2012) Behavior of solar cycles 23 and 24 revealed by microwave observations. Astrophys J 750:LL42.

Gopalswamy, N. (2008), Solar connections of geoeffective magnetic structures, J. Atmos. Sol. Terr. Phys., 70, 7028.

Gopalswamy, N. (2009), Coronal mass ejections and space weather, Climate and Weather of the Sun-Earth System (CAWSES): TERRAPUB, Tokyo, Selected papers from the Kyoto Symposium 2007(Edited by T.Tusuda, RFujii, K.Shibata and M.A.Geller, 77-120.

Gopalswamy, N. (2010), The CME link to geomagnetic storms, in Proceedings of the IAU Symposium, vol. 264, edited by A. G. Kosovichev, A. H. Andrei, and J.-P. Rozelot, 326 pp., Cambridge Univ. Press, Cambridge, U. K.

Gopalswamy, N., E. Aguilar-Rodriguez, S. Yashiro, S. Nunes, M. L. Kaiser, and R. A. Howard (2005), Type II radio bursts and energetic solar eruptions, J. Geophys. Res., 110, A12S07, doi: 10.1029/2005JA011158.

Gopalswamy, N., A. Lara, R. P. Lepping, M. L. Kaiser, D. Berdichevsky, and O. C. St. Cyr (2000), Interplanetary acceleration of coronal mass ejections, Geophys. Res. Lett., 27, 145.

Gopalswamy, N., B. Tsurutani, and Y. Yan (2015a), Short-term variability of the Sun-Earth system: An overview of progress made during the CAWSES II period, Prog. Earth Planet. Sci., 2, 13.

Gopalswamy, N., H. Xie, P. Mäkelä, S. Akiyama, S. Yashiro, M. L. Kaiser, R. A. Howard, and J. L. Bougeret (2010a), Interplanetary shocks lacking type II radio bursts, Astrophys. J., 710, 1111, doi:10.1088/0004-637X/710/2/1111.

Gopalswamy, N., P. Mäkelä, H. Xie, S. Akiyama and S. Yashiro (2009c), CME Interaction with Coronal Holes and their Interplanetary Consequences J. Geophys. Res., 114, A00A22.

Gopalswamy, N., S Yashiro , H. Xie, S. Akiyama, S. E. Aguilar-Rodriguez, M. L. Kaiser, R. A. Howard, and J. L. Bougeret (2008c), Radio-Quiet Fast and Wide Coronal Mass Ejections, ApJ, 674, 560, doi: 10.1086/524765.

Gopalswamy, N., S Yashiro , S. Akiyama, P. Mäkelä, H. Xie, M. L. Kaiser, R. A. Howard, and J. L. Bougeret (2008b), Coronal mass ejections, type II radio bursts, and solar energetic particle events in the SOHO era, Ann. Geophys., 26, 3033.

Gopalswamy, N., S. Akiyama, S. Yashiro, H. Xie, P. Mäkelä, and G. Michalek (2014), Anomalous expansion of coronal mass ejections during solar cycle 24 and its space weather implications, Geophys. Res. Lett., 41, 2673–2680, doi:10.1002/2014GL059858.

Gopalswamy, N., S. Yashiro, G Michalek, G Sternborg, A. Vourlidas, S. Freeland, and Howard (2009d), The SOHO/LASCO CME Catalog, Earth, Moon, and Planets, 104, 295-313.

Gopalswamy, N., S. Yashiro, H. Xie, S. Akiyama, and P. Mäkelä (2015b), Properties and geoeffectiveness of magnetic clouds during solar cycles 23 and 24, J. Geophys. Res., 10.1002/2015JA021446

Gopalswamy, N., S. Yashiro, H. Xie, S. Akiyama, S. E. Aguilar-Rodriguez, M. L. Kaiser, R. A. Howard, and J. L. Bougeret (2008), Radio-quiet fast and wide coronal mass ejections, Astrophys. J., 674, 560–569, doi:10.1086/524765.

Gopalswamy, N., S. Yashiro, S. Krucker, G. Stenborg, and R. A. Howard (2004), Intensity variation of large solar energetic particle events associated with coronal mass ejections, J. Geophys. Res., 109, A12105.

Gopalswamy, N., Z. Miki´c, D. Maia, D. Alexander, H. Cremades, P. Kaufmann, D. Tripathi and Y.-M. Wang (2006), The Pre-CME Sun, Space Sci Rev.123,303-339 doi:10.1007/s11214-006-9020-2.

Gopalswamy, N.; S. Yashiro, G. Michalek, H. Xie, P. Mäkelä, A. Vourlidas, and R. A. Howard (2010b), A Catalog of Halo Coronal Mass Ejections from SOHO, Sun and Geosphere, 5(1), 7-16.

Gosling JT (1993) The solar flare myth. J Geophys Res 98:18937–18949. doi:10.1029/93JA01896.

Gosling JT, Hundhausen AJ, Bame SJ (1976) Solar wind stream evolution at large heliocentric distances experimental demonstration and the test of a model. J Geophys Res 81:2111–2122.

Gosling, J T., and V. J Pizzo (1999), Formation and evolution of Corotating Interaction Regions and their three dimensional structure, Space Science Reviews 89: 21–52.

Gosling, J. T. (1996), Corotating and Transient Solar Wind Flows in Three Dimensions, Ann. Rev. Astron. Astrophys. 34, 35–73.

Gosling, J. T., D. J. McComas, J. L. Phillips, and S. J. Bame (1991), Geomagnetic activity associated with Earth passage of interplanetary shock disturbances and coronal mass ejections, J. Geophys. Res., 96, 7831–7839.

Grubor, D. P., Sulic´, D. M., Zigman, V., 2008. Classification of *X*-ray solar flares regarding their effects on the lower ionosphere electron density profile. Ann. Geophys., 26, 1731–1740.

Grubor, D., Sulic, D., Zigman, V., 2005. Influence of solar X-ray flares on the earth ionosphere wave guide. Serb.Astron., 171 29-35.

Han, F., Cummer, S. A., 2010. Midlatitude daytime D region ionosphere variations measured from radio atmospherics. J. Geophys. Res., 115, A10314, doi:10.1029/2010JA015715.

Hargreaves, J. K., 2003. The Solar-Terrestrial Environment. Cambridge University Press, New York.

Hathaway, H., (2010),The Solar Cycle, Living Rev. Solar Phys, Vol. **7**.

Hines, C. O., (1957), On the geomagnetic storm effect, J. Geophys. Res., 62, 491– 492.

Hodgson, R., (1859), On a curious appearance seen in the Sun., Mon. Not. R. Astron. Soc., XX, 15, 1859.

Holzer, R.E., and J. A. Slavin (1979), Magnetic flux transfer associated with expansions and contractions of the dayside magnetosphere. Journal of Geophysical Research 83, 3831.

Hutchinson, J. A., D. M. Wright, and S. E. Milan (2011), Geomagnetic storms over the last solar cycle: A superposed epoch analysis, J. Geophys. Res., 116, A09211.

Iyemori,T., (1990), Storm-time magnetospheric currents inferred from mid-latitude geomagnetic field variations, J.Geomag.Geoelectr., 42, 1249-1265.

Iyemori,T., and D. R. K. Rao (1996), Decay of the Dst field of geomagnetic disturbance after substorm onset and its implication to storm-substorm relation, Ann. Geophy. 14 , 608-618

J.-L. Bougeret, M.L. Kaiser, P.J. Kellogg, R.Manning, K. Goetz, et al., The radio and plasma waves investigation on the wind space craft, Space Sci. Rev. 71, 231 (1995).

Jacobs C, Poedts S, and Van der Holst B (2006), The effect of the solar wind on CME triggering by magnetic foot point shearing. Astron Astrophys 450:793–803.

Jenkins, J. B, (2009), The sun and How to Observe it, Springer, 2009 edition.

Kalegaev, V. V., I.I. Alexeev, I.S. Nazarkov, V. Angelopoulos, and A. Runov (2014), On the large-scale structure of the tail current as measured by THEMIS, Adv. Space Res., 54, 1773-1785.

Kane, R. P. (2010), Scatter in the plots of Dst(min) versus Bz(min), Planet. Space Sci., 58, 1792–1801.

Kilpua E.K.J., J.G. Luhmann, L.K. Jian , C.T. Russell , Y. Li (2014), Why have geomagnetic storms been so weak during the recent solar minimum and the rising phase of cycle 24?, J. Atmos. Sol. Terr. Phys., 107 (2014) 12–19.

Kim R-S, Gopalswamy N, Cho K-S, Moon Y-J, Yashiro S (2013) Propagation Characteristics of CMEs Associated with Magnetic Clouds and Ejecta. Sol Phys 284:77-88

Klein, L. W., and L. F. Burlaga (1982), Interplanetary magnetic clouds at 1 AU, J. Geophys. Res., **87**, 613.

Kolarski, A., Grubor, D., 2009. Study of the *X*-Ray Flare Induced Lower Ionosphere Changes by Simultaneous Monitoring of Two VLF Signals: GQD and NAA.URSI proceedings.

Kozyra, J. U (1989), Sources and losses of ring current ions - An update, Advances in Space Research 9(12): 171-182.

Kumar, A., Kumar, S., 2014. Space weather effects on the lowlatitude D-region ionosphere during solar minimum. Earth, Planets and Space, 66, 76-75.

Lean J.L., S.E McDonald, J.D. Huba, J.T Emmert, D.P Drob, C.L Siefring (2014) Geospace variability during the 2008-2009 whole heliosphere intervals. JGRA 119:3755–3776.

Liemohn, M.W., J. U. Kozyra, M . F. Thomsen. J. L. Roeder, G. Lu, J. E. Borovsky, and T . E. Cayton (2001), Dominant role of the asymmetric ring current in producing the stormtime Dst*. J. Geophys. Res. 106, 10,883–10,904.

Lindsay GM, Rusell CT, Luhmann (1995) Coronal mass ejection and stream interaction region characteristics and their potential geomagnetic effectiveness. J Geophys Res 100:16999.

Lopez, R. E., W. D. Gonzalez, V. Vasyliūnas, I. G. Richardson, C. Cid, E. Echer, G.D. Reeves, P. C. Brandt (2015), Decrease in SYM-H during a storm main phase without evidence of a ring current injection, , J. Atmos. Sol. Terr. Phys., 134, 118–129

Lui, A. T. Y.; McEntire, R. W.; Krimigis, S. M. (1987), Evolution of the ring current during during two geomagnetic storms, Journal of Geophysical Research (ISSN 0148-0227), vol. 92, July 1, 1987, p. 7459-7470.

Lynch BJ, Antiochos SK, DeVore CR, Luhmann JG, Zurbuchen TH (2008) Topological evolution of a fast magnetic breakout CME in three dimensions. Astrophys J 683:1192.

Mac-Mahon, R.M., W. D. Gonzalez (1997), Energetics during the main phase of geomagnetic superstorms. *J. Geophys. Res.* 102, 14199–14207.

MacQueen RM, Eddy JA, Gosling JT, Hildner E, Munro RH, Newkirk GA Jr, Poland AI, Ross CL (1974) The outer solar corona as observed from Skylab: preliminary results. APJ 187:L85.

MacQueen, R. M.; Eddy, J. A.; Gosling, J. T.; Hildner, E.; Munro, R. H.; Newkirk, G. A., Jr.;

Maeda, H., K. Sakurai, T. Ondoh, and M. Yamamoto (1962), Solar terrestrial relationships during the IGY and IGC, Annales Geophysicae, 18, 305–333.

Mäkelä, P., N. Gopalswamy, S. Akiyama, H. Xie, and S. Yashiro (2011), Energetic storm particle events in coronal mass ejection–driven shocks, J. Geophys. Res., 116, A08101, doi:10.1029/2011JA016683.

Makela, P., N., Gopalswamy, H., Xie, A.A., Mohamed, S., Akiyama, and S., Yashiro, (2013), Coronal hole influence on the observed structure of Interplanetary CMEs, 284: 59. doi:10.1007/s11207-012-0211-6.

Manju G., Pant, T. K., Devasia, C. V., Ravindran, S., Sridharan, R., 2009.Electrodynamical response of the Indian low-mid latitude ionosphere to the very large solar flare of 28 October 2003 – a case study. Ann. Geophys., 27, 3853–3860.

Manju G., Viswanathan, K. S., 2005. Response of the equatorial electrojet to solar flare related X-ray flux enhancements. Earth Planets Space, 57, 231–242.

Maunder, E. W (1904), Note on the distribution of sun-spots in heliographic latitude, 1874-1902, Royal Astronomical Society, Vol. 64, p.747-761.

Maurya, A. K., Singh, R., Veenadhari, B., Cohen, M. B., Kumar, S., Selvakumaran, R. Pant, P., Singh, A. K., Inan, U. S., 2012a. Morphological features of tweeks and nighttime D region ionosphere at tweek reflection height from the observations in the low-latitude Indian sector. J. Geophys. Res., 117, A05301, doi:10.1029/2011JA016976.

Maurya, A. K., Singh, R., Veenadhari, Pant, P., Singh, A.K., 2010. Application of Lightning discharge generated radio atmospherics/tweeks in lower ionospheric plasma diagnostics, Journal of Physics: Conference Series, 208, doi:10.1088/1742-6596/208/1/012061.

Maurya, A. K., Veenadhari, B., Singh, R., Kumar S., Cohen, M. B., Selvakumaran, R., Gokani, S., Pant, P., Singh, A. K., Inan, U. S., 2012b. Nighttime D region electron density measurements from ELF-VLF tweek radio atmospherics recorded at low latitudes. J. Geophys. Res., 117, A11308, doi:10.1029/2012JA017876.

Maurya, A.K., Phanikumar, D.V., Singh, R., Kumar, S., Veenadhari, B., Kwak, Y-S., Kumar, A., Singh, A.K., Kumar., K.N., 2014. Low-mid latitude D region ionospheric perturbations associated with 22 July 2009 total solar eclipse: Wave-like signatures inferred from VLF observations. J. Geophys. Res., DOI: 10.1002/2013JA019521.

Maurya, A.K., Singh, R., Kumar, S. Kumar, D.V., Veenadhari, B., 2014. Waves-like signatures in the D-region ionosphere generated by solar flares. General Assembly and Scientific Symposium (URSI GASS), 2014 XXXIth URSI, IEEE, 10.1109/URSIGASS.2014.6929796.

Mayaud, P.,(1975) Analysis of storm sudden commencements for the years 1868– 1967, J. Geophys. Res., 80(1), 111–122, 1975.

McRae, W. M., Thomson, N. R., 2000. VLF phase and amplitude: daytime ionospheric parameters. J. Atmos. Solar Terr. Phys., 62, 609–618.

McRae, W. M., Thomson, N. R., 2004. Solar flare induced ionospheric D-region enhancement from VLF phase and amplitude observations, J. Atmos. Solar Terr. Phys., 2004, 66, 77-87.

Messerotti M, Zuccarello F, Guglielmino SI, Bothmer V, Lilensten J, Noci G, Storini M, Lundstedt H (2009), Solar weather event modelling and prediction. Space Sci Rev. doi:10.1007/s11214-009-9574.

Michalek ,G., N. Gopalswamy and H. Xie (2007), Width of Radio-Loud and Radio-Quiet CMEs, Solar phys., 246, 409-414, doi: 10.1007/s11207-007-9062.

Mikic Z, and Linker J (1994) Disruption of coronal magnetic field arcades. Astrophys J 430:898–912 Miroshnichenko LI (2008) Solar cosmic rays in the system of solar-terrestrial relations. J Atmos Solar Terr Phys 70:450–466.

Mitra, A.P., 1974. Ionospheric Effects of Solar Flares. D. Reidel Publishing Company, Dordrecht-Holland.

Mohamed, A. A., N., Gopalswamy, S., Yashiro, S., Akiyama, P., Makela, H., Xie, and H. Jung (2012), The relation between coronal holes and coronal mass ejections during the rise, maximum, and declining phases of Solar Cycle 23. J. Geophys. Res. 117, 1103, doi:10.1029/2011JA016589.

Moos, N. A. F, (1910), Magnetic observations made at the Government observatory , Bombay, for the period 1846 to 1905 and their discussion , Part I: Magnetic data and instrument, Part II: The Phenomenon and its discussions, Govenmnet central press, Bombay.

Morfitt, D. G., Shellman, C. H., 1976. *MODESRCH*, an improved computer program for obtaining ELF/VLF/LF mode constants in an Earth-ionosphere waveguide, Nav. Electron. Lab. Cent., Interim Rep. 77T, San Diego, USA.

Mursula, K., and Zieger, B. (1996), The 13.5-day periodicity in the Sun, solar wind, and geomagnetic activity: The last three solar cycles, JGR, 101, 27077.

Nikolaeva, N. S., Y. I. Yermolaev, and I. G. Lodkina (2013), Modeling the time behavior of the Dst index during the main phase of magnetic storms generated by various types of solar wind, Cosmic Res., 51, 401–412.

Nikolaeva, N. S., Y. I. Yermolaev, and I. G. Lodkina (2015), Modeling of the corrected Dst* index temporal profile on the main phase of the magnetic storms generated by different types of solar wind, Cosmic Res., 53, 119–127.

Nishida, A (1983)., IMF control of the Earth's magnetosphere, Space Science Review 34, 185–200.

Nishida, A. (1966), Interpretation of SSC rise time, Rep. Ionos. Space Res. Jpn., 20, 42– 44.

Nishida, A., (1964), Transmission of storm sudden commencements through the interplanetary space; shock wave mode and non-shock mode, Rep. Ionos. Space Res. Japan, 18, 295.

Noyes R.W (1982), The Sun Our star, Harvard University press, Cambridge, 263.

Ogina, T. A.,(1986), The three dimensional MHD simulation of the interaction of the solar wind with the Earth's magnetosphere: The generation of field-aligned currents, J. Geophys. Res., 91, 6791.

Ogino, T., R. J. Walker, and M. Ashour-Abdalla (1992), A global magnetohydrodynamic simulation of the magnetosheath and magnetosphere when the interplanetary magnetic field is northward, IEEE Trans. Plasma Sci., 70, 487.

Ogino, T., R. J. Walker, M. Ashour-Abdalla, and J. M. Dawson (1986), An MHD simulation of the effects of the interplanetary magnetic field By component on the interaction of the solar wind with the Earth's magnetosphere during southward interplanetary magnetic field, J. Geophys. Res., 91, 10029.

Ohya, H., Shiokawa, K., Miyoshi, Y. 2011. Long-term variations in tweek reflection height in the D and lower E-regions of the ionosphere. J. Geophys. Res., 116, A10322, doi:10.1029/2011JA016800.

Oliveira, D. M., and J. Raeder (2014), Impact angle control of interplanetary shock geoeffectiveness, J.Geophys.Res.SpacePhysics, 119,8188–8201, doi:10.1002/2014JA020275.

Oliveira, D. M., and J. Raeder (2015), Impact angle control of interplanetary shockgeoeffectiveness: A statistical study, J.Geophys.Res., 10.1002/2015JA021147.

Ondoh, T.,(1963) Longitudinal distribution of SSC rise time, *J. Geomag. Geoelectr.*, **14**, 198–207.

Ontiveros, V., and J. A. Gonzalez-Esparza (2010), Geomagnetic storms caused by shocks and ICMEs, J. Geophys. Res., 115, A10244, doi:10.1029/2010JA015471.

Pant, P., 1993. Relation between VLF phase deviations and solar X-ray fluxes during solar flares.Astrophys. Space Sci. 209, 297–306.

Perrault, P., and S. I. Akasofu (1978), A study of magnetic storms, Geophysical Journal of Royal Astronomical Society 54, 547–573.

Phanikumar, D.V, Kwak, Y.-S., Patra, A. K., Maurya, A. K., Singh, R., Park, S.M., 2014 Response of the mid-latitude D-region ionosphere to the Total Solar Eclipse of 22 July 2009 studied using VLF signals from South Korean peninsula, Advances in Space Research. doi:10.1016/j.asr.2014.06.005.

Poland, A. I.; Ross, C. L. (1974), The Outer Solar Corona as Observed from Skylab:

Potgieter MS, Vos EE, Boezio M, De Simone N, Di Felice V, Formato V (2014), Modulation of galactic protons in the heliosphere during the unusual solar minimum of 2006 to 2009. SoPh 289:391–406.

Raeder, J. (2003), Global magnetohydrodynamics: A tutorial review, in Space Plasma Simulation, edited by J. Buchner, C. T. Dum, and M. Scholer, Springer, Berlin, doi:10.1007/3-540-36530-311.

Rastogi, R. G., Pathan, B. M., Rao, D. R. K., Sastry, T. S., and Sastri, J. H,1999. Solar flare effects on the geomagnetic elements during normal and counter electrojet periods. Earth Planets Space, 51, 947–957.

Rastogi, R., Klobuchar, J., 1990. Ionospheric Electron Content within the Equatorial F2 Layer Anomaly Belt. J. Geophys. Res., 95, 19045–19052.

Richardson, I. G., H. V. Cane, and E. W. Cliver (2002), Sources of geomagnetic activity during nearly three solar cycles (1972 –2000), J. Geophys. Res., 107(A8), 1187, doi:10.1029/2001JA000504.

Richardson, I., and H. V. Cane (2010), Near-Earth interplanetary coronal mass ejections during solar cycle 23 (1996–2009): Catalog and summary of properties, Sol. Phys., 264(1), 189–237.

Riley, P. and I. G., Richardson (2012), Using statistical multivariable models to understand the relationship between Interplanetary Coronal Mass Ejecta and Magnetic Flux Ropes Sol. Phys., **012,** 6-9.

Rishbeth, H., Garriott, O. K. 1969. Introduction to Ionospheric Physics. Academic Press, New York, London.

Russell, C. T (1990), The Magnetopause, Geophysical Monograph Series, Physics of magnetic flux ropes, 58.

Russell, C. T., M. Ginskey, and S. M. Petrinec (1994), Sudden impulses at lowlatitude stations: Steady state response for northward interplanetary magnetic field, J. Geophys. Res., 99, 253–261.

Samsonov, A. A. D. G. Sibeck, and J. Imber (2007), MHD simulation for the interaction of an interplanetary shock with the Earth's magnetosphere. J. Geophys. Res., Volume 112, Issue A12, DOI: 10.1029/2007JA012627.

Sandeep Kumar, B Veenadhari, S Tulasi Ram, R Selvakumaran, Shyamoli Mukherjee, Rajesh Singh, BD Kadam (2015), Estimation of interplanetary electric field conditions for historical geomagnetic storms, J. Geophys. Res., 120, 10.1002/2015JA021661.

Sastri J.H., 1975. The geomagnetic solar flare effect of 6 July 1968 and its implications. Ann.Geophys. 31, 481-485.

Scholer., M (1999) Origin, injection, and acceleration of CIR particles: theory, report of working group. Space Sci Rev 89:369–399.

Schwabe, Heinrich (1851), Solar observations during 1843, Astron. Nachr., 20(495), (Reprinted in Kosmos, edited by A. yon Humboldt. Also reprinted by A. J. Meadows, in Early Solar Physics, pp. 95-97, Pergamon, New York, 1970.)

Schwartz, S. J. (1998), Shock and discontinuity normals, mach numbers, and related parameters, in Analysis Methods for Multi-Spacecraft Data, edited by G. Paschmann and P. W. Daily, ISSI Sci. Rep. SR-001, ESA Publ. Div., Noordwijk, Netherlands.

Schwenn, R (2006) Solar wind sources and their variations over the solar cycle. Space Sci Rev 124:51–76.

Seeds., M (1994), Fundamentals of astronomy, Wadsworth Publishing Company.

Shinbori, A., T. Ono, and H. Oya (2002), SC-triggered plasma waves observed by the Akebono satellite in the polar regions and inside the plasmasphere, Adv. Polar Atmos. Res., 16, 126–135.

Shinbori, A., T. Ono, M. Iizima, A. Kumamoto, and H. Oya (2003b), Sudden commencements related plasma waves observed by the Akebono satellite in the polar region

and inside the plasmasphere region, J. Geophys. Res., 108, 1457, doi:10.1029/2003JA009964.

Shinbori, Yuji Tsuji, Takashi Kikuchi, Tohru Araki, and Shinichi Watari (2009), Magnetic latitude and local time dependence of the amplitude of geomagnetic sudden commencements, J. Geophys. Res., 114, A04217, doi: 10.1029/2008JA013871.

Sibeck, D.G., R. E. Lopez, and E. C. Roelof (1991), Solar wind control of the magnetopause shape, location and motion. Journal of Geophysical Research 96, 5489.

Singer, S. F. (1957) A New Model of Magnetic Storms and Aurorae, Transact. American Geophysical Union, Volume 38, Issue 2, p. 175-190

Singh, As. K., Singh, A. K., Singh, R., Singh, R. P., 2013. Solar Flare induced D-region ionospheric perturbations evaluated from VLF measurements. Astrophysics and Space Sciences, doi: 10.1007/s10509-013-1699-4.

Singh, As. K., Singh, R., Veenadhari, B., Singh, A.K., 2012. Response of low latitude D-region ionosphere to the total solar eclipse of 22 July 2009 deduced from ELF/VLF analysis, Advances in Space Research, http://dx.doi.org/10.1016/j.asr.2012.07.005.

Singh, R., Veenadhari, B., Cohen, M. B., Pant, P., Singh, A.K., Maurya, A.K., Vohat, P., Inan, U.S. 2010. Initial results from AWESOME VLF receivers: set up in low latitude Indian regions under IHY2007/UNBSSI. Current Science, 98 (3), 398-405.

Singh, R., Veenadhari, Maurya, A.K., Cohen, M. B., Kumar, S., Selvakumaran, R., Pant, P., Singh, A.K., Inan, U.S. 2011. D-region ionosphere response to the Total Solar Eclipse of 22 July 2009 deduced from ELF-VLF tweek observations in the Indian sector, Journal of Geophysical Research, doi:10.1029/2011JA016641.

Siscoe, G. L.: 1976, 'Three Dimensional Aspects of Interplanetary Shock Waves', *J. Geophys. Res*. 81, 6,235–6,241.

Smith E.J., and J. H. Wolf (1976) Observations of interaction regions and corotating shocks between one and five AU: Pioneers 10 and 11. GRL 3:137.

Smith, E. J., B. T. Tsurutani, J. A. Slvain, D. E. Jones, G. L. Siscoe and D. A. Mendis (1986), International Cometary Explorer Encounter with Giacobini-Zinner: Magnetic Field Observations, Science., 232, 382-385, doi: 10.1126/science.232.4748.382.

Solomon S.C., L. Qian , and A. G. Burns (2013) The anomalous ionosphere between solar cycles 23 and 24. JGR 118:6524–6535.

Sripathi S., Balachandran, N., Veenadhari, B., Singh, R.,Emperumal, K., 2013. Response of the equatorial and low latitude ionosphere to an intense *X*-class solar flare (X7/2B) as observed on 09 August 2011. J. Geophys. Res., doi:10.1002/jgra.50267.

Sugiura, M. (1964), Hourly values of equatorial *Dst* for the IGY, *Ann. Int. Geophys. Year*, **35**, 9–45.

Sugiura, M., and S. Chapman (1960), The average morphology of geomagnetic storms with sudden commencement, A bandl. Akad. Wiss., GottingenM ath. Phys. K1 (4), 1960.

Svestka Z (1976) Solar flares, Geophysics and Astrophysics Monographs Series, vol 8. D. Reidel, Dordrecht.

Takeuchi, T., C. T. Russell, and T. Araki (2002), Effect of the orientation of interplanetary shock on the geomagnetic sudden commencement, J. Geophys. Res., 107(A12), 1423, doi:10.1029/2002JA009597.

Tanaka, T. (1995), Generation mechanisms for magnetosphere-ionosphere current systems deduced from a three-dimensional

Tanaka, T. (2000a), The state transition model of the substorm onset, J. Geophys. Res., 105, 21,081, doi:10.1029/2000JA900061.

Tanaka, T. (2000b), Field-aligned current systems in the numerically simulated magnetosphere, in Magnetospheric Current Systems, Geophys.Monogr. Ser., vol. 118, edited by S. Ohtani et al., pp. 53–59, AGU, Washington, D. C.

Tanaka, T. (2007), Magnetosphere-ionosphere convection as a compound system, Space Sci. Rev., 133, 1, doi:10.1007/s11214-007-9168-4.

Tanaka, T. (2015), Substorm auroral dynamics reproduced by the advanced global M-I coupling simulation, in Auroral Dynamics and Space Weather, Geophys. Monogr. Ser., vol. **215**, edited by Y. Zhang and L. J. Paxton, 177 pp., AGU,Washington, D. C.

Tanaka, T., A. Nakamizo, A. Yoshikawa, S. Fujita, H. Shinagawa, H. Shimazu, T. Kikuchi, and K. K. Hashimoto (2010), Substorm convection and current system deduced from the global simulation, J. Geophys. Res., 115, A05220, doi:10.1029/2009JA014676.

Tanaka, T.,(1994), Finite volume TVD scheme on an unstructured grid system for three dimensional MHD simulation of inhomogeneous systems including strong background magnetic fields, J. Cornput. Phys., 111,381, 1994

Thomson, N. R., Clilverd, M. A., 2001. Solar flare induced ionospheric D-region enhancements from VLF amplitude observations. J. Atmos. Solar Terr. Phys., 63 (7), 1729–1737.

Thomson, N. R., Cliverd, M. A., McRae, W. M., 2007. Nightime D region parameters from VLF amplitude and Phase. J. Geopys. Res., 112, A07304, doi:10.1029/2007JA91227.

Thomson, N. R., McRae, W. M., 2009. Nighttime ionospheric D region: Equatorial and nonequatorial, J. Geophys. Res., 114, A08305, doi:10.1029/2008JA014001.

Thomson, N. R., Rodger, C. J., 2004. Dowdenand Dowden, R. L., 2004. Ionosphere gives size of greatest solar flare. Geophys. Res. Lett., 31, L06803, doi:10.1029/ 2003GL019345.

Thomson, N. R., Rodger, C. J., Clilverd, M. A., 2005. Large solar flares and their ionosperic D region enhancements. J. Geophys. Res., 110, A06306, doi:10.1029/2005JA011008.

Tousey, R., (1973), “The Solar Corona”, in Space Research XIII , (Eds.) Rycroft, M.J., Runcorn,S.K., Proceedings of open meetings of working groups on physical sciences of the 15th plenary meeting of COSPAR, Madrid, Spain, 10 – 24 May, 1972, p. 713, Akademie-Verlag, Berlin.

Tsunomura S (1998), Characteristics of geomagnetic sudden commencement observed in middle and low latitudes. Earth Planets Space 50:755–772.

Tsurutani BT, Gonzalez WD, Gonzalez ALC, Tang F, Arballo JK, Okada M (1995a) Interplanetary origin of geomagnetic activity in the declining phase of the solar cycle. J Geophys Res 100:21717.

Tsurutani, B. T, Ho CM, Arballo JK, Goldstein BE, Balogh A (1995b) Large amplitude IMF fluctuations in corotating interaction regions: Ulysses at mid latitudes. Geophys Res Lett 22:3397.

Tsurutani, B. T., and W. D. Gonzalez (1997), The interplanetary causes of magnetic storms: A review, in Magnetic Storms, Geophys. Monogr. Ser., vol. 98, edited by B. T. Tsurutani et al., pp. 77 – 89, AGU, Washington, D. C.

Tsurutani, B. T., E. Echer, F. L. Guarnieri, and W. D. Gonzalez (2011), The properties of two solar wind high speed streams and related geomagnetic activity during the declining phase of solar cycle 23, J. Atmos. Sol. Terr. Phys., 73, 164–177.

Tsurutani, B. T., R. L. McPherron, W. D. Gonzalez, G. Lu, N. Gopalswamy, and F. L. Guarnieri (2006), Magnetic storms caused by corotating solar wind streams, AGUMonograph 167, Recurrent magnetic storms, corotating solar wind streams.

Tsurutani, B. T., Verkhoglyadova, O. P., Mannucci, A. J., Lakhina, G. S., Li, G., Zank, G. P., 2009. A brief review of “solar flare effects” on the ionosphere. Radio Sci., 44, RS0A17, doi: 10.1029/2008RS004029.

Tsurutani, B. T., W. D. Gonzalez, A. L. C. Gonzalez, F. Tang, J. Arballo, and M. Okada (1995), Interplanetary origin of geomagnetic activity in the declining phase of the solar cycle, J. Geophys. Res., 100(A11), 21,717–21,733.

Tsurutani, B. T., W. D. Gonzalez, F. Tang, and Y. T. Lee (1992), Great magnetic storms, Geophys. Res. Lett., 19, 73.

Tsurutani, B. T., W. D. Gonzalez, F. Tang, S. I. Akasofu, and E. J. Smith (1988), Origin of interplanetary southward magnetic fields responsible for major magnetic storms near solar maximum (1978–1979), J. Geophys. Res., 93, 8519– 8531.

Tsurutani, B. T., W. D. Gonzalez, F. Tang, S. I. Akasofu, and E. J. Smith (1988), Origin of interplanetary southward magnetic fields responsible for major magnetic storms near solar maximum (1978–1979), J. Geophys. Res., 93, 8519.

Turner, N. E., D. N. Baker, T. I. Pulkkinen, and R. L. McPherron (2000), Evaluation of the tail current contribution to Dst, J. Geophys.Res., 105, 5431.

Ugarte-Urra I, Warren HP, Winebarger AR (2007), The magnetic topology of coronal mass ejection sources. Astrophys J 662:1293–1301.

Usadi, A., A. Kageyama, K. Watanabe, and T. Sato (1993), A global simulation of the magnetosphere with a long tail; Southward and northward interplanetary magnetic field, J. Geophys. Res., 98, 7503.

Valnicek, B., Ranzinger, P., 1972. X-ray emission and D-region ‘sluggishness’. Bull. Astron. Inst. Czechoslov. 23, 318–322.

Veenadhari B, R. Selvakumaran, R. Singh, A. K. Maurya, N. Gopalswamy, S. Kumar, T. Kikuchi (2012), CME-driven shocks and the associated sudden commencements/sudden impulses, J. Geophysical. Res., 117, A04210, doi:10.1029/2011JA017216.

Vinokur, M., (1989) An analysis of finite-difference and finite-volume formations of conservation laws, J. Cornput. Phys., 81, 1.

Vourlidas CA, Howard RA, Esfandiari E, Patsourakos S, Yashiro S, Michalek G (2011), Erratum: “comprehensive analysis of coronal mass ejection mass and energy properties over a full solar cycle” (2010, Astrophys J 722, 1522). Astrophys J 730:59.

Wait, J. R., Spices K. P., 1964. Characteristics of the earth ionosphere wave guide for VLF radio waves. NBS tech. Note 300, Natl. Bur. Of Stand, Boulder, Colorado USA.

Walker, R. J., T. Ogino, J. Raeder, and M. Ashour-Abdalla (1993), A global magnetohydrodynamic simulation of the magnetosphere when the interplanetary magnetic field is southward: The onset of magnetotail reconnection, J. Geophys. Res., 98, 17235.

Wang, C., C. X. Li, Z. H. Huang, and J. D. Richardson (2006), Effect of interplanetary shock strengths and orientations on storm sudden commencement rise times, Geophys. Res. Lett., 33, L14104, doi: 10.1029/2006GL025966.

Wang, C., H. Li, J. D. Richardson, and J. R. Kan (2010), Interplanetary shock characteristics and associated geosynchronous magnetic field variations estimated from sudden impulses observed on the ground, J. Geophys. Res., 115, A09215, doi: 10.1029/2009JA014833.

Wang, C., J. B. Liu, H. Li, Z. H. Huang, J. D. Richardson, and J. R. Kan (2009), Geospace magnetic field responses to interplanetary shocks, J. Geophys. Res., 114, A05211, doi:10.1029/2008JA013794.

Wang, C., Z. H. Huang, Y. Q. Hu, and X. C. Guo (2005), 3D global simulation of the interaction of interplanetary shocks with the magnetosphere, in 4th Annual IGPP International Astrophysics Conference on the Physics of Collisionless Shocks, AIP Conf. Proc., edited by G. Li, G. Zank, and C. T. Russell, pp. 320–324, Am. Inst. of Phys., Washington, D. C., doi:10.1063/1.2032716.

Wang, C.B., J.K Chao, C.-H Lin (2003), Influence of the solar wind dynamic pressure on the decay and injection of the ring current. J. Geophys. Res. 108 (A9), 1341, http://dx.doi.org/10.1029/2003JA009851.

Watanabe, K., and T. Sato (1990), Global simulation of the solar windmagnetosphere interaction: The importance of its numerical validity, J. Geophys. Res., 95, 75.

Watari S (1997) The effect of the high-speed stream following the corotating interaction region on the geomagnetic activities. Ann Geophys 15:662–670. doi:10.1007/s00585-997-0662-5.

Watermann J, Vainio R, Lilensten J, Belehaki A, Messeroti M (2009b) The state of space weather scientific modelling an introduction. Space Sci Rev 147:111–120.

Watermann J, Wintoft P, Sanahuja B, Saiz E et al (2009a) Models of solar wind structures and their interaction with the earth's space environment. Space Sci Rev 147:233–270.

Webb, D. F. (1991), The solar cycle variation of the rates of CMEs and related activity, *Adv. Space Res.*, *11*, 37–40.

Webb, D. F., N. U. Crooker, S. P. Plunkett, and O. C. St. Cyr (2001), The solar sources of geoeffective structures, in Space Weather, Geophys. Monogr. Ser., vol. 125, edited by S. Paul, J. S. Howard, and L. S. George, pp. 123– 142, AGU, Washington, D. C.

Webb, D.F. and Howard, R.A. (1994), The solar cycle variation of coronal mass ejections and the solar wind mass flux, *J. Geophys. Res.,* 99, 4201.

Weigel, R. S. (2010), Solar wind density influence on geomagnetic storm intensity, J. Geophys. Res., 115, A09201, doi:10.1029/2009JA015062.

Weiss, L. A., P.H. Reif, J. J. Moses, B. D. Moore, and R. A. Heelis (1992), Energy dissipations in substorms, Eur. Space Agency Spec. Pub., ESA-SP-335,309-319.

Wilken, B., C. K. Goertz ,D. N. Baker P. R. Higbie and T. A. Fritz (1982), The SSC on July 29, 1977 and its Propagation Within the Magnetosphere, J. Geophys. Res., 87, A8, 5901-5910.

Williams, D. J.,(1957), Ring current and radiation belts, U.S. Natl. Rep. Int. Union Geod. Geophys1. 983-1986, Rev. Geophys.,25, 570-578.

Wilson, R. M. (1987), Geomagnetic response to magnetic clouds, Planetary and Space Sci. 33, 329.

Wu, C. C. and R. P., Leeping(2011) Statistical comparison of magnetic clouds with Interplanetary Coronal Mass Ejections for solar Cycle 23, Sol. Phys., 269,441-453.

Wu, C. C., and R. P. Lepping (2006), Solar cycle effect on geomagnetic storms caused by interplanetary magnetic clouds, Ann. Geophys., 24, 3383– 3389.

Wu, C., and R. P. Lepping (2002), Effects of magnetic clouds on the Occurrence of geomagnetic storms: The first 4 years of Wind, J. Geophys. Res., **107**(A10), 1314, doi: 10.1029/2001JA000161.

Xie, H., N., Gopalswamy and O. C. St.Cyr (2013), Near-Sun Flux Rope Structure of CMEs, Sol Phys (2013) 284: 47. doi:10.1007/s11207-012-0209-0.

Xu, D., T. Chen, X. X. Zhang, and Z. Liu (2009), Statistical relationship between solar wind conditions and geomagnetic storms in 1998–2008, Planet. Space Sci., 57, 1500–1513.

Yashiro, S., N. Gopalswamy, G. Michalek, O. C. St. Cyr, S. P. Plunkett, N. B. Rich, and R. A. Howard (2004), A catalog of white light coronal mass ejections observed by the SOHO spacecraft, J. Geophys. Res., 109, A07105, doi:10.1029/2003JA010282.

Yermolaev, Y. I., N. S. Nikolaeva, I. G. Lodkina, and M. Y. Yermolaev (2010), Specific interplanetary conditions for CIR-Sheath-, and ICME-induced geomagnetic storms obtained by double superposed epoch analysis, Ann. Geophys., 28, 2177.

Yokouchi, Y., (1953) Principal magnetic disturbances at Kakioka, 1924–1951, Mem. Kakioka Geomag. Obs., 204–229.

Zhang, J., I. G. Richardson, D. F. Webb, N. Gopalswamy, E. Huttunen, J. C. Kasper, N. V. Nitta, W. Poomvises,1 B. J. Thompson, C.-C. Wu, S. Yashiro, and A. N. Zhukov (2007), Solar and interplanetary sources of major geomagnetic storms (Dst < 100 nT) during 1996–2005, J. Geophys. Res., 112, A10102, doi:10.1029/2007JA012321.

Zhang, J., et al. (2007), Solar and interplanetary sources of major geomagnetic storms (Dst ≤ 100 nT) during 1996– 2005, J. Geophys. Res., **112**, A10102, doi:10.1029/2007JA012321

Zhang, J., I. G. Richardson and D. F. Webb (2008a), Interplanetary origin of multiple-dip geomagnetic storms J. Geophys. Res., VOL. 113, A00A12, doi:10.1029/2008JA013228.

Zhang, J., K. P. Dere, R. A. Howard, and V. Bothmer (2003), Identification of solar sources of major geomagnetic storms between 1996 and 2000, Astrophys. J., 582, 520– 533.

Zhang, J., M. W. Liemonh, J. U. Kozyra, M. F. Thomsen, H. A. Elliott, and J. M. Weygand (2006), A statistical comparison of solar wind sources of moderate and intense geomagnetic storms at solar minimum and maximum, J. Geophys. Res., 111, A01104.

Zhang, Y., W. Sun, X. S. Feng, C. S., Deehr, C. D. Fry and M. Dryer (2008b), Statistical analysis of corotating interaction regions and their geoeffectiveness during solar cycle 23, J. Geophys. Res., VOL. 113, A08106, doi: 10.1029/2008JA013095.

Zigman, V., Grubor, D., Suli´c, D., 2007. D-region electron density evaluated from VLF amplitude Δt during *X*-ray solar flares. J. Atmos. Solar Terr. Phys., 69(7), 775–792.

Zirker, J.B. (2001), Journey form Centre of the sun, Princeton University Press.